2011

Mass Conservation Analysis For The Lower St. Johns River Using Continuous And Discontinuous Galerkin Finite Element Methods

Lillie E. Thomas
University of Central Florida

MASS CONSERVATION ANALYSIS FOR THE LOWER ST. JOHNS RIVER USING CONTINUOUS AND DISCONTINUOUS GALERKIN FINITE ELEMENT METHODS

by
LILLIE E. THOMAS
B.S. University of Central Florida, 2008

A thesis submitted in partial fulfillment of the requirements
for the degree of Master of Science
in the Department of Civil, Environmental, and Construction Engineering
in the College of Engineering and Computer Science
at the University of Central Florida
Orlando, Florida

Spring Term
2011

Major Professor: Scott C. Hagen

ABSTRACT

This thesis provides a mass conservation analysis of the Lower St. Johns River for the purpose of providing basis for future salinity transport modeling. The analysis provides an assessment of the continuous (CG) and discontinuous (DG) Galerkin finite element methods with respect to their mass conservation properties. The following thesis also presents a rigorous literature review pertaining to salinity transport in the Lower St. Johns River, from which this effort generates the data used to initialize and validate numerical simulations. Two research questions are posed and studied in this thesis: can a DG-based modeling approach produce mass conservative numerical solutions; and what are the flow interactions between the river and the marshes within the coastal region of the Lower St. Johns River?

Reviewing the available data provides an initial perspective of the ecosystem. For this, salinity data are obtained and assembled for three modeling scenarios. Each scenario, *High Extreme*, *Most Variable*, and *Low Extreme*, is 30 days long (taken from year 1999) and represents a unique salinity regime in the Lower St. Johns River. Time-series of salinity data is collected at four stations in the lower and middle reaches of the Lower St. Johns River, which provides a vantage point for assessing longitudinal variation of salinity. As an aside, precipitation and evaporation data is presented for seven stations along the entire St. Johns River, which provides added insight into salinity transport in the river.

A mass conservation analysis is conducted for the Lower St. Johns River. The analysis utilizes a segmentation of the Lower St. Johns River, which divides the domain into sections

based on physical characteristics. Mass errors are then calculated for the CG and DG finite element methods to determine mass conservative abilities. Also, the flow interactions (i.e., volume exchange) between the river and marshes are evaluated through the use of tidal prisms. The CG- and DG- finite element methods are then tested in tidal simulation performance, which the results are then compared to observed tides and tidal currents at four stations within the lower portion of the Lower St. Johns River. Since the results show that the DG model outperforms the CG model, the DG model is used in the tidally driven salinity transport simulations. Using four stations within the lower and middle part of the Lower St. Johns River, simulated and observed water levels and salinity concentrations are compared.

Dedicated with love to my amazing parents, Lemuel and Betty Thomas, Jr., for their endless love and support.

ACKNOWLEDGMENTS

The following thesis would not have come to a completion without the wonderful support of my loving parents Lemuel and Betty Thomas, Jr. Their endless encouragement helped me to venture this incredible task. Due to their efforts and sacrifices, I am one step closer to my dream and future career. To them, I will be forever grateful and appreciative of all that they are and have done. Also, I would like to thank my sister, Tiffany, and brothers, Lemuel and Brian Thomas, for their never-ending encouragement. Thank you for giving me the strength and drive to continue this program. I will be forever thankful.

The opportunity and ability to work on this incredible project was given to me by my extraordinary advisor, Dr. Scott C. Hagen. He provided me with the knowledge and equipment to explore the many possibilities associated with this project. His advice throughout this project is greatly appreciated and I thank him for letting me be a part of the UCF CHAMPS Laboratory (http://www.champs.cecs.ucf.edu). I would also like to thank my other committee members, Dr. Dingbao Wang and Dr. Peter Bacopoulos, for their input to improve this thesis, advice and support.

My experience at UCF has helped me to grow. With the help of the NSF UCF EXCEL (http://www.excel.ucf.edu) program and the opportunities provided by Dr. Cynthia Young and Dr. Michael Georgiopoulos, I had the great privilege to pass on my knowledge and encouragement to the future engineering students. The students and my fellow tutors within the

program gave me inspiration to explore other aspects within my career choice and always kept me on my toes. I will always remember the great minds that I had the opportunity to encounter.

The UCF CHAMPS Laboratory gave me the opportunity to explore a unique aspect of civil and environmental engineering. I would like to thank the past and present members for all of their shared knowledge, advice, and great times: Derek Giardino, Dr. Ammarin Daranpob, Stephen Medeiros, Davina Passeri, Alfredo Ruiz, Matthew Bilskie, Hitoshi Tamura, and Daina Smar. I especially would like to give a heartfelt thank you to Dr. Peter Bacopoulos for guiding me throughout my time within the UCF CHAMPS Laboratory, UCF EXCEL, and this entire project. I consider him a mentor and am truly grateful for all his advice and feedback on this thesis.

Finally, I would like to thank Dr. Ethan Kubatko at The Ohio State University for providing the numerical code that is applied herein and for offering his modeling expertise over the course of this thesis.

This research was funded in part under Award No. 1045151 from the National Science Foundation (NSF) and Contract No. W912EP-06-D-0012 from Taylor Engineering, Inc. and the U.S. Army Corps of Engineers (USACE). The statements and conclusions are those of the authors and do not necessarily reflect the views of NSF, Taylor Engineering, Inc., USACE, or their affiliates.

TABLE OF CONTENTS

LIST OF FIGURES

LIST OF TABLES

CHAPTER 1 INTRODUCTION

Estuaries and salt marshes are highly interconnected ecosystems. Diverse plant and animal species are dependent on these ecosystems for shelter and food. The U.S. Fish and Wildlife Service reported in 1996 that approximately 1.14 million acres of estuarine ecosystems remained in Florida. Dahl (1998) stated that the population decreased by 71% due to coastal urban expansion. Salinity transport models, given they accurately describe the physics, can aid in determining the health of an estuary by displaying possible salinity changes due to outside influences like construction and land alterations.

The St. Johns River is the longest river in the state of Florida with a length of 500 km. It sits within 16 counties and has a drainage basin of approximately 22,000 km^2. However, this thesis will only focus on the lower or northern portion of the river (see Figure 1.1), which begins from the mouth of the river at Mayport, FL to Lake George; a total length of approximately 200 km. The river has a very slow flow rate due to its very small slope, which on average is 2.2 cm per kilometer (Toth, 1993). Additionally, numerous coastal wetlands surround the lower 40 km of the river, all of which are hydraulically connected to the river via the many tidal creeks fringe off the main river stem. The 61.2 km^2 (15.1×10^3 acres) of coastal wetlands, 46.0 km^2 (11.3×10^3 acres) of them located north of the main river stem and 15.2 km^2 (3.77×10^3 acres) of located south of the main river stem, will be the main focus of this study on longitudinal salinity transport.

Salinity transport is driven by the balance between the incoming ocean water at Mayport and the freshwater discharge resulting from the watershed. Sucsy and Morris (2002) stated that "the incoming ocean tide exists as a nearly pure progressive shallow-water wave over the lower 50 km of the river, from the mouth to Jacksonville, with maximum flow occurring near the time of high water." They continue on to mention that "between Orange Park (river km 60) and Palatka (river km 130), the tidal wave takes on the characteristics of a standing wave causing the maximum flood to precede high water by nearly 3 hours near Green Cove Springs (river km 79)." Based on these facts, the Lower St. Johns River is tidally active. Secondly, the oceanic ebb and flood tides within the nearby estuaries contribute to the salinity transport within the river. It should also be noted that the lower portion of the St. Johns River obtains an estimated 60% of its total annual freshwater flow from sources upstream of Buffalo Bluff (river km 148).

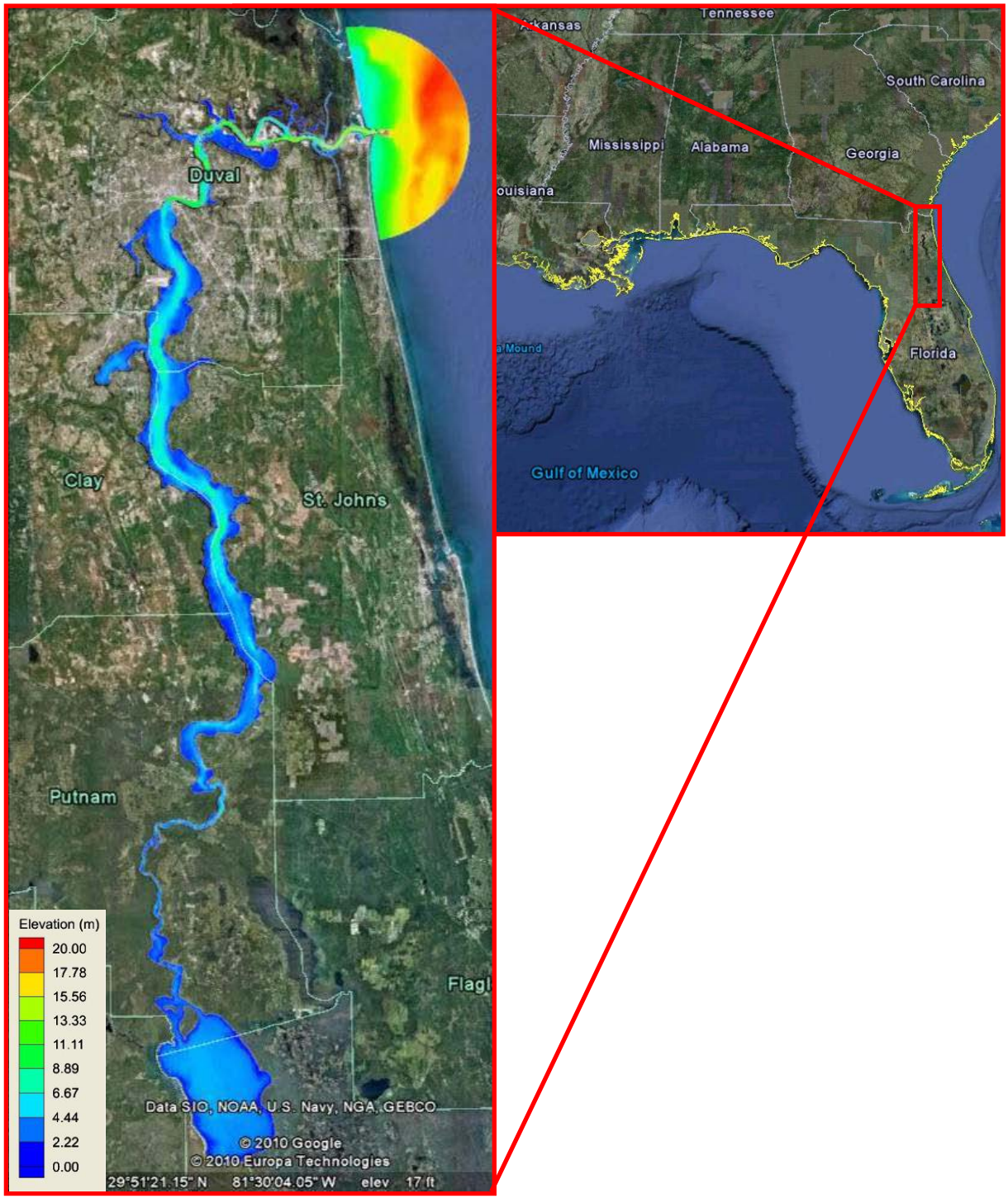

Figure 1.1: Contoured depths within the Lower St. Johns River (northeastern Florida)

(*Background: Google Earth, 2010*)

Mathematical models are used as both diagnostic and prognostic tools, for the purpose of understanding the existing system and in the planning of future impacts, respectively. Such future impacts include engineering projects which can potentially alter the natural system, either positively or negatively. As an example, the Jacksonville Port Authority and the United States Army Corps of Engineers have planned channel enhancements for the port in Jacksonville. The planned enhancement will include the deepening of the channel by two feet (60 cm) within the lower 40 km of the river, starting from the river's mouth in Mayport, FL to Jacksonville, FL. Also, the western portion of the Blount Island channel will be deepened by eight feet (2.5 meters). These alterations could cause the salinity characteristics to change due to an increase volume of ocean water. This could lead to changes to the surrounding estuaries, which are homes, feeding grounds, and nurseries to many species of plant and animal life (Sucsy and Morris, 2002; Dyer, 1973; Gunnison, 1978; Carter, 1988).

There remains an unanswered research question related to salinity transport in the Lower St. Johns River: what are the flow interactions between the river and the marshes within the coastal region of the Lower St. Johns River? To study and answer this question, a fully coupled hydrodynamic-transport model will be used to simulate salinity transport in the Lower St. Johns River including the wetlands surrounding the coastal region. In addition, the model will be evaluated based on mass conservation to provide insight on enhancing physics-based simulations. This thesis begins with an extensive literature review (Chapter 2) that explains estuaries and the processes related to longitudinal salinity transport within estuaries. Chapter 3 and Chapter 4 present the domain decomposition and modeling scenarios, respectively. Chapters 5, 6, and 7 present the finite element mesh, land cover analysis, and model setup. Chapter 8

presents the mass conservation analysis. Model results are compared to observed data in order to validate the hydrodynamics and longitudinal salinity transport (Chapter 9). Finally, Chapter 10 includes the conclusions and discussion of future work.

CHAPTER 2 LITERATURE REVIEW

The major goal of this thesis is to apply a computational model in order to examine salinity transport in the lower St. Johns River and local marshes, and the dependence of salinity content in the river on the marsh system. Therefore, it is necessary to understand relevant components of the hydroscience of this subset of the larger ecosystem and how the components interact to influence salinity levels, and vice versa. The following literature review will look into two major sections required for this study: 1) estuaries and their hydrodynamic and chemical components, and the interaction with plant and animal life; and 2) salinity transport models, along with relevant past studies of the St. Johns River and similar ecological systems.

2.1. Estuaries

2.1.1. What They Are

Estuaries are numerous along Florida's coastline and play a role in the state's overall ecology. There are several definitions of an estuary (Wolanski, 2007). The simplest definition denotes an estuary as the location where the river meets the sea (Molles, Jr., 2008). Furthermore, Wolanski (2007) stated that an estuary is a "buffer zone between river (freshwater) and ocean (saltwater) environments that may be affected by tidal oscillations." He continued in detail with the following:

> "An estuary is a semi-enclosed body of water connected to the sea as far as the tidal limit or the salt intrusion limit and receiving freshwater runoff, recognizing that the freshwater inflow may not be perennial (i.e. it may occur only for part of the year) and that the connection to the sea may be closed for part of the year (e.g. by a sand bar) and that the tidal influence may be negligible. The definition includes fjords, fjards, river mouths, deltas, rias, lagoons, tidal creeks, as well as the more classical estuaries. It recognizes commonalities with predominantly brackish areas such as the Baltic Sea, and the freshwater – poor coastal waters in arid zones."

Dyer (1973) has gone further to provide information to classify estuaries based on the estuary's specific hydrologic cycle, topography, and salinity structure. Considering the hydrologic cycle, estuaries can be classified as positive, the amount of freshwater entering the estuary exceeds the amount leaving through evaporation, or negative, when the opposite occurs which causes hypersaline conditions. An example of a negative estuary is the Laguna Madre in Texas. A majority of estuaries in existence are considered to be positive (Dyer, 1973).

The topography of estuaries can be split into four different categories: (1) coastal plain estuaries, (2) fjords, (3) bar-built estuaries, and (4) miscellaneous. Coastal plain estuaries (also referred to as drowned river valleys) were formed by the flooding of low-incised valleys caused by the melting of glaciers during the last ice age. They usually have a triangular cross section with a maximum depth of 30 meters. Fjords were formed similarly to that of coastal plain estuaries, however, these valleys are narrower and longer in comparison, and their cross section

is usually a rectangular shape. Bar-built estuaries were formed in the same manner as the coastal plain estuaries; however, with the formation of a sand bar due to the accumulation of sediment caused by wave breakage at the beach. Lastly, the fourth category, which will not be discussed in detail, includes all other estuaries, especially deltas and tectonic estuaries, formed in other ways not discussed in the first three categories. A delta, however, is considered to be a bar-built estuary when the sand bar is formed from the river's outflow and scouring. Tectonic estuaries are formed during the shifting of the Earth's tectonic plates and the mixture of fresh and sea water occurs. (Dyer, 1973; NOAA Ocean Service Education: website http://oceanservice.noaa.gov/education/kits/estuaries/estuaries04_geology.html accessed on April 1, 2010).

Dyer (1973) and the National Oceanic and Atmospheric Administration Ocean Service (2008) have classified estuaries based on their stratification and salinity distributions. The four classifications consist of the following: 1) highly stratified salt wedge type, 2) fjords, 3) partially mixed, and 4) homogeneous with the subcategories of a) vertically homogenous and b) laterally (sectionally) homogeneous. The highly stratified salt wedge estuary occurs when the river rapidly discharges into the weak ocean currents, which causes the fresh water to keep the ocean currents from transporting the sea water upstream. The freshwater floats on top of the weak tidal currents, and causes a salt wedge to be formed on the bottom. Very little mixing occurs between sea water and fresh water; however, the salinity concentration will be "virtually constant along the estuary," and the location of the salt wedge varies due to the weather and tidal conditions. The second category, fjords, is similar to the highly stratified salt wedge type, but the formation of a salt wedge does not occur due to lack of water circulation caused by shallow barriers, also

known as sills. Partially mixed estuaries, compared to the previous two types, have mixing which occurs at all depths of the water column. It should be noted that the lower layers will have a higher salinity concentration than the upper layers with the mid-depth of the estuary having the highest salinity concentration. Also, the salinity concentration will be the highest at the mouth of estuary since the seawater enters at that location, and will decrease gradually when moving upstream. The St. Johns River can be classified as a partially mixed estuary. According to Dyer (1973), since information is lost during the analysis process (averaging causes the small vertical variations to be nearly extinct), homogenous estuaries are hard to determine if they exist. Vertically homogeneous estuaries have very small cross sections and the tidal flow dominates the fresh water flow, which causes the bottom velocity shear forces to be very large. When these forces are large enough, the water column is able to be mixed, horizontally, making the estuary vertically homogeneous. Lastly, the laterally or sectionally homogeneous estuaries occur when the estuary's width is small causing the lateral shear forces to be large, creating lateral homogeneous mixing.

An estuary may also be classified by the level of salinity within the system based on the Thalassic series, which divides the three major types of water (fresh, brackish, and marine) into different categories based on the concentration. Dahl (1956) demonstrates the changes to this series over several decades. The series is measured in parts per thousand (PPT or ‰) and shown in Figure 2.1. For example, if oligohaline brackish water has an upper limit of 3‰, then it represents three pounds of salt per 1,000 pounds of water. According to Sucsy and Christian (2009), several areas of the St. Johns River can be classified with the following zones: polyhaline, mesohaline, and oligohaline.

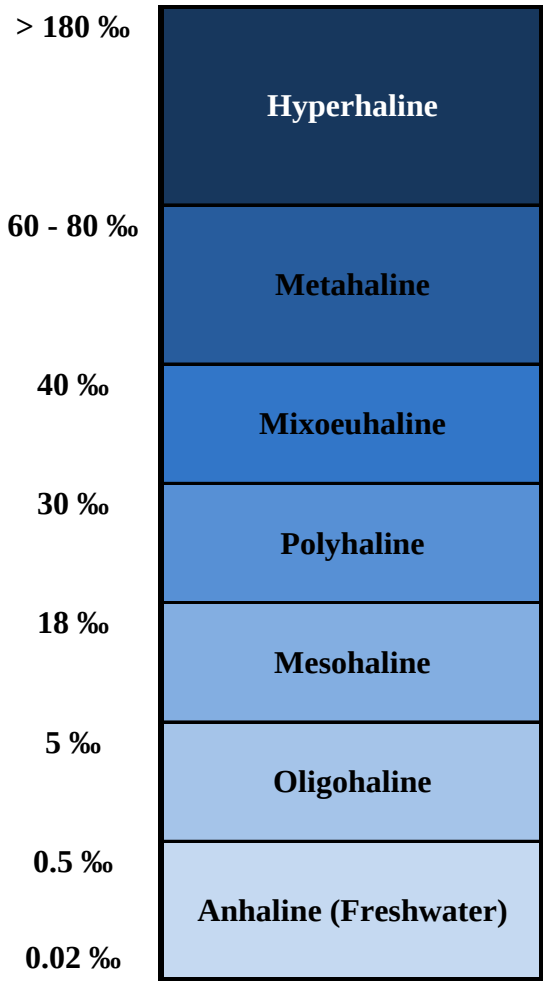

Figure 2.1: Salinity concentration subdivisions based on the Thalassic series (*Source: Dahl, 1956; Por, 1972; Bulger et. al., 1993; Sucsy and Christian, 2009*)

Two ecosystems, estuaries and salt marshes, are often misidentified. According to Molles (2008), a salt marsh is the transition of the land to the sea containing mainly herbaceous vegetation along sandy shores, and contains a network of tidal creeks through which the

fluctuating tides flow. The lower St. Johns River contains both ecosystems; an in-depth discussion on their interactions will be shown later in this review.

Several interactive processes occur within estuaries which help build and maintain the health of the ecosystem. Herein, sediment and salinity transport will be the two processes of focus. As the incoming tides of the sea and the outfall of a river join, sediment from the two different sources meet. When sediment from the river enters the estuary, it becomes deposited as the velocity decreases. This decrease in velocity occurs when the tidal flood encounters the downstream flow. Additionally, currents are generated by the collision of the freshwater and sea water. These currents, with the aid of wave action, create deltas, tidal flats, and tidal creeks in the estuary. Sediment from the sea comes from surrounding peninsulas, dunes, and the sea itself (Gunnison, 1978).

The health of the estuary depends mainly on the amount of salinity within it. Gunnison (1978) states that "estuarine basin morphometry[1] can play a determining role in the establishment or lack of salinity gradients, the development of sedimentary features, and the degree of fluctuation of tides." Not only does the collision of freshwater and seawater cause a chemical reaction, but a physical reaction as well. The salinity content of seawater causes it to have a higher density than freshwater, so the saline mixture flows below the outgoing freshwater. During this time, with the aid of turbulence, the formation of brackish water (i.e. mixture of fresh

[1] The estuarine basin morphometry is the geometric characteristics of an estuary. The geometric characteristics include volume, surface area, depth (mean, minimum, maximum), maximum length and width, and shape (Cornell University Facilities Services Utilities and Energy Management: website http://www.utilities.cornell.edu/utl_lsceis_glossary.html accessed May 6, 2010; limgis 2001: website http://ces.iisc.ernet.in/energy/monograph1/Glossary.html accessed May 6, 2010).

and sea water) occurs. Gunnison (1978) also mentions that these patterns of the outward flow depend on the "morphometry of the estuary basin, direction and height of tides and winds, Coriolis forces, degree of stratification (thermal and saline), and the current velocity". The intensity of each component will determine the specific characteristics of an estuary. For instance, if the freshwater outflow pattern is strong, it will have a higher influence in the composition of brackish water (Gunnison, 1978).

The physical and biological components of an estuary are sensitive to environmental changes. Dyer (1973) stated that deepening an estuary will increase the estuary's volume, but the intertidal zones, areas which are dry during low tide and flood at high tide, will decrease the tidal flow. Environmental changes cause the mixing processes and circulation patterns to change. Evidence of such changes can be measured in terms of species behavior within the ecosystem (Calliari et. al., 2008; Ewing et. al., 1995; Teh et. al., 2008). Today, estuaries are undergoing constant stress caused by land use in local areas. Based on a 2004 study conducted by the National Oceanic and Atmospheric Administration's National Marine Fisheries Service and the U.S. Fish and Wildlife Service, the coastal wetlands[2] along the Atlantic coast decreased by approximately 0.1 % (14,980 acres) compared to values in 1998 (Dahl and Stedman, 2008). However, the 1996 report prepared by the U.S. Fish and Wildlife Service showed that there were approximately 11.4 million acres of wetlands found in Florida alone. It must be noted that 90%

[2] Wetlands are "lands that are seasonally or permanently flooded by shallow water as well as lands where the water table is close to the surface; in either case the presence of abundant water has caused the formation of hydric soils and has favored the dominance of either hydrophytic or water tolerant plants" (Stephenson and Hodgson,1996). According Carter (1988), wetlands, especially those located in coastal regions (marshes), "act as nurseries and feeding grounds for crustaceans, fish and birds, repositories for pollutants, nutrients and organics, and as protection against wave attack".

were considered freshwater systems and the remaining ten-percent were estuarine ecosystems. However, in 1845 approximately 20.3 million acres existed, but in 1996 only 56 % remained (11.4 million acres). The estuarine ecosystems considered at that time was a total of 1,137,100 acres and included salt marsh wetlands (also considered estuarine emergent), estuarine shrubs, and estuarine and marine nonvegetated (shores, mud flats, bars, shoals) and vegetated wetlands (Dahl, 1998).

The reports considering coastal wetlands and Florida's wetlands also looked into the trends that dealt with declines of these ecosystems. Dahl and Stedman (2008) stated that these coastal ecosystems undergo a tremendous amount of stress. These "anthropogenic stressors" not only originate from the land, but also to the changes of the sea. The stresses can range from dredging and shoreline hardening along with other human activities, to coastal storms, tidal surges, and the increasing event of saltwater intrusion. These stressors will cause the available plant life to slowly die out causing these areas to decrease and subside (Dahl and Stedman, 2008). The 1996 report based on Florida's status emphasized that the decrease to estuaries was caused by coastal erosion from the result of coastal development and storms during that time period. Dahl (1998) points out that 20% of the estuarine shrub losses were caused by an agricultural practice, five-percent were caused by another form of practice that was unidentifiable. Also, a 71% decrease in estuarine shorelines was caused by coastal urban expansion. Again, the remaining 29% were caused by a practice that could not be identified (Dahl, 1998).

2.1.2. External Influences

The circulation processes in the estuaries are influenced externally by tides, wind, and oceanic events, which can be considered as upwellings, oceanic eddies, and storms (Wolanski, 2007). The tides are ubiquitous and should always be considered. The tide can be defined as a "sequence of sinusoidal, tidal harmonic components that are different for every location on the earth" (Funakoshi, 2006; Macmillan, 1966; Boon, 2004). Tides have a direct role in the formation of estuaries and the plant and animal life that resides there. The tides are cyclical with a flood phase and an ebb phase; the flood generally high tide and the ebb generally low tide (Wolanski, 2007).

The tides can be described in terms of tidal constituents (Macmillan, 1966; Boon, 2004), as shown in Table 2.1.

Table 2.1: Dominant Tidal Constituents and Occurrences (*Source: Bacopoulos, 2005; Wolanski, 2007*)

Dominant Tidal Constituents		
Diurnal Constituents	**Period (hrs.)**	**Origin**
K_1	23.93	Principal Lunar and Solar
O_1	25.82	Principal Lunar
P_1	24.04	Principal Solar
Q_1	26.87	Lunar Ellipse
S_1	24	
Semi-Diurnal Constituents	**Period (hrs.)**	**Origin**
M_2	12.42	Principal Lunar
S_2	12	Principal Solar
N_2	12.66	Lunar ellipse
K_2	11.97	Declinational Lunar and Solar

These constituents can combine at different phases causing modulations in amplitude; one such example is the spring-neap cycle (fluctuation between maximum tidal range and minimum tidal range), which is about 14 days (Wolanski, 2007; Boon, 2004). Tides can be classified based on their amplitude as shown in Table 2.2.

Table 2.2: Tides Classification (*Source: Wolanski, 2007*)

Tides Classification	
Type	**Range**
Micro-tidal	tidal range < 2m
Meso-tidal	2m < tidal range < 4m
Macro-tidal	4m < tidal range < 6m
Hyper-tidal	tidal range > 6m

Another influential factor on estuarine circulation is wind. Obviously, wind occurring over the surface of the sea creates wind waves. Funakoshi (2006) describes the main characteristics of wind waves as the following: 1) short tidal period (1 to 30 seconds), 2) the influence on the shallow layer within deep waters, and 3) the movement of water is similar in magnitude in the vertical and horizontal directions. Depending on the strength and intensity, wind waves may or may not play a role on the estuary's circulation patterns. Griffin and LeBlond (1990) studied the role of wind during the exporting of freshwater from estuaries in the Strait of Georgia during the spring-neap tides. Based on 18 years of salinity data, the authors stated that "salinity fluctuations in the southern Strait of Georgia are highly correlated with the wind". The northwesterly winds in the area increased the freshwater exportation towards the sea, especially when mixing in the area was low. Prandle (1992) reported the research conducted by

Schroeder et. al. (1992) dealing with the shallow, tributary[3] estuary, Weeks Bay, in Alabama, USA with the use of retrieved salinity data from a two-year field study. It was stressed that local wind forcing is very important, however, the presence of non-local winds can influence the salinity behavior in an estuary. A winter front with winds ranging from less than 5 m/s^2 to 16 m/s^2 caused the waters within Weeks Bay to be completely mixed. Concerning a recent study on the Lower St. Johns River, Bacopoulos et. al. (2009) demonstrated the forcings caused by wind are important when considering the dynamics within nearby estuaries. An 122-day time period was selected for the study, so that calm and severe weather (Hurricane Ophelia) could be considered. The major results were that the meteorological forcing is "equal to or greater than that of astronomic tides and generally supersedes the impact of freshwater river inflows," along with "winds and pressure variations acting over the continental shelf and deep ocean are major contributors to the storm tide." Based on these facts, all dynamics of storm tides near and far from an estuary of interest "must be considered when one is interested in water levels inside of the estuary" (Bacopoulos et. al., 2009).

Estuarine ecohydrology looks at the ecological and physical processes involved with an estuary's hydrological cycle. The concept is to recognize the relationship between ecosystem health and the biology and physics of the estuary.

Two measures of the physically processes in the estuary are the residence time and the flushing rate. The residence time relates to the length of time a particle will spend in a particular dynamic system. This value is never uniform since it varies with position within the estuary.

[3] Schroeder et al (1992) defined a tributary estuary as "an estuary located within a large main estuarine system where the larger estuary serves as the tributary estuary's 'coastal ocean' salt source".

The density variations between freshwater and saltwater drive a baroclinic current, which together with the barotropic current, can create stagnation zones. Within these zones, the residence time can increase significantly, which can trap particles and cause the water quality to degrade immensely. For instance, a well flushed estuary will have a low level of oxygen depletion due to the high flow within the system.

The Tweed Estuary, U.K. has a residence time of approximately thirteen hours and results in the event of no oxygen depletion (Wolanski, 2007). However, a well flushed estuary will have a slightly higher level of oxygen depletion, but not as high as poorly flushed estuaries. The Bottom Waters of Ise Bay, Japan experiences oxygen depletion based on its' residence time of about 50 days (Wolanski, 2007). Unfortunately, the Humber-Ouse Estuary, U.K. endures dissolved oxygen depletion and high turbidity since it is a poorly flushed estuary with a residence time of several weeks (Wolanski, 2007). It should be noted that the residence time is not the only factor in determining the health and condition of an estuary; other factors include, but are not limited to, dissolved nutrients, heavy metal levels, plankton, suspended particulate matter, and the appearance of algae blooms.

According to Wolanski (2007), the residence time only considers the time for a water particle to leave the first time, but sometimes the same particle can re-enter with the falling or rising tide. Another concept to consider is the exposure time the estuary experiences, which is the amount of time a particle spends in the estuary, and when the particle permanently exits the estuary. This value can increase if most of the particles leaving with the ebb tides then return with the rising tide. The exposure time is another indicator in determining how much new water

enters into the estuary. This would aide in considering those estuaries with high metal levels or other pollution problems. Due to the nature of the circulation outside the estuary, this value is very difficult to determine specifically (Wolanski, 2007).

2.1.3. Roles and Importance

Salt marshes are also associated with the mouth of the river, but its landscape is based on the tides and the content of the brackish water (Molles, Jr., 2008). These unique systems comprise 5.2% of the Earth's surface and only 2% of the ocean's volume according to Wolanski (2007).

Estuaries and salt marshes are connected through several channels known as tidal streams or tidal creeks. Waterways are subject to change from the different interactions on the land itself and this same principle applies to tidal creeks. The channels are unable to hold the amount of water necessary to flood the salt marshes, so the ebb (outgoing) tides erode the creeks causing the flood (incoming) tides to reconstruct the area (Gunnison, 1978).

Estuaries are the home to several different species of animals and also to 60% of the world's population, due to the popularity of real estate located along the estuaries and the coast. The protection of these areas is incredibly important since coastal waters supply approximately 90% of the global fish catch (Wolanski, 2007).

Diverse plant and animal species are highly dependent on these ecosystems for shelter and food. Estuaries support "herbivorous, detritivorous, and carnivorous organisms that move up into the marsh with the flooding tides in order to feed." The relationship between estuaries and marshes must be strong since these estuarine species depend on the productivity level of the

nearby marshes (Gunnison, 1978). These ecosystems are the safe havens for several organisms. The coast and shorelines are necessary to maintain the life of these areas. Wolanski (2007) states that:

> "…The shoreline can change from sandy to muddy, diminishing the quality of life population on its shore. Increased muddiness and turbidity in the estuary result. This smothers the benthos and degrades the ecosystem by decreasing the light available for photosynthesis. This degradation is further increased by dredging and dumping of dredged mud within the estuary."

These organisms that live on or in the bottom of the estuaries are unique and can easily die along with the resident fauna if the dissolved oxygen (DO) levels become less than 1.0 mg/L (Wolanski, 2007). Dissolved oxygen levels can be easily altered if the turbidity levels increase at an incredibly high rate.

The increase in salinity due to a high level of salt water intrusion can cause some plant life to overgrow and suffocate other nearby plant life, and it can also cause lethal doses of salinity. However, this depends on the plant life and salinity levels specific to an estuary and salt marsh. Scientists use several indicator species to determine drastic changes in salinity and plant life. Ewing et. al. (1995) conducted experiments on *Spartina patens* (Ait.[4]) Muhl.[5] sods from

[4] Ait.: The abbreviation for Aiton. Some plant names indicate the author's name, in this case, the Scottish botanist William T. Aiton (1766 – 1849). (The International Plant Names Index: website http://www.ipni.org/ipni/idPlantNameSearch.do?id=10360882&back_page=%2Fipni%2FeditSimplePlantNameSearch.do%3Ffind_wholeName%3Dspartina%2Bpatens%26output_format%3Dnormal accessed May 25, 2010; Clivia Society – The Noble Family of Clive: website http://www.cliviasociety.org/william_t_aiton_william_hooker_john_lindley.php accessed May 25, 2010)

brackish marsh sites from the Falgout Canal located in the southeastern part of Louisiana. It was determined that "an increase in soil salinity can result in decreased growth of plants in three ways: 1) the low external water potential may cause a water deficit in the plant; 2) uptake of salts from the soil solution may result in the excess of ions in the plant tissue, which interferes with metabolic functions; and 3) excessive Na^+ or Cl^- concentration may inhibit nutrient ion uptake". These factors can cause the production of these plants and other wetland plants to decrease in productivity, and can have the appearance of a shorter height or lower amount of biomass (Ewing, et. al., 1995).

Animal species can also be used as indicators to salinity changes. These salinity changes can occur from rapid, heavy precipitation, mixing during storms, and from the organisms' own activity. Borg, et. al. (2008) conducted experiments on planktonic copepods (small crustaceans that float and drift in sea water and be can be found in freshwater environments) species *Acartia tonsa* and *Acartia clausi*, which can tolerate less than 5 to 30 PSU[6] and 0 to 52 PSU, respectively. Sudden salinity changes over a 20 hour period caused the survival rate of the species to decrease slowly, since each experienced shock. This experiment showed that the *Acartia tonsa* was able to handle a salinity decrease of approximately 10 PSU more than the *Acartia clausi*. The *Acartia tonsa* occur in sharp salinity gradients, while *Acartia clausi* do not

[5] Muhl: The abbreviation for the grass genus *Muhlenbergia*. It was names after the American botanist Gotthilf Henry Ernest Muhlenberg (1753 – 1815). (The International Plant Names Index: website http://www.ipni.org/ipni/idPlantNameSearch.do?id=10360882&back_page=%2Fipni%2FeditSimplePlantNameSearch.do%3Ffind_wholeName%3Dspartina%2Bpatens%26output_format%3Dnormal accessed May 25, 2010; The Tortoise Reserve: website http://www.tortoisereserve.org/research/Muhlenberg.html accessed May 25, 2010)

[6] Practical salinity units (PSU): Concentration of dissolved salts in water measured through conductivity, so the scale is dimensionless. (National Aeronautics Space Administration (NASA): website http://science.nasa.gov/glossary/practical-salinity-unit/ accessed May 25, 2010).

occur in sharp salinity gradients often since they can be found in the middle portions of estuaries (Borg, et. al., 2008).

2.1.4. Behavior

It is often stated that estuaries are very complicated, especially from a behavioral point of view. Liu et. al. (2001) made the point that this complicated natural system deals with the occurrence of salt water intrusion. Mixing occurs when the salt water and fresh water meet causing a complex stratification pattern and associated density currents. Due to this meeting of these water bodies and the formation of these patterns, sediment will be disturbed causing higher turbidity levels compared to a river system. The new current pattern influences the transportation of the disturbed sediment that is caused by the conflicting flows of the fresh and salt water. Liu et. al. (2001) also stated that this created transportation pattern also known as a cohesive sediment transport can lead to ecological and economical problems from the increase in turbidity (Liu, et. al., 2001).

The vertical mixing component depends on the changes of the water column from top to bottom within the ecosystem. These changes can be influenced by the downward force of the wind, turbulence from the bottom of the estuary, and the turbulent forces caused by the incoming tides and river flow. Wolanski (2007) mentions that vertical mixing can be characterized into three categories: pycnocline, thermocline, and lutocline. A pycnocline is the density interface when there is an intense stratification in suspended solids, salinity, and the temperature. Specifically, the thermocline is referred to as a “salinity step structure”, and the lutocline is the

actual density difference that caused the factors stated above. It has been observed that the vertical eddy diffusion coefficient, K_z, will be at its maximum at the half way point of the water column since any variations of salinity and temperature located near the surface and bottom are slight. Knowing this, K_z will be at its minimum at the pycnocline due to buoyancy effects at this location (Wolanski, 2007).

Due to the nature of this research effort, the vertical mixing components will not be considered for the modeling effort. As it will be shown further in the thesis, these specific parameters along with several others will cause the complexity of the model to increase and will have a higher probability to be inaccurate.

The lateral components of the mixing parameter are very important since the majority of the water entering and exiting the estuaries are in the horizontal axis. The lateral mixing of an estuary can vary based on the actual width. In very wide estuaries, the Coriolis force causes the flow's horizontal force to be vastly more present when compared to an estuary of lesser width. This force causes the seaward flow and landward flows to be at opposite ends, which creates a flood channel (tidally-averaged net inflow) on one side and an ebb channel (tidally-averaged net outflow) on the opposite side. Also, the tidal currents in a deeper estuary are much larger than those in a shallow wetland since there are more frictional forces present. The deeper estuary will have a larger water column and with that comes other conflicting forces that build on each other. A shallow estuary's water column is not large enough to give these conflicting forces room to diverge, so there is less energy available and it will slowly dissipate (Wolanski, 2007).

Similar to the vertical coefficient of mixing, the lateral component has a tide-averaged longitudinal diffusivity, *B*, which originated from the K_z value. Knowing this value, it can be determined how the longitudinal mixing of a particular estuary can be enhanced through lateral trapping. Lateral trapping occurs when the upstream water flow moves with the flood tide into a lateral embayment. It is then followed with the water returning into the estuary and mixing with "untagged" water through the use of the ebb tide. Equation (2.1) demonstrates the calculation of the longitudinal coefficient.

$$B = \frac{K_z}{(1+\varepsilon)} + \frac{\varepsilon U_{max}^2}{2k(1+\varepsilon)^2\left(1+\varepsilon+\frac{\sigma}{k}\right)} \tag{2.1}$$

where: ε = ratio of the lateral embayment volume to the estuary's volume,

U_{max} = Peak tidal creek,

1/k = Characteristic exchange time between the embayment and the estuary,

σ = tidal frequency (*Source: Wolanski, 2007*).

Equation (2.1) would have to be modified to include estuaries that are bounded by intertidal wetlands that include salt marshes and mangroves. This occurs since Equation (2.1) does not consider the differences in water depth of these two different areas. This will cause the exchanging of these two ecosystems to occur at different times during the tidal cycle. This is demonstrated in Equation (2.2).

$$B = \frac{K_z}{(1+\varepsilon)} + \frac{\pi \varepsilon U_{max}^2 a^2}{48\sigma(1+\varepsilon)} \quad (2.2)$$

where: a = the fraction of time to that the wetland is inundated by the tides (*Source: Wolanski, 2007*).

The longitudinal diffusivity coefficient is a helpful parameter when determining the intensity of the lateral mixing in an estuary. Wolanski (2007) shared common values; for instance an estuary with wetland-fringed tidal creeks would be considered to have a very strong lateral mixing with a B value in the range of 10 to 40 m^2/s. For an estuary without the presence of nearby wetlands will have a very small B value within the range of 1 to 10 m^2/s (Wolanski, 2007).

Lateral mixing components are important to the research efforts of this project due to the fact that it plays an incredible role of the interaction between estuaries and surrounding marshes and other wetlands. The importance of these factors will be further discussed when considering an accurate procedure to represent the overall mixing process in a numerical model.

Overall circulation within estuaries helps control the general health of the ecosystem. It can influence the salinity concentration, color and turbidity, temperature, and major chemical concentrations of oxygen, carbon dioxide, and other nutrients. As mentioned earlier, the salinity concentration is constantly changing due to the changes in incoming and outgoing water flows. However, the circulation constituents are able to keep the salinity concentration constant and consistent based on tidal behaviors. The color and turbidity levels from suspended organic matter and dissolved humic (decomposed organic plant and animal matter) substances are based on the estuary's internal mixing. Circulation helps to maintain a certain temperature range so

that organisms are able to survive under extreme conditions. Chemical concentrations react to one another and are influenced by the salinity, turbidity, and temperature within an estuary. Also, the current biological conditions of an ecosystem are determined by the concentrations of chemicals and nutrients. According to Gunnison (1978), the amount of carbon dioxide available in an estuary is highly influenced by the salinity concentration; as the salinity increases, the concentration of carbon dioxide experiences an inverse effect. He stated that "salt water does have a chemical feature that tends to favor the solubilization of carbon dioxide", which is shown in Equation (2.3).

$$CO_2 \leftrightarrow CO_2(aq) + H_2O \leftrightarrow H_2CO_3 \leftrightarrow H^+ + HCO_3^- \leftrightarrow H^+ + CO_3^{=} \quad (2.3)$$

Due to the nature of the bicarbonate (HCO_3^-) and carbonate ($CO_3^{=}$) ions, the direction of the reaction shown in Equation (2.3) would move towards the right side based on the presence of excess cations of strong bases (Na^+) compared to the anions of strong acids (Cl^-). Based on this fact, the carbon dioxide concentration will gradually increase toward the incoming seaward flow. The same inverse effect between salinity and carbon dioxide also occurs when considering oxygen and salinity along with temperature; as the salinity concentration increases and temperature rises, the oxygen levels will gradually decrease. Gunnison (1978) further discusses that any changes of oxygen and carbon dioxide are mainly based on the biological constituents within the estuary.

The nutrient levels within the estuaries are based on a biological sense. There are several different and highly complex mineral cycles that take place in the estuary and can only react

fully based on the amount of chemical elements available for utilization. These cycles provide estuaries with all the nutrients necessary to be fully productive. The cycling of carbon, nitrogen, phosphorus, and sulfur are important within an estuary, however, the carbon cycle will only be discussed due to its' direct correlation to salinity.

The carbon cycle is very important for a marsh-estuarine ecosystem. In general, the plants and algae (also considered as the primary producers) help create the new formulation of organic compounds from carbon dioxide, an inorganic form of carbon, produced through photosynthesis or directly from the atmosphere. These organic compounds are then used by the primary producers for the formulation of new plant material, biological maintenance, which is done through the respiration process, and the remaining compounds are then stored. Within this food chain, the animals, insects, and other herbivores (also considered as the primary consumers) feed on the primary producers. The primary consumers utilize the primary producers to gain carbon, so that it may also be used for biological maintenance through the respiration process. The carnivores (also known as the secondary consumers) feed on the primary consumers to gain carbon for their biological maintenance and other processes. Decomposer microorganisms will feed on any organism not consumed by either the primary or secondary consumers. The decomposer microorganisms breakdown non-living organic material as well as plant fragments (all considered to be detritus) to retrieve carbon dioxide to aid in their respiration processes to maintain their metabolism. It should be noted that the rate of decomposition is dependent on the material properties and the surrounding environmental conditions.

2.2. Transport

When exploring salinity transport within estuaries, all important constituents, which include the following: riverine inflow, the tides, rainfall and evaporation, the wind, and oceanic events (i.e. an upwelling, an oceanic eddy, and storms) need to be explored as well (Hsu, et. al., 2002). However, each estuarine system is different from one region to the next, so some constituents will be stronger than others, or closely nonexistent. Due to this fact, the lower St. Johns River must be investigated in order to realistically model salinity transport.

The St. Johns River is considered to be the longest river within the state of Florida. The 500 km blackwater river, with a drainage basin of 22,000 km^2, flows northward with a slope of approximately 2.2 cm per kilometer. This very low slope allows tidal processes to extend 170 km from the river's mouth in Mayport, Jacksonville, FL, to Florida's second largest lake, Lake George, with an area of 172 km^2 (Sucsy and Morris, 2002; Sagan, 2007). This study will be concentrating on the lower, northern portion, 161 km of the St. Johns River, hence the name Lower St. Johns River (LSJR). This area contains the St. Johns partially stratified estuary and the extent of the tidal and freshwater reach, which is predominantly controlled by daily and seasonal wind driven events (Sagan, 2007; Sucsy and Christian, 2009).

Salinity data is being collected on a daily basis with a 30-minutes time increment from several stations along the Lower St. Johns River. Four United States Geological Survey (USGS) monitoring stations provide salinity data for this thesis and as shown in Figure 2.2. These four stations will be used for this study to aid in the salinity transport model process. The recorded salinity data from these specific locations will help create a perception of the salinity distribution

within the Lower St. Johns River and the surrounding estuaries, as shown in Figure 2.3. These findings will be discussed later within this thesis.

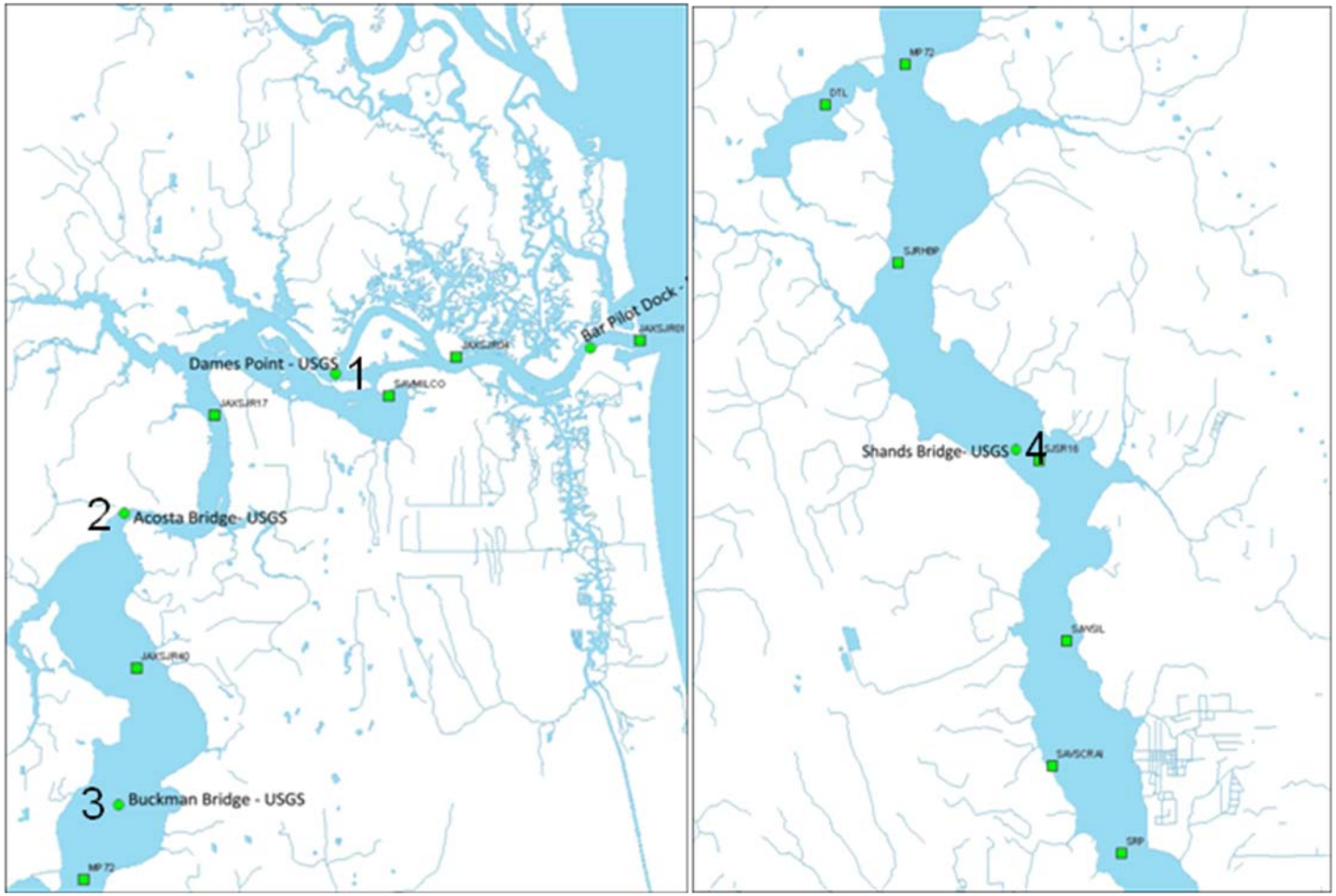

Figure 2.2: The four field stations obtaining water quality measurements, specifically salinity, operated by the USGS (Bacopoulos, 2010 - unpublished).

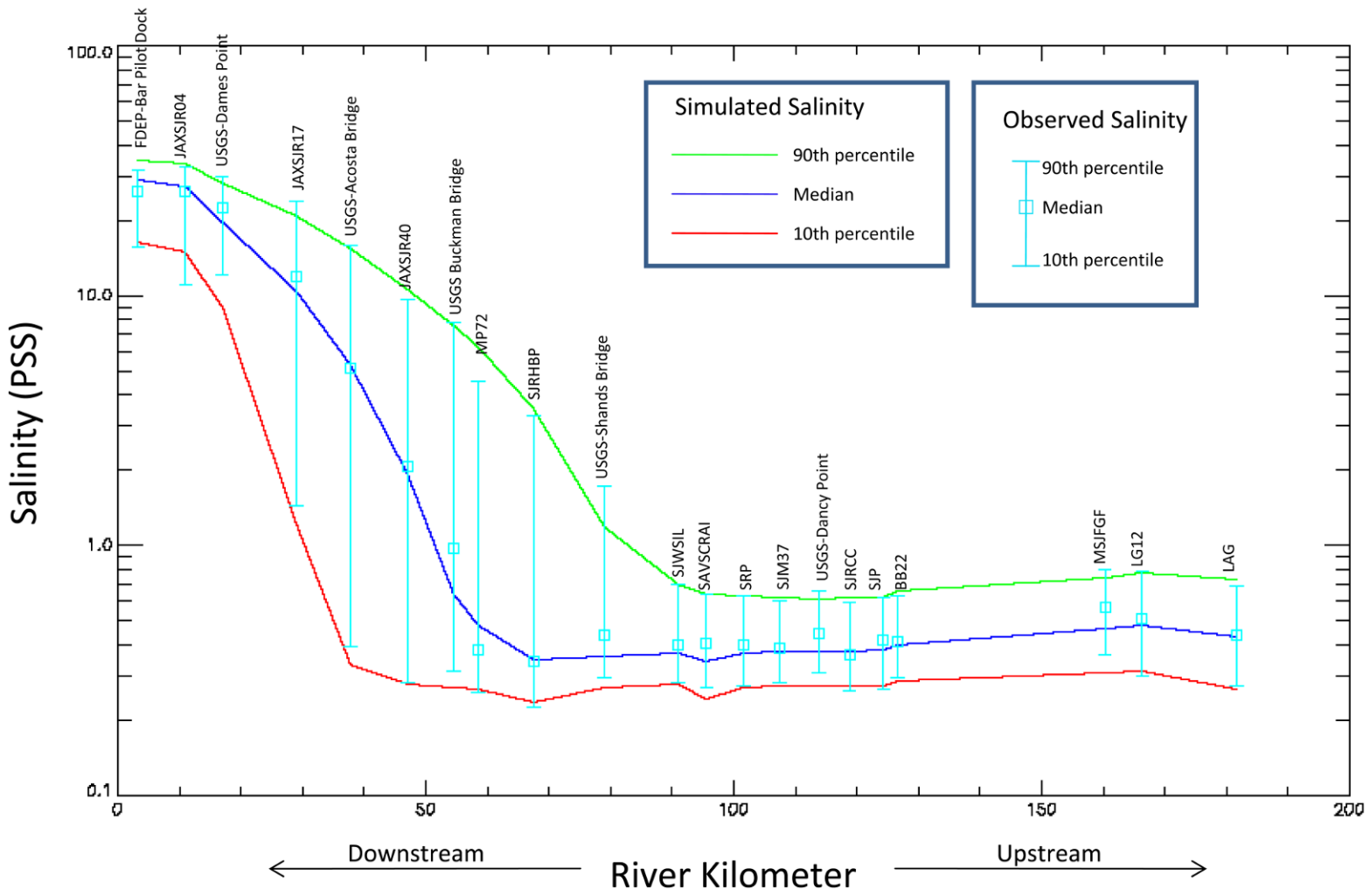

Figure 2.3: Salinity distribution within the Lower St. Johns River based on current available data (Bacopoulos, 2010 - unpublished; Sucsy and Morris, 2002).

The lower St. Johns River is constantly studied by the St. Johns River Water Management District due to its structural diversity of "drowned relic lagoons and marsh areas whose openness is maintained by the presence of a constant artesian source" (Stewart, et. al., 2009). Also, there is a growing concern of the increase in withdrawal of surface waters and the potential impacts of widening the channel within Mayport, Jacksonville, FL., which includes the possibility of increase in salinity (Stewart, et. al., 2009).

Currently, the St. Johns River Water Management District is compiling several analyses for the Alternative Water Supply Cumulative Impact Assessment. As stated earlier, the river will be experiencing future changes to meet the water demands for surrounding communities. This report, which is still under review, consists of a discussion on the following: a) hydrodynamic modeling of the Lower St. Johns River and Lake George, b) impact assessment on possible water conservation measures through the use of different salinity scenarios, and c) a scientific analysis pertaining to possible negative impacts on the surrounding ecology. The four different scenarios for water conservation are surface water withdrawals of 265 million gallons per day (MGD), the channel deepening of the Jacksonville Harbor in Mayport, FL, the diversion of wastewater streams to be treated for reuse and to reduce nutrient concentration, and the occurrence of sea level rise. Based on the nature of this project, the different hydrodynamic models used on the Lower St. Johns River and the possible impacts of the channel deepening in Mayport, FL will be discussed in more detail (Sucsy and Christian, 2009).

Dr. Peter Sucsy and David Christian (2009) concentrated on extending the capabilities of a hydrodynamic model for the Lower St. Johns River and Lake George for the assessment

project. The original model entitled the Lower St. Johns River Hydrodynamic Model (LSJRHM) uses the Environmental Fluid Dynamics Code (EFDC), which deals with pollution load reduction goals (PLRGs) and total maximum daily loads (TMDLs). However, the model had to be modified, so that it may accomplish evaluations for the Alternative Water Supply Cumulative Impact Assessment. "The extended version of the LSJRHM is called the Lower St. Johns River extended hydrodynamic model (LSJREHM). The model includes forcings by: (a) ocean water level; (b) tributary and spring discharge; (c) discharge from wastewater streams; (d) rainfall and evaporation; (e) wind; and (f) specified salinity at inflow locations and at the open ocean boundary." An 11 year (1995-2005) model simulation was done and the model's results were compared to observations of the discharge, tidal water level, and salinity for calibration, and it was shown that the tidal water level errors were "less than 15%". The authors noted that this specific experiment only considered "the upstream extent of marine salinity because of possible detriment to submerged aquatic vegetation (SAV)" (Sucsy and Christian, 2009). Previous studies have shown that a salinity level equivalent to five PSU is the highest stress level submerged aquatic vegetation is able to withstand. According to the model results, the highest level of salinity exceeding five PSU was near Shands Bridge (Sucsy and Christian, 2009).

The salinity distribution from the study gave interesting results. The greatest salinity range on a daily basis occurred within the narrow navigational channel between Dames Point and Acosta Bridge. The authors point out that the typical salinity range for Dames Point is approximately 5 to 15 PSU. However, the salinity decreases slowly between Acosta Bridge and Buckman Bridge, and then quickly decreases when traveling from Buckman Bridge to Shands Bridge. The Lower St. Johns River has a very unique distribution when concerning the different

salinity characteristics. The tidal forces entering the Lower St. Johns River slowly decreases and is demonstrated by the decrease in salinity. For instance, upstream of Shands Bridge, the river has a salinity level of less than 0.1 PSU, which can be considered part of the freshwater portion of the river (Sucsy and Christian, 2009).

The model just discussed "can be used to examine alterations in salinity, water level, and flushing from upstream water withdrawals throughout the Lower St. Johns River, Lake George, and Crescent Lake" (Sucsy and Christian, 2009). For the Alternative Water Supply Cumulative Impact Assessment, different salinity scenarios were investigated to determine the detrimental effect of different factors that could alter salinity levels within the Lower St. Johns River. The four factors that were considered for this portion of the study were the following: 1) upstream water withdrawal for surrounding residents; 2) the dredging of the Jacksonville Harbor and the St. Johns River's entrance; 3) wastewater stream diversions for possible reuse and nutrient removal; 4) sea level rise caused by climate change. Concerning the nature of this thesis, the second factor will only be discussed.

The dredging of the Lower St. Johns River entrance and the Jacksonville Harbor "would alter the hydrodynamic flow in the reach of the river with the largest amount of tidal influence which could impact the longitudinal salinity intrusion" (Giardino, 2009). Sucsy and Christian (2009) looked into four different scenarios with a model period of 1995 to 2005 to determine the effects of the changes on salinity. It should be noted that data for 1995 was used as a "spin up" for the model, so that the remaining ten years of the model period could be used for comparison

on an hourly basis. The portion of the river that was observed was between Astor and the Lower St. Johns River mouth.

Scenario A, also known as the Base Case, is based on the 1995 bathymetry (NAVD88[7]) and consists of the same boundary conditions used in the preliminary study to test salinity for the LSJREHM model. The model used two different channel depths: one at 38 feet (NAVD88) in the main channel and another at 33 feet (NAVD88) on the western side of the Blount Island. For the remaining scenarios, all channel cells were changed "by an equal amount even if the increased depth exceeded the new minimum channel depth" (Sucsy and Christian, 2009).

Scenario B considers the dredging of the specified area by two feet in the main channel to Dummond Point, giving a new minimum depth of 40 feet (NAVD88), and five feet added to the western side of Blount Island, giving a new minimum depth in the area of 38 feet (NAVD88) (Sucsy and Christian, 2009).

The future of the Lower St. Johns River will be shown in Scenario C. It considers the dredging of the main channel to Fuller Warren Bridge, which adds seven feet to Scenario A (Base Case) to provide a new minimum depth of 45 feet (NAVD88), along with the dredging of Blount Island by 12 feet (based on the Base Case) (Sucsy and Christian, 2009).

Finally, Scenario D is similar to Scenario C, with the difference of the additional dredging of the St. Johns River mouth seaward towards Mayport, Jacksonville, FL to give a new minimum depth of 50 feet (NAVD88). Please note that the dredging of the Fuller Warren Bridge

[7] North American Vertical Datum of 1988

and western side of Blount Island remained the same within this scenario (Sucsy and Christian, 2009).

The model was run for each scenario and all results were compared along with the other three salinity scenarios (e.g. upstream withdrawal, wastewater stream diversion, sea level rise). When comparing among the four scenarios (Base Case, Scenario B – D), Scenarios C and D had very similar effects on the salinity, except for the jetties located at the river's mouth. The model showed that the "greatest increase in average salinity by deepening Scenarios C and D is 2.2 PSU near Talleyrand Terminal", which is considered to be the upstream limit of the dredging. Conversely, the greatest increase in average salinity was approximately 0.5 PSU in Scenario B.

Comparing the channel dredging to the other three factors (upstream water withdrawal, wastewater stream diversions, sea level rise) aided in determining the most alternating effect on salinity. Sucsy and Christian (2009) stated that Scenarios C and D within the dredging study had the greatest effect on salinity concentration within the Lower St. Johns River. They were then "followed by full withdrawal, wastewater reuse, and channel deepening Scenario B". It was not surprising that sea level rise had the least effect on salinity due to the fact that the sea is rising 2.2 mm/year at Mayport, Jacksonville, FL (Sucsy and Christian, 2009).

Due to sea level rise, one must consider sea level anomalies as well since they play a role in estuarine processes, which are the differences between the total sea level and the average sea for specific location at time of the year (Texas Grant Consortium: website http://www.tsgc.utexas.edu/topex/activities/elnino/sld005.html accessed May 21, 2010). James T. Morris (2000) stated that "these anomalous tidal components change the frequency of

flooding intertidal salt marshes, the area of marsh flooded at high tides and hydraulic gradients". Sea level anomalies affect the salt balance within an estuary. For example, when the sea level is low, the water level decreases causing the amount of salinity with sediment pores (i.e. pore water salinity) to increase. This causes the production of the estuary to decrease due to the heightened salinity concentration. Morris (2000) studied North Inlet, South Carolina, which contains a largely forested 75 km^2 tidally dominated salt marsh estuary with little surface water inflow. The freshwater input for the estuary is approximately 3% of the tidal volume and is considered to exceed the salt marsh's freshwater input. Morris (2000) continued to point out that a "source of water from outside the watershed is required to account for the decrease in salinity of water leaving the estuary. Concerning sea level in this area, the experiment resulted in a long-term increasing trend for the relative annual sea level along with an interannual variation within this trend. This resulted from "an 18.6 year lunar nodal cycle that is due to changes in the moon's orbit" (Morris, 2000). The salt marsh within the Oyster Landing and Goat Island had the highest production rates in the summer months, which were also the months with the highest evapotranspiration rate and porewater[8] salinity concentrations. This was caused by a decline in flooding due to negative sea level anomalies. However, "the increased variation in salinity that accompanies low sea level arises due to the susceptibility of exposed sediments to dilution of their porewater by precipitation" (Morris, 2000). It was also shown that making small changes in the mean sea level will cause a drastic change in the occurrence of flooding. For instance,

[8] Porewater salinity: Salinity contained within the water filling all spaces of an ecosystem's sediment. (U.S. Geological Survey (USGS): website http://toxics.usgs.gov/definitions/pore_water.html accessed May 21, 2010)

decreasing and increasing of the mean sea level reduced and increased the flood frequency, respectively.

In June and July of 2009, National Oceanic Atmospheric Administration (NOAA) sea level stations, which are managed by the Center for Operational Oceanographic Products and Services (CO-OPS), recorded an unpredictable increase in sea levels in the U.S. East coast. It was determined that the beginning occurrence of these elevated levels in June ensued with a "perigean-spring tide, an extreme predicted tide when the moon is closest to the Earth during a spring tide" (Sweet, et. al., 2009). The perigean-spring tidal event augmented the East coast's sea level anomaly (due to their "unexpected timing and geographic scope"), which caused flooding along the coast. Consideration of force mechanisms were done since they also play a role in tidal interactions within ecosystems along the coast. These mechanisms can influence transport patterns in estuaries, which will be shown in an upcoming section of this thesis. For this study, two mechanisms were explored: a) northeasterly (NE) wind forces and b) the Florida Current's changing transport. The wind forces were shown to have a large impact along the coast. The Northeasterly winds are considered to be a negative affect due to sea levels rising from the convergence of the sea along the coast. However, the Southwesterly winds, a positive forcing, caused a diverging affect to occur making the sea levels to decrease. The Florida Current had higher transport momentum occurring in the summer months when compared to the fall months. Sweet et. al. (2009) noted that short period winds had an impact on the strength of the Florida Current transport mechanism. "Lee et. al. (1985) and Lee and Williams (1988) found that short term variations in FC [Florida Current] transport with periods of less than10 days were correlated to local northerly/southerly winds" (Sweet, et. al., 2009).

2.2.1. Salinity Transport Specifics

Salinity transport is a highly complex process due to many physical characteristics, which were previously discussed. Based on this fact, "salinity distribution in an estuary is determined by several forcing mechanisms that create the energy necessary for salinity transport" (Giardino, 2009). The research done by Derek Giardino demonstrated the different forcing mechanisms for salinity transport with the use of two analyses: 1) "… historical data analysis of primary forcing mechanisms to determine the importance of each individual influence", and 2) "… tidal hydrodynamics analysis for the Lower St. Johns River to determine the required tidal constituents for an accurate resysnthesis" (Giardino, 2009). This was done on historical salinity data by examining the impact of several natural processes occurring in the area (i.e. precipitation, tides, and wind), specifically "freshwater inflow, tidal advection, density circulation, geometry, and meteorological impacts" (Giardino, 2009).

However, freshwater inflow is considered to be the most influential forcing mechanism. The freshwater input "provides seasonal and transient variations" of freshwater to the estuary and salt marsh. Giardino (2009) provides an example concerning the Savannah River estuary in Georgia. The estuary contained tidal gates, which caused an increase in salinity content due to the increasing occurrence of the spring-neap tide causing the freshwater inflow pattern to decrease. Once the gates were removed, the velocity during the neap tide decreased greatly. The lack of energy present caused the turbulent forces to decrease causing very little mixing within the estuary of the two water sources. This caused the salinity concentration to increase when moving upstream in the estuary.

In the Lower St. Johns River, as shown in Figures 2.4 through 2.7, the salinity concentration decreases as the freshwater flows into the river. The opposite reaction occurs when the freshwater recedes; the salinity concentration increases.

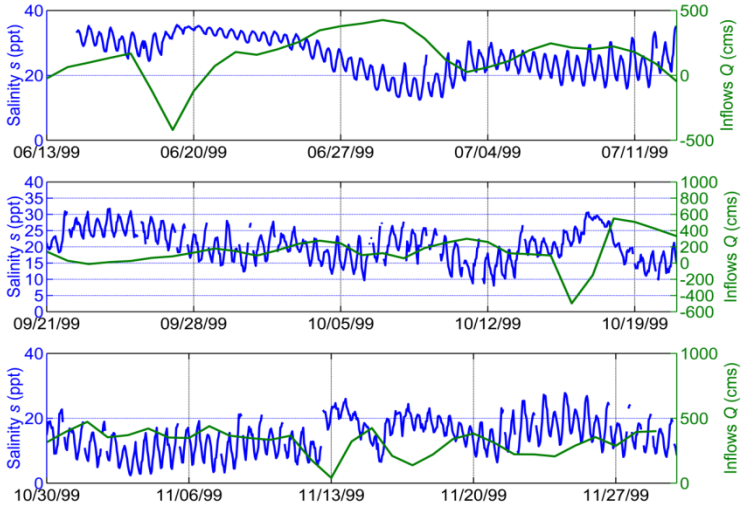

Figure 2.4: Observed salinity data behavior compared to the inflow of freshwater at the Dames Point station for the *High Extreme*, *Most Variable*, and *Low Extreme* time periods.

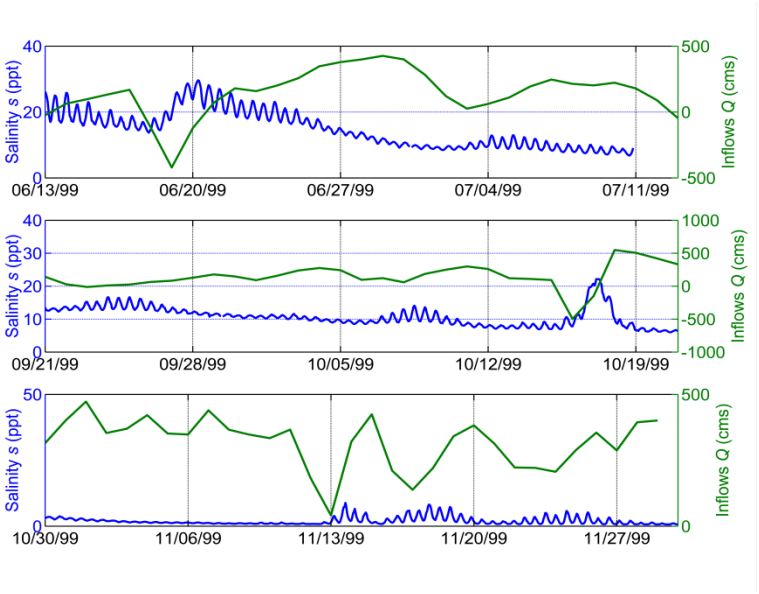

Figure 2.5: Observed salinity data behavior compared to the inflow of freshwater at the Acosta Bridge station for the *High Extreme*, *Most Variable*, and *Low Extreme.*

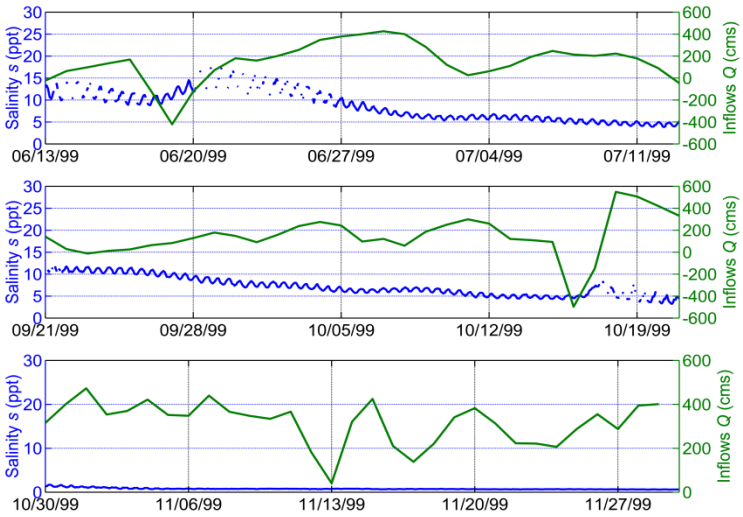

Figure 2.6: Observed salinity data behavior compared to the inflow of freshwater at the Buckman Bridge station for the *High Extreme*, *Most Variable*, and *Low Extreme*.

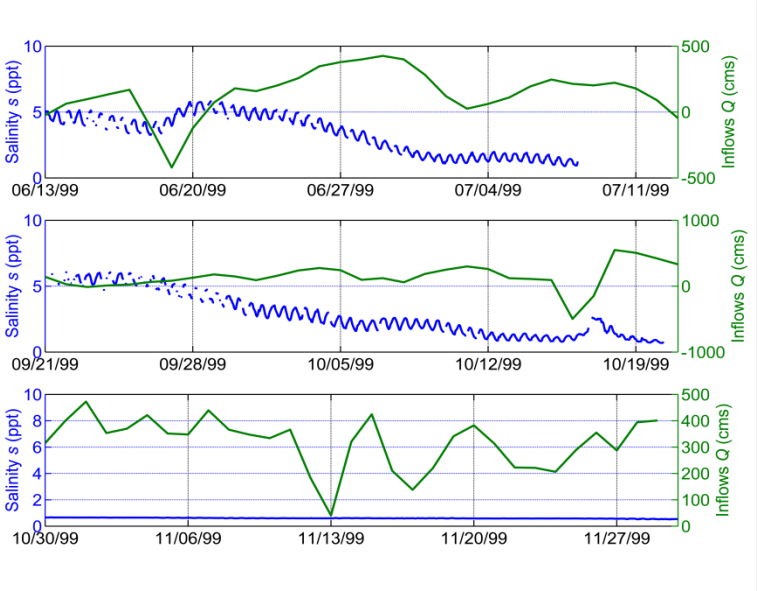

Figure 2.7: Observed salinity data behavior compared to the inflow of freshwater at the Shands Bridge station for the *High Extreme*, *Most Variable*, and *Low Extreme*.

During the *High Extreme* and *Most Variable* time spans, the freshwater inflow rate and salinity relationship is very noticeable. However, the *Low Extreme* displays a very evident relationship, for the Dames Point and Acosta Bridge stations. This is not the case for Buckman Bridge and Shands Bridge data stations. The salinity concentrations are within the oligohaline zone (five parts per thousand), so the effect of the freshwater inflow is very slight.

On the other hand, evaporation and precipitation patterns are also included in freshwater inflow. For instance, an estuary that undergoes a large amount of evaporation will become a hypersaline environment due to the decrease of freshwater content making the salinity less diluted, therefore becoming negative. The converse effect will occur with an estuary experiencing high rain (precipitation) events. The increase of freshwater will make the dilution

process increase (positive) causing the salinity concentration to decrease. The St. Johns River is an example of a positive estuary due to high experience to precipitation (Giardino, 2009).

Another physical mechanism to consider is that caused by the winds on a short term basis (occurrences within days to weeks). The magnitude (strength) and direction of the wind over the water's surface will have an impact on transport and circulation within the estuary. For example, wind caused by storm events will have a higher impact on an estuarine ecosystem rather than long term winds. It was pointed out that freshwater will continue to be the most influential mechanism since long term winds are averaged out. This causes the effect of this mechanism to be less influential (Giardino, 2009).

The physical attributes, mainly geometry and geography, of the estuary is another mechanism to consider when looking into salinity transport. Two estuaries (Neuse and Pamlico), located adjacent to the water body Pamlico Sound, North Carolina, had different results when the two dimensional salinity transport model (SIMSYS 2D) was applied. The Neuse resulted in 25% increase of salinity when compared to the Pamlico estuary due to its bathymetry and orientation. Also, this estuary had a 75% increase in the inflow patterns resulting in a wider range of diverse water levels and velocity magnitudes (Giardino, 2009).

Residual circulation (also known as subtidal ocean water level forcing) will also have an effect on salinity transport since it concerns the short period (approximately 30 hours) tidal oscillations. The research of Liu et. al. (2007) proved that residual circulation has a higher impact in an estuary with high salinity gradients and deep bathymetry. The St. Johns River, however, contains many shallow estuaries, so this mechanism would be assumed to have a low

residual circulation. Most portions of the river would not be excluded since they have deep bathymetries.

2.2.2. Salinity Transport Equations

Within this section of the literature review, a broad understanding of numerically representing salinity transport within an estuary will be done. Assumptions made are based on the previous works of Dyer (1973) and Fischer (1976).

Before quantifying a system, a material or mass balance should be completed to determine the amount of salt being accumulated and/or leaving the system.

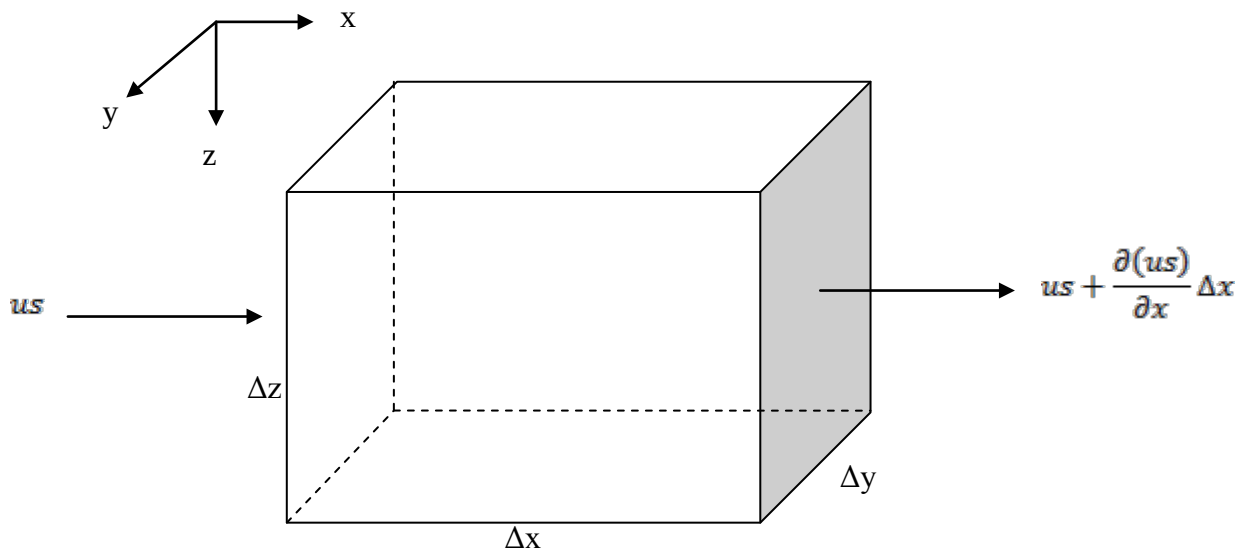

Figure 2.8: Salt transport through one elemental volume *(Source: Dyer, 1973).*

Conducting a mass balance requires the system to be disassembled into small pieces, or referred to as, by Dyer (1973), elemental volumes, as shown in Figure 2.8. For this case, the system will

be an estuary. As the water enters the estuary's elemental volume, it will have a velocity component (u) and a salinity concentration (s). Dyer (1973) points out that the "salt can be considered [as] a conservative property and can be treated with a continuity equation". The general mass balance equation, $In = Out + AR$, mathematically shows that the inflows will equal the outflows in addition to any accumulation along the way. The advective (or transport) flow of salt through any face over a period of time will result in the velocity and salinity components multiplied by the length and width of that side, and the change of time. For instance, one can determine the flow of salt through the $\Delta y \Delta z$ face by the following: $us\Delta y\Delta z\Delta t$. Determining the salt's flow for the opposite side of the elemental volume requires the mass balance equation. Salt may or may not accumulate over time, so the new equation will be the following:

$$us + \frac{\partial(us)}{\partial x}\Delta x \rightarrow us(\Delta y \Delta z \Delta t) + \frac{\partial(us)}{\partial x}\Delta x(\Delta y \Delta z \Delta t) \quad . \tag{2.4}$$

Therefore, the net inflows for the x, y, and z directions are listed below, respectively:

$$-\frac{\partial(us)}{\partial x}\Delta x(\Delta y \Delta z \Delta t) \ , \tag{2.5}$$

$$-\frac{\partial(vs)}{\partial y}\Delta y(\Delta x \Delta z \Delta t) \ , \tag{2.6}$$

$$-\frac{\partial(ws)}{\partial z}\Delta z(\Delta x \Delta y \Delta t) . \tag{2.7}$$

Dyer (1973) continues to state that diffusion occurs at a molecular level as water moves through the estuary. This will result in the product of the molecular diffusion coefficient for salt, the change of salinity with respect to space, the length, width of that side, and the change of time. This can be demonstrated using the ΔyΔz face once more: $-\varepsilon\frac{\partial s}{\partial x}\Delta y\Delta z\Delta t$. Again, the same principle applies to the opposite side of the elemental volume, but with accumulation over time:

$$-\varepsilon\frac{\partial s}{\partial x}\left(\Delta y\Delta z\Delta t\right)-\frac{\partial}{\partial x}\left(\varepsilon\frac{\partial s}{\partial x}\right)\Delta x\left(\Delta y\Delta z\Delta t\right)\ . \tag{2.8}$$

Therefore, the net diffusion for the x, y, and z directions are listed below, respectively:

$$\frac{\partial}{\partial x}\left(\varepsilon\frac{\partial s}{\partial x}\right)\Delta x\left(\Delta y\Delta z\Delta t\right)\rightarrow\varepsilon\frac{\partial^2 s}{\partial x^2}\Delta x\left(\Delta y\Delta z\Delta t\right)\ , \tag{2.9}$$

$$\frac{\partial}{\partial y}\left(\varepsilon\frac{\partial s}{\partial y}\right)\Delta y\left(\Delta x\Delta z\Delta t\right)\rightarrow\varepsilon\frac{\partial^2 s}{\partial y^2}\Delta y\left(\Delta x\Delta z\Delta t\right)\ , \tag{2.10}$$

$$\frac{\partial}{\partial z}\left(\varepsilon\frac{\partial s}{\partial z}\right)\Delta z\left(\Delta x\Delta y\Delta t\right)\rightarrow\varepsilon\frac{\partial^2 s}{\partial z^2}\Delta z\left(\Delta x\Delta y\Delta t\right)\ . \tag{2.11}$$

An instantaneous mass balance equation may now be formulated based on the equations above. Through the addition of Equations (2.5) through Equation (2.7) and Equations (2.9) through (2.11), the following will occur:

$$\frac{\partial s}{\partial t}\Delta x\Delta y\Delta z\Delta t =$$

$$-\frac{\partial(us)}{\partial x}\Delta x(\Delta y\Delta z\Delta t)-\frac{\partial(vs)}{\partial y}\Delta y(\Delta x\Delta z\Delta t)-\frac{\partial(vs)}{\partial z}\Delta y(\Delta x\Delta z\Delta t) \tag{2.12}$$

$$+\varepsilon\frac{\partial^2 s}{\partial x^2}\Delta x(\Delta y\Delta z\Delta t)+\varepsilon\frac{\partial^2 s}{\partial y^2}\Delta y(\Delta x\Delta z\Delta t)+\varepsilon\frac{\partial^2 s}{\partial z^2}\Delta z(\Delta x\Delta y\Delta t)\ .$$

After dividing the whole equation by the ΔxΔyΔzΔt term:

$$\frac{\partial s}{\partial t}=-\frac{\partial(us)}{\partial x}-\frac{\partial(vs)}{\partial y}-\frac{\partial(ws)}{\partial z}+\varepsilon\left(\frac{\partial^2 s}{\partial x^2}+\frac{\partial^2 s}{\partial y^2}+\frac{\partial^2 s}{\partial z^2}\right)\ . \tag{2.13}$$

It was indicated that "many analyses do neglect the tidal fluctuation cross-products and the salt balance values averaged over a tidal cycle and neglecting molecular diffusion" (Dyer, 1973). By doing so, the new mass balance equation would then become:

$$\frac{\partial \bar{s}}{\partial t}=-\frac{\partial(\overline{us})}{\partial x}-\frac{\partial(\overline{vs})}{\partial y}-\frac{\partial(\overline{ws})}{\partial y}-\frac{\partial(\overline{u's'})}{\partial x}-\frac{\partial(\overline{v's'})}{\partial y}-\frac{\partial(\overline{w's'})}{\partial z}\ , \tag{2.14}$$

where: $\bar{s}$ = Tidal mean salinity

$\bar{u}, \bar{v}, \bar{w}$ = tidal mean velocity in the longitudinal, lateral, and vertical directions, respectively

u', v', w' = turbulent velocity fluctuations of a period less than a few minutes in the longitudinal, lateral, and vertical directions, respectively

s' = turbulent velocity fluctuation of a period less than a few minutes in salinity.

Equation (2.14) contains advection (first three terms on the right) and eddy-diffusion terms (last three terms on the right) when using the new assumption. It should be noted that the eddy-diffusion terms are made up of turbulent velocities caused by the occurrence of eddies over a short period of time. This will cause the eddy-diffusion terms to overpower the advection terms due to the fact that these terms are based on the molecular level. When a steady state condition is present, the change of the tidal mean salinity will become zero, which will cause the advection and eddy-diffusion terms to be in equilibrium. However, the eddy diffusion terms may be rewritten in terms of a constant multiplied by the salinity gradient, which is shown below:

$$\left(\overline{u's'}\right) = -K_x \frac{\partial \bar{s}}{\partial x}, \tag{2.15}$$

$$\left(\overline{v's'}\right) = -K_y \frac{\partial \bar{s}}{\partial y}, \tag{2.16}$$

$$\left(\overline{w's'}\right) = -K_z \frac{\partial \bar{s}}{\partial z}. \tag{2.17}$$

Wolanski (2007) demonstrates the determination of K_x using the following equation under steady-state for a tidal creek:

$$AK_x \frac{dS}{dx} = eWS, \tag{2.18}$$

where: A = the cross-sectional area of the tidal creek

K_x = longitudinal diffusion coefficient

e = free water evaporation rate

W = surface area of the water body

S = salinity concentration.

With the equation above and field data, the longitudinal diffusion coefficient could be easily calculated. Rewriting Equation (2.14) with Equations (2.15) through (2.17) will create the classical Fickian[9] form of the salt continuity equation; a second degree differential equation concerning the change of salinity over changing length with a constant diffusion factor:

$$\frac{\partial \bar{s}}{\partial t} = -\frac{\partial\left(\overline{us}\right)}{\partial x} - \frac{\partial\left(\overline{vs}\right)}{\partial y} - \frac{\partial\left(\overline{ws}\right)}{\partial z} + \frac{\partial}{\partial x}\left(K_x \frac{\partial \bar{s}}{\partial x}\right) + \frac{\partial}{\partial y}\left(K_y \frac{\partial \bar{s}}{\partial y}\right) + \frac{\partial}{\partial z}\left(K_z \frac{\partial \bar{s}}{\partial z}\right). \tag{2.19}$$

As mentioned earlier, each type of estuary functions differently from another and contains different physical processes. According to Dyer (1973), the continuity volume equation for "a stratified estuary, an estuary with no spatial variation of salinity in the y-direction, but with variations in the x and z directions" is the following:

$$\frac{\partial \overline{bu}}{\partial x} + \frac{\partial \overline{bw}}{\partial z} = 0, \tag{2.20}$$

[9] Fickian form of a salt continuity equation is based on Adolf Fick's diffusion law. Through the inspiration of Fourier, he proposed that "the flux of matter is proportional to the gradient of its concentration denoted by y with a proportionality factor, k." This concept was combined with the conservation of matter concept to create the following: $\frac{\partial c}{\partial t} = -D\frac{\partial^2 c}{\partial x^2}$ (Philibert, 2005; Tyrrell, 1964).

where $\bar{b}$ = the breadth (also referred to as the width) of the estuary.

Applying the estuary's width to Equation (2.19) results to below:

$$\frac{\partial\left(\overline{bs}\right)}{\partial t}=-\frac{\partial\left(\overline{bus}\right)}{\partial x}-\frac{\partial\left(\overline{bvs}\right)}{\partial y}-\frac{\partial\left(\overline{bws}\right)}{\partial z}+\frac{\partial}{\partial x}\left(K_x\bar{b}\frac{\partial\bar{s}}{\partial x}\right)+\frac{\partial}{\partial y}\left(K_y\bar{b}\frac{\partial\bar{s}}{\partial y}\right)+\frac{\partial}{\partial z}\left(K_z\bar{b}\frac{\partial\bar{s}}{\partial z}\right). \tag{2.21}$$

However, for a partially mixed estuary, due to the increasing turbulent mixing within the system, the vertical diffusion term is present throughout the entire water column, as shown in Equation (2.22):

$$\frac{\partial\bar{s}}{\partial t}=\bar{u}\frac{\partial\left(\bar{s}\right)}{\partial x}+\bar{w}\frac{\partial\left(\bar{s}\right)}{\partial z}-\frac{\partial}{\partial z}\left(K_z\frac{\partial\bar{s}}{\partial z}\right),\qquad where\frac{\partial\bar{s}}{\partial t}=0\,. \tag{2.22}$$

As shown in the previous sections of this literature review, K_z term may be calculated, but with high difficulty. It should be noted that the $K_z\frac{\partial\bar{s}}{\partial z}$ will be equivalent to zero when the vertical depth is equivalent to the surface elevation and the negative value of the mean water depth (Wang, et. al., 1980).

2.2.3. Applications of Salinity Transport Equations

Using the theories and equations from the previous sections, the salinity transport equations can be used in many different applications. For instance, Wang et. al. (1980) used these concepts to create a semi-implicit laterally averaged two-dimensional model for estuarine circulation and transport for the Potomac River. The tidal, wind, and density mechanisms were also incorporated into this model. To determine the effectiveness of the proposed model, the results of the semi-implicit formulation was compared to the explicit formulation.

The model was based on the following governing equations proposed by Blumberg (1977, 1978) and Elliot (1976):

$$\frac{\partial}{\partial x}(uB)+\frac{\partial}{\partial z}(wB)=0, \tag{2.23}$$

$$\frac{\partial}{\partial t}(B_0\eta)+\frac{\partial}{\partial x}\int_{-H}^{\eta}(uB)\,dz=0, \tag{2.24}$$

$$\frac{\partial}{\partial t}(uB)+\frac{\partial}{\partial x}(uuB)+\frac{\partial}{\partial z}(uwB)-\frac{\partial}{\partial x}\left(BN_x\frac{\partial u}{\partial x}\right)-\frac{\partial}{\partial z}\left(BN_z\frac{\partial u}{\partial z}\right)+ ku|u|\left|\frac{\partial B}{\partial z}\right|+gB\frac{\partial \eta}{\partial x}+\frac{gB}{\rho_0}\frac{\partial}{\partial x}\int_z^0\rho dz'=0, \tag{2.25}$$

where u, w = longitudinal and vertical velocities, respectively,

B = estuary's width,

s = salinity concentration,

H = mean water depth,

η = surface elevation,

K_x = longitudinal diffusivity,

K_z = vertical diffusivity,

N_x = longitudinal viscosity,

N_z = vertical viscosity,

k = boundary friction coefficient.

The above equations quantify the system's continuity (Equations (2.23) and (2.24)) and momentum (Equation (2.25)). A very similar version of Equation (2.21) was also used for the system's salt conservation; however, it was only used in the x and z-directions due to the fact this model is in two dimensions. Once boundary conditions were set, each formulation ran simulations that entailed circulation patterns specifically from the tides, wind, and density. It resulted in both versions of the models to give similar results concerning calculated velocities and densities. The semi-implicit formulation was also more efficient than the explicit formulation based on the resolution in the horizontal field. However, the explicit formulation was more accurate. Unfortunately, the semi-implicit formulation was unable to simulate the estuary's standing waves (also known as seiches) very well. However, this model is of great importance to the researchers due to the fact that the Potomac estuary has a highly complex geometry and this model aides in the study of tidal and salinity circulation within it. A further discussion concerning the calculations done by the model can be found in Wang et. al. (1980).

Liu et. al. (2007) used a laterally integrated two-dimensional hydrodynamic model that incorporated salinity transport to determine the effect of alternating the channel connection to the

Danshuei River estuary in Taiwan through the use of a river loop configuration. It was pointed out that the use of a two-dimensional hydrodynamic model "offers an efficient and practical tool for the narrow and partially mixed estuaries". Again, the salinity conservation equations used within the proposed model are similar to equations (2.20) and (2.21) with the assumption of salinity's density equivalent to 7.5×10^{-4} ppt^{-1}. Several parameters, such as the cross-sectional area and bottom friction characteristics, were assumed to be uniform and constant, respectively. Once the model was calibrated and verified, the model displayed an increase in saltwater intrusion with the anticipated river loop configuration, which can cause an increase in salinity concentrations. The Danshuei River estuary model can be used in future management planning for this area and aid in understanding estuary hydrodynamics and salinity circulation (Liu, et. al., 2007).

The salinity equations may also be used to study pollutant transport, which was demonstrated in a three dimensional transport model for the Pearl River Estuary in southern China by Chau and Jiang (2002). The modelers wanted to determine the effect of wastewater discharge on the estuary's ecosystem along with the intensity. This model will not be discussed in great detail, but all specifics may be found in Chau and Jiang (2002), since the subject of this thesis will be considering a two-dimensional model. However, the Chau and Jiang (2002) paper demonstrates that the salinity equations can be altered to fit a specific coordinate system (orthogonal curvilinear and sigma coordinate), the physical behaviors of an estuary, and the use pollutant's concentration and density specifics instead of those of salinity. Nonetheless, the specifics of the pollutant's "turbulent and molecular diffusion coefficients increase as the salinity increases" and this consideration must be made during any alterations (Kuo, 1973). With this

study, it was concluded that this model aided in determining the wastewater discharge had a "strong" effect on the estuary and its accuracy will be improved (Chang and Jiang, 2002).

2.3. Sources and Sinks

Fluctuations of salinity levels of a natural estuarine system are caused by hydrological events, which include but not limited to precipitation, evaporation, and evapotranspiration. For this thesis, two major factors were considered when determining the reasons of salinity fluctuations, which were 1) natural hydrologic cycles, and 2) plant salinity usage.

2.3.1. Natural Hydrologic Cycles

Precipitation, evaporation, and evapotranspiration are three major hydrologic cycles that may be observed and recorded. Specific rates are then calculated based on different locations and more specifically vegetation types. The St. Johns Water Management District maintains eight stations, which seven of them were used for initial analysis of the area, seen in Figure 2.10. Unfortunately, each station did not contain all data points within the scenarios (see Table 2.3). Figure 2.11 through Figure 2.13 display the precipitation for each modeling scenario specified above.

Table 2.3: Missing data for each station maintained by the St. Johns Water Management District.

Station ID	Missing Dates
1122	10/30 - 11/18/1999
1361	10/30 - 11/12/1999
1130	10/30 - 11/11/1999
1010	6/17 - 7/13/1999
	9/28 - 10/19/1999
1100	11/1 - 11/30/1999

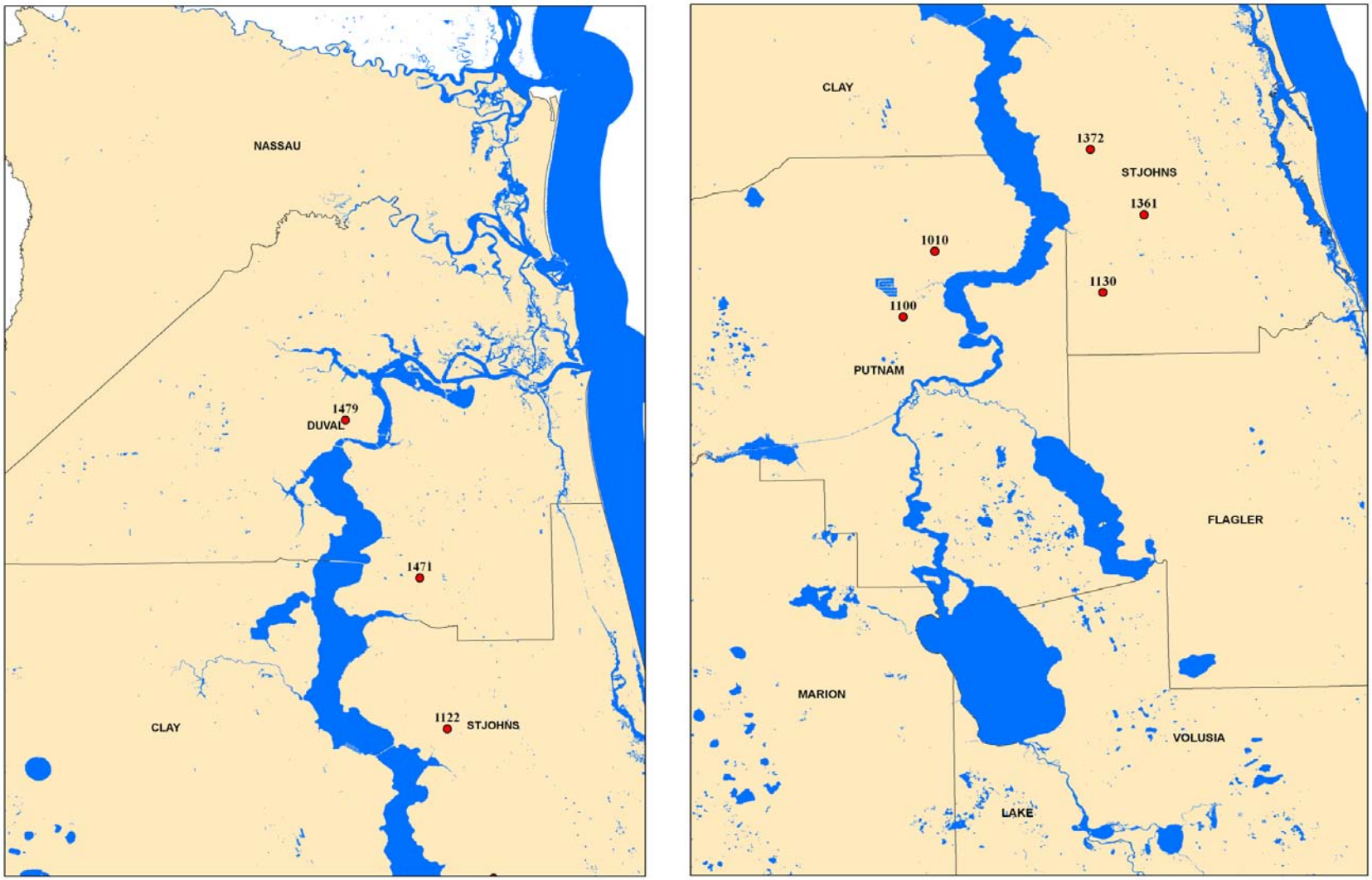

Figure 2.9: St. Johns River Water Management District data station locations.

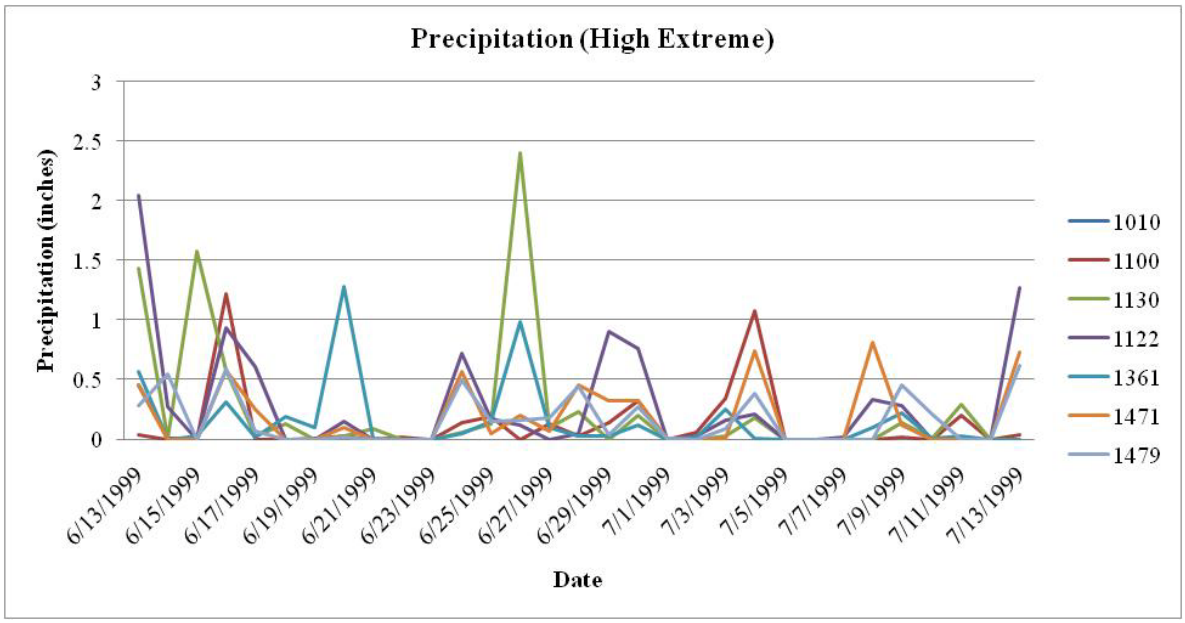

Figure 2.10: Precipitation data of the *High Extreme* scenario recorded by the St. Johns River Water Management District.

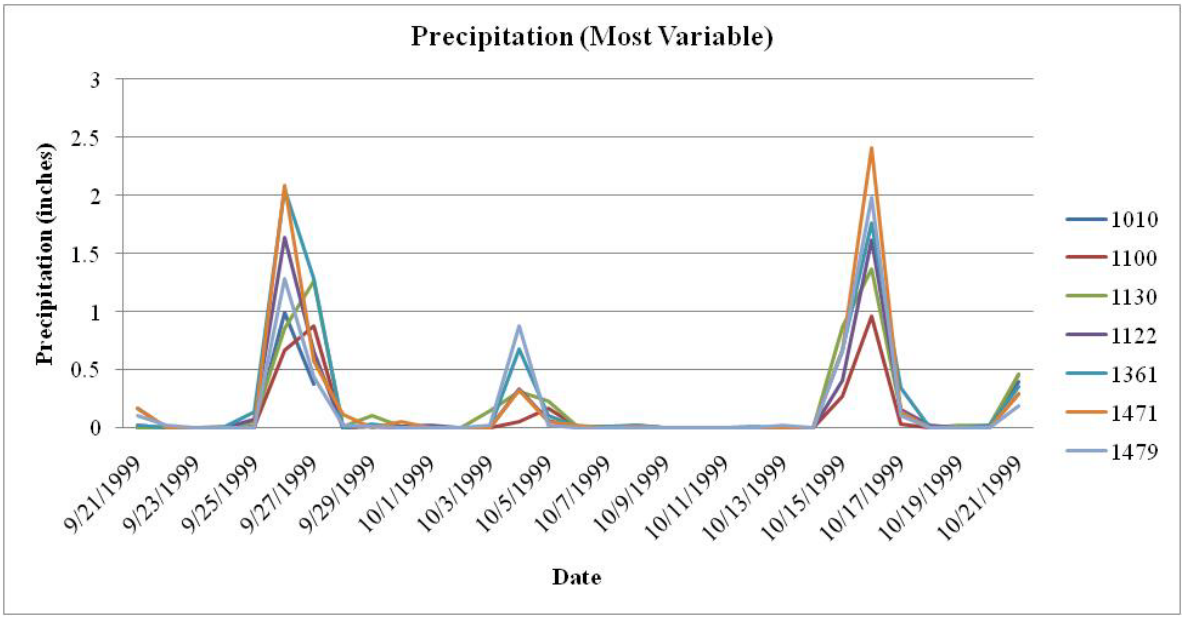

Figure 2.11: Precipitation data of the Most *Variable* scenario recorded by the St. Johns River Water Management District.

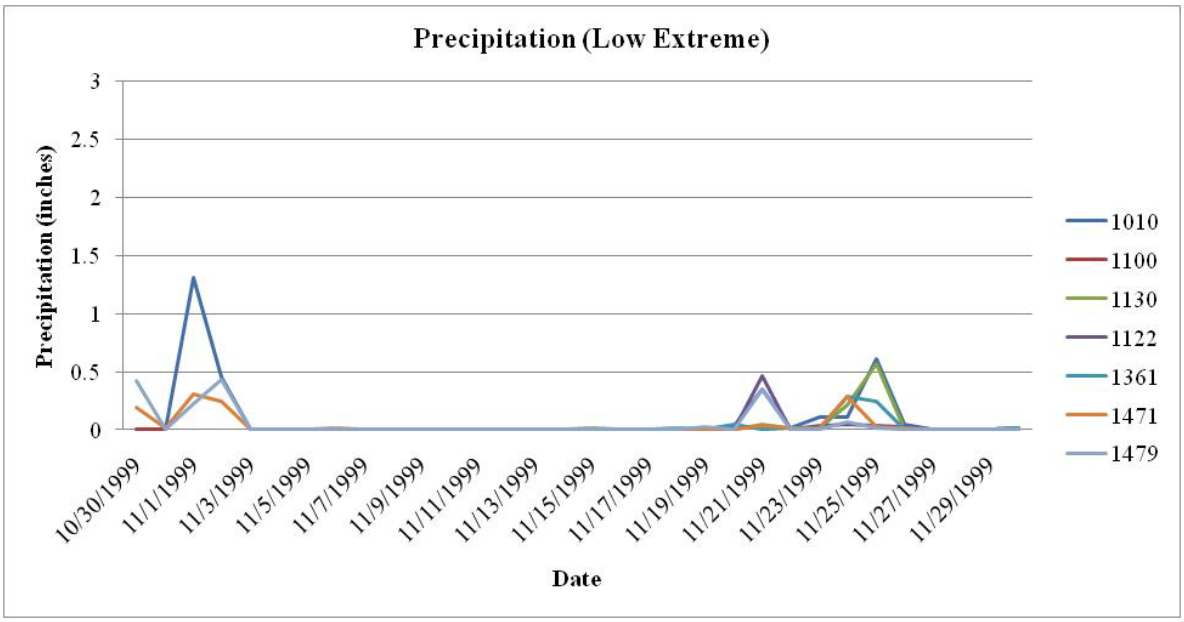

Figure 2.12: Precipitation data of the *Low Extreme* scenario recorded by the St. Johns River Water Management District.

Precipitation and evaporation stations are also maintained by the National Oceanic Atmospheric Association – National Climate Data Center (NOAA NCDC), which data is recorded on a daily basis (see Figure 2.12 through Figure 2.15). It should be noted that the data recorded by the NOAA NCDC's station Gainesville 11 WNW is the only station located in the vicinity of the Lower St. Johns River.

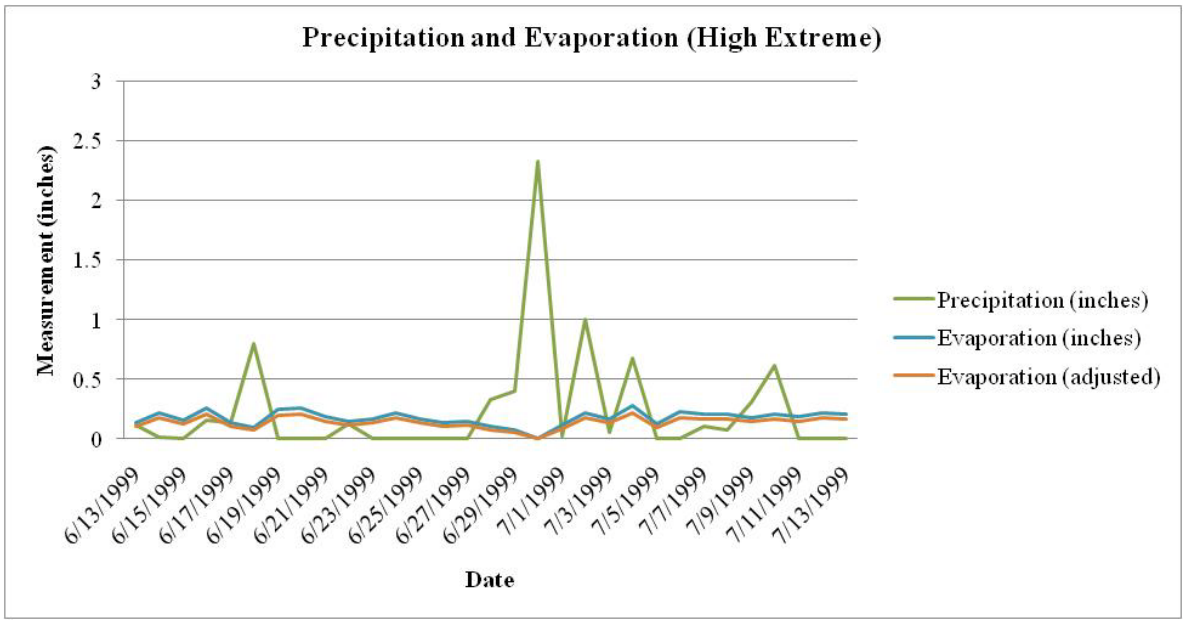

Figure 2.13: Precipitation and evaporation data during the *High Extreme* scenario recorded by the NOAA NCDC.

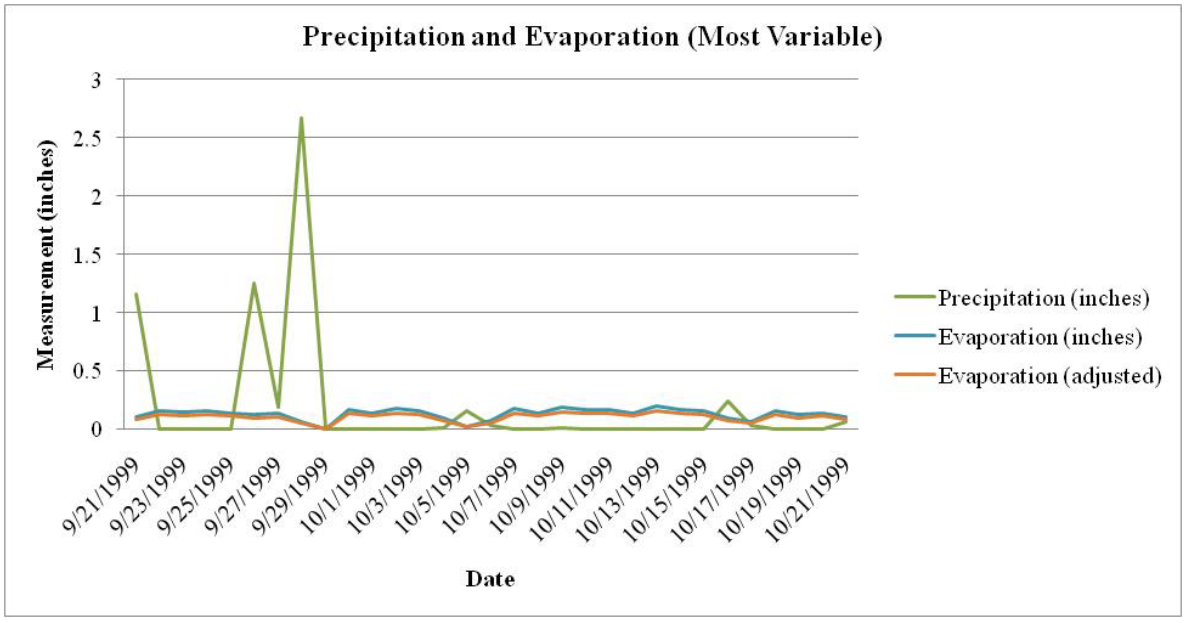

Figure 2.14: Precipitation and evaporation data during the *Most Variable* scenario recorded by the NOAA NCDC.

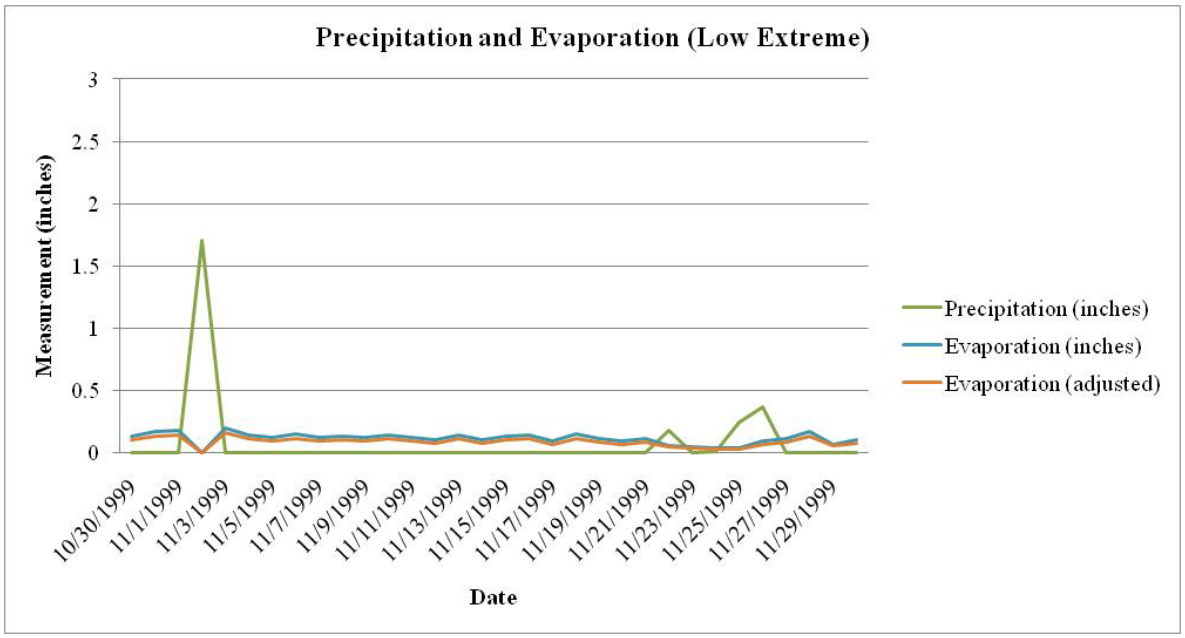

Figure 2.15: Precipitation and evaporation data during the *Low Extreme* scenario recorded by the NOAA NCDC.

Several studies were done to determine the specific evaporation rates for areas containing vegetation type. As shown by Cronk and Fennessy (2001), many scientists have estimated various evaporation rates, which are displayed in Table 2.4. Ramey (2004) also provided evaporation rates for different water bodies to demonstrate the difference of evaporation location to location (see Table 2.5).

Table 2.4: Evaporation rates based on vegetation type and location (*Source: Cronk and Fennessy, 2001*).

Vegetation Type	Location	ET (mm/d)	Reference
Reed Swamp	Czechoslovakia	6.9	Smid 1975
	Czechoslovakia	3.2	Priban and Ondok 1985
Freshwater marsh	Florida	5.1	Dolan et al 1984
Low arctic bog	Canada	4.5	Roulet and Woo 1986
Quaking fen	Netherlands	2.5	Koerselman and Beltman 1986
Coastal marsh (wet)	Ontario, Canada	3.1	Lafleur 1990b
Coastal marsh (dry)	Ontario, Canada	2.6	Lafleur 1990b
Reed Swamp	North Germany	~ 10	Herbst and Kappen 1999

Table 2.5: Evaporation rates for open water in different locations (*Source: Ramey, 2004*).

Location	Category	Evaporation Rate Range	Notes
World	Open Water	30 in/yr to 103 in/yr	
Orlando, FL	Open Water Lake	58 in/yr	0.04 in/day (Jan.) to 0.26 in/day (May)
North FL	Lake	33 in	for the 6 warmest months of the year

Evapotranspiration is the combination of the evaporation and transpiration processes and varies with each vegetation type. This information is important during estuarine studies because it provides a higher accuracy when demonstrating ecological processes. As displayed in Table 2.6, Ramey (2004) provided several values of evapotranspiration losses over evaporation losses rates for specific plants that occur in wetland environments. The USGS (2006) also conducted a study at the Tule Lake Refuge at Tule Lake, CA to establish evapotranspiration loss rates for specific land cover classifications, which are shown in Table 2.7.

Table 2.6: Ratios of evapotranspiration losses and evaporation losses for specific plant species (*Source: Ramey, 2004*).

Evapotranspiration Losses over Evaporation Losses			
Plant Scienitific Name	**Plant Common Name**	**Ratio (ET/E)**	**Notes**
Eichhornia	water hyacinth	1.26, 1.62, 2.7	
Typha latifolia	cattail	1.75, 1.8, 2.5, 2.0	
Acorus calamus		2	
Scirpus validus	bulrush	1.9	
Panicum rigidulum	panic grass	1.58	
Juncus effusus	rush	1.52	
Carex lurida		1.33	
Alternanthera philoxeroides	alligator weed	1.26	
Pontederia cordata	pickerelweed	1.2	
Justicia americana		1.17	
Nymphaea odorata	water lily	1	plants actually reduce water loss
Lemna minor	small duckweed	0.9	
Wolffia columbiana	water meal	0.89	
Spirodela polyrhiza	giant duckweed	0.85	

Table 2.7: Evapotranspiration loss rates for specific land use categories based on the study conducted in Tule Lake Refuge, Tule Lake, CA (*Source: USGS, 2006*).

***Land Use Category**	**Evapotranspiration Loss (ft/yr)**	**Notes**
Grain Production	2.5	
Seasonal wetland	2.9	
Emergent Wetland	2.63	
Open water	4.07	Pan Evaporation Coefficient = 0.9

* Location: Tule Lake Refuge, Tule Lake, CA

2.3.2. Plant Salinity Usage

The second factor considered during this study was plant salinity usage. It was thought that plants may cause a drop (sink) or a rise (source) in salinity levels during the estuaries' lifecycle. However, several sources have shown that this is not the case. The salinity within an estuarine ecosystem is taken in by the plant during natural process since it cannot exclude particular ions, but the true nature of this practice is unknown (Cheeseman, 1988). However, plant species located in an estuarine ecosystem tolerate the salinity.

Salinity studies are always conducted to determine the limit of salinity tolerance. These studies have shown that salinity, along with other factors like nitrogen and oxygen, concentration can play a negative role in the growth of these estuarine and marsh plants. For instance, Linthurst and Seneca (1981) explored the effects of the mentioned factors above on the growth of *Spartina alterniflora* Loisel; the three salinity levels of 15, 30, and 45 ppt, and two nitrogen levels of 0 and 168 kg/ha, were used with zero and oxygen saturated conditions. The authors mentioned that "Woodhouse, et. al. (1974) found that salinity concentration >45‰ caused dieback of *S. alterniflora*," and that it grows best in a salinity concentration of 10 ‰. The results of this particular study showed similar effects; "the possible mechanisms of survival under low nitrogen, low O_2, and high salinity conditions affect the energetic of the plant."

Hester et. al. (2001) explains that when these plants are within lowered or elevated salinity levels for a prolonged period time, they experience "a water deficit", which would cause transpirational water loss to be minimum. That would then lead to the plants to have smaller leaf sizes and have an overall shorter growth form. This was also proven in studies by Brown et. al.

(2006) and Bradley and Morris (1991) concerning the effects of salinity and soil conditions on nutrient update and growth, which high salinity levels and drought conditions also caused negative effects. More information concerning the effects of salinity levels can also be found in Pearcy and Utsin (1984) and Nestler (1977).

2.4. Discontinuous Galerkin Finite Element Method

The shallow water equations are suitable in modeling free surface flow in the deep ocean, coastal, ocean, estuaries, rivers, open channels, and coastal floodplain (Tan, 1992; Vreugdenhil, 1994; Kubatko, et. al., 2009). More importantly, and as will be shown in this thesis, they can be coupled with a transport equation to facilitate the simultaneous solution of hydrodynamics and transport. The model presented in this thesis utilizes the shallow water equations, which are shown below:

$$\frac{\partial \zeta}{\partial t}+\frac{\partial}{\partial x}\left(Hu\right)+\frac{\partial}{\partial y}\left(Hv\right)=0\,, \tag{2.26}$$

$$\frac{\partial}{\partial t}\left(uH\right)+\frac{\partial}{\partial x}\left(Hu^2+\frac{1}{2}g\left(H^2+h^2\right)\right)+\frac{\partial}{\partial y}\left(Huv\right)=g\zeta\frac{\partial h}{\partial x}-\tau uH+F_x\,, \tag{2.27}$$

$$\frac{\partial}{\partial t}\left(vH\right)+\frac{\partial}{\partial x}\left(Huv\right)+\frac{\partial}{\partial y}\left(Hv^2+\frac{1}{2}g\left(H^2+h^2\right)\right)=g\zeta\frac{\partial h}{\partial y}-\tau vH+F_y\,, \tag{2.28}$$

where ζ: elevation of the free surface measured from the geoid (positive upwards),

h: bathymetric depth measured from the geoid (positive values below datum, NAVD88),

$H = \zeta + h$: total height of the water column,

g: gravitational constant,

u: depth-averaged velocity in the x-direction,

v: depth-averaged velocity in the y-direction,

τ: bottom friction factor,

F_x: any additional forcings present due to Coriolis force, surface stresses, etc in the x-direction,

F_y: any additional forcings present due to Coriolis force, surface stresses, etc in the y-direction (Kubatko, 2009).

The discontinuous Galerkin finite element method is, according to Aizinger and Dawson (2002), "based on formulating the SWEs [shallow water equations] as a system of conservation laws, or advection-diffusion equations." A "weak" formulation is obtained by "integrating the equations over a single element, and approximating the unknowns by piecewise, possibly discontinuous, polynomials." During the several experiments of Kubatko et. al. (2006, 2009), several advantages were noted and are as follows: "their ability to capture smooth physically damped solution to the wave propagation problem; their ability to handle advection dominated flows including problems with hydraulic jumps or bores (discontinuities); their inherent elemental mass and momentum conservation properties, which make them ideal for coupling flow and transport models; and the ease with which both *h* (grid) and *p* (polynomial order) refinement, and also adaptivity can be implemented."

According to Kubatko et. al. (2009), the shallow water equations must be rewritten in "divergence form" to be used within the discontinuous Galerkin method, which are shown below:

$$\frac{\partial w_i}{\partial t} + \nabla \bullet \mathrm{F}_i\left(\mathrm{w}\right) = s_i\left(\mathrm{w}\right), \tag{2.29}$$

where i: 1, 2, or 3 (i.e. the row number),

w_i: ith component of the **w** vector

$$\mathrm{w} = \left[\zeta, \quad uH, \quad vH\right]^T, \tag{2.30}$$

$\mathbf{F}_i$: ith row in the flux function matrix

$$\mathrm{F} = \left[\mathrm{f}_x, \quad \mathrm{f}_y\right] = \begin{bmatrix} uH & vH \\ Hu^2 + \frac{1}{2}g\left(H^2 - h^2\right) & Huv \\ Huv & Hv^2 + \frac{1}{2}g\left(H^2 - h^2\right) \end{bmatrix}, \tag{2.31}$$

s_i: ith component of the **s** vector, used for source and/or sink terms

$$\mathrm{s} = \left[0, \quad g\zeta\frac{\partial h}{\partial x} + F_x - \tau uH, \quad g\zeta\frac{\partial h}{\partial y} + F_y - \tau vH\right]^T. \tag{2.32}$$

Using Equations (2.30) through (2.32), the shallow water equations can be written in the "concise form",

$$\frac{\partial \mathrm{w}}{\partial t}+\frac{\partial \mathrm{f}_x}{\partial x}+\frac{\partial \mathrm{f}_y}{\partial y}=\mathrm{s}\,. \tag{2.33}$$

Continuing with the explanation of Kubatko et. al. (2006), new notation must be initiated before the DG finite element can begin. A domain of $\Omega \subset \mathbb{R}^2$ is defined for non-overlapping, triangulated elements; each element *e* will have an individual set domain of Ω_e and boundary of $\partial\Omega_e$. When an inner product over the set domain and boundary occurs, it will be denoted by $(.\,,.)_{\Omega_e}$ and $\langle .\,,.\rangle_{\partial\Omega_e}$, respectively. For the outward unit normal vector and fixed unit normal vector of an element's boundary, the notation **n** and $\mathbf{n}_i$ (for the *i*th edge) will be used respectively.

Approximating the vector **w** values requires the vector $\mathbf{w}_h$, which will include all of the "space of piecewise smooth functions that are differentiable over an element, but [will] allow discontinuities between elements". This mentioned space will be shown as V_h, and all values within $v \in V_h$ along the element's boundary will be $v^{(\mathrm{in})}$ when approaching from the element's interior, and $v^{(\mathrm{ex})}$ when approaching from the exterior. Once completed, the shallow water equations are then put into a "discrete weak form", which is caused by replacing the **w** vector with the newly defined $\mathbf{w}_h$ vector. Each equation is then multiplied by the "test function" $v \in V_h$ and integrated over each element and with the integration-by-parts method to result with the following equation:

$$\left(\frac{\partial}{\partial t}\left(w_h\right)_i, v\right)_{\Omega_e}-\left(\nabla v, \mathrm{F}_i\right)_{\Omega_e}+\left\langle \mathrm{F}_i \bullet \mathrm{n}, v\right\rangle_{\partial\Omega_e}=\left(s, v\right)_{\Omega_e}, \tag{2.34}$$

where $(w_h)_i$: ith component of w_h.

Further details about the discontinuous Galerkin method as applied to the shallow water equations are available in Kubatko (2005), Kubatko et. al. (2006, 2009), Aizinger and Dawson (2002)

The advection-diffusion equation includes, in the given order, the time-dependent term, advection term, and diffusion term (Sudirham, et. al., 2006):

$$\frac{\partial c}{\partial t}+\sum_{i=1}^{d}\frac{\partial}{\partial x_i}\left(u_i\left(t,\bar{x}\right)c\right)-\sum_{i,j=1}^{d}\frac{\partial}{\partial x_j}\left(D_{ij}\left(t,\bar{x}\right)\frac{\partial c}{\partial x_i}\right)=0 \tag{2.35}$$

where d: number of spatial dimensions,

c: concentration of the constituent,

D_{ij}: diffusion coefficients.

Neglecting diffusion yields the following simplification (Aizinger and Dawson, 2002):

$$\frac{\partial c}{\partial t}+\sum_{i=1}^{d}\frac{\partial}{\partial x_i}\left(u_i\left(t,\bar{x}\right)c\right)\equiv\frac{\partial c}{\partial t}+\nabla\left(uc\right)=0\,. \tag{2.36}$$

Integrating Equation (2.36) in the vertical over the total height of the water column generates the following two-dimensional form:

$$\frac{\partial\left(cH\right)}{\partial t}+\nabla\left(uHc\right)\equiv\frac{\partial\left(cH\right)}{\partial t}+\nabla\left(\mathrm{q}c\right)=0\ or\ g \tag{2.37}$$

where g: source term.

The same procedure applied to Equation (2.29) is applied to Equation (2.37); using the same test function $v \in V_h$ and integrating over the element's boundary results in the equation below:

$$\left(\frac{\partial (cH)}{\partial t}, v \right)_{\Omega_e} - (\mathrm{q}c, \nabla v)_{\Omega_e} + \langle c\mathrm{q} \bullet \mathrm{n}, v \rangle_{\partial \Omega_e} = (g, v)_{\Omega_e} . \tag{2.38}$$

Further details about the discontinuous Galerkin method as applied to the advection-diffusion equation are available in Aizinger and Dawson (2002), Cockburn (2003), and Sudirham et. al. (2006).

As mentioned earlier, Kubatko et. al. (2009) have conducted tests to examine the performance of both the continuous (CG) and discontinuous Galerkin (DG) methods. The ADCIRC (ADvanced CIRCulation) model uses the continuous Galerkin method to solve situations using the shallow water equations. The CG method "solves the momentum equations and a reformulation of the continuity equation" based on piecewise linear elements (Kubatko, 2010). Kubatko continues to state that it is a "robust mass-conserving wetting and drying algorithm", which is one of the main reasons the DG method was chosen to be incorporated into a salinity transport model. Not only is it able to "accurately and robustly hand advection-dominated scenarios", it is has "element (local) conservation properties". This provides for more accurate representations and approximations of the numerical solutions. Kubatko et. al. (2009) "observed that the CG solution errors were greater than the corresponding DG solution errors – generally by an order of magnitudes." Even though the DG method is more expensive than CG method, it is ideal for the coupling of hydrodynamics and transport modeling and it relies more on the physics than a user-selected generalized wave continuity equation (GWCE) weighting

factor (i.e. τ_0) (Kubatko, et. al. 2009, Kubatko, 2010, Dawson and Proft, 2004). Further discussion on the comparison of the discontinuous and continuous Galerkin method and applications can be found in Dawson et. al. (2006), Aizinger and Dawson (2007), Dawson and Proft (2004), Aizinger and Dawson (2002).

2.5. Previous Mass Conservation Studies

The future salinity transport model for the Lower St. Johns River deals with the movement of salinity within the river and the surrounding estuaries. As stated earlier, it is important to ensure the accuracy of a mathematical model by using mass conservation tests. The researcher must make certain that the mass is conserved within the hydrodynamic model before it can be coupled with transport (Naifar et. al., 2007; Dawson et. al., 2004). Similar procedures were done with other numerical models and these experiments were proved to be very useful in several selected numerical methods, especially the discontinuous Galerkin method (Kubatko et. al., 2009).

Gourgue et. al. (2009) focused on determining an appropriate wetting-drying approach for a discontinuous finite element discretization for linear elevation elements. The Thacker test case was used to demonstrate a firmly mass conservative method for the Scheldt Estuary located near Belgium and the Netherlands. As a test run, these researchers set a domain to be a closed circular basin, so that no water may enter or leave the control volume. However, it was realized that the inclusion of bottom stress was necessary to maintain stability for this particular test. The ending results showed that the mass volume remained nearly constant with the difference

between final and initial water volume having a magnitude order of 10^{-15}. When applied to the Scheldt River and its Estuary, the method proved successful when concerning the wetting and dry algorithm. The dry areas presented no water transport was occurring.

With mass conservation tests, Wang et. al. (2008) were able to determine that a proposed model was not conserving mass during finite element runs and revision was necessary. The goal of the project was to establish the effectiveness of the coupling of a water quality model and a three-dimensional hydrodynamic model. It was stated that "the issue of conservation of volume and mass is critical…Without it, a small error introduced by the large magnitude physical transport can easily, if not completely, obscure the accuracy of the smaller magnitude biogeochemical processes." The presented Eulerian-Lagrangian transport scheme within the Eulerian-Lagrangian Circulation (ELCIRC) model was shown to not conserve mass. This was observed in a conservative tracer experiment for the salinity transport within the Danshuei River estuary with the same initial and boundary conditions specified from previous hydrodynamic runs. The researchers then presented an alternative method, which included a consistent finite volume/finite difference procedure. Using the basics of mass conservation, Wang et. al. (2008) were able to demonstrate the conservation of mass locally and globally within the Danshuei River estuary in Taiwan. It also provided a stronger correlation between the computed and measured salinity concentrations. Simply put by Wang et. al. (2008), the volume flux used within the mass flux calculation from one control volume to the next must be consistent.

Further understanding of mass conservation, possible origins of mass errors, and the applications of mass conservation can be found in Berger et. al. (2002), Oliveira et. al. (2000) Shaha et. al. (2010).

CHAPTER 3 DOMAIN DECOMPOSITION

The mass conservation analysis requires that the domain be segmented into sections. The segmentation is based on physical characteristics. Due to the low slope of the overall Lower St. Johns River, it is suggested to base each segment on the river's width. With this approach, the depth variation along the river can be considered smooth, and the width of the river's main channel (i.e. branches were excluded from the analysis) is used as the partitioning factor. As shown in Figure 3.1, each river section has a qualitatively consistent width. Quantitatively, the lowest portion of the river (R_1) has a maximum width of 1.48 km, then the river widens gradually to where the maximum width of portion R_2 is 5.01 km. The near 5-km river width is maintained through portion R_3 (5.43 km), after which the river narrows abruptly to a maximum width of 2.06 km through portion R_4. The ocean boundary O_b and Lake George L_G are considered to be the endpoints of the river partitioning. Marsh A (M_A) and Marsh B (M_B) are given their own partition so to examine their mass conservation characteristics as isolated sub-systems to include the intracoastal waterways, I_A and I_B, respectively. Table 3.1 provides the geometric dimensions of each river section, which include the following: area, volume, approximate width, average depth with standard deviation.

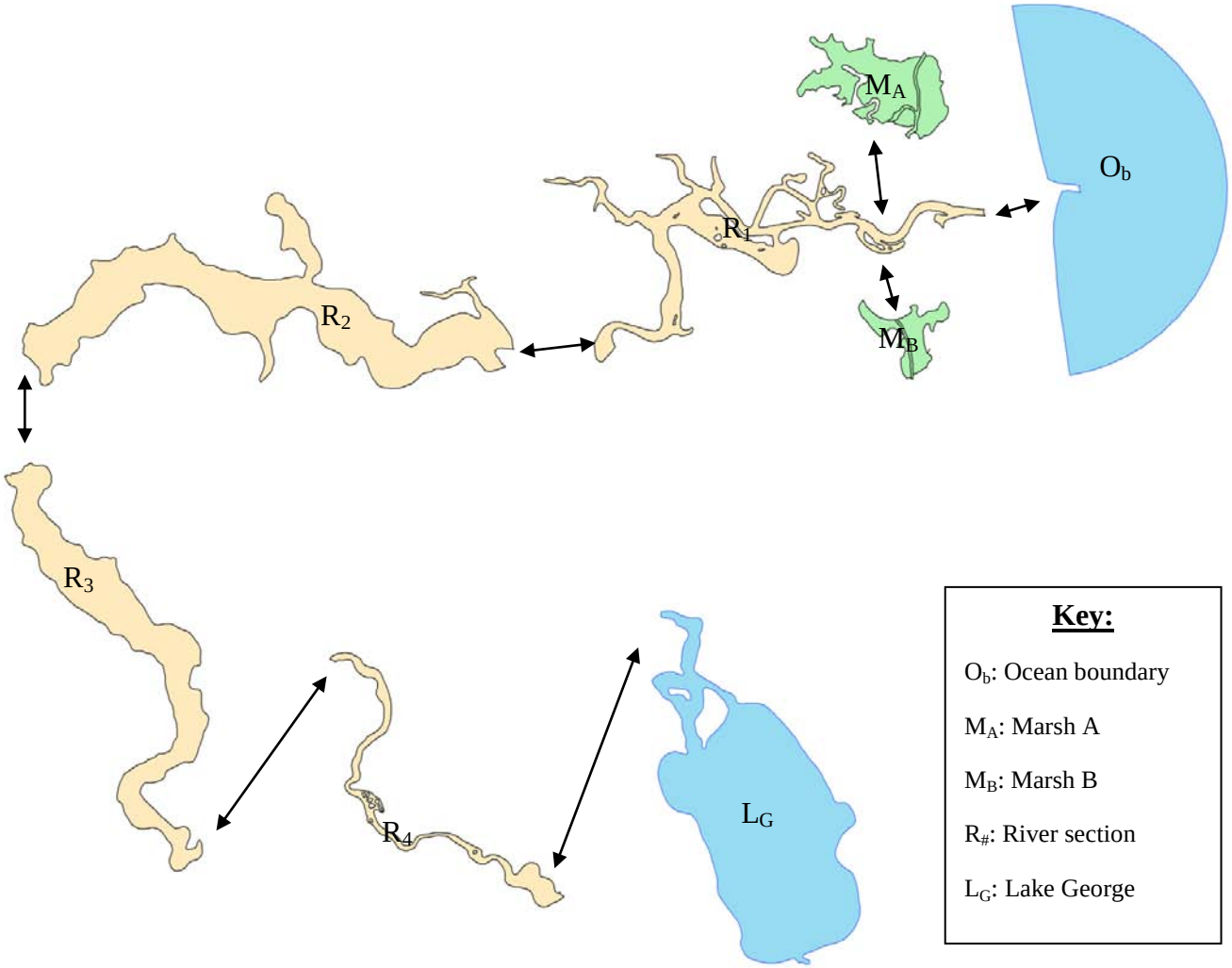

Figure 3.1: Partitioning of the Lower St. Johns River as used for the testing of mass conservation.

Table 3.1: Geometric dimensions for each of the river partitions used within the mass conservation analaysis (refer to Chapter 8).

Name	Symbol	River (km) Start	River (km) End	Area (km^2)	Volume ($10^{-3} \times km^3$)	w_{approx} (m)[a]	Depth (m)	
							Average (μ)	Standard Deviation (σ)
Ocean Boundary	O_b	-10	0	291.6	1225.6	10 km[c]	11.2	4.1
Intracoastal A	I_A	3	10	2.1	1.5	300	2.2	1
Intracoastal B	I_B	5	10	0.8	0.7	160	2.7	0.7
*Marsh A	$*M_A$	2	12	40.3	+3.0 (-2.4) [b]	7 km[d]	0.1	0.7
*Marsh B	$*M_B$	3	6	12.5	+0.3 (-1.4) [b]	2 km[d]	-0.2	0.7
River Section 1	R_1	0	40	68.9	112	1720	4.5	4
River Section 2	R_2	40	85	190.7	178.8	4240	2.7	1.5
River Section 3	R_3	85	130	120.7	97.4	2680	2.6	1.3
River Section 4	R_4	130	165	21.8	17.6	630	2.4	1.1
Lake George	L_G	165	200	193.7	146.3	5530	2	1

Note: $M_A = *M_A + I_A$

$M_B = *M_B + I_B$

[a] w_{approx} (m) = Area ÷ (End - Start)

[b] +volume: bathymetric volume

-volume: topographic volume

[c] w_{approx} (m): approximated coastline distance from the river's inlet to the ocean boundary

[d] w_{approx} (m): approximated inland distance from river bank to the marsh defined boundary

CHAPTER 4 MODELING SCENARIOS

An effective model requires the relevant physical processes to be accurately simulated. Moreover, an effective model must consider its three potential sources of error: formulation; numerics; and data. In this context, the following thesis will employ the shallow water equations, along with the advection-diffusion equation, as its 'formulation,' an associated algorithm (continuous and discontinuous Galerkin finite element method and Runge-Kutta methods for spatial and time discretization, respectively) as the 'numerics,' and data used in the model mesh, initial conditions, boundary conditions, and validation as 'data.' This chapter will present the modeling scenarios used for numerical experimentation.

The model herein will employ daily salinity data collected from four USGS stations (refer to Chapter 2, Figure 2.2). For the USGS stations, there were three, one-month data sets identified, where each record was unique (detailed shortly hereafter) with respect to apparent meteorological and hydrological influence.

The first data set, *High Extreme*, contains observed data from June 13, 1999 through July 12, 1999. This data set is rather complete (at least 83% capture rate) and captures the higher activity usual of the hurricane season. It should be noted that this time "period does not represent the maximum salinity value recorded". As displayed in Figure 4.1, the tides have an influence on salinity concentrations. For instance, the salinity levels at Dames Point (located in the lowest region of the Lower St. Johns River) increase to one of the highest concentrations (35 psu) towards the end of the first week. During the second and third weeks, the salinity

concentration decreases to the lowest concentration (13 psu) before increasing once again at the start of the fourth week. This behavior occurs in Acosta Bridge as well. However, as you move further upstream (refer to Buckman Bridge and Shands Bridge), the salinity levels decrease from the highest concentration in the second week to an average salinity concentration; during the third and fourth weeks, Buckman Bridge maintained a salinity concentration in the range of 5 to 7 psu, and Shands Bridge had a range of 1 to 3 psu. As stated earlier, the salinity decreases as you move upstream, which can be seen the observations of the four stations for all three modeling scenarios. A more in-depth analysis of this data set and the others to follow may be found in Giardino (2009).

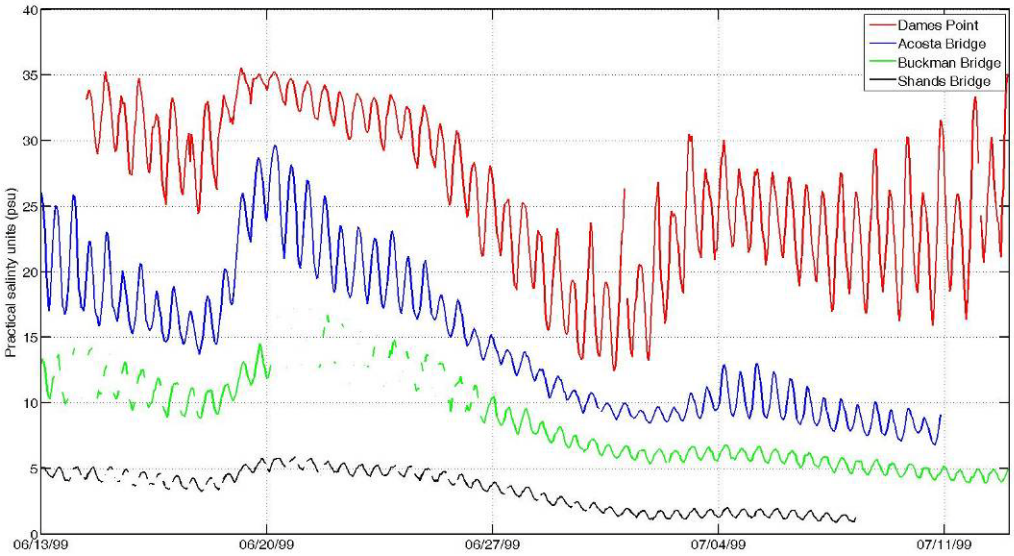

Figure 4.1: Observed salinity concentrations on an hourly basis during the *High Extreme* time period.

The second data set, *Most Variable*, contains observed data from September 21, 1999 through October 20, 1999. This data set has continuous records for Dames Point and Acosta Bridge, but is somewhat (less than 20%) lacking for Buckman Bridge and Shands Bridge locations. The *Most Variable* data collection is particularly important since it contains "meteorological impacts on salinity in the St. Johns River including Hurricane Irene passing offshore on October 17, 1999" (Giardino, 2009). The salinity concentration at all four stations were the highest on this date (Dames Point – 31 psu; Acosta Bridge – 22 psu; Buckman Bridge – 8 psu; Shands Bridge – 3 psu) and returned to the decreasing trend after the meteorological event. Also evident in the data is the autumnal transition from hot/humid to cool/dry, which is marked by the decline in salinity within in the first, second, and third week.

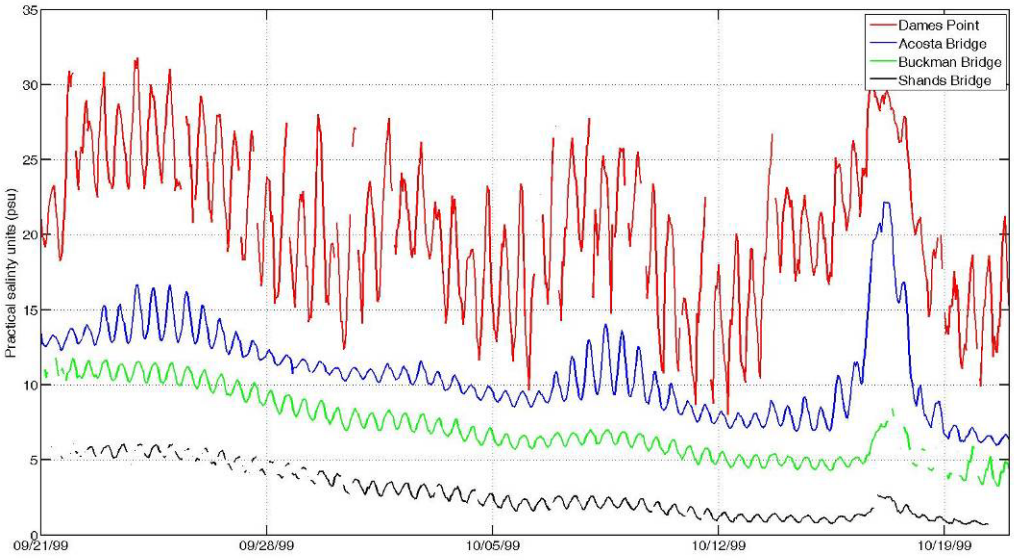

Figure 4.2: Observed salinity concentration on an hourly basis during the *Most Variable* time period.

The third data set, *Low Extreme*, contains observed data from October 30, 1999 through November 29, 1999. Giardino (2009) noted that "this dataset is actually the most complete dataset in terms of data availability with all four stations exceeding 96% data returns." During this time period, Shands Bridge contains very low and almost consistent salinity levels. This is due to high freshwater inflow around this area, which can cause the station to record no salinity levels. Also, the data variability "does not extend past 0.02 psu which is below the error tolerance on a salinity gauge" (Giardino, 2009; Janzen 2003). Based on that reasoning, Giardino (2009) suggested that Shands Bridge not be used for model verification. It should be noted that Buckman Bridge maintained a salinity concentration of approximately 0.6 psu starting within the first week. During the first two weeks, Acosta Bridge, Buckman Bridge, and Shands Bridge displayed a decrease in salinity. However, Dames Point displayed decreases and increases in salinity more frequently within these two weeks compared to the other stations. Acosta Bridge followed the trend at Dames point during the end of the second week through the end of the scenario; the highest salinity concentrations occurred at the end of the second week and the mid of the third and fourth weeks (Dames Point – 28 psu; Acosta Bridge – 8.8 psu).

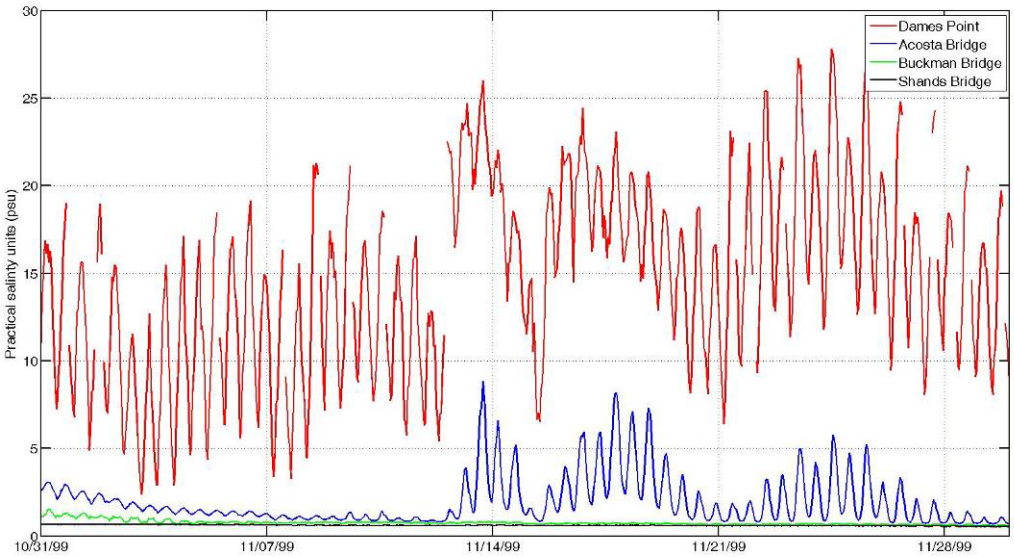

Figure 4.3: Observed salinity concentration on an hourly basis during the *Low Extreme* time period

CHAPTER 5 FINITE ELEMENT MESH

Modeling herein relies on one finite element mesh, MARSH. This mesh is a byproduct of the high-resolution model for the South Atlantic Bight developed by Bacopoulos et. al. (2011) and hones in on the Lower St. Johns River coastal region. The MARSH mesh consists of 30,472 nodes and 56,262 elements, and is the most comprehensive mesh in terms of geometric/physical system description by resolving all hydraulic watercourses as well as intertidal zones and the marsh areas of the Lower St. Johns River (Figure 5.1). This mesh resolution ranges from 1.9 km in the ocean boundary to 38.6 m leading to Lake George. The marsh areas have a resolution ranging from 52 m to 148 m. A minimum of three elements (total of four nodes) expand the channel and intracoastal waterways. It is also relevant to note that bottom friction attributes are assigned differently for the coastal wetlands (higher, i.e., Manning's n = 0.050) versus the fully wetted regions (lower, i.e., Manning's n = 0.025), as applicable for the MARSH mesh. The mesh is forced on the open ocean boundary as well as on the north and south boundaries of the Atlantic Intracoastal Waterway using model data from the large-scale MARSH mesh of Bacopoulos et. al. (2011).

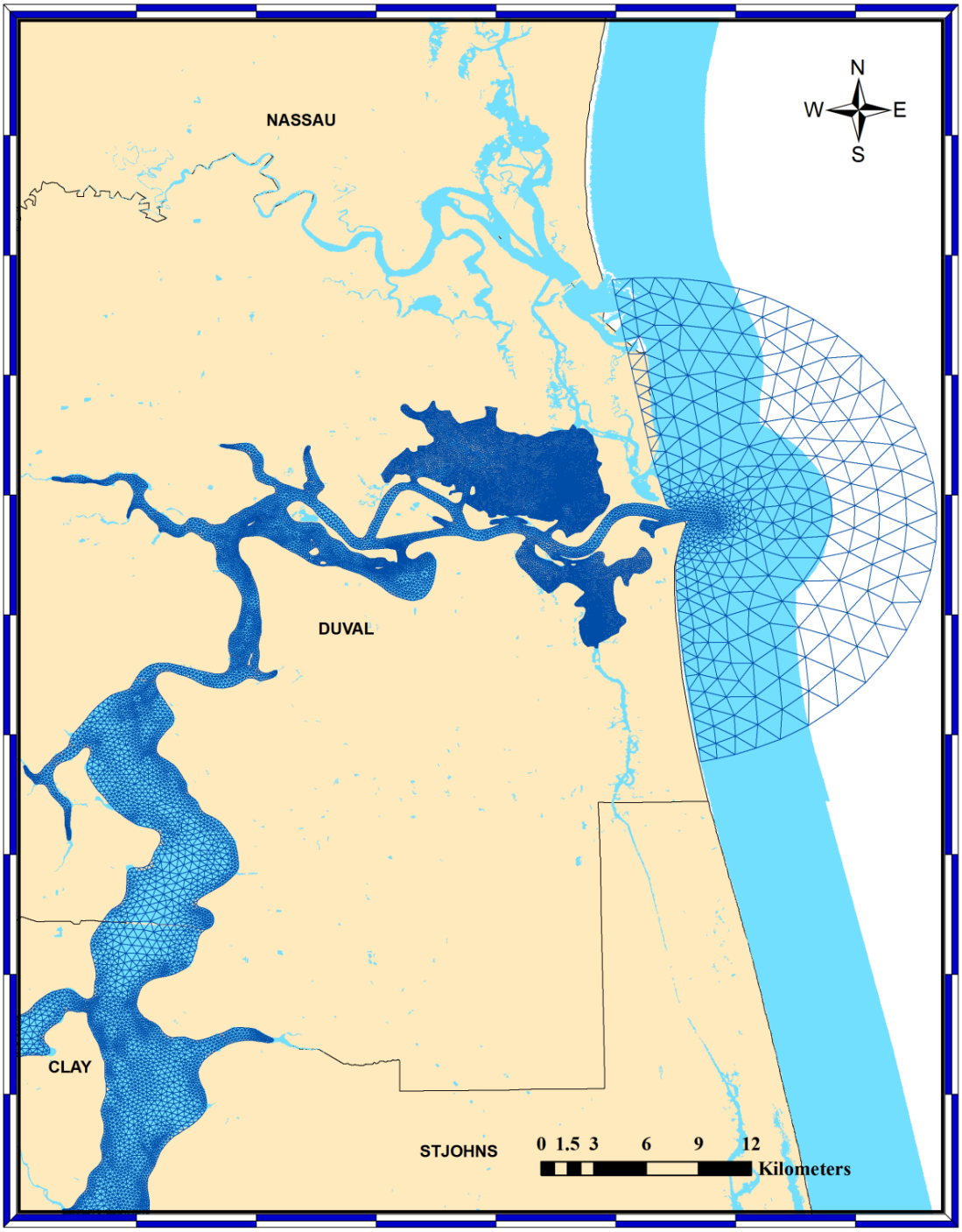

Figure 5.1: MARSH mesh contains the most detail due to the inclusion of the salt marshes and estuaries in the area.

CHAPTER 6 LAND COVER ANALYSIS

This thesis will focus on the two largest coastal marshes, within the Lower St. Johns River, to determine the impact of marshes on circulation and salinity transport. The northern marsh will be established as Marsh A, and the southern marsh will be distinguished as Marsh B as shown in Figure 6.1. A historical land cover analysis, based on the NLCD 1992, NLCD 2001, and NLCD 2006 data sets, is performed to establish an understanding of the land cover changes within these two marshes.

The National Land Cover Data for the years 1992, 2001, and 2006 (NLCD 1992, NLCD 2001, NLCD 2006) land cover data are used to calculate the differences in vegetation within the marshes historically, as shown in Figures 6.2 through 6.7.

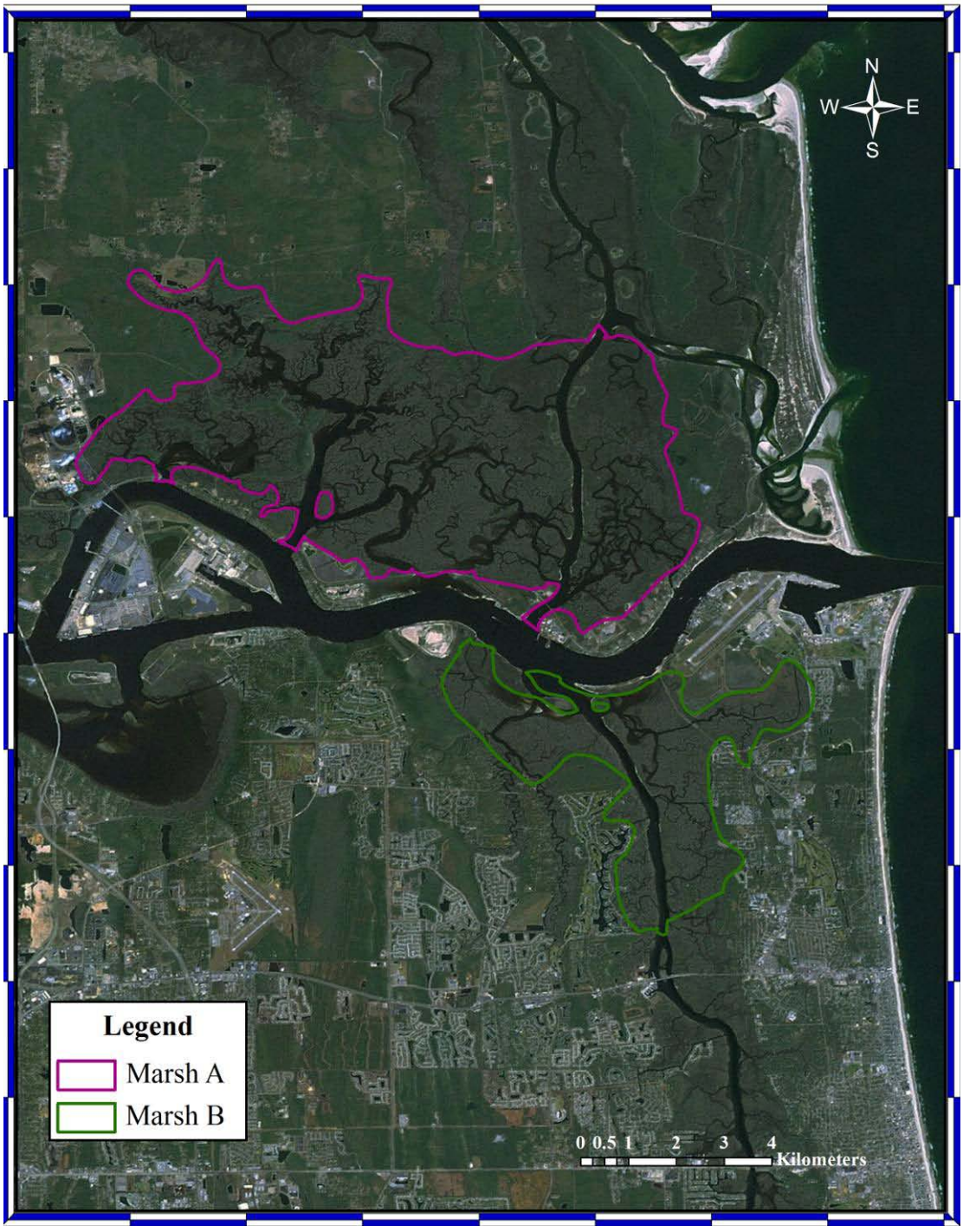

Figure 6.1: Satellite image of the two coastal marshes, Marsh A and Marsh B within the Lower St. Johns River.

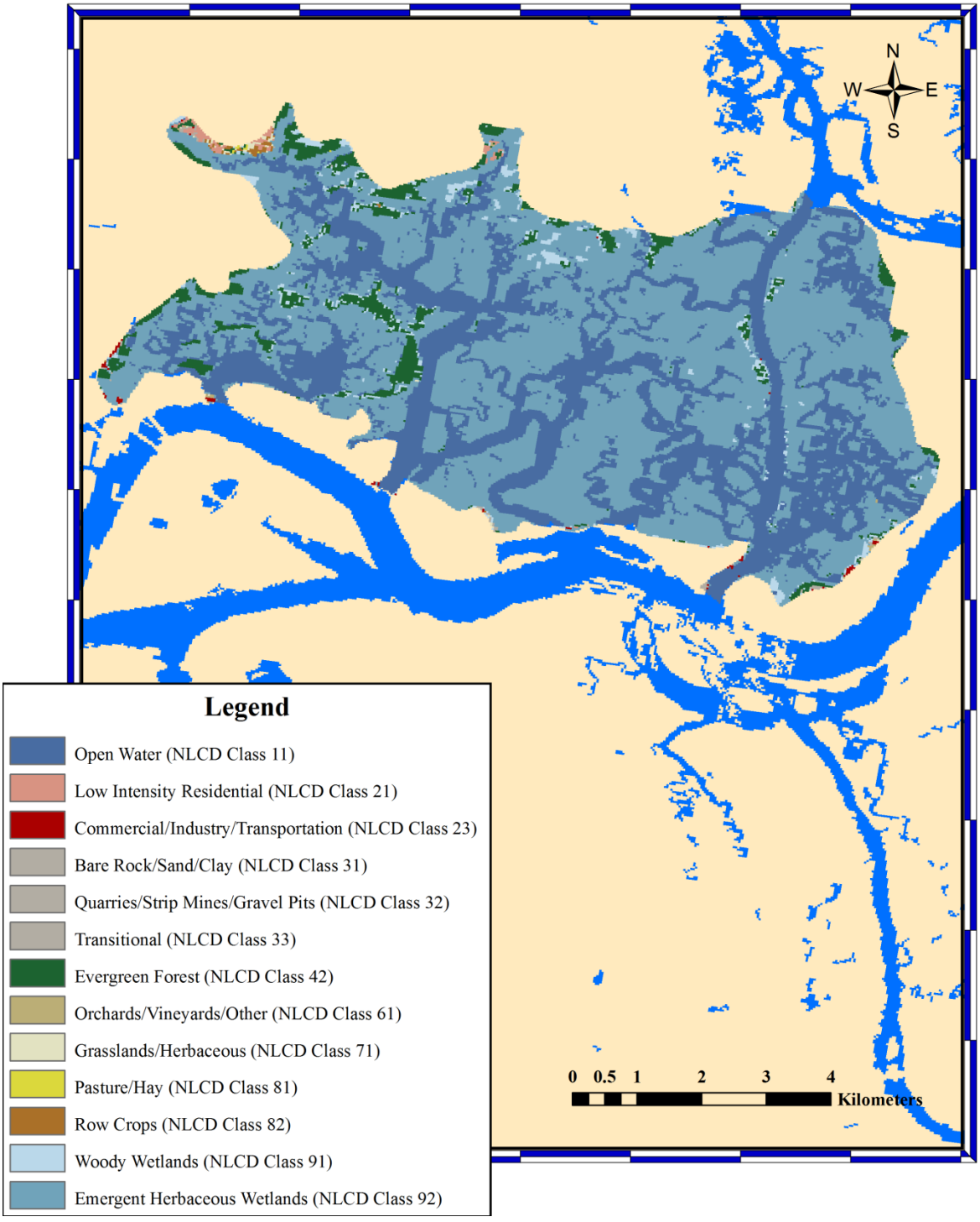

Figure 6.2: NLCD 1992 land cover distribution of Marsh A.

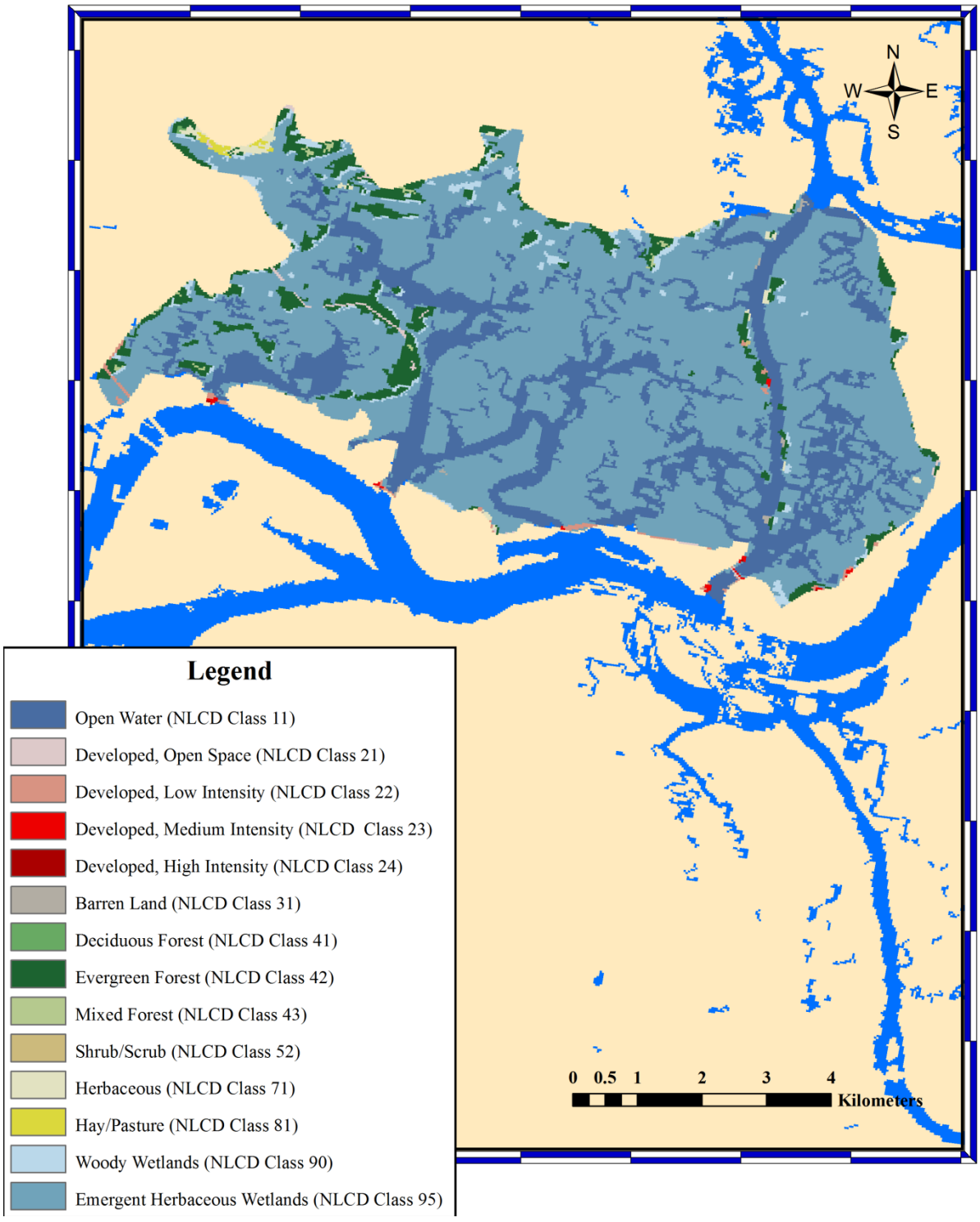

Figure 6.3: NLCD 2001 land cover distribution of Marsh A.

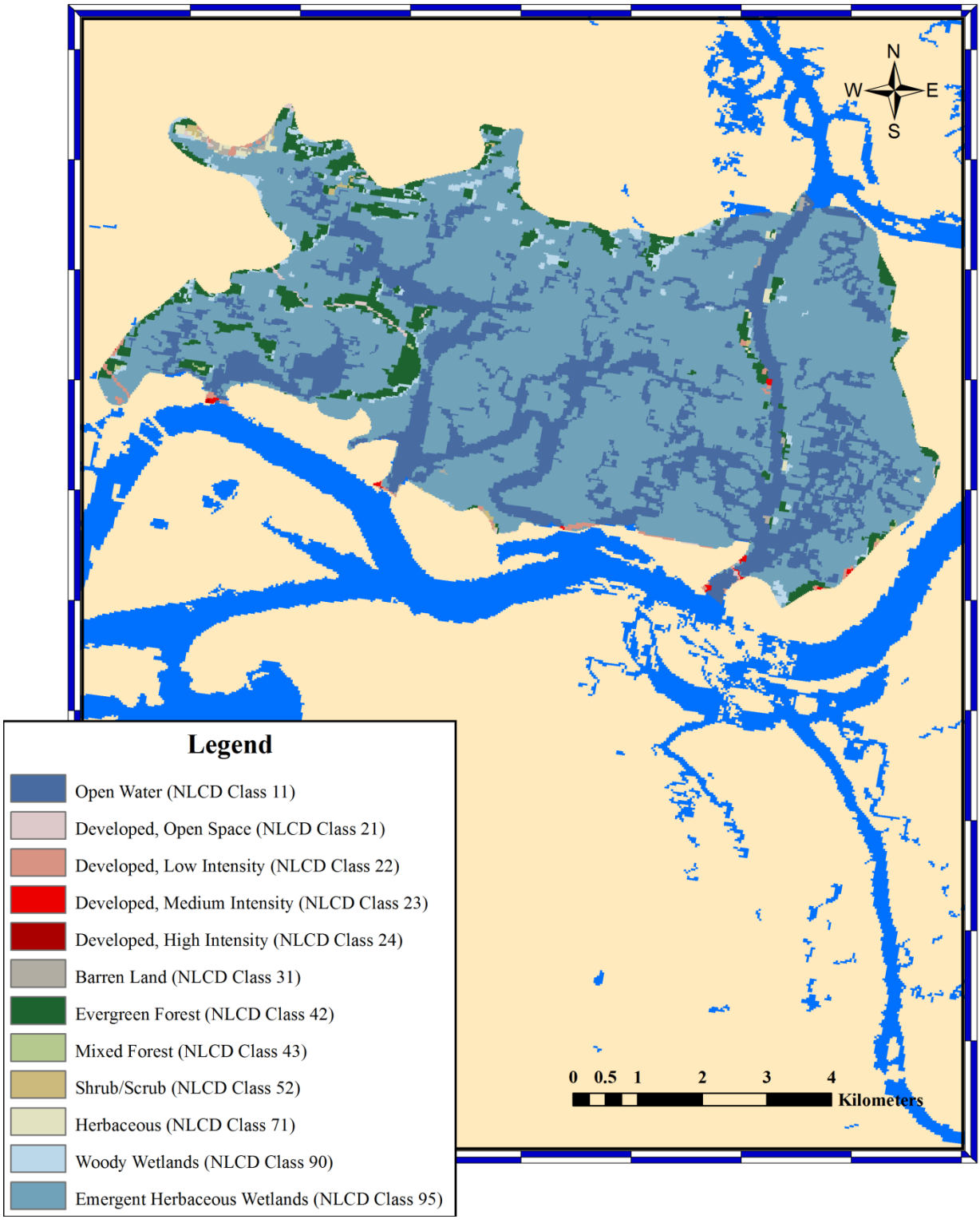

Figure 6.4: NLCD 2006 land cover distribution of Marsh A.

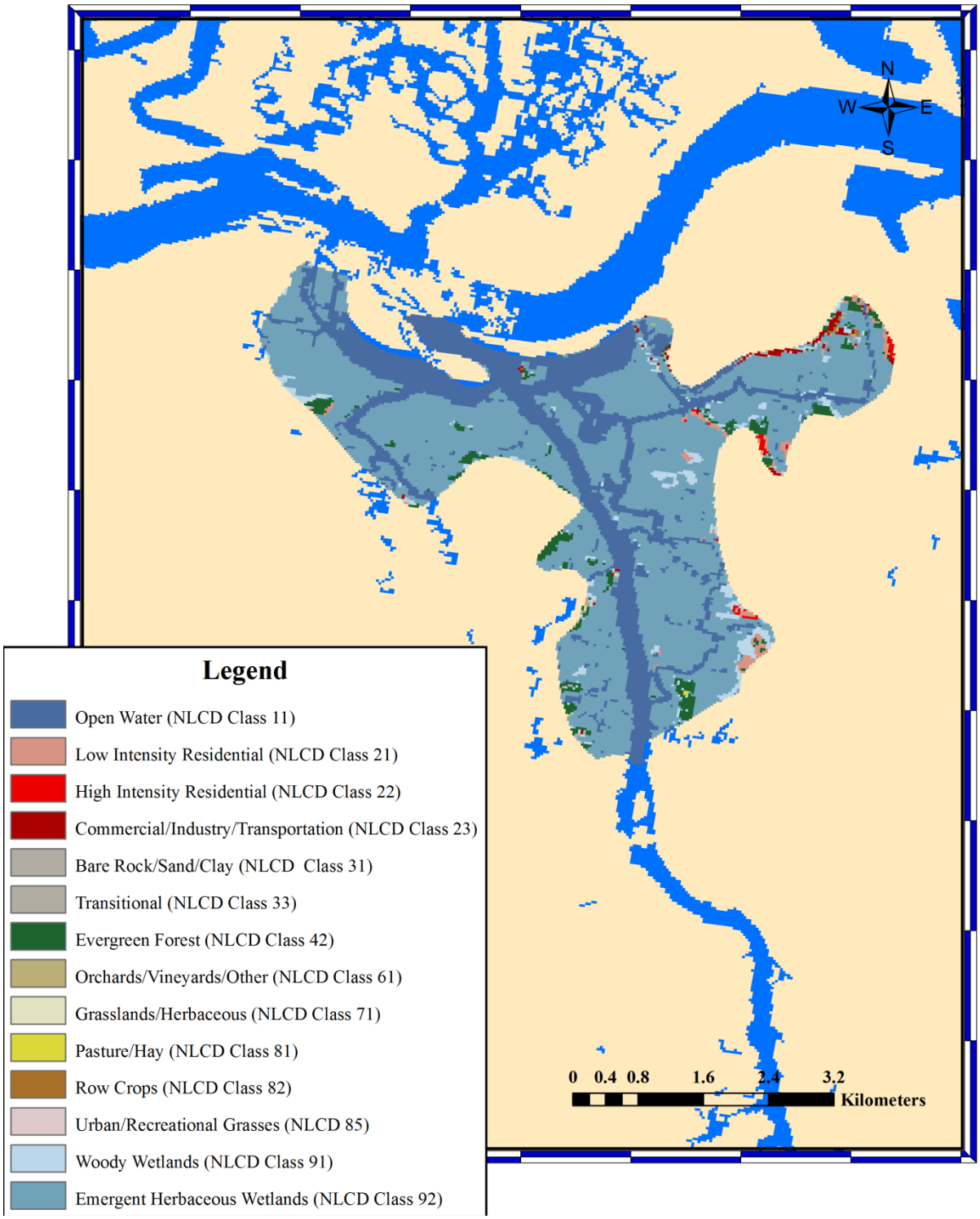

Figure 6.5: NLCD 1992 land cover distribution of Marsh A.

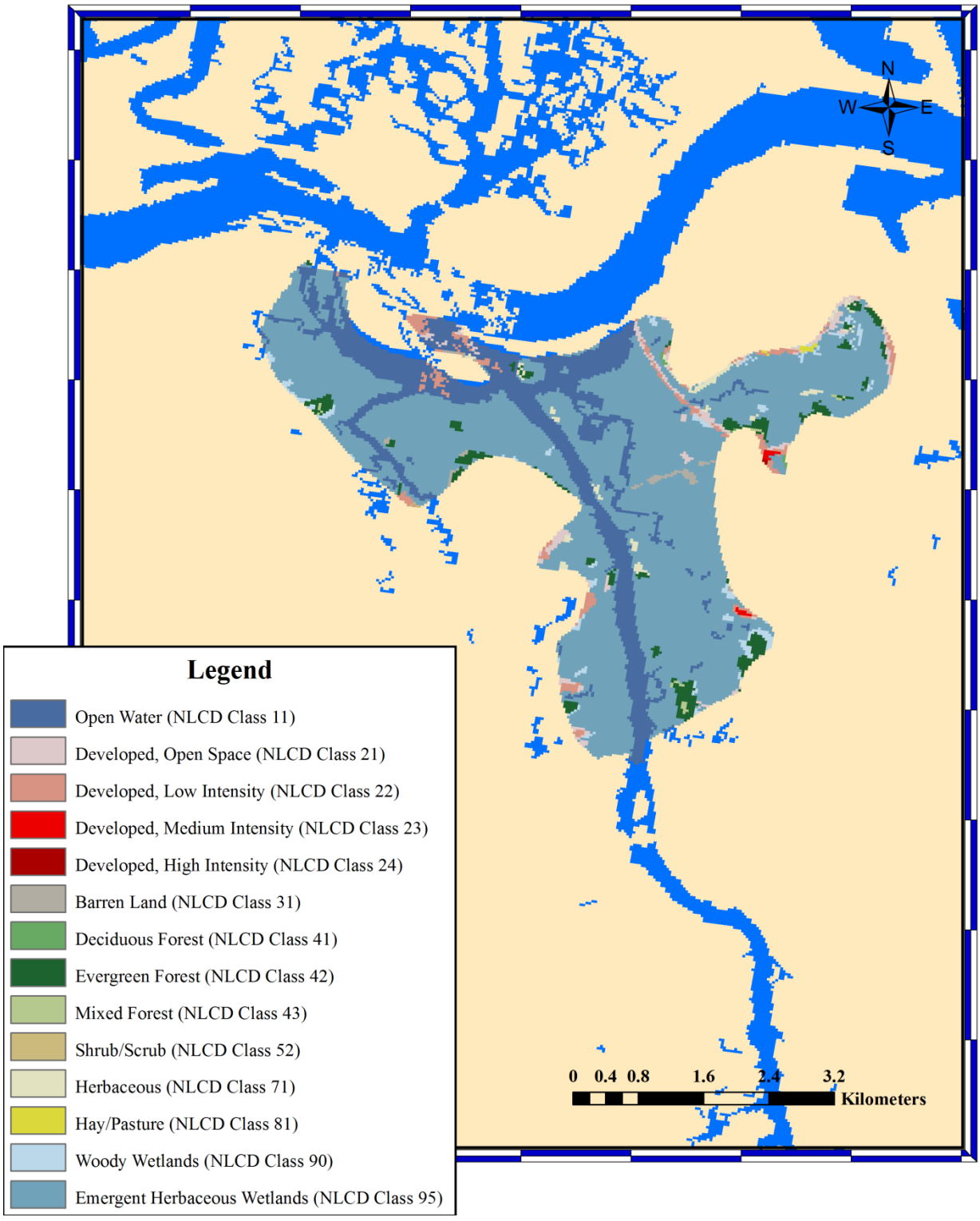

Figure 6.6: NLCD 2001 land cover distribution of Marsh B.

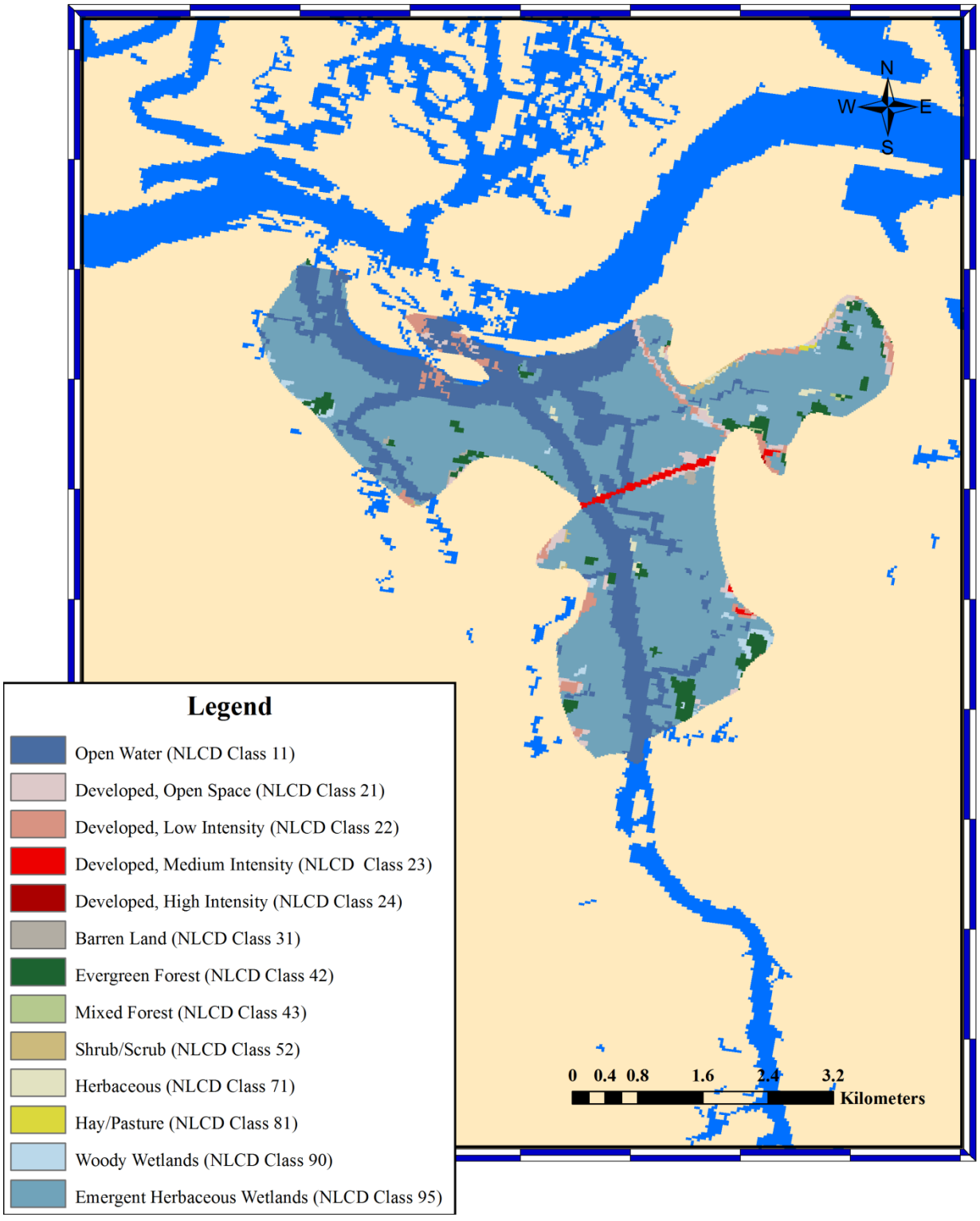

Figure 6.7: NLCD 2006 land cover distribution of Marsh B.

Marsh A has an approximate area of 46.0 square kilometers (11.3×10^3 acres), while Marsh B is approximately 15.3 square kilometers (3.77×10^3 acres), which means that Marsh A is about three times larger in size. The land cover data is analyzed within each marsh. The NLCD 2001 and 2006 data sets are based on the same land cover classification, however, the NLCD 1992 data set is reclassified based on the 2001 classification with Orchards/Vineyards/Other (class 61) excluded from the analysis (see Appendix F). Based on the previous study of Bacopoulos (2009), the three main land cover classifications that will be focused on are Open Water (class 11), Woody Wetlands (class 90), and Emergent Herbaceous Wetlands (class 95). Percentages are calculated for each land cover type, which are shown in Tables 6.1 and 6.2. It is noticed that both Marsh A and B mainly consisted of approximately 66.6% and 69.1% or less of Open Water and Emergent Herbaceous Wetlands, respectively; Woody Wetlands approximately 3% or less of both marshes. Based on this fact, the primary land cover classifications to be considered within the model are Open Water and Emergent Herbaceous Wetlands. A trend is also observed among the changes within the two main land cover classifications. As the Open Water percentage decreased, the Emergent Herbaceous Wetlands percentage increased, and vice versa. This may be due to some areas being flooded, which would cause the vegetation count to be lower during the data capture procedure. Based on this land cover analysis, the marsh areas of the Lower St. Johns River have not gone through a significant amount of change between the years of 1992 and 2006. Further explanation of the land cover classifications can be found in Appendix F.

Table 6.1: NLCD Land cover distribution and comparison for Marsh A.

Marsh A							
Value	Name	1992		2001		2006	
		Count	Percentage	Count	Percentage	Count	Percentage
11	Open Water	20143	33.8	12134	23.7	28378	23.7
21	Developed, Open Space	0	0.00	136	0.266	313	0.261
22	Developed, Low Intensity	167	0.280	191	0.373	562	0.469
23	Developed, Medium Intensity	0	0.00	59	0.115	137	0.114
24	Developed, High Intensity	89	0.149	4	0.00781	8	0.00668
31	Barren Land	97	0.163	51	0.100	322	0.269
41	Deciduous Forest	0	0.00	9	0.0176	0	0.00
42	Evergreen Forest	2837	4.76	2994	5.85	7016	5.86
43	Mixed Forest	0	0.00	90	0.176	53	0.0443
52	Shrub/Scrub	0	0.00	5	0.00977	208	0.174
71	Herbaceous	67	0.112	251	0.490	403	0.337
81	Hay/Pasture	13	0.0218	79	0.154	0	0.00
82	Cultivated Crops	76	0.127	0	0.00	0	0.00
90	Woody Wetlands	1176	1.97	1083	2.12	2528	2.11
95	Emergent Herbaceous Wetlands	34961	58.6	34108	66.6	79794	66.6
Total		59626	100	51194	100	119722	100

Table 6.2: NLCD Land cover distribution and comparison for Marsh B.

Marsh B							
Value	Name	1992		2001		2006	
		Count	Percentage	Count	Percentage	Count	Percentage
11	Open Water	5394	27.2	3330	19.6	10209	25.7
21	Developed, Open Space	1	0.00505	338	1.99	922	2.32
22	Developed, Low Intensity	215	1.09	402	2.36	997	2.51
23	Developed, Medium Intensity	58	0.293	25	0.147	323	0.812
24	Developed, High Intensity	128	0.647	3	0.0176	4	0.0101
31	Barren Land	69	0.349	88	0.518	80	0.201
41	Deciduous Forest	0	0.00	13	0.0765	0	0.00
42	Evergreen Forest	625	3.16	557	3.28	1418	3.57
43	Mixed Forest	0	0.00	30	0.176	26	0.0654
52	Shrub/Scrub	0	0.00	4	0.0235	106	0.267
71	Herbaceous	8	0.0404	163	0.959	204	0.513
81	Hay/Pasture	5	0.0253	17	0.100	24	0.0604
82	Cultivated Crops	16	0.0808	0	0.00	0	0.00
90	Woody Wetlands	609	3.08	284	1.67	401	1.01
95	Emergent Herbaceous Wetlands	12667	64.0	11749	69.1	25045	63.0
Total		19795	100	17003	100	39759	100

CHAPTER 7 MODEL SETUP

This thesis uses CG- and DG- based versions of the ADCIRC (ADvanced CIRCulation) 2DDI model to perform the comparison between the two finite element methods. The parameters used for running the model are presented in this chapter.

The four experiments for the continuous and discontinuous Galerkin finite element methods required the same set of main parameters for the MARSH mesh. The model is set to run in nonlinear mode with finite amplitude and advective terms enabled. Wetting and drying capability is disabled with the minimum water depth set to 1.0 meter. Uniform Manning's *n* roughness ($n = 0.020$) and eddy viscosity ($\nu_T = 0$ m^2/s) are set. Tidal forcing on the shelf open boundary is applied and boundary conditions are originated from the model presented in Bacopoulos et. al. (2011).

The observed and modeled salinity data (refer to Chapter 2: Figure 2.3) provided by the St. Johns Water Management District (Sucsy and Morris, 2002) are used to initialize the salinity field in the model. Per guidance provided by Kubatko et. al. (2008), a polynomial space of degree $p = 1$ and second-order Runge-Kutta methods are utilized for time discretization. The three time periods selected in the year 1999 are each of length equal to 30 days (i.e. *High Extreme* = June 13th – July 13th; *Most Variable* = September 21st – October 21st; *Low Extreme* = October 30th – November 29th). A time step of 1 second is used. All simulations are initialized with still-water conditions (i.e. cold start) and the boundary conditions are ramped up during the first half day of the simulation.

CHAPTER 8 MASS CONSERVATION ANALYSIS

The continuous (CG) and discontinuous (DG) finite element methods are each applied so as to assess the mass conservation properties of the two with respect to hydrodynamic and salinity transport simulation in the Lower St. Johns River. The analysis is applied to the Lower St. Johns River at global (entire domain) and regional (partitions shown in Chapter 6) stand points. This chapter is presented in two sections: (1) the algorithms used for both methods, and (2) the results.

8.1. Algorithms/Methods

Based on the studies conducted within Oliveira et. al. (2000), Kolar et. al. (1994), Blain and Massey (2005), and Dietrich et. al. (2008), the following algorithm is applied to the Lower St Johns River to evaluate the mass conservation properties of both finite element methods.

The concept of mass conservation is to quantify the fluxes either entering or exiting a defined control system or volume as well as the mass being accumulated and/or generated within the system. The general mass balance equation is shown below:

$$IN = OUT + AR - GR\,, \tag{8.1}$$

where: IN = influx mass rate,

OUT = outflux mass rate,

AR = accumulation rate,

GR = generation rate.

Note that the "*GR*" term is assumed to be zero since water is not to be generated within the system, but only accumulating ("*AR*") within the control volume as a function of the net flux (*IN* – *OUT*) through the boundaries of the control volume. The depth-integrated continuity equation of mass for water can be expressed as (Kolar et. al., 1992; Randall, 2006; Kinnmark and Gray, 1984; Dawson and Mirabito, 2008):

$$\frac{\partial \zeta}{\partial t} + \nabla \cdot \left(H\boldsymbol{U} \right) = 0 , \tag{8.2}$$

where: ζ = free surface deviation from the geoid,

∇ = two dimensional gradient operator,

H = total height of the water column ($H = \zeta + h$; h = bathymetric depth),

$\boldsymbol{U}$ = depth-integrated horizontal (longitudinal) velocity.

When equation (8.2) is integrated over space and time, the following is yielded

$$\int_{t_0}^{t} \int_{\Omega} \left[\frac{\partial \zeta}{\partial t} + \nabla \cdot \left(H\boldsymbol{U} \right) \right] d\Omega dt = 0 , \tag{8.3}$$

where: Ω = domain; may be the entire domain for a global check of mass conservation, or element(s) for a local check of mass conservation,

t = time,

t_0 = start time of simulation.

The first term within Equation (8.3) is integrated over time to determine accumulation, and the second term is used to determine the net flux once the divergence theorem[10] has been applied, which is shown in Equation (8.4):

$$\underbrace{\int_{\Omega}\left(\zeta_t-\zeta_0\right)d\Omega}_{accumulation}+\underbrace{\int_{t_0}^{t}\left[\int_{\partial\Omega}H\boldsymbol{U}\cdot\boldsymbol{n}\,d\left(\partial\Omega\right)\right]dt}_{net\ flux}=0\cdot \tag{8.4}$$

As shown in Kolar et. al. (1994), the dependent variables in the above equation are estimated with their discrete counterparts. The accumulation portion of Equation (8.4) is integrated over the domain once the ζ term has been approximated with linear Lagrange basis functions, which is shown below:

$$\int_{\Omega}\left(\zeta_t-\zeta_{t_0}\right)d\Omega=\sum_{e}\left|\overline{\zeta_t}-\overline{\zeta_{t_0}}\right|_e A_e\,, \tag{8.5}$$

where: A_e = area of an element *e*,

$\overline{\zeta_t}$, $\overline{\zeta_{t_0}}$ = the average of nodal values of ζ within the element,

$\sum_e$ = summation of all elements in the domain.

[10] According to Wolfram MathWorld (2011), the divergence theorem is a "mathematical statement of the physical fact that, in the absence of the creation or destruction of matter, the density within a region of space can change only by having it flow into or away from the region through its boundary." For instance, let V represent a volume in space with a boundary of ∂V. "The volume integral of the divergence ∇·F of F over V and the surface integral of F over the boundary ∂V of V are related by $\int_V\left(\nabla\cdot F\right)dV=\int_{dV}dA$." When the divergence theorem is then applied again, the following results $\int_S\left(\nabla\cdot F\right)dA=\int_{dS}\left(F\cdot\hat{n}\right)dS$ where S is a region in the plane A with a boundary or ∂S (Wolfram MathWorld: website http://mathworld.wolfram.com/DivergenceTheorem.html accessed March 21, 2011).

The second term of Equation (8.4) contains the boundary integral to represent the net flux within the domain at a perpendicular projection based on the **n** unit outward normal vector, as represented in Equation (8.6)

$$Q_{net} = \int_{\partial\Omega} H\boldsymbol{U} \cdot \boldsymbol{n}\, d\left(\partial\Omega\right). \tag{8.6}$$

The time discretization of the above equation is approximated with the trapezoidal rule with the ending result shown below

$$\int_{t_0}^{t}\left[\int_{\partial\Omega} H\mathrm{U}\cdot\mathrm{n}\, d\left(\partial\Omega\right)\right]dt = \int_{t_0}^{t} Q_{net}\,dt \approx \sum_{k}\frac{1}{2}\left[Q_{net}^{t_k+\Delta t} + Q_{net}^{t_k}\right]\Delta t\,, \tag{8.7}$$

where: k = time step index.

However, the continuous and discontinuous Galerkin methods have two different procedures to calculate the net flux shown in Equation (8.6); the CG finite element methods uses the "classical" method and the DG finite element method uses the "direct" method.

The "classical" method requires that Equation (8.6) be evaluated using the exact (or Gauss) quadrature rule (see Kolar, et. al. (1994)), which results in the integral in one dimension that forces the water column depth (H) and horizontal velocity ($\boldsymbol{U}$) values to be at the element's boundary:

$$Q_{net,CG} \equiv \int_{\partial\Omega} H\boldsymbol{U} \cdot \boldsymbol{n}\, d\left(\partial\Omega\right) = \sum_{eb}\frac{L_{eb}}{6}\left[2H_1\boldsymbol{U}_{n1} + H_1\boldsymbol{U}_{n2} + H_2\boldsymbol{U}_{n1} + 2H_2\boldsymbol{U}_{n2}\right]_{eb}, \tag{8.8}$$

where: L_{eb} = length of element (e) edge (b),

n = subscript represents the normal vector component (i.e. $\boldsymbol{U}_n = \boldsymbol{U} \cdot \boldsymbol{n}$),

1, 2 = subscripts represent locally numbered nodes at the ends of the element's edge,

CG = subscript represents fluxes are calculated based on the CG method.

The discrete computation of the mass error on an elemental basis is the addition of Equations (8.5) and (8.8), which results in Equation (8.9):

$$E_{CG} = \underbrace{\sum_{e}\left[\overline{\zeta_t} - \overline{\zeta_{t_0}}\right]_e A_e}_{accumulation} + \underbrace{\sum_{k}\frac{1}{2}\left[Q_{net,CG}^{t_k+\Delta t} + Q_{net,CG}^{t_k}\right]\Delta t}_{net\ flux}. \tag{8.9}$$

As mentioned above, the DG finite element method uses the "direct" method, which employs the numerical fluxes from simulations directly, as represented below:

$$Q_{net,DG} = \int_{\partial\Omega} H\boldsymbol{U}\cdot\boldsymbol{n}\, d\left(\partial\Omega\right) = \sum_{eb}\widehat{F_{eb}}, \tag{8.10}$$

where: $\widehat{F_{eb}}$ = numerical flux computed with the DG finite element method for the element's edge (*eb*).

For the "direct" method, the discrete computation of the mass error on an elemental basis is the addition of Equations (8.5) and (8.10), which results in Equation (8.11):

$$E_{DG} = \underbrace{\sum_{e}\left[\overline{\zeta_t} - \overline{\zeta_{t_0}}\right]_e A_e}_{accumulation} + \underbrace{\sum_{k}\frac{1}{2}\left[Q_{net,DG}^{t_k+\Delta t} + Q_{net,DG}^{t_k}\right]\Delta t}_{net\ flux}. \tag{8.11}$$

The elemental mass errors are normalized by the element's volume:

$$E_{CG,V\ or\ DG,V} = \frac{E_{CG\ or\ DG}}{Vol_e}, \tag{8.12}$$

where: Vol_e = discretized water column volume of the element e, which is approximated with the trapezoidal rule for all time increments (i.e. $Vol_e = \sum_k \frac{1}{2}\left[Vol_e^{t_k+\Delta t} + Vol_e^{t_k} \right]$),

ECG, V or *DG, V* = reported as percentages (100% × L^3/L^3).

The equation used to average the elemental mass errors onto each node is shown below:

$$E_i = \frac{1}{A}\sum_{e=1}^{n_e} E_e A_e \ , \tag{8.13}$$

where: E_i = mass error for node *i*,

A = total area of elements that share node *i*,

n_e = number of elements sharing node *i*,

E_e = mass error of element *e*,

A_e = mass error of element *e*.

8.2. Results

The algorithm presented in the previous section is applied to a three-day tidal flow solution. The solutions are generated from model runs setup as follows. Simulations begin from still-water conditions at the initiation of a tidal epoch (Schureman, 1941) (refer to Chapter 9). Tidal forcing includes the K1, O1, M2, S2, N2, K2, and Q1 tidal constituents and is ramped over the first twelve hours. By this setup of the model runs, five complete and dynamically stable semi-diurnal tidal cycles to occur. Per the suggestion of Oliveira et. al. (2000), a small step of 1 minute is selected to represent the time variability within the accumulation and net flux

components of Equations (8.9) and (8.11). The above procedure is applied to the CG and DG methods and the results are then analyzed.

8.2.1. Mass Errors

There are several trends recognized during the analysis of the mass errors. For instance, mass imbalance is recognized in local areas with complex geometry and abrupt bathymetric gradients, as shown in Figure 8.1. It should be noted that mass errors are very small values, so these values will be presented as logarithms of the absolute value of the mass errors to prevent abnormality within the log function. From a global standpoint, the DG method ($10^{-8.822}$%) is more mass conservative than the CG method ($10^{-8.306}$%). Based on the literature presented earlier, this is expected. The DG finite element method is able to provide adaptivity to complex geometry and bathymetry locally and globally. The CG finite element method lacks this property, so it is unable to handle these types of discontinuities on a nodal basis (i.e., locally).This was the same result on a local basis of the subdivisions of the Lower St. Johns River (refer to Chapter 3: Figure 3.1 and Table 3.1). Mass error, as a volumetric measure, is calculated as mass error [m^3] = mass error [%] × estuary volume [m^3] ÷ 100% = 0.09 m^3 for DG and 0.29 m^3 for CG.

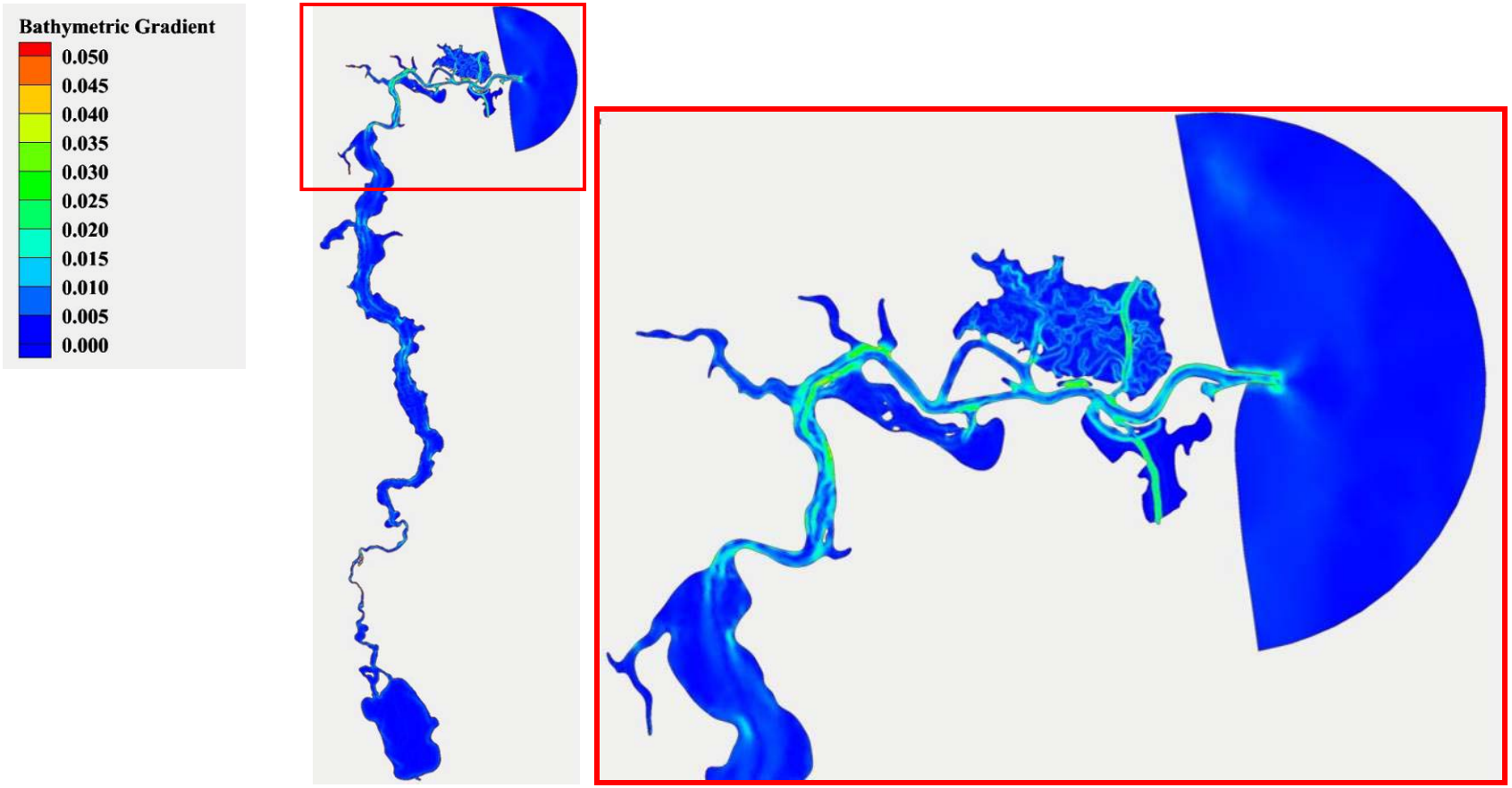

Figure 8.1: Bathymetric gradients within the Lower St. Johns River (inset: the lower 40 km of the river).

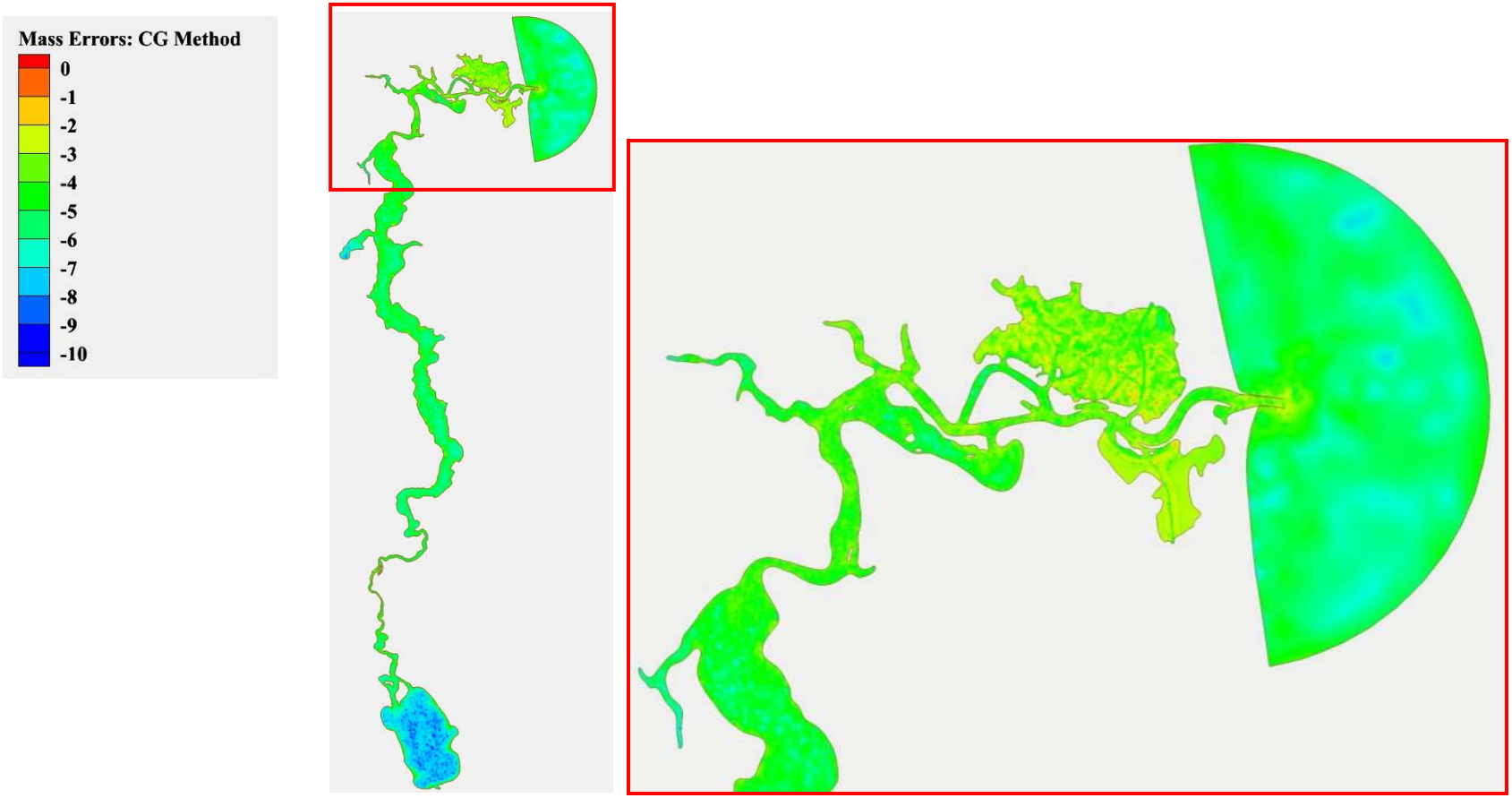

Figure 8.2: Mass Errors, reported as ($\log_{10}$ of %), of the CG finite element method within the Lower St. Johns River (inset: the lower 40 km of the river).

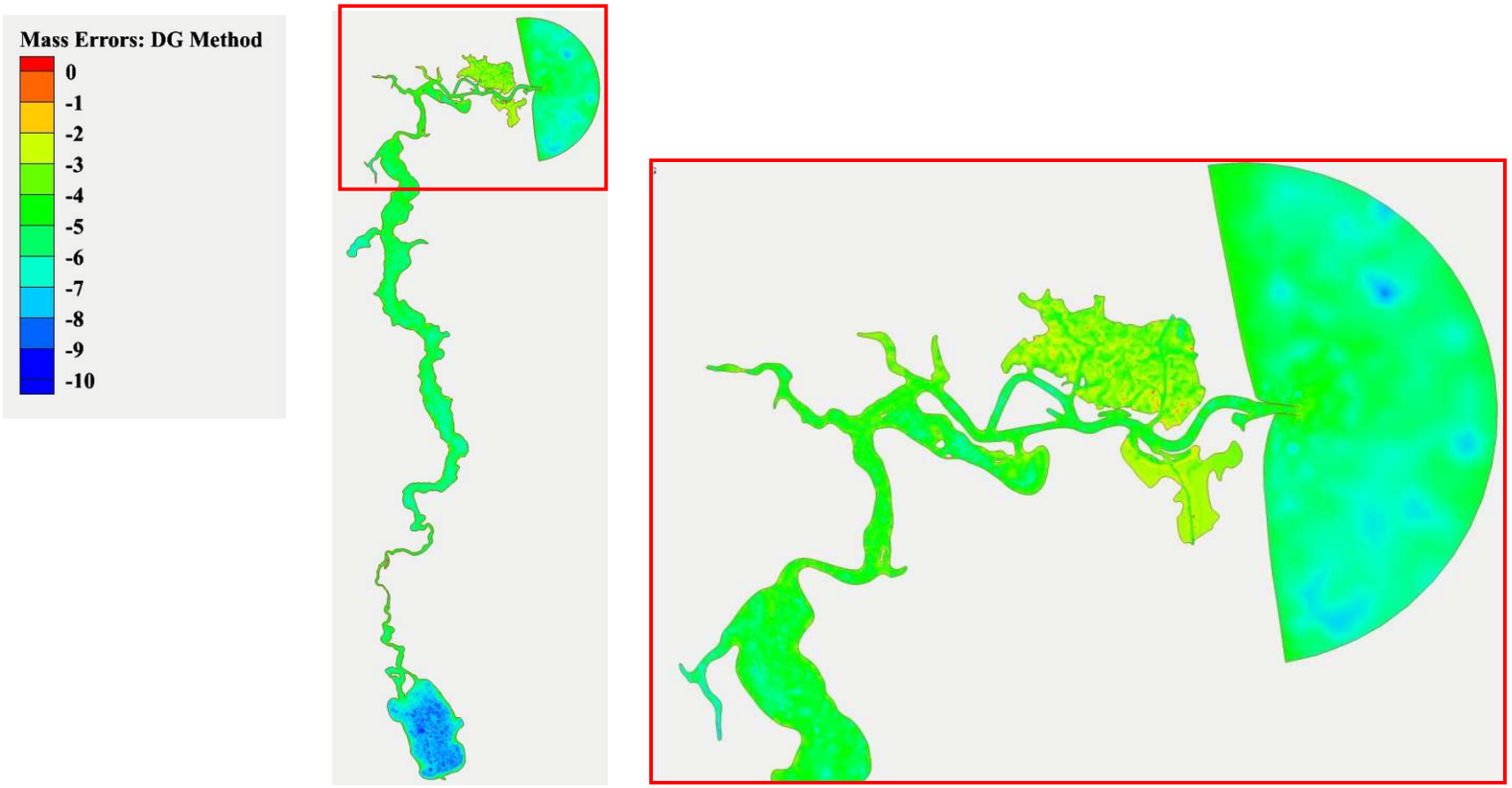

Figure 8.3: Mass Errors, reported as ($\log_{10}$ of %), of the DG finite element method within the Lower St. Johns River (inset: the lower 40 km of the river).

As presented in Table 8.1, the mass errors are the greatest within the two intracoastal and marsh subdivisions. The least local mass error occurs in the ocean boundary and Lake George subdivisions. River Sections 1 and 4 had greater mass errors than River Sections 2 and 3. This is due to the level of complexity of the river sections. It has been shown that all river sections have an approximate length of 40 km (± 5 km), however their areas are greatly different (refer to Chapter 3: Table 3.1). For instance, River Sections 1 and 4 have the smallest areas and approximate widths compared to River Sections 2 and 3. Graphically (refer to Chapter 3: Figure 3.1), River Sections 2 and 3 do not contain islands or tidal branches like River Sections 1 and 4. Based on these facts, the geometric characteristics of each subdivision have an influence on the mass errors (i.e. small areas and widths, along with river winding and tidal branches cause large mass errors).

Table 8.1: Mass errors for the CG and DG finite element methods for each subdivision and globally.

Subdivision Symbol	**Mass Error ($\log_{10}$ of %)**	
	E_{CG}	**E_{DG}**
O_b	-6.854	-7.894
I_A	-4.829	-6.984
I_B	-4.472	-6.045
$*M_A$	-4.952	-6.566
$*M_B$	-4.235	-5.581
R_1	-5.744	-5.922
R_2	-7.873	-8.332
R_3	-7.148	-8.485
R_4	-5.978	-6.112
L_G	-9.491	-9.852
Global	-8.306	-8.822

8.2.2. Tidal Prisms

Tidal prisms are calculated as the volume of water transported over half of a tidal cycle. In this case, the tidal cycle is primarily driven by M2 tidal constituent with a period of approximately 12.42 hours, which will result in the length of a half-tidal cycle to be 6.21 hours.

$$TP = \frac{|Q_{net}|}{2N_{M2}} = \frac{|Q_{net}|}{12}, \tag{8.14}$$

where: Q_{net} = net flux calculated in equations (8.8) and (8.10) ,

N_{M2} = number of times that the M2 tide occurs within the simulation (i.e., 6 times within 3 days).

Since the numerical values of tidal prisms are very large, they will be presented as logarithmic values. Figure 8.4 and Figure 8.5 are graphical representations of the tidal prisms within the Lower St. Johns River.

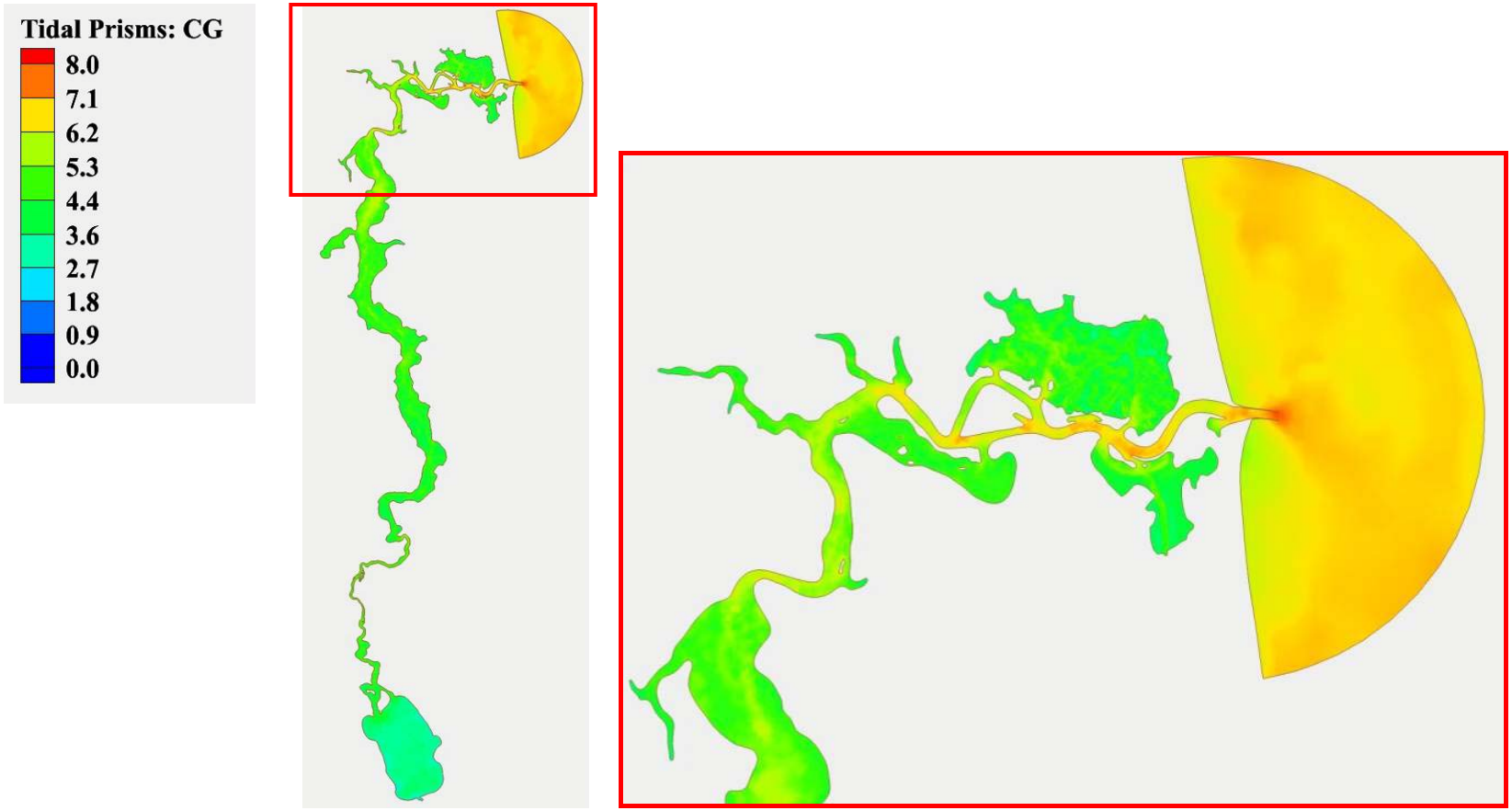

Figure 8.4: Tidal Prisms, reported as ($\log_{10}$ of m^3), of the CG finite element method within the Lower St. Johns River (inset: the lower 40 km of the river).

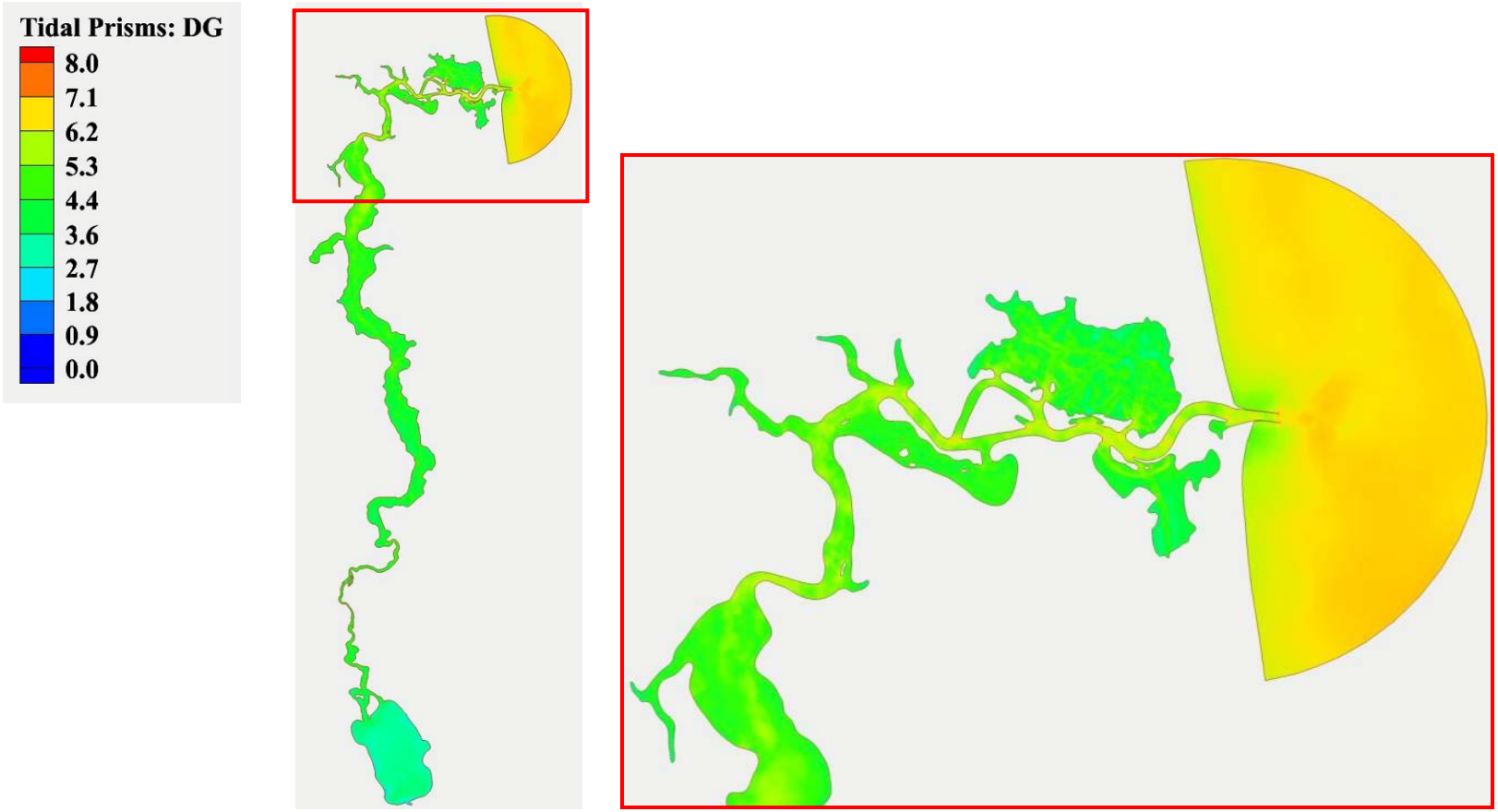

Figure 8.5: Tidal Prisms, reported as ($\log_{10}$ of m^3), of the DG finite element method within the Lower St. Johns River (inset: the lower 40 km of the river).

The main trend observed is the correlation of the tidal prism to mass errors; large tidal prisms are associated with large mass errors, and vice versa. This correlation occurs due to the fact that the net flux is involved in the calculation of the mass errors. As shown earlier, the tidal prisms for each finite element method are calculated differently. The net flux calculated within the CG method is approximated from nodal variables, while the DG method employs simulated numerical fluxes directly. This results in smaller tidal prisms calculated with the DG method when compared to the CG method. Also, the DG method is then able to provide a smoother spatial transition than the CG method, as shown in Figure 8.4 and Figure 8.5.

Equation (8.15) is used to calculate the percentage of a subdivision's tidal prism volume of the global or full domain tidal prism volume:

$$\%_{Subdivision,Global} = \left(\frac{TP_{Subdivision}}{TP_{Global}} \right) 100 , \tag{8.15}$$

where: $TP_{Subdivision}$ = tidal prism volume of a subdivision,

TP_{Global} = tidal prism volume of the global domain.

For example, the largest tidal prism from the DG method is the ocean boundary, which was approximately 38% of the global tidal prism (see Table 8.2):

$$\%_{O_b,Global} = \left(\frac{O_b}{Global} \right) 100 = \left(\frac{10^{8.924} m^3}{10^{9.341} m^3} \right) 100 = 38.3\% . \tag{8.16}$$

The second largest tidal prism occurs within River Section 1 at approximately 37% of the global tidal prism. For the CG method, the opposite occurs with River Section 1 being the largest

(56%) and the ocean boundary being the second largest (32%). However, in both cases, it is proven that these two subdivisions encompass approximately 75% of the entire domain. The remaining quarter of the domain mainly consists of the remaining river sections. Lake George is the smallest of the tidal prisms, which is approximately 0.5% of the global. The marshes and their corresponding intracoastal waterways are approximately 11% of the global Marsh A and its water way (i.e. $M_A = *M_A + I_A$) having the largest tidal prism of the two. This is due to the fact that Marsh A is highly more complex in terms of geometry (refer to Chapter 3: Figure 3.1); it contains a highly complex and intricate tidal creek system when compared to Marsh B. Since the tidal creeks are able to carry more flow throughout the system, it has a large tidal prism (i.e., transporting a larger volume of water within a half cycle). Also as shown in Chapter 3 (see Table 3.1), Marsh A (including its intracoastal waterway) is larger in terms of area, volume, and width when compared to Marsh B.

Table 8.2: Calculated tidal prisms for each subdivision and the entire domain, along with the percentage of the entire domain.

Subdivision Symbol	Tidal Prism (log_{10} of m^3)		Percentage of Global (%)	
	TP_{CG}	TP_{DG}	CG	DG
O_b	9.308	8.924	31.70	38.3
I_A	7.648	7.358	0.69	1.0
I_B	7.7078	6.826	0.80	0.3
$*M_A$	8.276	8.249	2.94	8.1
$*M_B$	7.618	7.602	0.65	1.8
R_1	9.553	8.907	55.72	36.8
R_2	8.491	8.272	4.83	8.5
R_3	8.112	7.885	2.02	3.5
R_4	7.78	7.362	0.94	1.0
L_G	7.264	7.027	0.29	0.5
Global	9.807	9.341		

.

The tidal prism of the Lower St. Johns River was previously estimated by Sucsy and Morris (2002) to be 85×10^6 by integrating one-half of a sine curve with the amplitude of 6000 m^3/s (peak tidal discharge at the river's mouth) over a period of 12.42 hours. These authors also note the previous estimates stated within Morris (1995) of $53 – 150 \times 10^6$ m^3. Sucsy and Morris (2002) conclude that approximately 95% of the Lower St. Johns River's tidal prism is held within the lower 160 river km of Buffalo Bluff (4.5×10^6 m^3). Comparing the DG results of the entire domain ($10^{9.341}$ or 203×10^6 m^3) to those of Sucsy and Morris (2002) ($10^{7.929}$ or 85×10^6 m^3), the results presented are clearly larger. There are three suggested reasons to partly explain this: (1) the tidal prism calculations presented in this thesis are based on the integration of tidal prisms containing full nonlinear tides, while others have translated tidal peak discharges into

tidal prisms, (2) the above calculations include a portion of the continental shelf, along with the Atlantic Intracoastal Waterway and surrounding marshes, and (3) the included global tidal prism is an amassing of the individual tidal prisms based on the subdivisions of the Lower St. Johns River.

CHAPTER 9 VALIDATION

Model results are compared to the observed data (cf. Chapter 2. Literature Review for an overview on the observed data) provided by the USGS for the purpose of validating the model in terms of simulating hydrodynamics and longitudinal salinity transport within the Lower St. Johns River.

9.1. Tides and Tidal Currents

Since the hydrodynamics drive the salinity transport, then it is logical to validate the tides first in that if the tidal frequencies are simulated well, then the salinity distribution throughout the river will be represented well. Tidal data is retrieved from four gauging stations near the mouth of the river (see Figure 9.1 and Table 9.1).

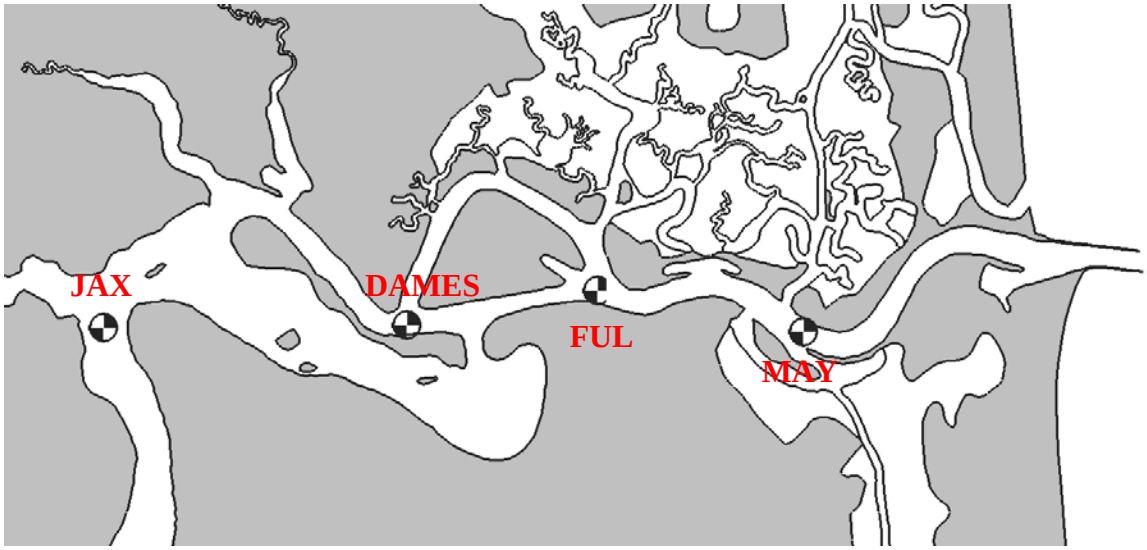

Figure 9.1: Locations of the four tidal gage stations, which were used for tidal validation.

Table 9.1: Station locations used to retrieve data for observations and validation.

			Location			
Name	**Source**	**Station ID**	**River km**	**°W**	**°N**	**Variable(s) Measured**
St. Augustine, FL	NOAA NDBC	SAUF1	-	81.265	29.8567	Winds, Pressures
Jacksonville, FL	USGS	2246500	40	81.6652	30.3205	Discharge
Buffalo Bluff, FL	USGS	2244040	160	81.6833	29.5961	Discharge
Mayport, FL	NOS	MAY	10	81.4587	30.3837	Tides, Tidal Currents
Fulton, St. Johns River, FL	NOS	FUL	15	81.5085	30.392	Tides, Tidal Currents
Dames Point, FL	NOS	DAMES	20	81.5583	30.3867	Tides, Tidal Currents
Jacksonville, Navy Fuel Depot, FL	NOS	JAX	30	81.6282	30.3838	Tides, Tidal Currents
Dames Point, FL	USGS	Dames Point	20	81.5583	30.3867	Water levels, Salinity
Acosta Bridge, FL	USGS	Acosta Bridge	40	81.6652	30.3205	Water levels, Salinity
Buckman Bridge, FL	USGS	Buckman Bridge	60	81.6707	30.187	Water levels, Salinity
Shands Bridge, FL	USGS	Shands Bridge	80	81.6174	29.9878	Water levels, Salinity

The gauging stations report the following: tides as water levels based on NAVD88; and tidal currents based on the along-shore component of the depth-integrated velocity vector. These quantities are then resynthesized with the use of the following equations:

$$\zeta(t) = \sum_{n=1}^{N} A_{\zeta_n} \cos\left[\omega_n t - \varphi_{\zeta_n}\right], \tag{9.1}$$

$$U(t), V(t) = \sum_{n=1}^{N} A_{U,V_n} \cos\left[\omega_n t - \varphi_{U,V_n}\right], \tag{9.2}$$

where: $\zeta(t)$ = time series of water surface levels,

$U(t)$, $V(t)$ = time series of the along-shore component of the velocity vector,

n = 1,…, N: number of tidal constituents,

A_n = amplitude of reconstructed cosine waves,

ω_n = frequency of reconstructed cosine waves,

φ_n = phase of reconstructed cosine waves.

The ending result will be the superposition of multiple cosine waves representing the following tidal constituents: M2, N2, S2, K1, and O1, which embodies more than 90% of the tidal signal according to Bourgerie (1999). The time to complete a spring-neap cycle is used to observe the domain's tidal patterns; this will be the first approximate 14.77 days of a tidal epoch. The tidal epoch is based on an approximate 18.6 year cycle of the moon's nodules and begins when all tidal cycles are in phase with each other (Schureman, 1941). The modeled results are compared

to the stations' observations; the use of root mean square error formula (Equation (9.3)) aided in verifying the performance of the tidal resysnthesis per station:

$$RMS = \frac{1}{N}\sqrt{\sum_{N}\left(x_{\mathrm{mod}_n} - x_{obs_n}\right)^2}\ , \tag{9.3}$$

where: N = total number of data points (30 d × 24 hr/d = 720),

x_{mod_n} = modeled water level or velocity signals containing N data points,

x_{obs_n} = observed water level or velocity signals containing N data points.

The RMS errors are normalized by using the tide range (m) and peak current (m/s) as the normalizing factors as shown in equations (9.4) and (9.5):

$$RMS(\%) = \frac{RMS}{\zeta_{obs,range}}100\,, \tag{9.4}$$

$$RMS(\%) = \frac{RMS}{U_{obs,peak}}100\,, \tag{9.5}$$

where: RMS = root mean square reported as cm or cm/s,

$\zeta_{obs,\,range}$ = full range of the observed water level within the entire record (cm),

$= \zeta_{obs,max} - \zeta_{obs,min}$,

$U_{obs,peak}$ = the absolute value of the maximum velocity within the entire record (cm/s),

$= U_{obs,\,max} - U_{obs,\,min}$.

The selection of data used within the model-data comparisons is very important. For tidal resysnthesis, the tides are the only components simulated in the model using the MARSH mesh. Based on this fact, data gauges recording tidal data would be the best choice, which supports the choice to use the data stations used by Bourgerie (1999). However, the salinity stations (refer to Figure 2.2 in Chapter 2, and Figure 9.2 through Figure 9.4) used by Sucsy and Morris (2002) records full-signal data, which contains not only tidal data, but data concerning wind and pressure effects, freshwater flows, baroclinic effects, etc. Comparing resynthesized tidal data to this data set would cause more errors resulting in high RMS error value; for this reason, the tides and tidal currents will be resynthesized based on the stations used in Bourgerie (1999) for both the CG and DG finite element methods.

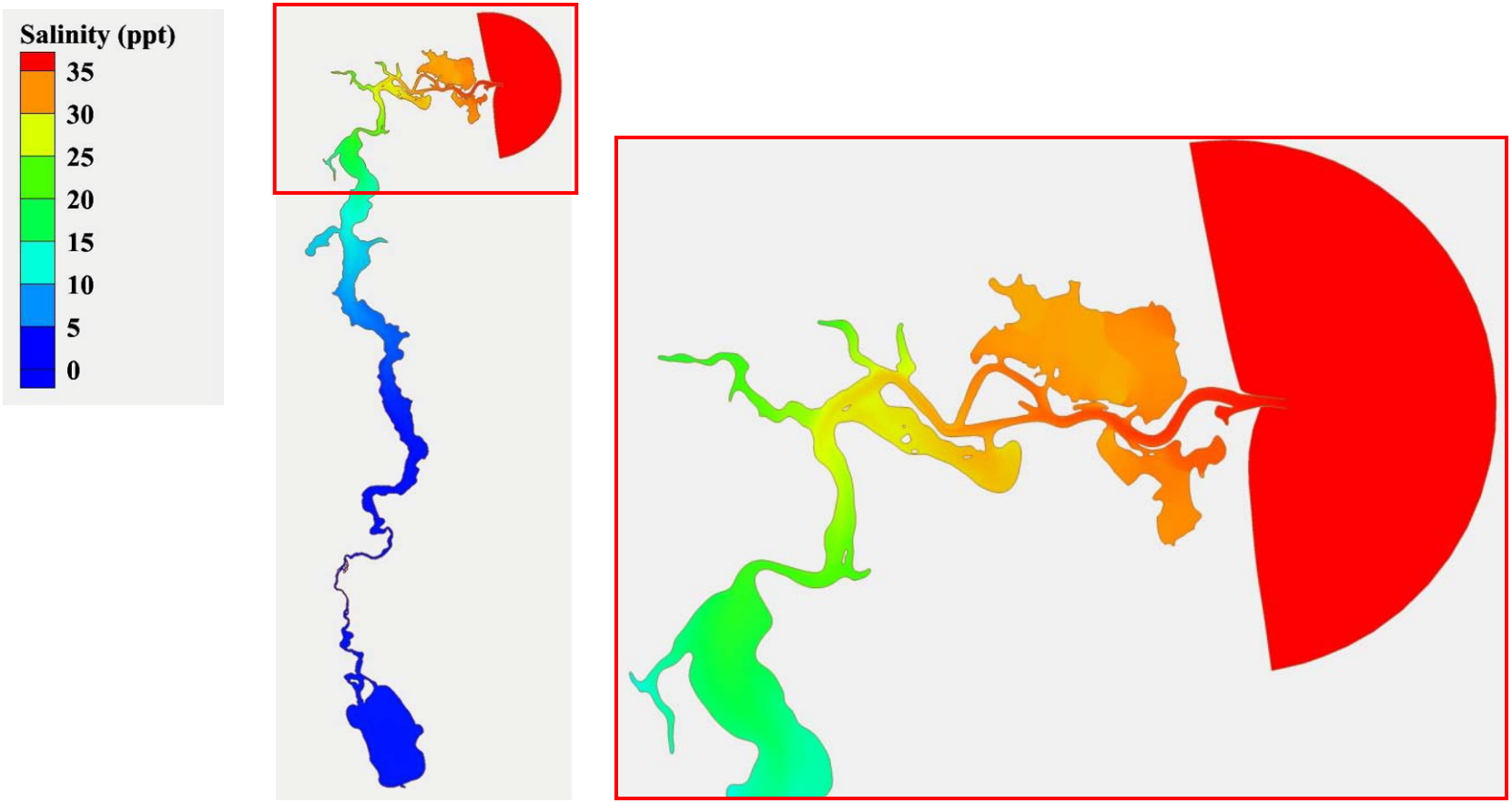

Figure 9.2: Initial conditions of salinity (ppt) within the Lower St. Johns River (inset: the lower 40 km of the river) during the *High Extreme* modeling scenario.

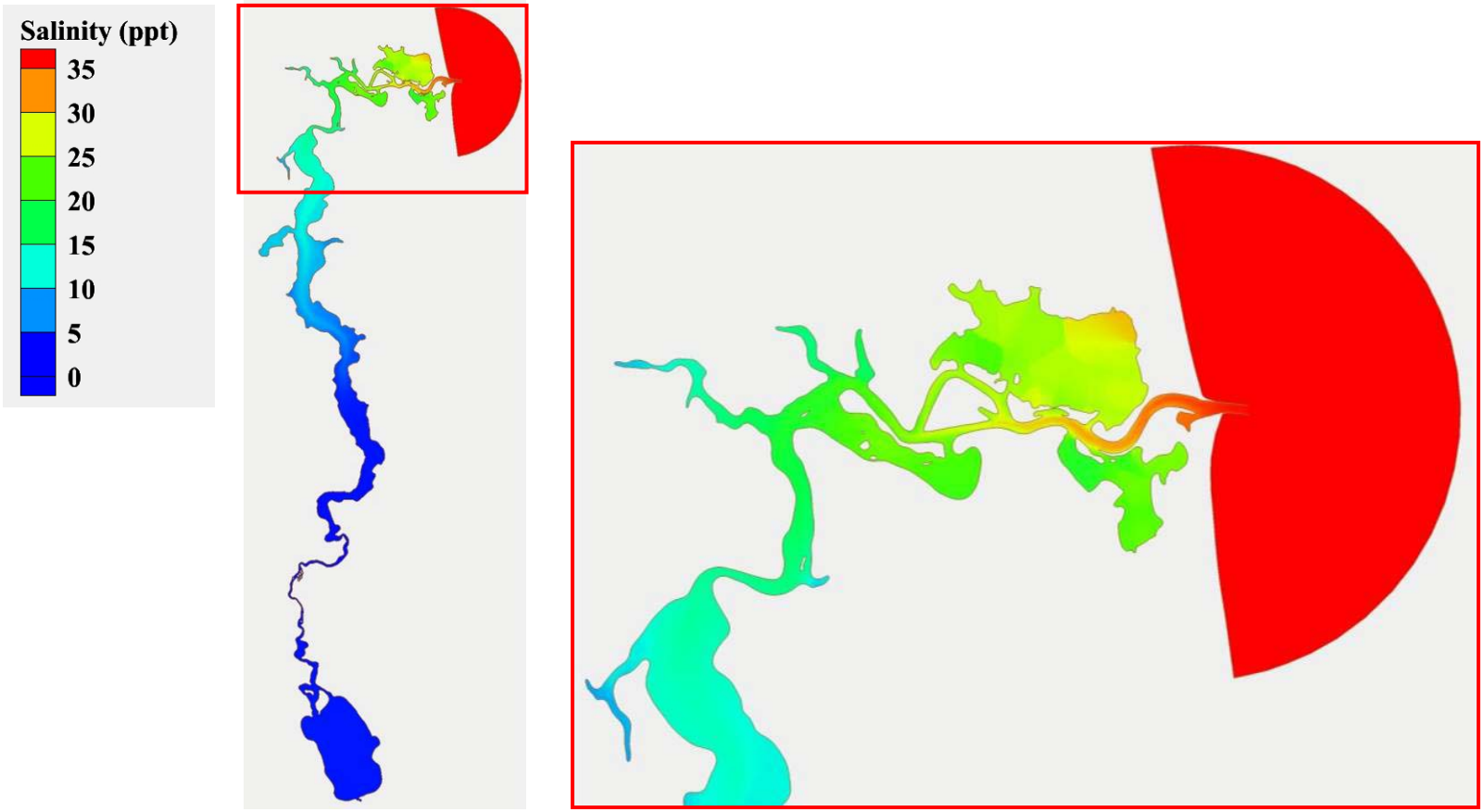

Figure 9.3: Initial conditions of salinity (ppt) within the Lower St. Johns River (inset: the lower 40 km of the river) during the *Most Variable* modeling scenario.

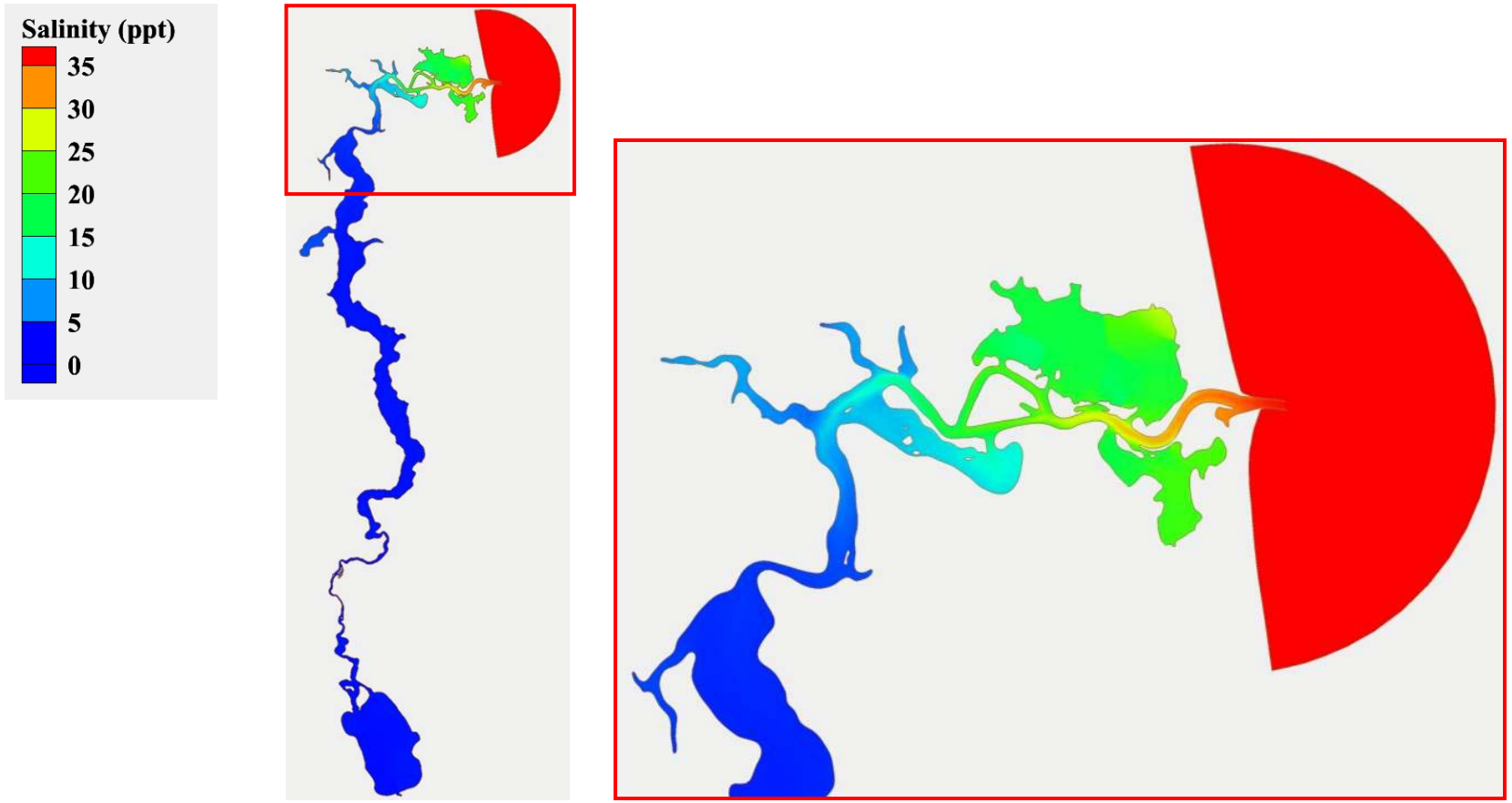

Figure 9.4: Initial conditions of salinity (ppt) within the Lower St. Johns River (inset: the lower 40 km of the river) during the *Low Extreme* modeling scenario.

As shown in Table 9.2, the DG finite method has the lowest RMS errors for all three modeling scenarios when compared to the CG finite element method on average and overall. However, both finite element methods show that the RMS errors decrease from stations MAY to DAMES, but then increase at the JAX station. The normalized RMS values for the tides range in the following: *High Extreme* – DG: 3.9% to 5.1% and CG: 4.2% to 6.8%, *Most Variable* – DG: 2.8% to 5.0% and CG: 3.4% to 7.2%, *Low Extreme* – DG: 3.2% to 4.5% and CG: 3.5% to 6.5%. Graphically (refer to Appendix B), the modeled tides of both methods are in phase with the observations. However, peaks modeled by the DG method are approximately 10 cm lower than those modeled with the CG method. This trend also applies to the troughs with the DG method approximately 10 cm lower than the CG method.

However, the tidal currents had higher RMS errors comparative to tides as shown in Table 9.3. The RMS errors decrease from the MAY station to the FUL station, but increase at the DAMES station, followed by another decrease at the JAX station. The normalized RMS values for the tides range in the following: *High Extreme* – DG: 11.9% to 18.2% and CG: 12.3% to 18.7%, *Most Variable* – DG: 12.9% to 18.5% and CG: 13.2% to 19.1%, *Low Extreme* – DG: 12.1% to 17.9% and CG: 12.3% to 18.4%. As shown in Appendix B, the DG and CG methods underestimate the peaks and troughs of the observed data, especially at the DAMES and JAX stations, with modeled results at the DAMES station being the worse of the two. When comparing the two finite element methods, the DG method has smaller peaks of the largest ebbs (the peaks) when compared to the CG method. The opposite occurs with the largest floods (the troughs); the DG method has larger troughs when compared to the CG method. Overall, the tidal fluctuations are captured well in the modeled tidal water levels and velocities, especially with the

DG method based on the RMS errors. Graphical representations of the tidal resysnthesis of the water levels and tidal velocities for each gage station can be found in Appendix B.

Table 9.2: Root mean square errors (%) for the tides per station used in the Bourgerie (1999) study during all modeling scenarios for the CG and DG finite element methods.

Tides: High Extreme										
Station ID:	**MAY**		**FUL**		**DAMES**		**JAX**		**Average**	
	CG	DG	CG	DG	CG	DG	CG	DG	CG	DG
Maximum (cm)	103.9		83.3		74.0		59.3		80.1	
Minimum (cm)	-93.2		-78.3		-68.5		-53.6		-73.7	
Range (cm)	197.2		161.6		142.5		113.0		153.6	
RMS (cm)	8.3	8.1	7.7	6.3	7.0	5.2	7.6	5.6	7.7	6.3
RMS (%)	4.2	4.1	4.8	3.9	4.9	3.9	6.8	5.0	5.2	4.2
Tides: Most Variable										
Station ID:	**MAY**		**FUL**		**DAMES**		**JAX**		**Average**	
	CG	DG	CG	DG	CG	DG	CG	DG	CG	DG
Maximum (cm)	90.9		74.7		67.2		51.2		71.0	
Minimum (cm)	-89.4		-75.0		-64.3		-48.9		-69.4	
Range (cm)	180.3		149.6		131.5		100.0		140.4	
RMS (cm)	6.0	5.7	6.2	4.2	4.4	4.3	7.2	5.0	6.0	4.8
RMS (%)	3.4	3.2	4.1	2.8	4.9	3.3	7.2	5.0	4.9	3.6
Tides: Low Extreme										
Station ID:	**MAY**		**FUL**		**DAMES**		**JAX**		**Average**	
	CG	DG	CG	DG	CG	DG	CG	DG	CG	DG
Maximum (cm)	102.5		82.8		73.3		58.3		79.2	
Minimum (cm)	-94.3		-79.2		-68.4		-53.4		-73.8	
Range (cm)	196.8		162.1		141.7		111.6		153.1	
RMS (cm)	7.0	6.7	6.9	4.3	6.8	4.8	7.3	5.0	7.0	5.4
RMS (%)	3.5	3.4	5.2	3.2	4.8	3.4	6.5	4.5	4.8	3.6

Table 9.3: Root mean square errors (%) for the tidal currents per station used in the Bourgerie (1999) study during all modeling scenarios for the CG and DG finite element methods.

Tidal Currents: High Extreme										
Station ID:	**MAY**		**FUL**		**DAMES**		**JAX**		**Average**	
	CG	DG	CG	DG	CG	DG	CG	DG	CG	DG
Ebb (cm/s)	151.4		113.9		110.5		92.1		117.0	
Flood (cm/s)	136.7		102.2		98.3		82.4		105.0	
Peak (cm/s)	151.4		113.9		110.5		92.1		117.0	
RMS (cm/s)	20.9	18.0	14.0	13.9	20.7	20.1	14.1	12.8	17.4	16.2
RMS (%)	13.8	11.9	12.3	12.2	18.7	18.2	15.3	13.9	15.0	14.1

Tidal Currents: Most Variable										
Station ID:	**MAY**		**FUL**		**DAMES**		**JAX**		**Average**	
	CG	DG	CG	DG	CG	DG	CG	DG	CG	DG
Ebb (cm/s)	138.3		102.4		102.2		84.3		106.8	
Flood (cm/s)	122.3		97.7		97.3		79.5		99.2	
Peak (cm/s)	138.3		102.4		102.2		84.3		106.8	
RMS (cm/s)	20.9	18.1	13.5	13.3	19.5	18.9	13.4	12.2	16.8	15.6
RMS (%)	15.1	13.1	13.2	12.9	19.1	18.5	15.9	14.4	15.8	14.7

Tidal Currents: Low Extreme										
Station ID:	**MAY**		**FUL**		**DAMES**		**JAX**		**Average**	
	CG	DG	CG	DG	CG	DG	CG	DG	CG	DG
Ebb (cm/s)	150.4		112.9		110.5		91.9		116.4	
Flood (cm/s)	133.9		102.6		99.8		83.1		104.9	
Peak (cm/s)	150.4		112.9		110.5		91.9		116.4	
RMS (cm/s)	21.4	18.4	13.9	13.7	20.4	19.8	13.9	12.6	17.4	16.1
RMS (%)	14.2	12.3	12.3	12.1	18.4	17.9	15.1	13.7	15.0	14.0

9.2. Winds and Pressures

Based on the study of Bacopoulos et. al. (2009), it has been shown that the "meteorological forcing for the St. Johns River is equal to or greater than that of astronomic tides." This thesis presents the winds and pressures of the Lower St. Johns River, so that observations may be made concerning the effects on the water levels and salinity concentration.

The data for the winds and pressures within the Lower St. Johns River are collected to create surface forcing fields for realistic boundary conditions. The National Oceanic and Atmospheric Administration's (NOAA) National Data Buoy Center (NDBC) provides standard meteorological data. The C-MAN station SAUF1, located on the coast near St. Augustine (81.2650°W and 29.8567°N) approximately 45 km south of Mayport, FL, is selected since it is the nearest NDBC station to the Lower St. Johns River containing winds and pressures for the year 1999. The raw data for the three modeling scenarios are retrieved (National Data Buoy Center, 2011), and provided wind speeds (V (m/s)) and directions (θ (degrees)) measured clockwise from true north in one hour intervals. Using the equations below, the recorded wind vectors are translated in form usable for model input:

$$V_x = -V \sin\theta \,, \tag{9.6}$$

$$V_y = -V \cos\theta \,. \tag{9.7}$$

During the *High Extreme* scenario, the wind speeds range from 5 ± 5 m/s with the highest peak of 15 m/s on June 19th (Figure 9.5 (a)), and directed 0 to 360 degrees north (Figure 9.5 (b)). However, there are two time periods that showed the intense changes in behavior: June 18th through June 24th, and July 2nd through July 6th. During June 18th through June 24th, the wind speeds reached a maximum of 15 m/s at 225° southwest. For July 2nd through July 6th, the winds reached a maximum of 10 m/s at 315° southeast. The pressures remained positive during this time period between the range of 0 hPa to 10 hPa, which can be seen in Figure 9.5(c).

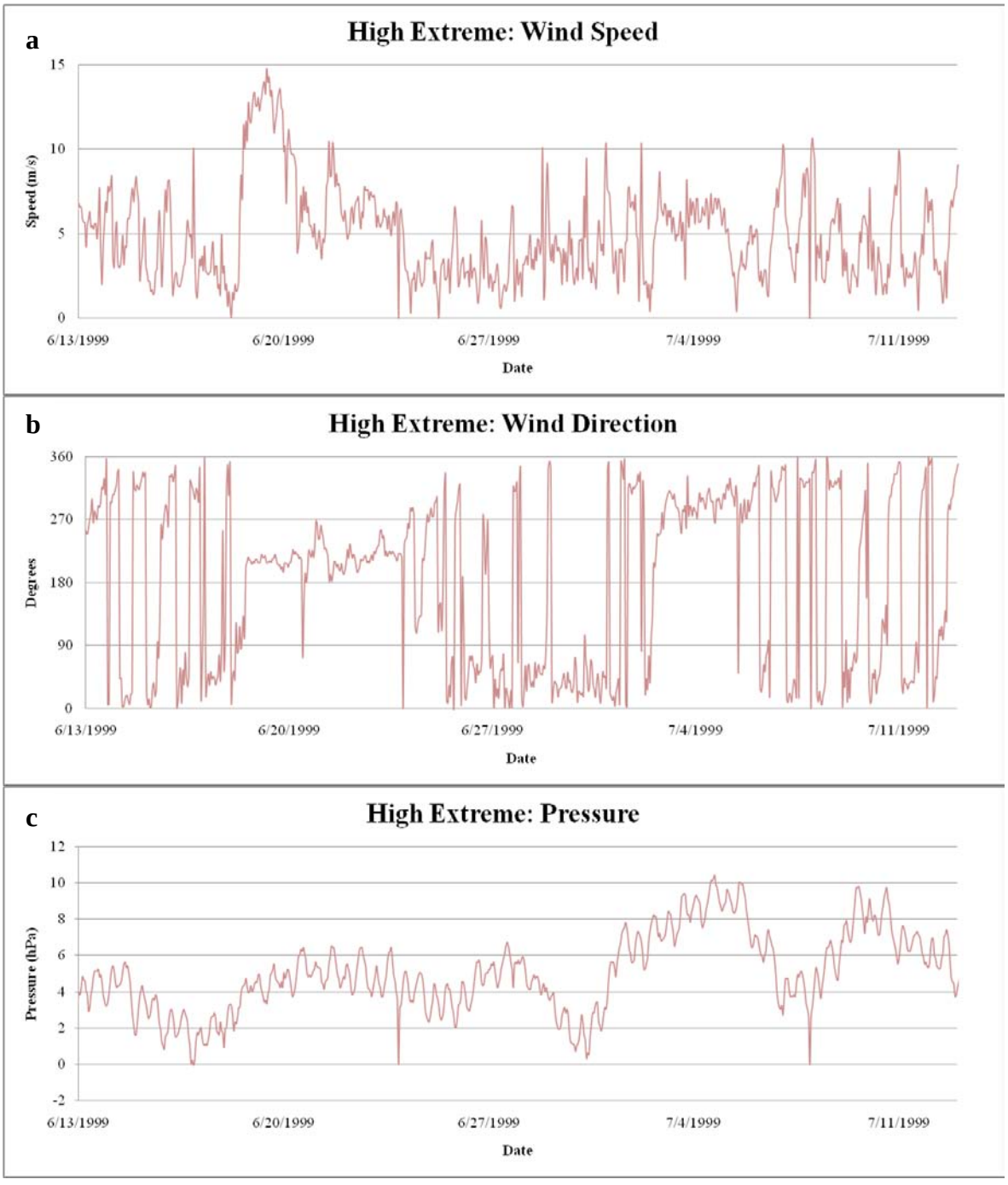

Figure 9.5: Wind speed (a) and direction (b), along with pressures (c), for the *High Extreme* modeling scenario based on the NOAA C-MAN Station SAUF1.

The *Most Variable* scenario (Figure 9.6 (a) – (c)) contains the highest wind speed (25 m/s) of the three modeling scenarios, which occurred on October 16th during the passing of Hurricane Irene between October 14th and 18th (Avila, 1999). During that time, the winds are directed 270° south to a northern heading of 90°. It should be noted that the pressure dropped from 3 hPa on October 14th to -16hPa on October 18th. All other observations of wind speeds are on average 5 ± 5 m/s and wind pressures remain between 0 hPa and 9 hPa.

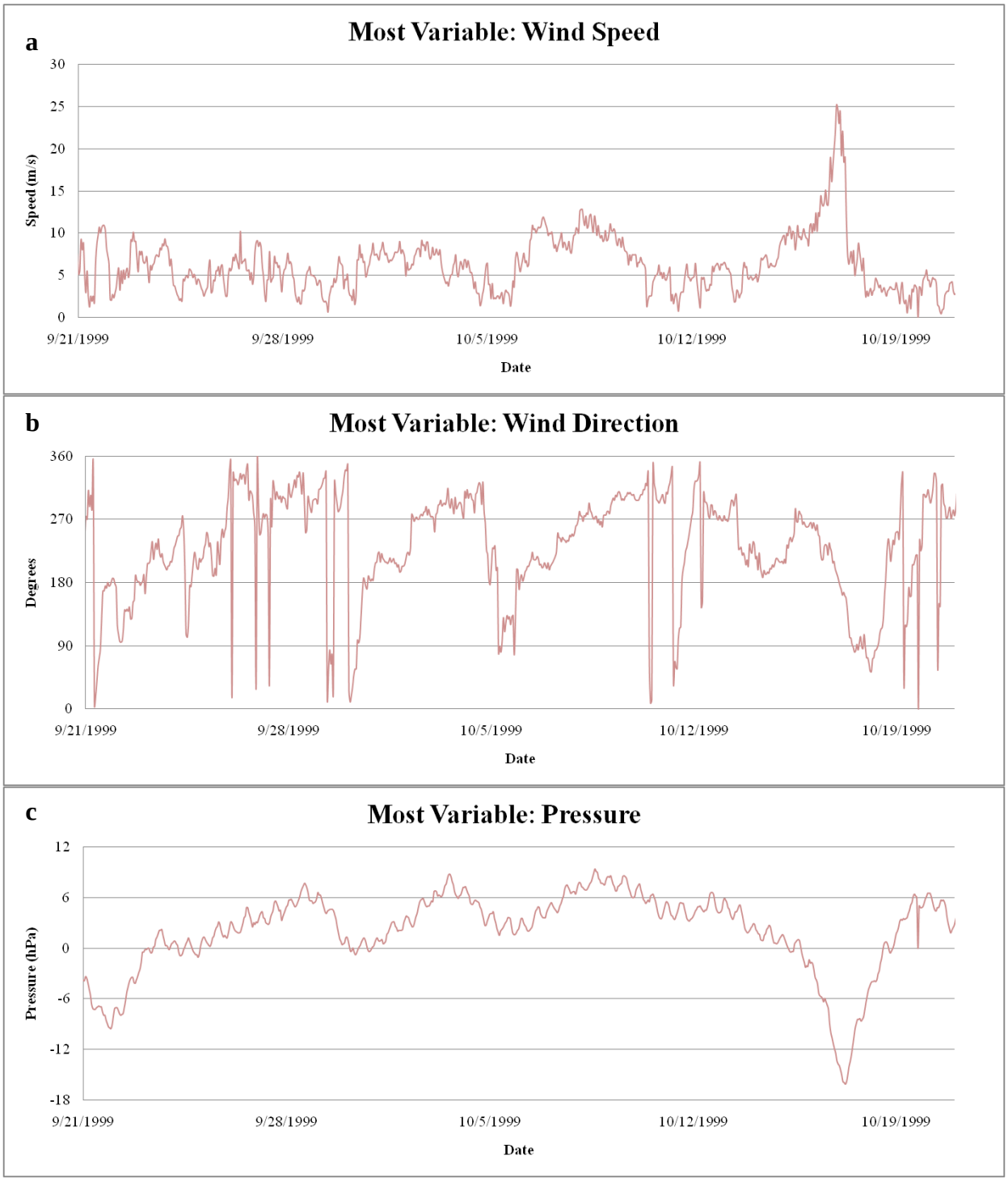

Figure 9.6: Wind speed (a) and direction (b), along with pressures (c), for the *Most Variable* modeling scenario from the NOAA C-MAN Station SAUF1.

Lastly, the *Low Extreme* displays the most erratic behavior of the three modeling scenarios as shown in Figure 9.7 (a) - (c). There are two incidences of the highest winds during this time period, which are November 2nd through 4th and November 12th through 19th. During November 2nd to November 4th, the winds reached the highest speed of 15 m/s and transitioned from 270° south to approximately 90° north as shown in Figure 9.6 (b). The pressures fluctuated from -6hPa to the highest of 16 hPa. November 12th through November 19th displayed winds ranging from 8 m/s to approximately 15 m/s in the 270° south to 150° northwest. The pressures transitioned from 6 hPa to the lowest of -3 hPa to the highest 13 hPa (see Figure 9.7 (c)).

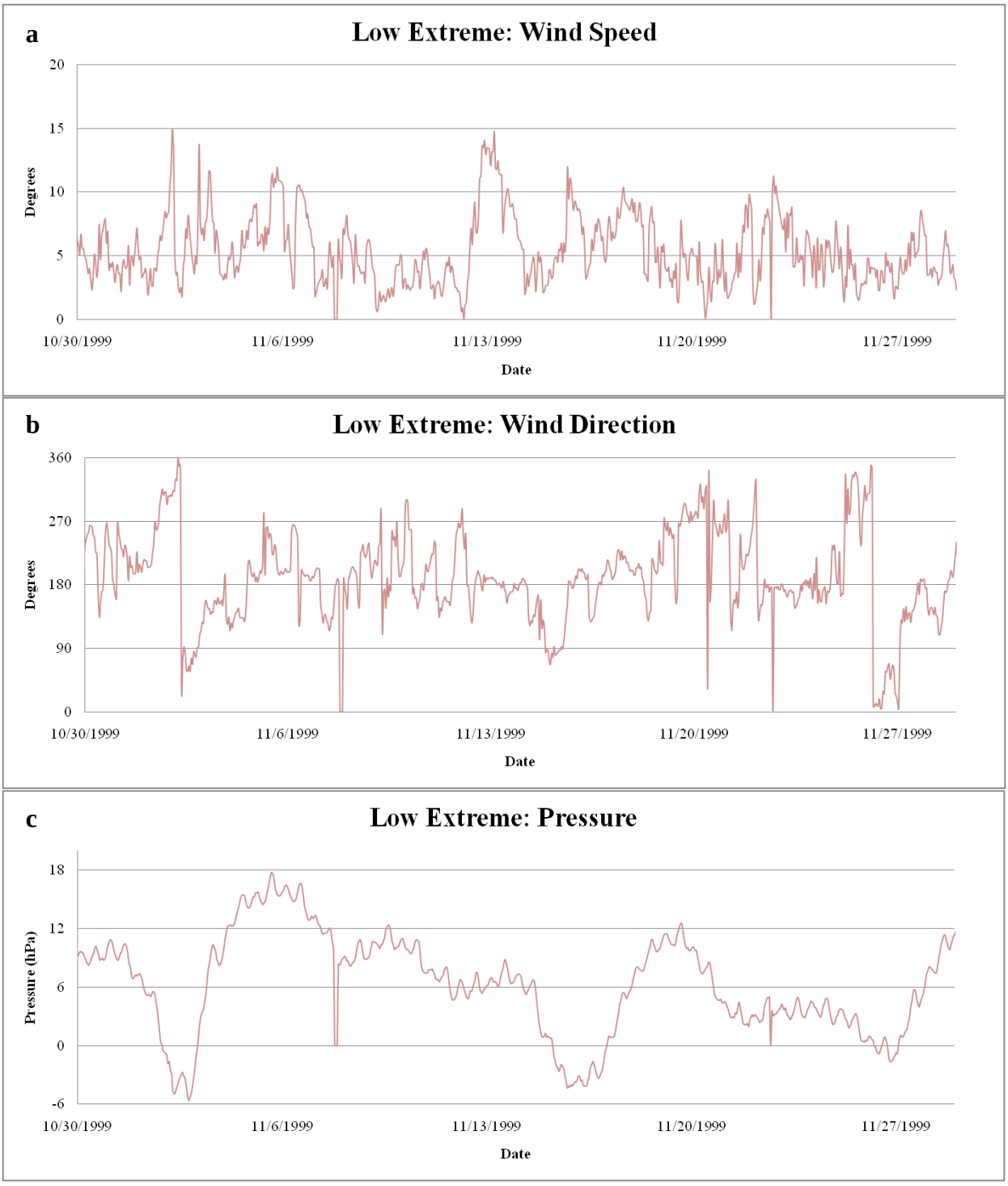

Figure 9.7: Wind speed (a) and direction (b), along with pressures (c), for the *Low Extreme* modeling scenario from the NOAA C-MAN Station SAUF1.

9.3. Riverine Inflows

The influential intensity of the incoming freshwater flows is high in the upper regions of the Lower St. Johns River. As stated earlier by Sucsy and Morris (2002), the freshwater inflows intensify with the decreasing tidal influences. This is one reason for the very low readings at Shands Bridge recorded below the precision of the USGS gauge. It is important to assess the influences of riverine streamflows to assess the effects on salinity concentrations on stations located in the upper reaches of the river (i.e. Buckman Bridge and Shands Bridge).

The freshwater inflow data are collected from two USGS stations (USGS WaterWatch – Streamflow Conditions, 2011). For this study, the following stations provided daily discharge data near the middle of the Lower St. Johns River (40 river kilometer) and upstream (160 river kilometer), respectively: Jacksonville, FL (station 02246500) and Buffalo Bluff, FL (Station 02244040). It is noted that the data collected at the Buffalo Bluff station are used for the purpose of creating realistic boundary conditions, and the Jacksonville station aides in the validation of river inflows.

As shown in Figure 9.8 through Figure 9.13, the river inflows are graphed and fluctuate on magnitudes of m^3/s, where negative values are related to upstream flows, and positive values are related to those of the downstream flows. The river inflows for the three modeling scenarios are selected to maintain data consistency. All of the modeling scenarios do not display the inflow rates to surpass 400 m^3/s downstream and upstream for the Buffalo Bluff station (see Figure 9.8, Figure 9.10, and Figure 9.12). For the Jacksonville station, the fluctuations of the flow rates are

more prevalent when compared to Buffalo Bluff, which is expected due to the station's location as shown in Table 9.1 and Figure 9.9, Figure 9.11, and Figure 9.13.

During the *High Extreme*, Buffalo Bluff (Figure 9.8) shows a noticeable peak in upstream freshwater flows during the entire 30 days of the scenario on June 18th. Within the scenario, the downstream flow rates range within 0 m^3/s to354 m^3/s. However, the Jacksonville station (Figure 9.9) displayed -670 m^3/s to 1016 m^3/s.

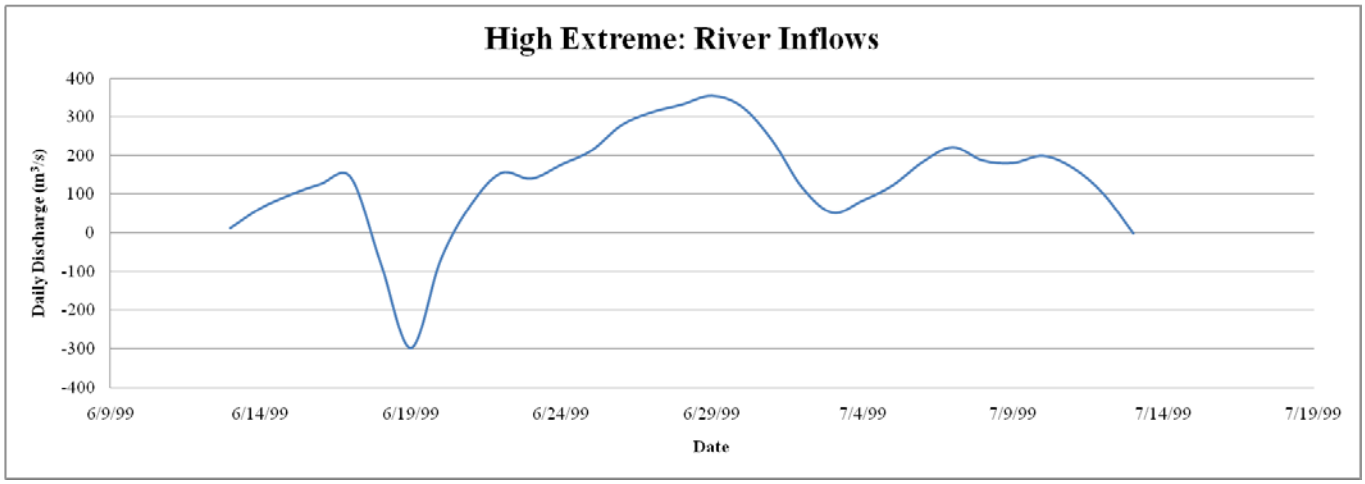

Figure 9.8: River inflows from USGS Station 02244040 located near Buffalo Bluff, FL during the *High Extreme* modeling scenario.

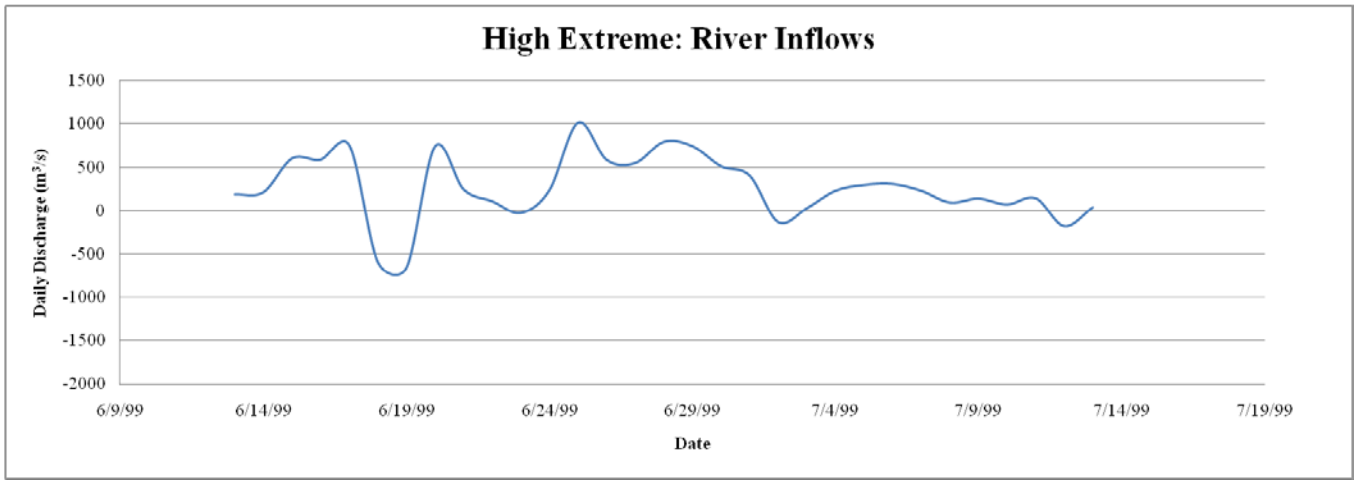

Figure 9.9: River inflows from USGS Station 02246500 located in Jacksonville, FL during the *High Extreme* modeling scenario.

The *Most Variable* scenario consists of a more consistent flow pattern at Buffalo Bluff (Figure 9.10); however, there is a peak upstream inflow rate of approximately 377 m^3/s during the time of Hurricane Irene on the June 17th, followed by 385 m^3/s downstream on June 18th. This is also present within the Jacksonville station (Figure 9.11); this station had the highest upstream discharge (-1795 m^3/s) and downstream discharge (1266 m^3/s) compared to the other modeling scenarios.

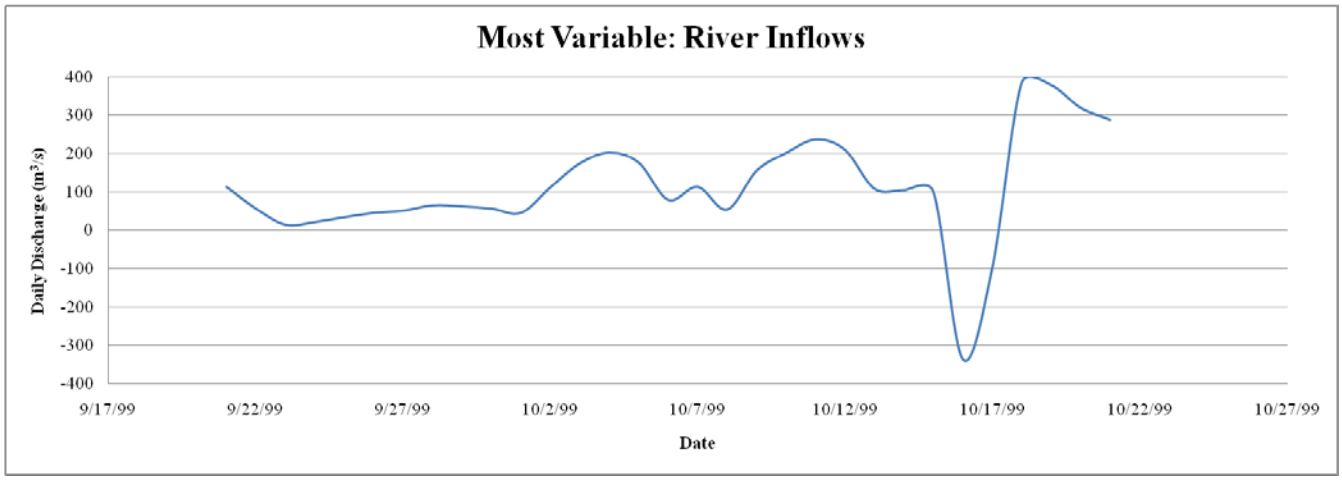

Figure 9.10: River inflows from USGS Station 02244040 located near Buffalo Bluff, FL during the *Most Variable* modeling scenario.

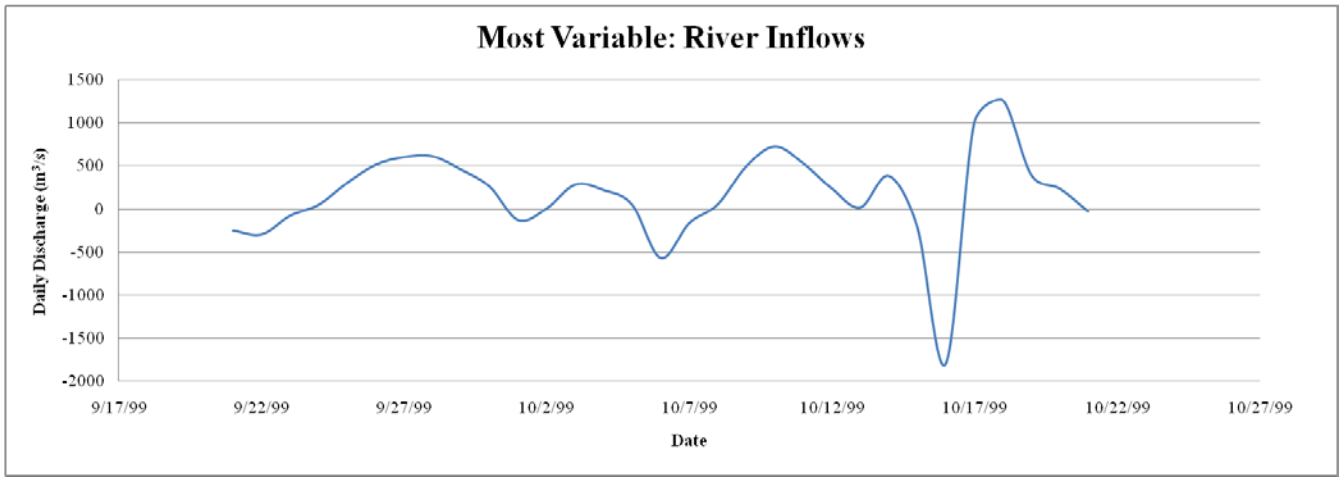

Figure 9.11: River inflows from USGS Station 02246500 located in Jacksonville, FL during the *Most Variable* modeling scenario.

Lastly, the *Low Extreme* modeling scenario has the most erratic pattern for the downstream, however, no upstream river inflows are present. The lowest downstream peak occurs on November 13th in Buffalo Bluff (Figure 9.12), where it nears 93 m^3/s; the highest

downstream peak is a reported 396 m^3/s. The Jacksonville station (Figure 9.13), on the other hand, recorded an upstream discharge of 405 m^3/s and a downstream value of 875 m^3/s.

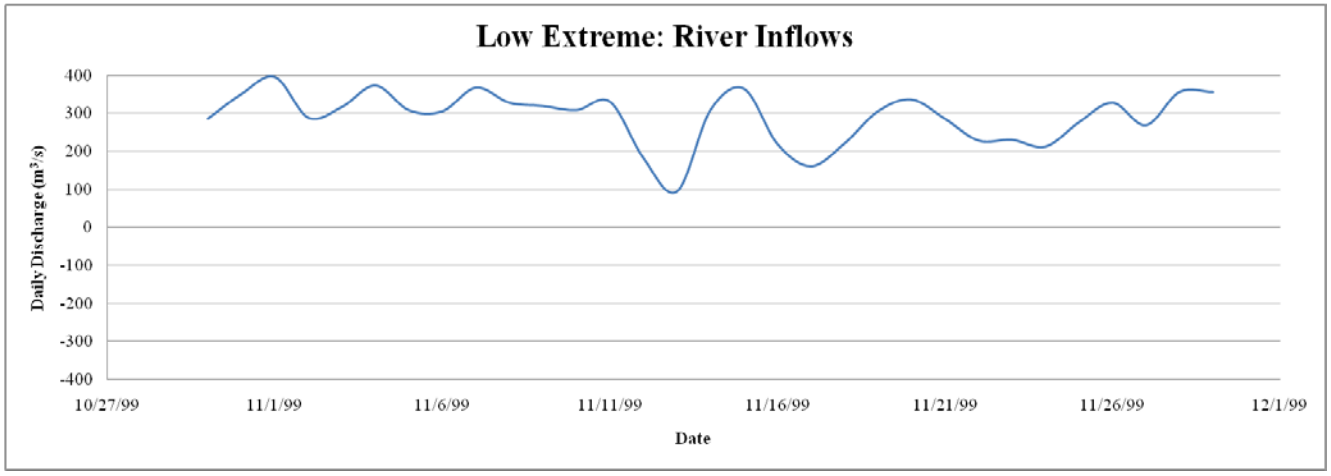

Figure 9.12: River inflows from USGS Station 02244040 located near Buffalo Bluff, FL during the *Low Extreme* modeling scenario.

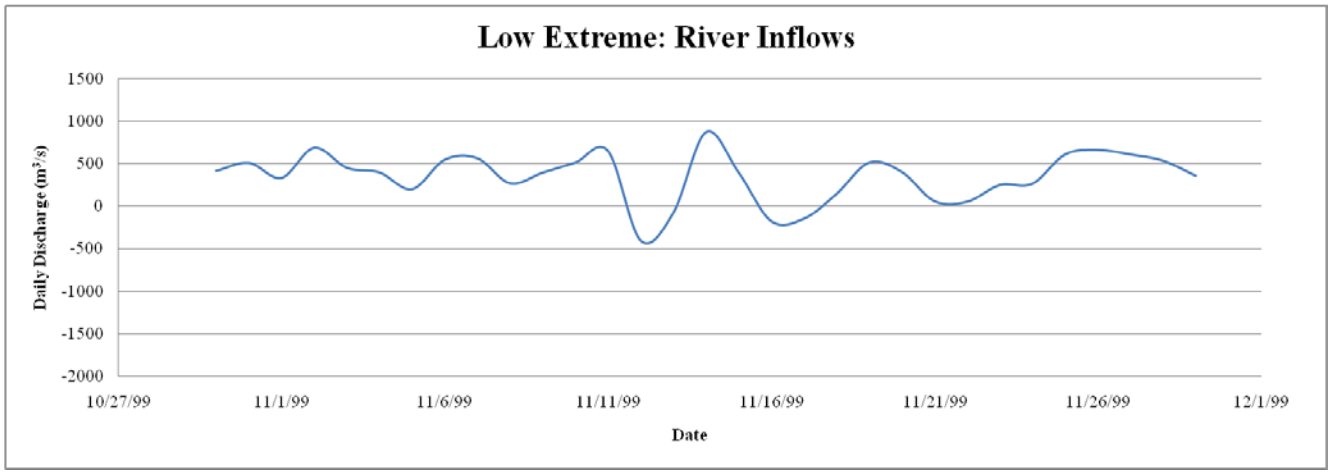

Figure 9.13: River inflows from USGS Station 02246500 located in Jacksonville, FL during the *Low Extreme* modeling scenario.

The daily discharge rates are validated using the USGS station 02246550 located in Jacksonville to compare the use of only tides against additional forcings. Since the Lower St. Johns River is a very slow moving river with a very low slope and tidally driven, it is expected that the RMS errors will decrease as additional forcings are added into the model.

As shown in Table 9.4, the RMS errors of the modeled discharge with the inclusion of river inflows, winds, and pressures with the tides has the lowest RMS error for all three modeling scenarios: *High Extreme* – 20%, *Most Variable* – 14%, and *Low Extreme* – 22%. It should be noted that the *Most Variable* modeling scenario has the lowest RMS error, which is mainly driven by a meteorological event (i.e. Hurricane Irene). The river inflow validation plots can be found in Appendix E.

Table 9.4: Root mean square errors (%) for the daily discharges modeled with three different combinations: (1) tides, (2) tides and inflows, and (3) tides, inflows, and winds and pressures during all modeling scenarios.

Daily Discharge: High Extreme						
	Tides		Tides and Inflows		Tides, Inflows, and Winds and Pressures	
Station ID:	Buffalo Bluff	Jacksonville	Buffalo Bluff	Jacksonville	Buffalo Bluff	Jacksonville
	DG	DG	DG	DG	DG	DG
Maximum (m^3/s)	354	1016	354	1016	354	1016
Minimum (m^3/s)	-294	-670	-294	-670	-294	-670
Range (cm)	651	1676	651	1676	651	1676
RMS (cm)	-	393	-	390.0	-	331
RMS (%)	-	23	-	23	-	20.0

Daily Discharge: Most Variable						
	Tides		Tides and Inflows		Tides, Inflows, and Winds and Pressures	
Station ID:	Buffalo Bluff	Jacksonville	Buffalo Bluff	Jacksonville	Buffalo Bluff	Jacksonville
	DG	DG	DG	DG	DG	DG
Maximum (m^3/s)	385	1266	385	1266	385	1266
Minimum (m^3/s)	-337	-1795.0	-337	-1795.0	-337	-1795.0
Range (cm)	722	3061	722	3061	722	3061
RMS (cm)	-	531	-	542	-	418.0
RMS (%)	-	17	-	18	-	14.0

Daily Discharge: Low Extreme						
	Tides		Tides and Inflows		Tides, Inflows, and Winds and Pressures	
Station ID:	Buffalo Bluff	Jacksonville	Buffalo Bluff	Jacksonville	Buffalo Bluff	Jacksonville
	DG	DG	DG	DG	DG	DG
Maximum (m^3/s)	396	875	396	875	396	875
Minimum (m^3/s)	93	-405.0	93	-405.0	93	-405.0
Range (cm)	303	1280	303	1280	303	1280
RMS (cm)	-	347	-	315	-	282.0
RMS (%)	-	27	-	25	-	22.0

9.4. Water Levels and Salinity

The modeled water levels and salinity concentrations are compared to the observed water levels and salinity data used in the Sucsy and Morris (2002) study (i.e., Dames Point, Acosta Bridge, Buckman Bridge, and Shands Bridge) to establish the performance of the DG finite element method concerning salinity transport. The MARSH mesh is used during the modeling process to formulate a basis on the effect of the tidal creeks and surrounding marshes on circulation within the Lower St. Johns River.

9.4.1. Water Levels

The simulated water levels are in adequate agreement with the observed data (refer to Appendix B). As shown in all modeling scenarios for the USGS station located at Dames Point, the model fluctuates in and out of phase. It is observed that the RMS errors of the *High Extreme* and *Most Variable* modeling scenarios increased from Dames Point to Buckman Bridge, and then decreased at Shands Bridge (see Table 9.5). The RMS errors range in the following: *High Extreme* – 9.0% to 26.2%, *Most Variable* – 13.3% to 48.4%, and *Low Extreme* – 5.8% to 31.6%. It should be noted that water level data of the *Low Extreme* was not available for Buckman Bridge. On average, *Most Variable* has the highest RMS error (30.5%) and *Low Extreme* has the lowest RMS error (15.6%). As stated earlier, the observed data from the four USGS stations record full-signal data, which contains not only tidal data, but data concerning wind and pressure effects, freshwater flows, baroclinic effects, etc. The simulated water levels are strictly tidal

based; that is, there are no other physical forcings present. Comparing the tidal-based results with a full-signal observed data would cause high RMS errors.

Table 9.5: Root mean square errors (%) for the water levels per station used in the Sucsy and Morris (2002) study during all modeling scenarios for the DG finite element methods.

Water Levels: High Extreme										
Station ID:	**DAMES**		**ACOSTA**		**BUCKMAN**		**SHANDS**		**Average**	
	CG	DG	CG	DG	CG	DG	CG	DG	CG	DG
Maximum (cm)	67.9		34.2		30.4		35.3		42	
Minimum (cm)	-91.1		-49.1		-39.7		-38.9		-54.7	
Range (cm)	159		83.3		70.1		74.2		96.7	
RMS (cm)	-	14.2	-	19.0	-	18.4	-	17.4	-	17.3
RMS (%)	-	9.0	-	22.8	-	26.2	-	23.5	-	20.4
Water Levels: Most Variable										
Station ID:	**DAMES**		**ACOSTA**		**BUCKMAN**		**SHANDS**		**Average**	
	CG	DG	CG	DG	CG	DG	CG	DG	CG	DG
Maximum (cm)	80.7		63.3		41.2		71.8		64.3	
Minimum (cm)	-55.9		-20.3		1.4		6.0		-17.2	
Range (cm)	136.6		83.6		39.8		65.8		81.5	
RMS (cm)	-	18.1	-	19.6	-	19.2	-	24.4	-	20.3
RMS (%)	-	13.3	-	23.4	-	48.4	-	37.1	-	30.5
Water Levels: Low Extreme										
Station ID:	**DAMES**		**ACOSTA**		**BUCKMAN**		**SHANDS**		**Average**	
	CG	DG	CG	DG	CG	DG	CG	DG	CG	DG
Maximum (cm)	75.2		46.1		N/A		37.2		52.8	
Minimum (cm)	-69.5		-40.3		N/A		-1.9		-37.2	
Range (cm)	144.7		86.4		N/A		39.1		90.1	
RMS (cm)	-	8.4	-	8.1	-	N/A	-	12.4	-	9.6
RMS (%)	-	5.8	-	9.4	-	N/A	-	31.6	-	15.6

As stated earlier, the Jacksonville station (USGS station 02246500) is used for validation purposes of comparing tidal forcings and additional forcings (winds, pressures, and inflows) for the four observation locations (Dames Point, Acosta Bridge, Buckman Bridge, and Shands

Bridge) for water levels. Again, for comparison purposes, the RMS errors are calculated for each station.

The RMS errors for each observation location are presented in Table 9.6. The water levels and salinity concentrations are modeled based on the additional forcings (river inflows, winds and pressures) along with tides. With respect to water levels, the additional forcings improve the modeled quantities on average: *High Extreme* – 20.4% versus 20.2%, *Most Variable* – 30.5% versus 23.5%, and *Low Extreme* – 15.6% versus 13.2%. It is observed that the RMS errors for the *Most Variable* modeling scenario decreased for all locations when river inflows and winds and pressures are added to the model. However, the other two scenarios present opposite results. The RMS errors of the Dames Point and Acosta Bridge stations increase by 0.5% - 0.9% and 1% - 3%, respectively. However, the RMS errors of the Buckman Bridge and Shands Bridge increased by 0.1% and 2% to 11%, respectively. This reinforces the fact that the tidal influences are the strongest at Dames Point and Acosta Bridge compared to Buckman Bridge and Shands Bridge. The graphical representations can be seen in Appendix C.

Table 9.6: Root mean square errors (%) for the water levels per station used in the Sucsy and Morris (2002) study during all modeling scenarios for the DG finite element method with modeled tides, river inflows, and winds and pressures.

Water Levels: High Extreme										
Station ID:	**DAMES**		**ACOSTA**		**BUCKMAN**		**SHANDS**		**Average**	
	CG	DG	CG	DG	CG	DG	CG	DG	CG	DG
Maximum (cm)	67.9		34.2		30.4		35.3		42	
Minimum (cm)	-91.1		-49.1		-39.7		-38.9		-54.7	
Range (cm)	159		83.3		70.1		74.2		96.7	
RMS (cm)	-	15.1	-	19.9	-	18.3	-	15.9	-	17.3
RMS (%)	-	9.5	-	23.8	-	26.1	-	21.5	-	20.2

Water Levels: Most Variable										
Station ID:	**DAMES**		**ACOSTA**		**BUCKMAN**		**SHANDS**		**Average**	
	CG	DG	CG	DG	CG	DG	CG	DG	CG	DG
Maximum (cm)	80.7		63.3		41.2		71.8		64.3	
Minimum (cm)	-55.9		-20.3		1.4		6.0		-17.2	
Range (cm)	136.6		83.6		39.8		65.8		81.5	
RMS (cm)	-	15.4	-	15.7	-	15.6	-	16.3	-	15.7
RMS (%)	-	11.2	-	18.8	-	39.2	-	24.8	-	23.5

Water Levels: Low Extreme										
Station ID:	**DAMES**		**ACOSTA**		**BUCKMAN**		**SHANDS**		**Average**	
	CG	DG	CG	DG	CG	DG	CG	DG	CG	DG
Maximum (cm)	75.2		46.1		N/A		37.2		52.8	
Minimum (cm)	-69.5		-40.3		N/A		-1.9		-37.2	
Range (cm)	144.7		86.4		N/A		39.1		90.1	
RMS (cm)	-	9.7	-	10.7	-	N/A	-	8.1	-	9.5
RMS (%)	-	6.7	-	12.4	-	N/A	-	20.6	-	13.2

9.4.2. Salinity

The tidal creeks that branch out off the main river channel take in incoming saline waters. On this basis, it is hypothesized that the tidal creeks would have higher salinity concentrations compared to other portions of the river. Again, this may be due to the "trapping" behavior of the creeks due to their branching and winding manners. This section provides the resulting groundwork of creating a two-dimensional salinity transport model of the Lower St. Johns River. The results are used to study salinity fluctuations and variations, along with trends within the river.

Based on the RMS errors (Table 9.7), the modeled salinity concentrations did somewhat well at Dames Point and Acosta Bridge. However, as one enters into territory of lower salinity concentrations (i.e. Buckman Bridge and Shands Bridge), the RMS errors are incredibly high, especially at Buckman Bridge. This trend can also be seen in Figure 9.14 through Figure 9.17. The large discrepancies between the observed and modeled salinity may be due to the fact that the observed data is a full signal (tides, river inflows, winds, etc) while the modeled data is based on the tides alone.

Table 9.7: Root mean square errors (%) for the salinity levels per station used in the Sucsy and Morris (2002) study during all modeling scenarios for the DG finite element methods.

Salinity: High Extreme					
Station ID:	**DAMES**	**ACOSTA**	**BUCKMAN**	**SHANDS**	**Average**
	DG	DG	DG	DG	DG
Maximum (ppt)	35.6	29.6	17.2	5.9	22.1
Minimum (ppt)	12.5	6.8	3.9	0.9	6.0
Range (ppt)	23.1	22.8	13.3	5.0	16.1
RMS (ppt)	6.3	7.2	20.3	7.0	10.2
RMS (%)	27.2	31.5	151.7	140.2	87.7
Salinity: Most Variable					
Station ID:	**DAMES**	**ACOSTA**	**BUCKMAN**	**SHANDS**	**Average**
	DG	DG	DG	DG	DG
Maximum (ppt)	31.8	22.2	11.8	6.1	18
Minimum (ppt)	8.0	6.0	3.3	0.7	4.5
Range (ppt)	23.8	16.2	8.5	5.4	13.5
RMS (ppt)	6.3	3.8	18.3	6.5	8.7
RMS (%)	26.7	23.2	214.5	121.5	96.5
Salinity: Low Extreme					
Station ID:	**DAMES**	**ACOSTA**	**BUCKMAN**	**SHANDS**	**Average**
	DG	DG	DG	DG	DG
Maximum (ppt)	27.8	8.8	1.7	0.7	9.8
Minimum (ppt)	2.4	0.7	0.6	0.5	1.0
Range (ppt)	25.4	8.1	1.1	0.2	8.8
RMS (ppt)	6.9	1.8	22.4	0.4	7.9
RMS (%)	27.3	22	2020.1	276.0	586.3

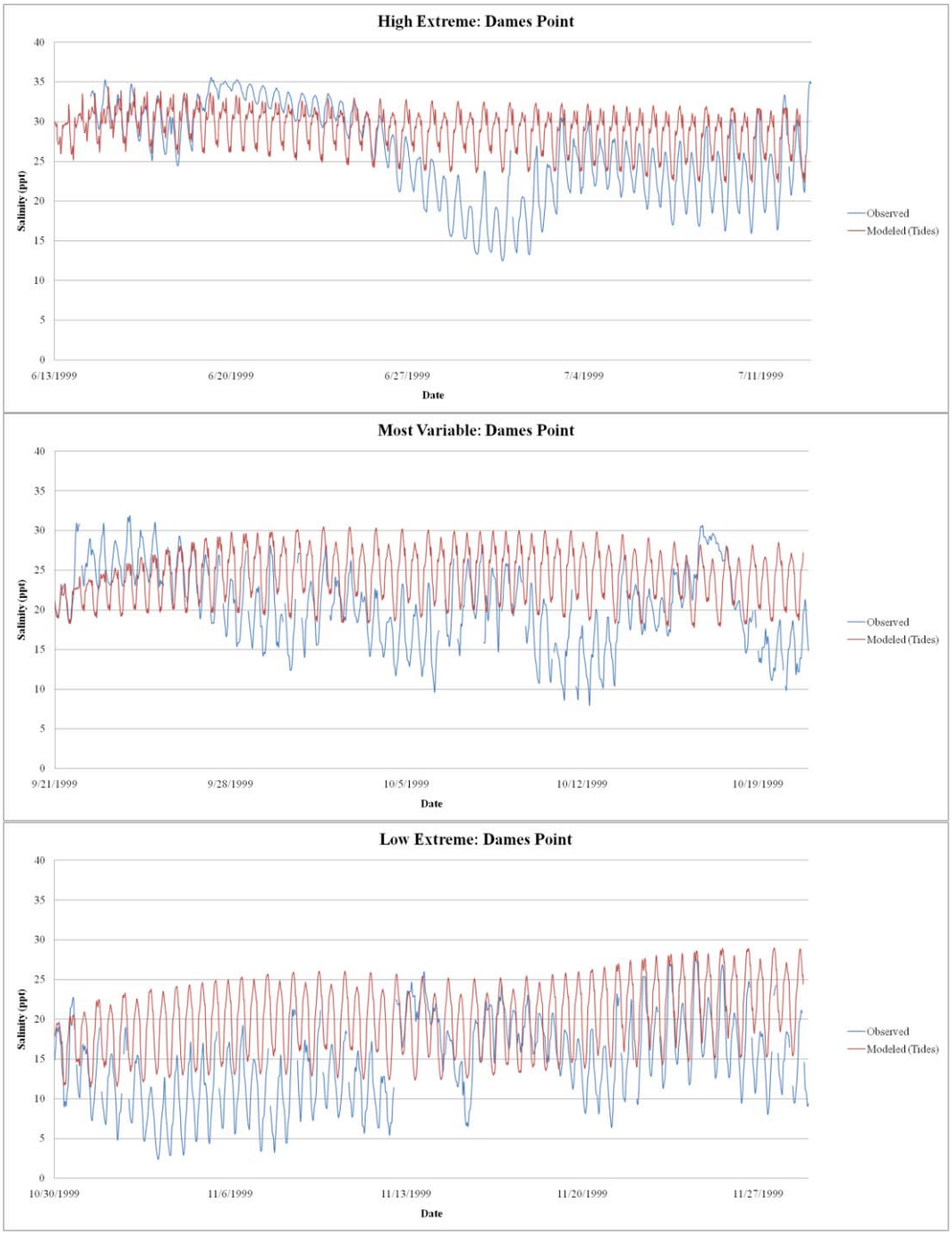

Figure 9.14: Observed salinity versus modeled salinity within the MARSH mesh at the Dames Point station for *High Extreme*, *Most Variable*, and *Low Extreme*.

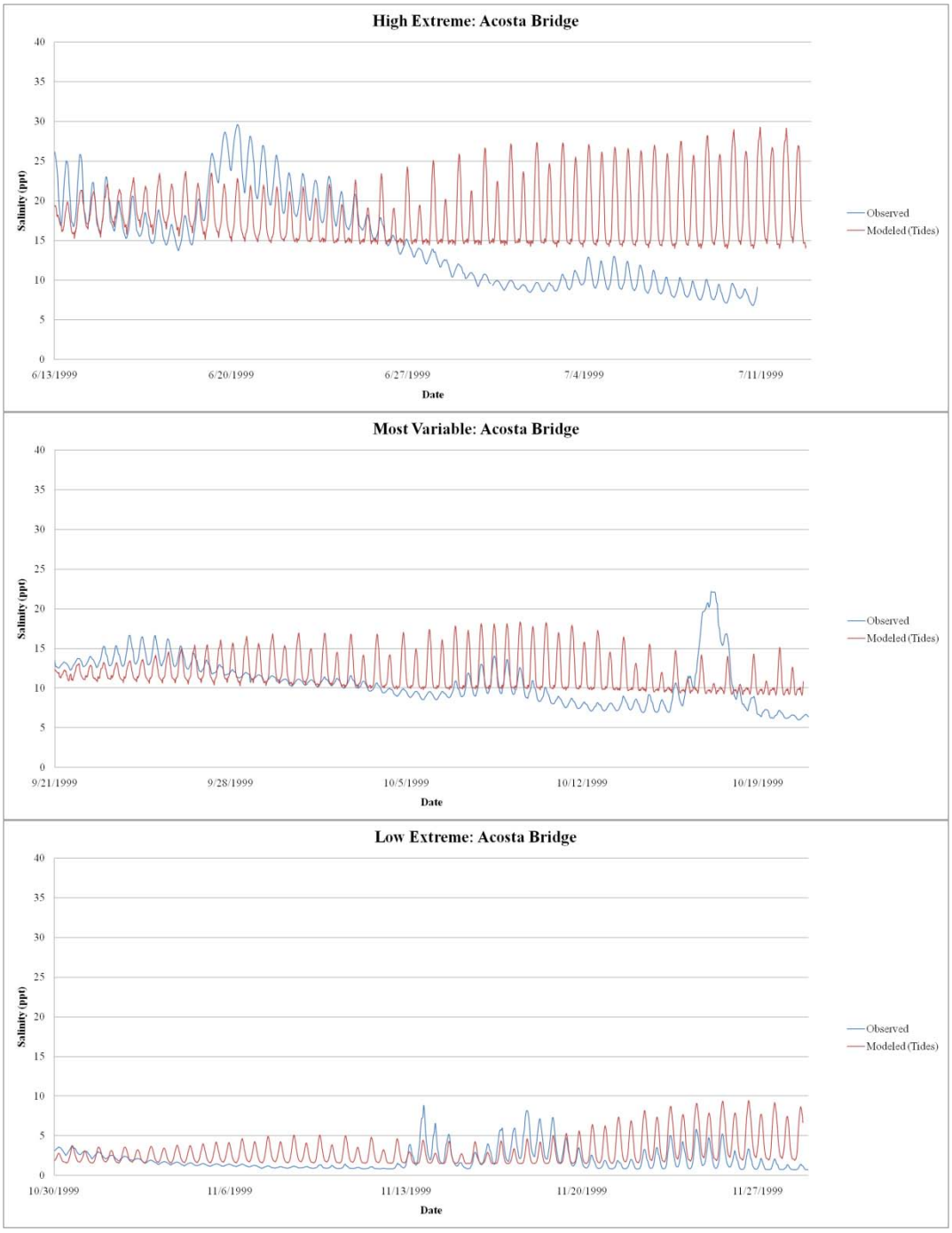

Figure 9.15: Observed salinity versus modeled salinity within the MARSH mesh at the Acosta Bridge station for *High Extreme*, *Most Variable*, and *Low Extreme*.

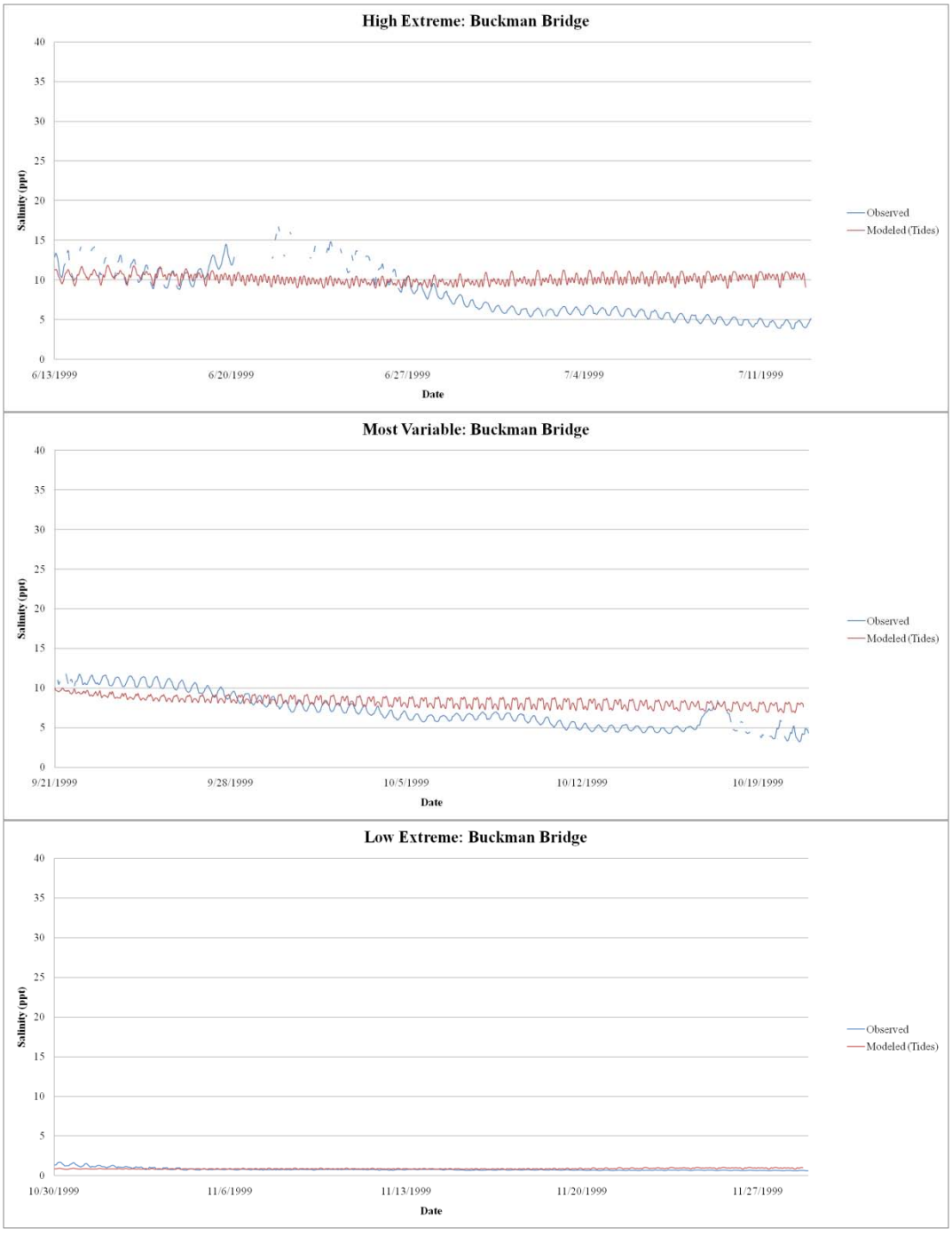

Figure 9.16: Observed salinity versus modeled salinity within the MARSH mesh at the Buckman Bridge station for *High Extreme*, *Most Variable*, and *Low Extreme*.

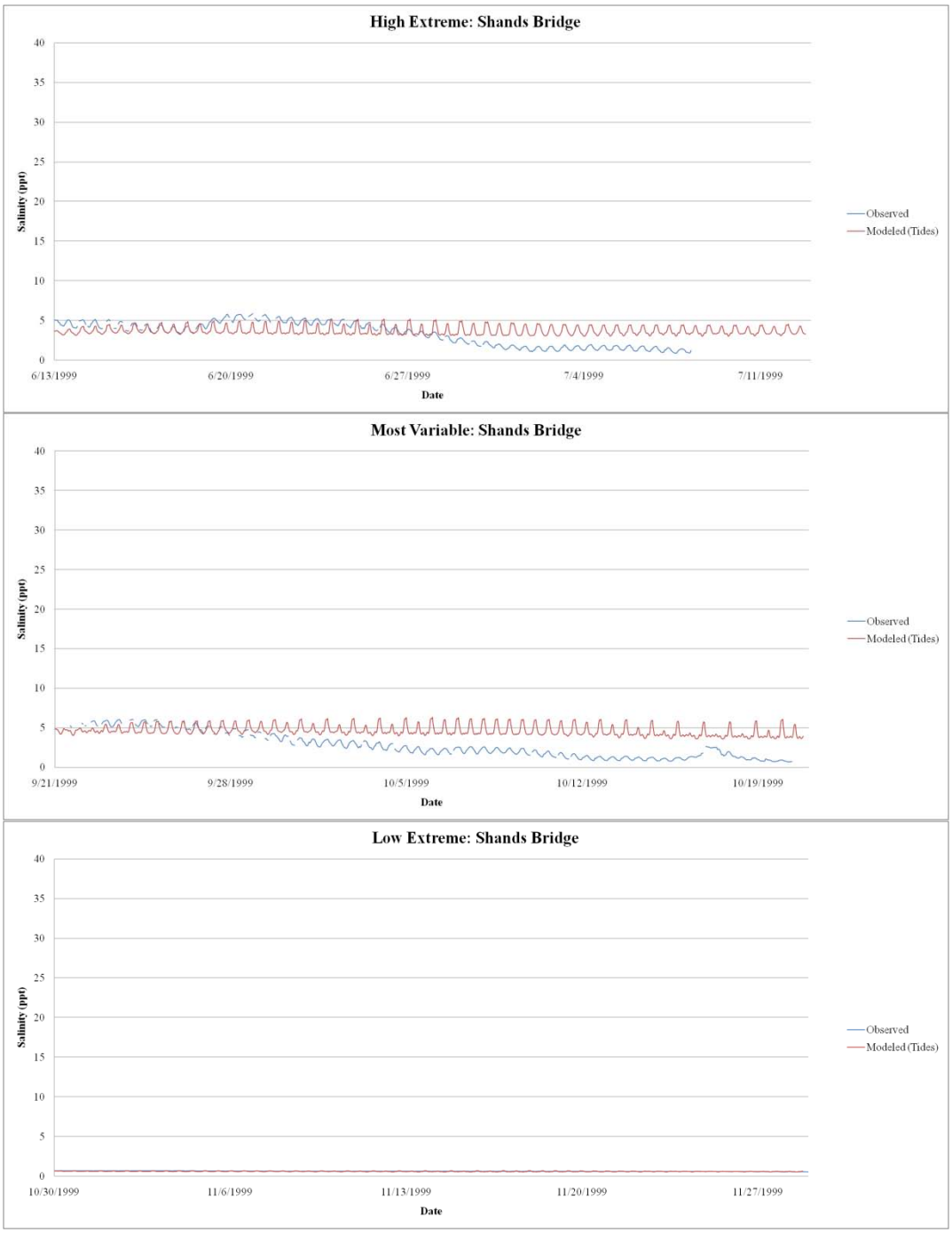

Figure 9.17: Observed salinity versus modeled salinity within the MARSH mesh at the Shands Bridge station for *High Extreme*, *Most Variable*, and *Low Extreme*.

Dames Point has the highest salinity concentration due to its location near the river's mouth, which is represented within the results. Again referring to Figure 2.3 in Chapter 2, the salinity concentration decreases when moving upstream which again is clearly shown in the results. Also, the marshes will contain the highest salinity concentrations compared to other portions of the river due to the fact they are located near the coast and that the hydraulic connectivity between the marsh and river permits for flow (and thus salinity) exchange.

The salinity concentrations are simulated with additional forcings and RMS errors are calculated as well. Similar to water levels, the RMS errors improved on average for each modeling scenario, which can also be seen graphically in Figure 9.18 through Figure 9.21, and Table 9.8. It should be noted that a similar trend was observed among all three modeling scenarios; Dames Point and Acosta Bridge RMS errors increased substantially, while the errors for Buckman Bridge and Shands Bridge decreased immensely. Graphically, the salinity concentrations modeled with tides, inflows, and wind and pressure forcings performed very well. This strengthens the importance of comparing modeled results with additional forcings to observed data with a full signal. Also, it aids in witnessing the effects of tides, inflows, and winds and pressures on salinity concentration throughout the Lower St. Johns River. However, these presented validation results are preliminary results based on present historical data and set parameters within the model. Future salinity transport modeling will require a deeper analysis of the historical data and improvement on parameter selection.

Table 9.8: Root mean square errors (%) for the salinity levels per station used in the Sucsy and Morris (2002) study during all modeling scenarios for the DG finite element method with modeled tides, river inflows, and winds and pressures.

Salinity: High Extreme					
Station ID:	**DAMES**	**ACOSTA**	**BUCKMAN**	**SHANDS**	**Average**
	DG	DG	DG	DG	DG
Maximum (ppt)	35.6	29.6	17.2	5.9	22.1
Minimum (ppt)	12.5	6.8	3.9	0.9	6.0
Range (ppt)	23.1	22.8	13.3	5.0	16.1
RMS (ppt)	10.1	12.4	8.8	1.5	8.2
RMS (%)	43.7	54.2	65.6	29.2	48.2

Salinity: Most Variable					
Station ID:	**DAMES**	**ACOSTA**	**BUCKMAN**	**SHANDS**	**Average**
	DG	DG	DG	DG	DG
Maximum (ppt)	31.8	22.2	11.8	6.1	18
Minimum (ppt)	8.0	6.0	3.3	0.7	4.5
Range (ppt)	23.8	16.2	8.5	5.4	13.5
RMS (ppt)	10.0	6.8	7.3	3.2	6.8
RMS (%)	41.9	42.0	85.5	58.9	57.1

Salinity: Low Extreme					
Station ID:	**DAMES**	**ACOSTA**	**BUCKMAN**	**SHANDS**	**Average**
	DG	DG	DG	DG	DG
Maximum (ppt)	27.8	8.8	1.7	0.7	9.8
Minimum (ppt)	2.4	0.7	0.6	0.5	1.0
Range (ppt)	25.4	8.1	1.1	0.2	8.8
RMS (ppt)	12.5	2.0	7.0	0.1	5.4
RMS (%)	49.2	24.3	635.5	44.8	188.5

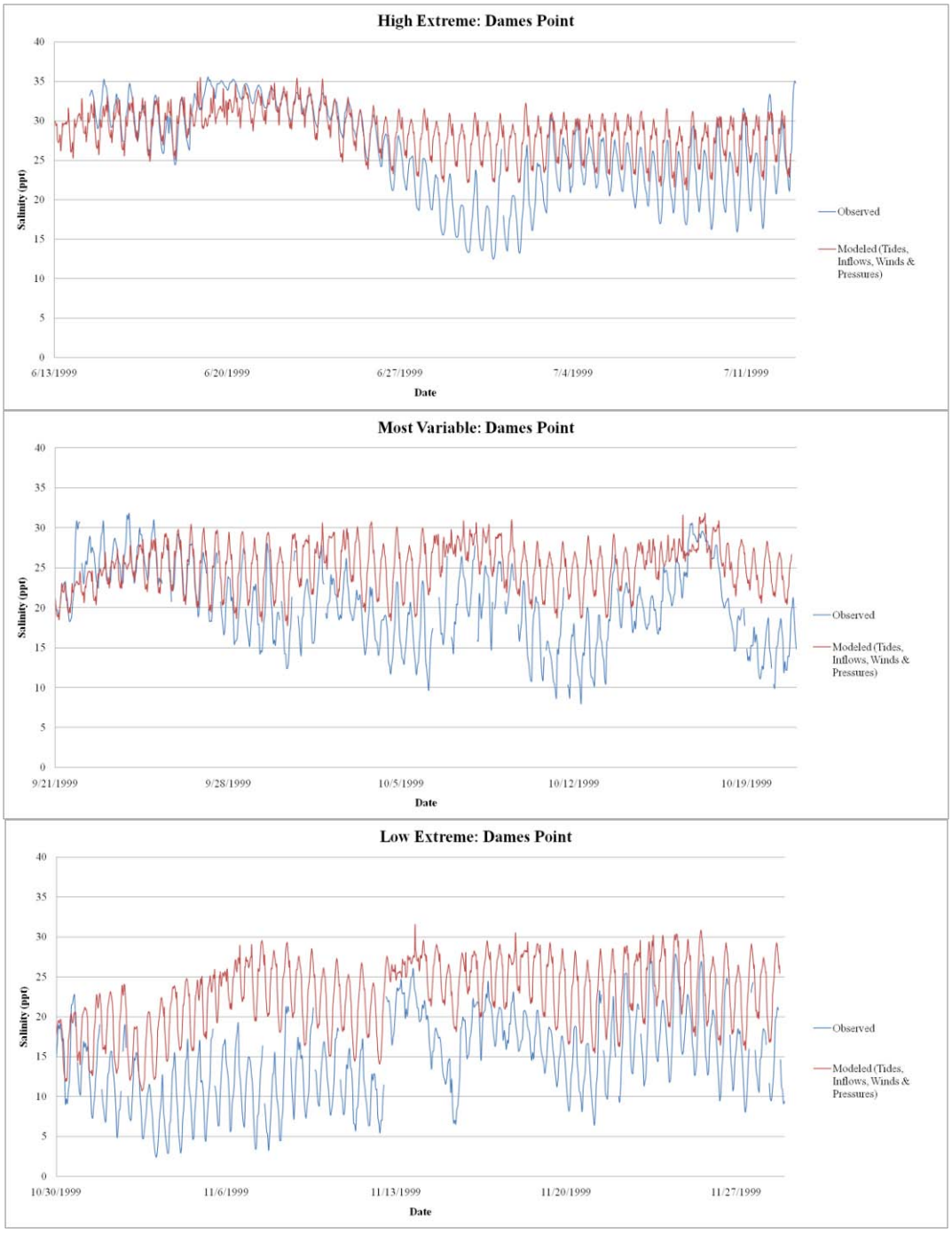

Figure 9.18: Observed salinity versus modeled salinity with tidal, inflow, and winds and pressure forcings within the MARSH mesh at the Dames Point station for *High Extreme*, *Most Variable*, and *Low Extreme*.

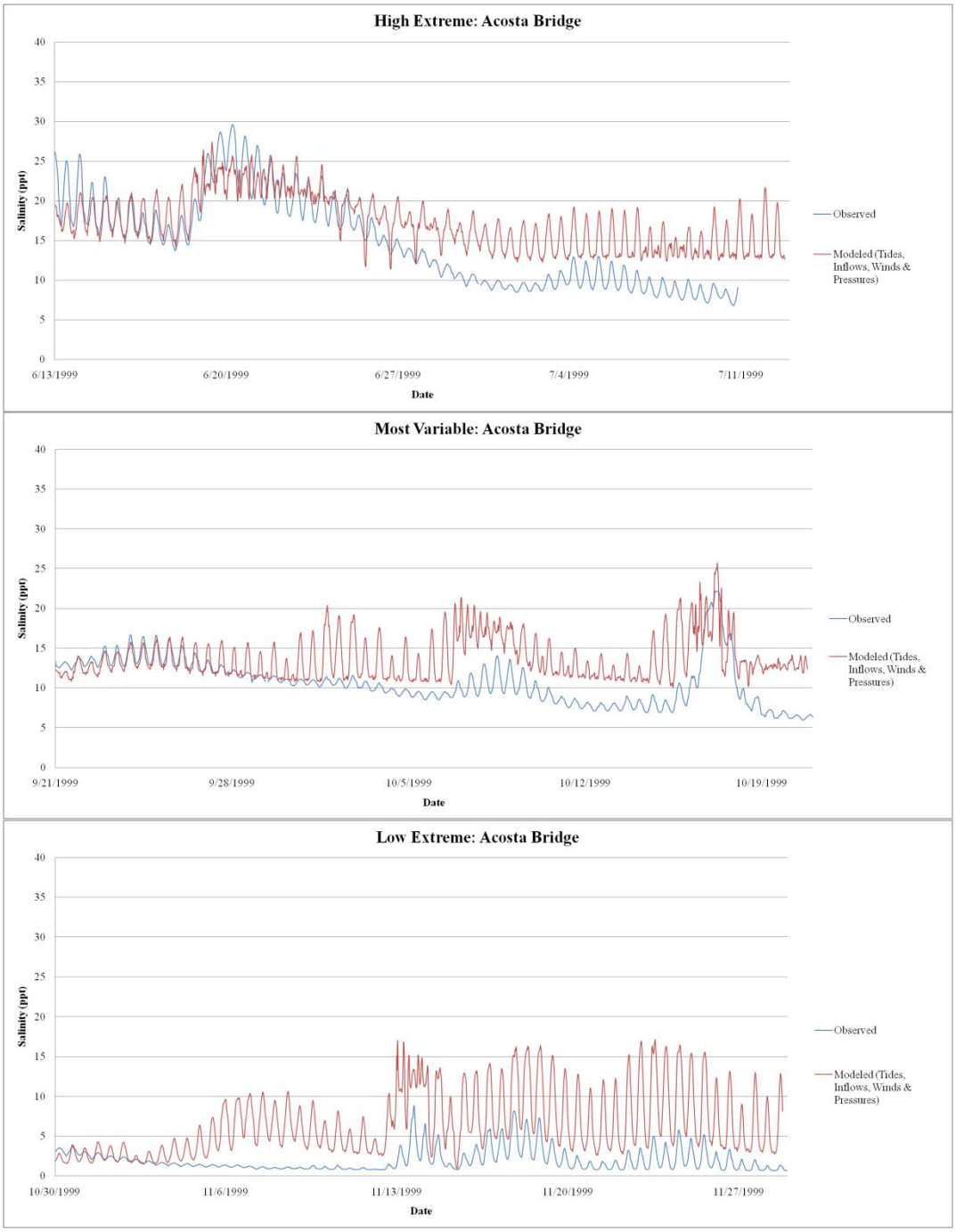

Figure 9.19: Observed salinity versus modeled salinity with tidal, inflow, and winds and pressure forcings within the MARSH mesh at the Acosta Bridge station for *High Extreme*, *Most Variable*, and *Low Extreme*.

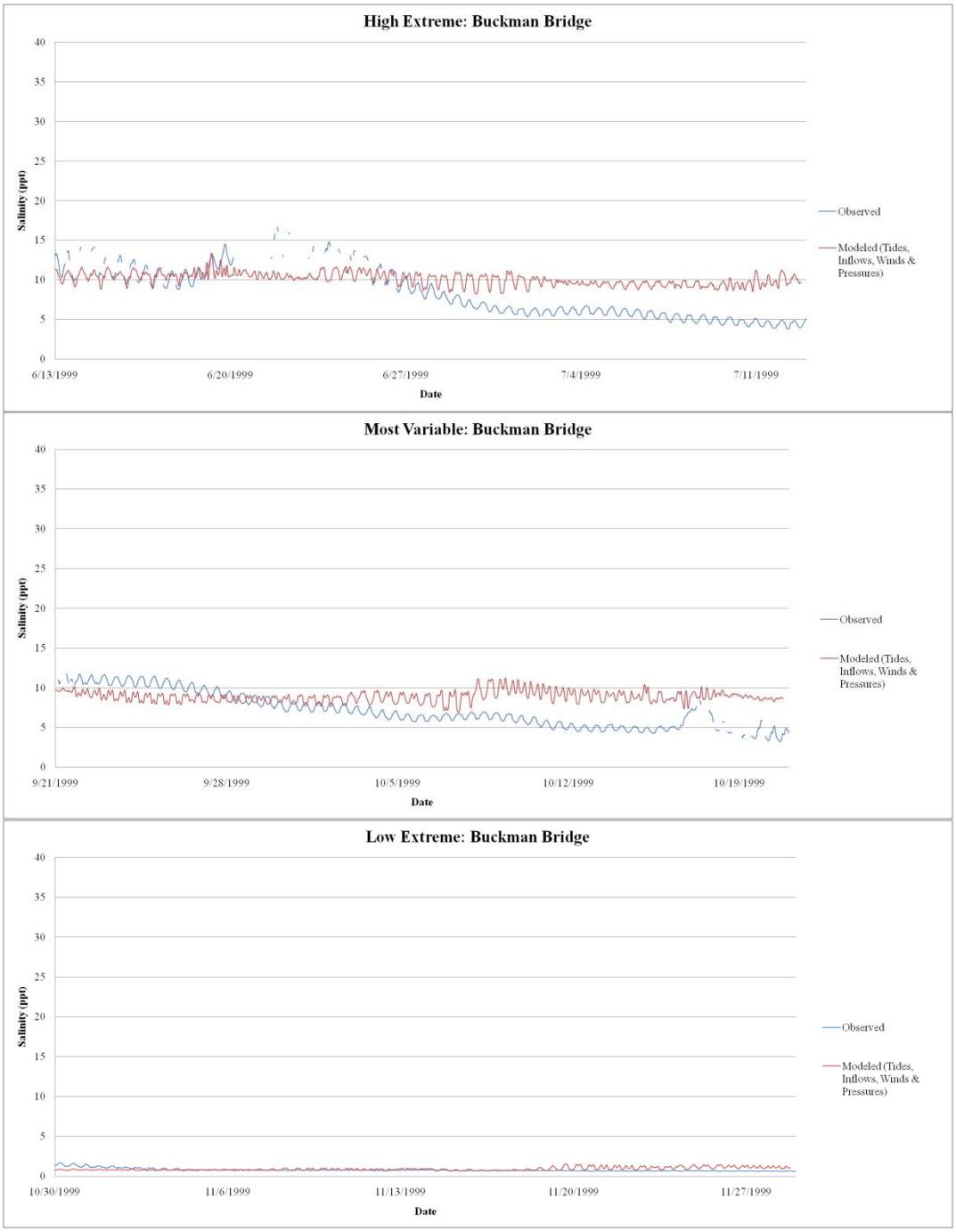

Figure 9.20: Observed salinity versus modeled salinity with tidal, inflow, and winds and pressure forcings within the MARSH mesh at the Buckman Bridge station for *High Extreme*, *Most Variable*, and *Low Extreme*.

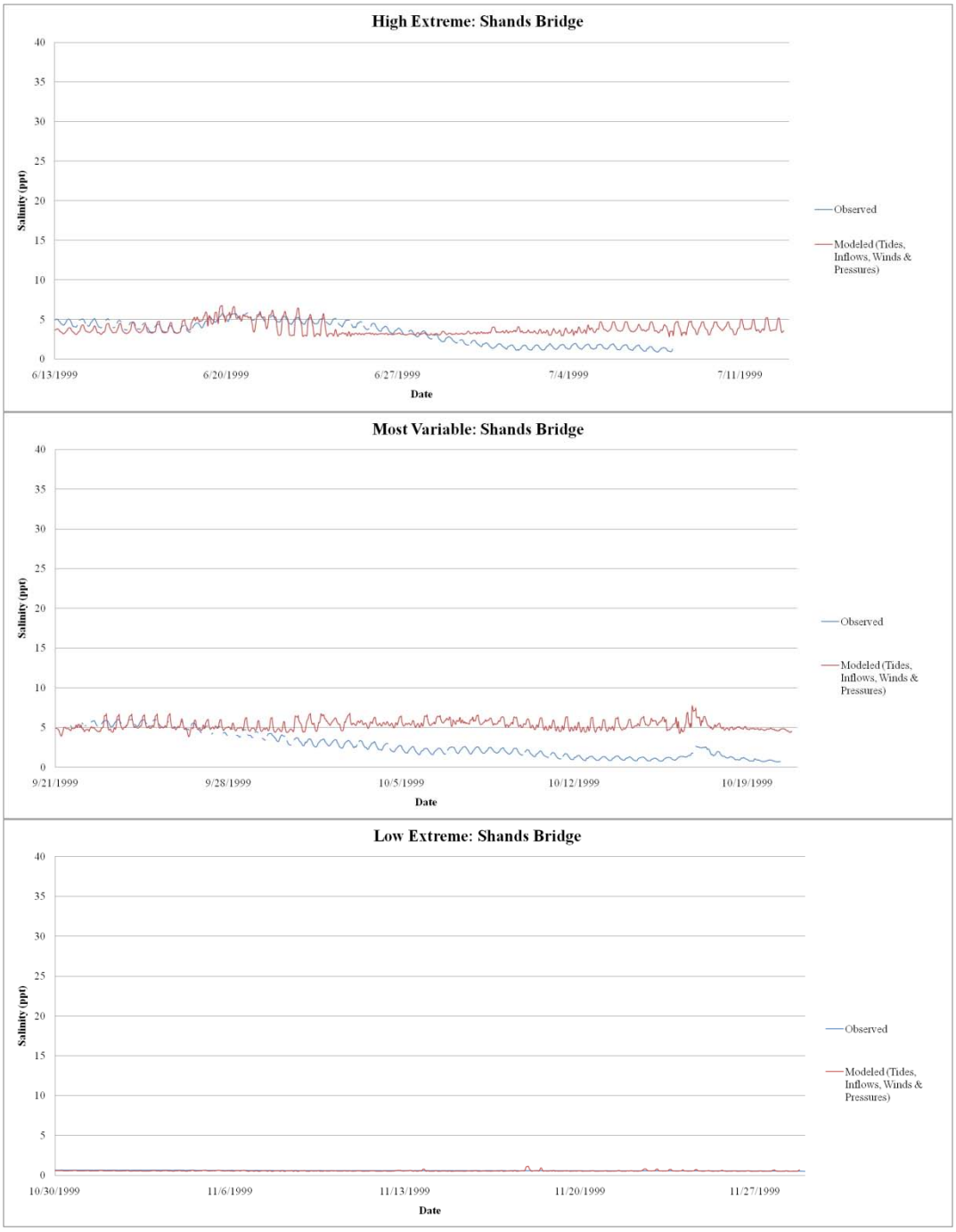

Figure 9.21: Observed salinity versus modeled salinity with tidal, inflow, and winds and pressure forcings within the MARSH mesh at the Shands Bridge station for *High Extreme*, *Most Variable*, and *Low Extreme*.

CHAPTER 10 CONCLUSIONS

Salinity transport is a complex physical process, the modeling of which is a common task in the coastal-related scientific and engineering communities. In the modeling pursuit, identifying the physical forcings to drive the salinity transport problem is an important task as is the selection of a model that ensures mass conservation (globally, but more importantly locally). This approach leads to more physics-based modeling. Such practice enables the modeler to gain scientific insight into the salinity transport process. The underlying concept of this thesis fits into the above context as: to provide a modeling tool that can directly assist in salinity studies on the Lower St. Johns River. However, in the development of the modeling tool, it is key to identify the model as producing mass-conservative numerical solutions.

Historical data for three time periods in 1999 (*High Extreme*, *Most Variable*, and *Low Extreme*) were analyzed. This provided insight on salinity fluctuations at four stations located within the lower 10 river km to 40 river km of the Lower St. Johns River. These time periods present influences by the changing of seasons (Spring to Winter) and meteorological events (i.e. Hurricane Irene). Also, these stations give the opportunity to observe the longitudinal variation of salinity transport within the river due to tidal influences. The analysis reinforces the fact the Lower St. Johns River is tidally driven and tides are the main driver in the salinity transport. Based on this fact, it would be expected that the salinity decreases as you move upstream into areas where tidal forcings are not strong (i.e. Shands Bridge). Therefore, this thesis confirms the perception of the influential physical processes on longitudinal variation of salinity.

A comparison between the continuous (CG) and discontinuous Galerkin (DG) finite element methods was done to observe the mass conservation properties of each algorithm within a hydrodynamic (CG) coupled hydrodynamic-transport (DG) model. Mass imbalance was recognized in local areas of complex geometry and abrupt bathymetric gradients. This suggests that mass balance is based on the geometry of the domain. This is also the case with the subdivision of the Lower St. Johns River. Mass errors increase with increasing complexity of the subdivision. The highest mass errors occurred in subdivisions with intricate geometries, i.e., those that have the smallest areas and widths and/or contain either tidal branches or islands. For example, both marshes had large mass errors. Among the two marshes, the northern marsh (Marsh A) had lower mass error than the southern marsh (Marsh B). Note that Marsh A has the larger area of the two marsh subdivisions as well as many more bathymetric features, e.g., tidal creeks, than Marsh B. In short, the DG finite element method is more mass conservative than the CG finite element method.

Large mass errors were found to occur in areas with large tidal prisms. In the analysis, tidal prisms were found to be influenced by the geometric characteristics of the domain. Subdivisions with the largest tidal prisms had large areas, volumes, and widths. These features give these subdivisions the ability to contain and transport larger amounts of water, and hence, they have larger tidal prisms. The marshes combined make up a significant portion of tidal prism in the Lower St. Johns River (11%). The northern marsh has larger tidal prism (9% of global) than the southern marsh (2% of global). Based on the results, both marshes play a role in the flow interaction between the river and marshes with the northern marsh being more tidally active than the southern marsh.

Tidal validation was performed for each of the finite element methods, i.e., CG and DG. This resulted in the validation of tides and tidal currents within 3% - 7% and 12% - 19% RMS error, respectively. Based on the RMS errors, the discontinuous Galerkin method was found to outperform the continuous Galerkin method. Water level and salinity was validated for the DG method. Phasing between observed and modeled water levels was captured more sufficiently compared to that of salinity with RMS errors of 6% - 48% and 22% - 2020%, respectively. The inclusion of additional forcings (i.e. wind forcings and river inflows), improved the capture of phase since the observed data used for the validation of water levels and salinity contains a full signal. It also aided in increasing accuracy during time periods greatly influenced by meteorological events (i.e. *Most Variable* with Hurricane Irene) and areas with less tidal influence (i.e. Buckman Bridge and Shands Bridge).

The discontinuous Galerkin method demonstrated better mass conservation properties than the continuous Galerkin method. Therefore, it is then suggested that the discontinuous Galerkin finite element method be used for salinity transport modeling for the Lower St. Johns River. This thesis provides a foundation for future salinity transport modeling in the Lower St. Johns River by providing an extensive study on a mass conservative model that performs fairly well in the replication of tidally driven salinity.

APPENDIX A
STATION HISTORICAL SALINITY DATA

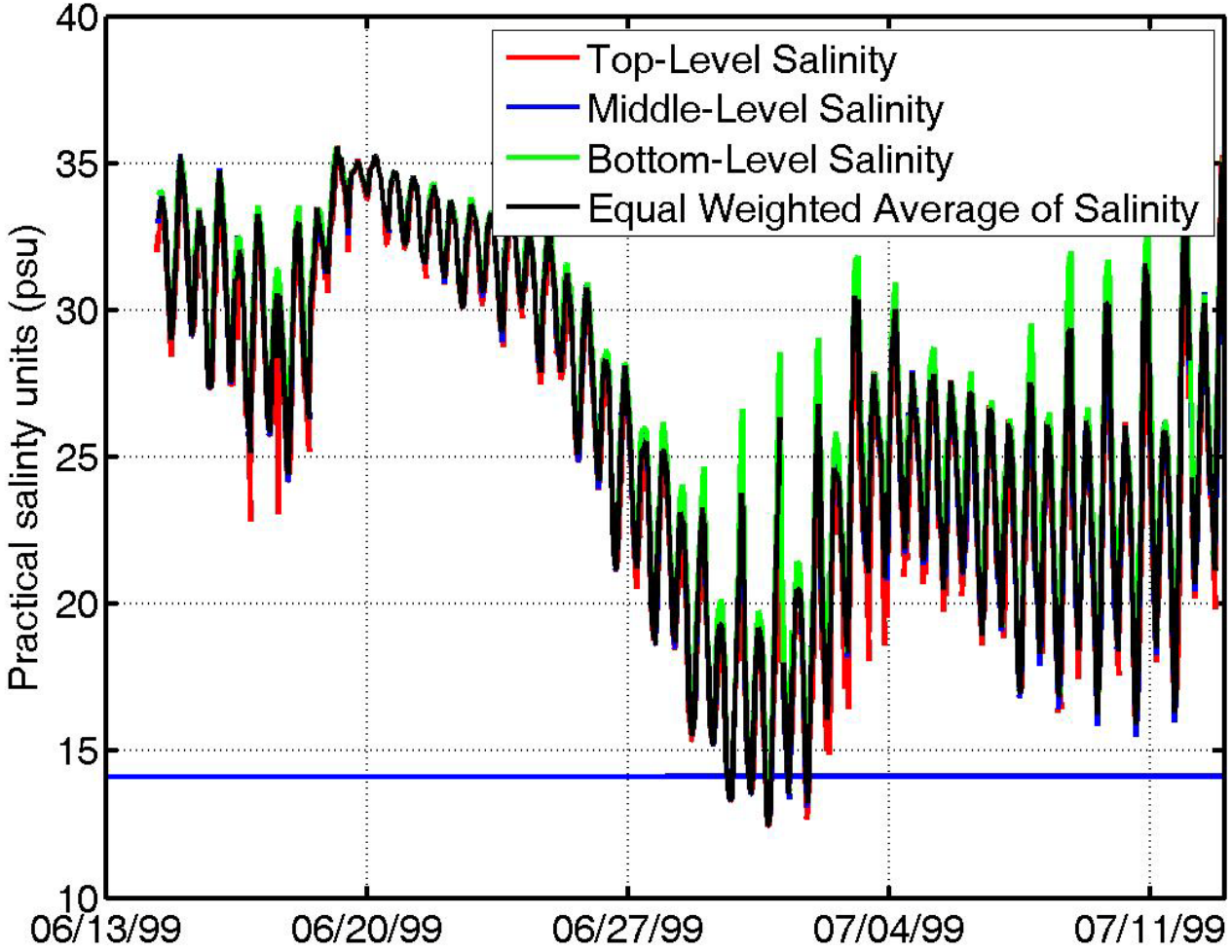

Figure A.1: Historical salinity data for Dames Point during *High Extreme* event.

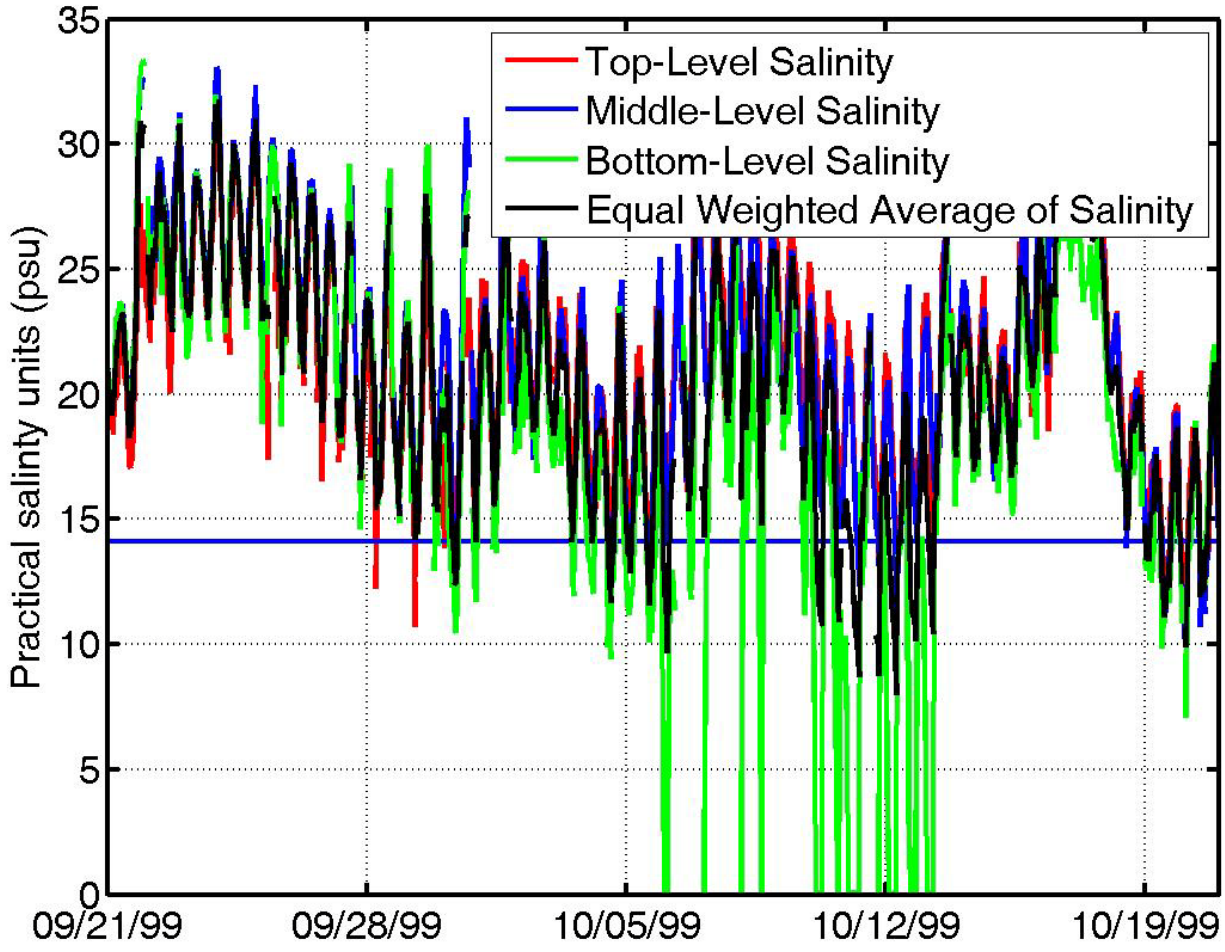

Figure A.2: Historical salinity data for Dames Point during the *Most Variable* event.

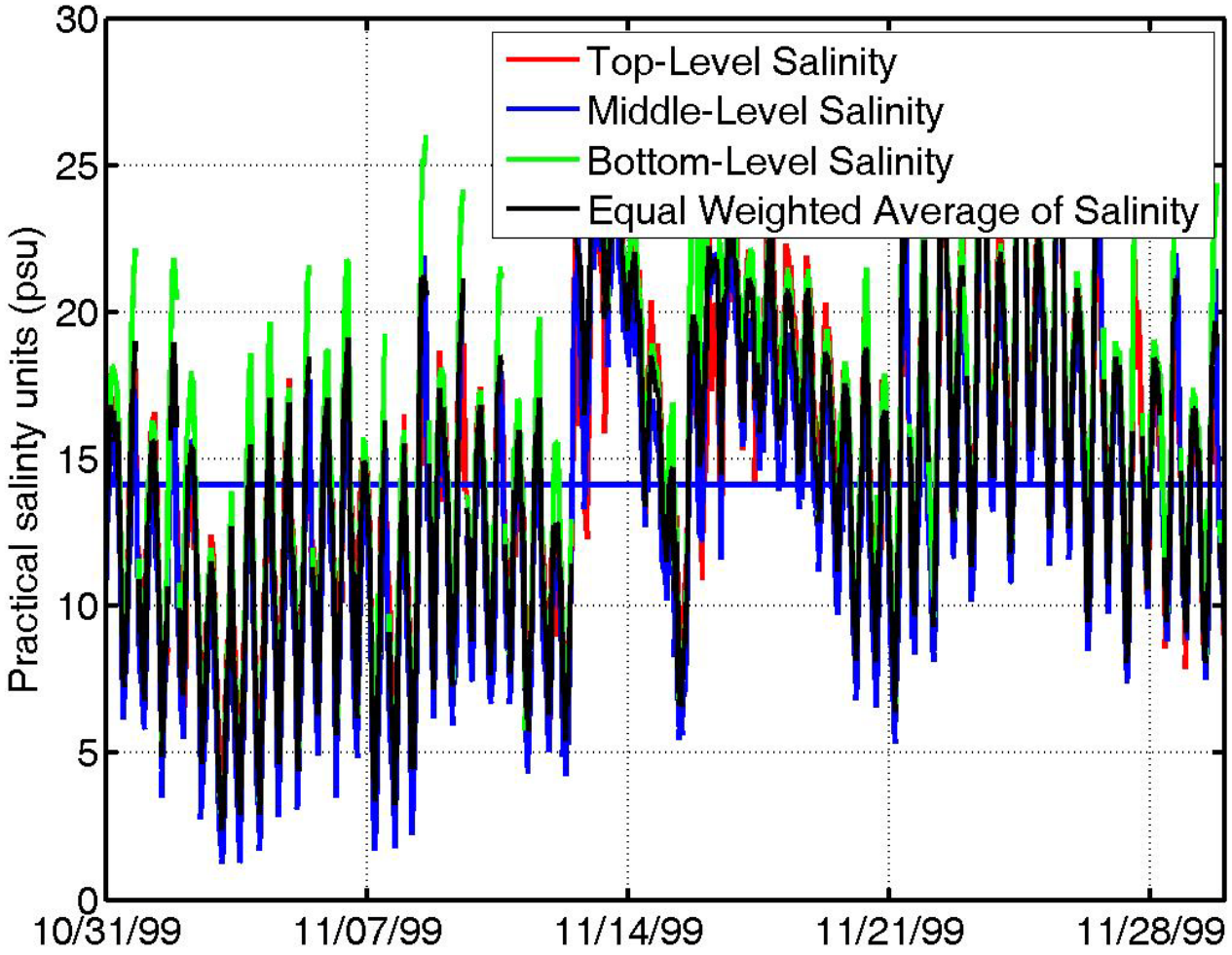

Figure A.3: Historical salinity data for Dames Point during the *Low Extreme* event.

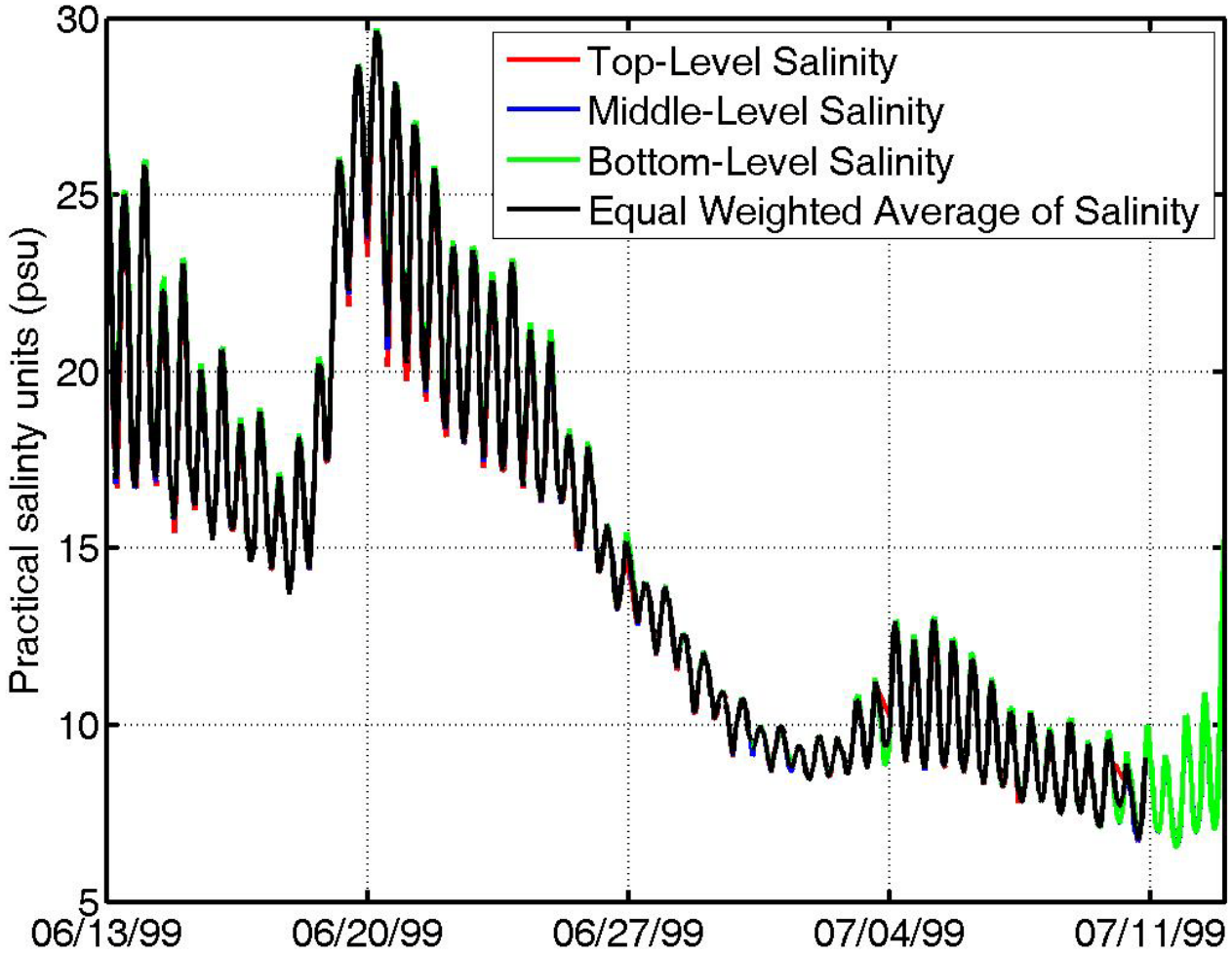

Figure A.4: Historical salinity data for Acosta Bridge during the *High Extreme* event.

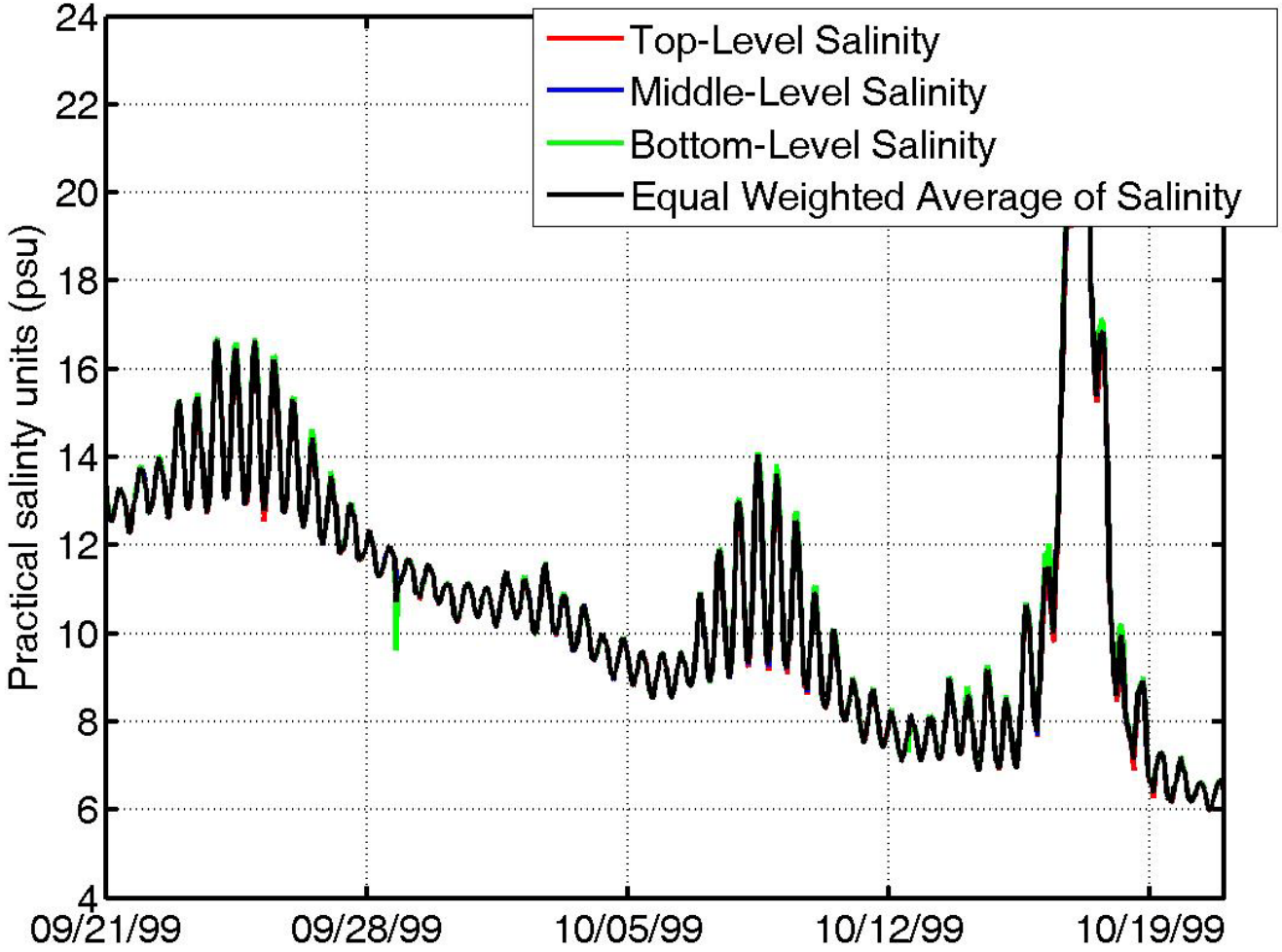

Figure A.5: Historical salinity data for Acosta Bridge during the *Most Variable* event.

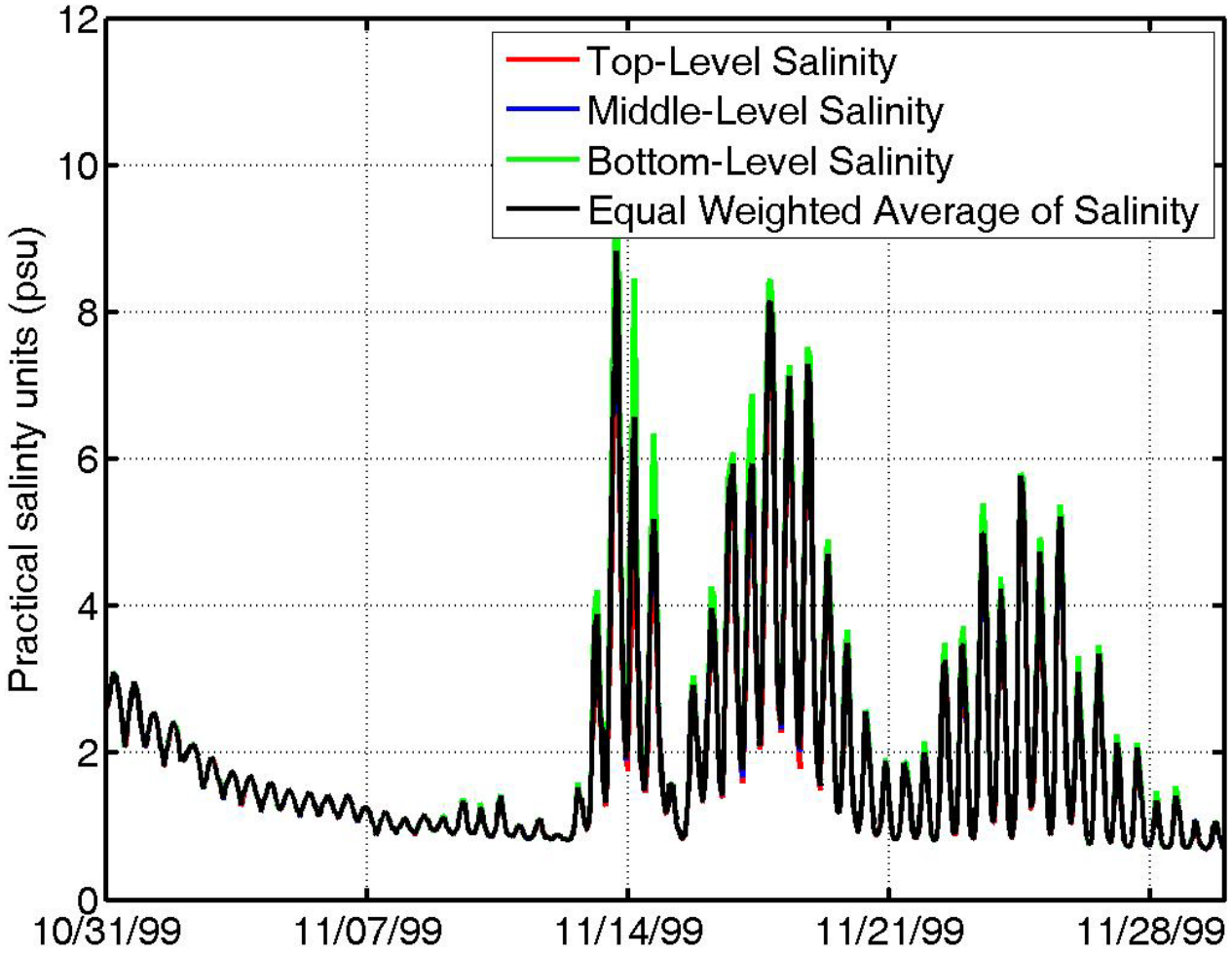

Figure A.6: Historical salinity data for Acosta Bridge during the *Low Extreme* event.

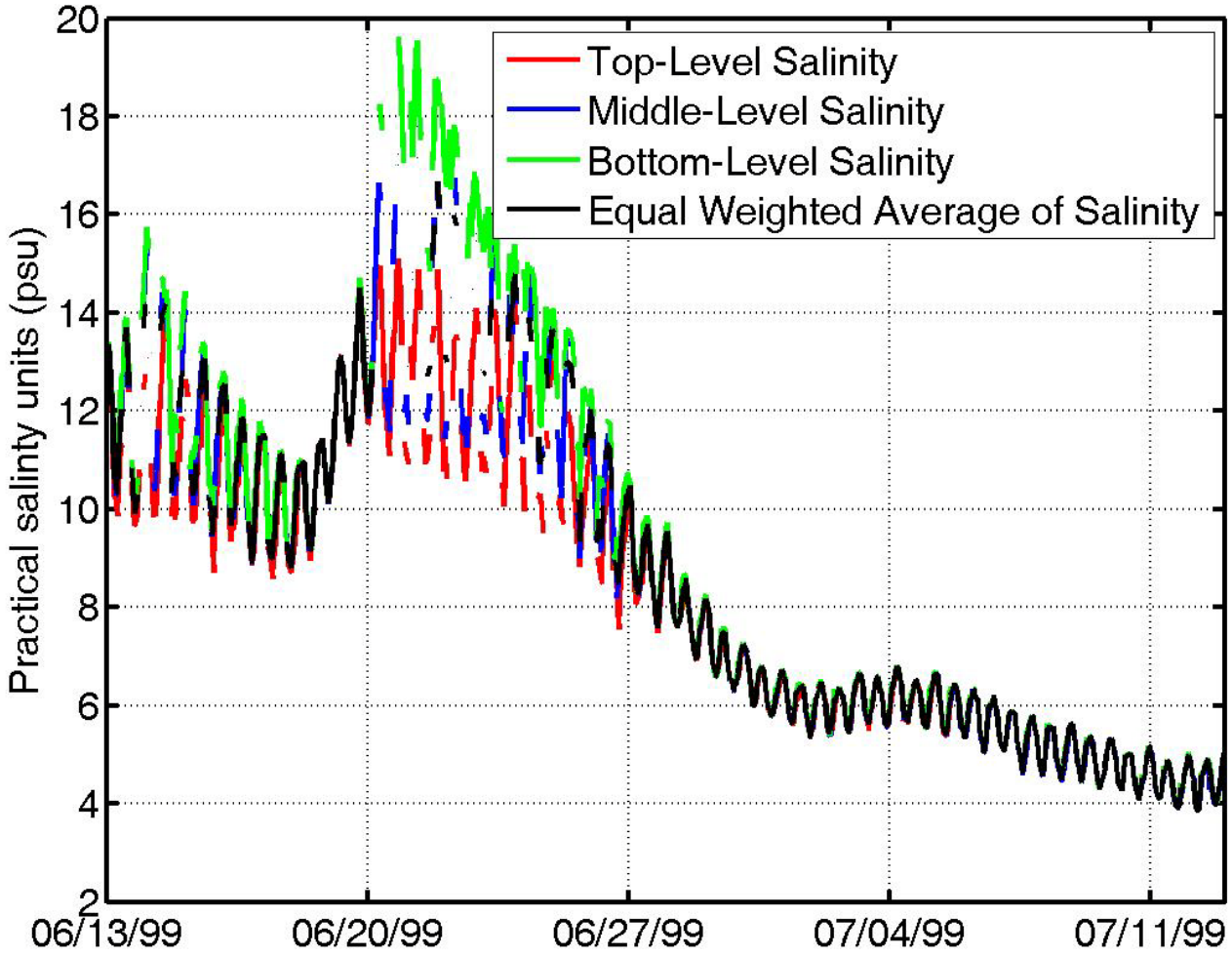

Figure A.7: Historical salinity data for Buckman Bridge during the *High Extreme* event.

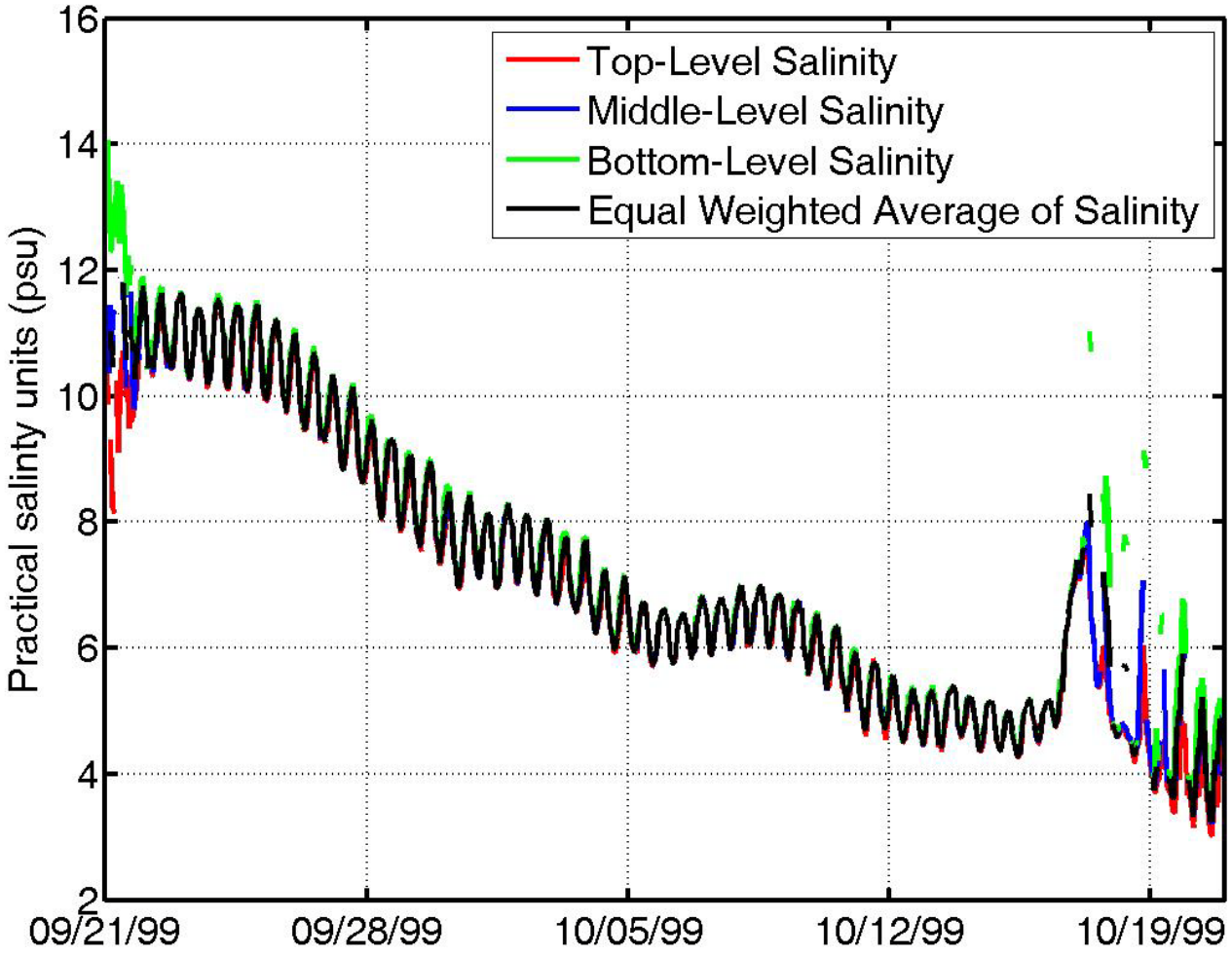

Figure A.8: Historical salinity data for Buckman Bridge during the *Most Variable* event.

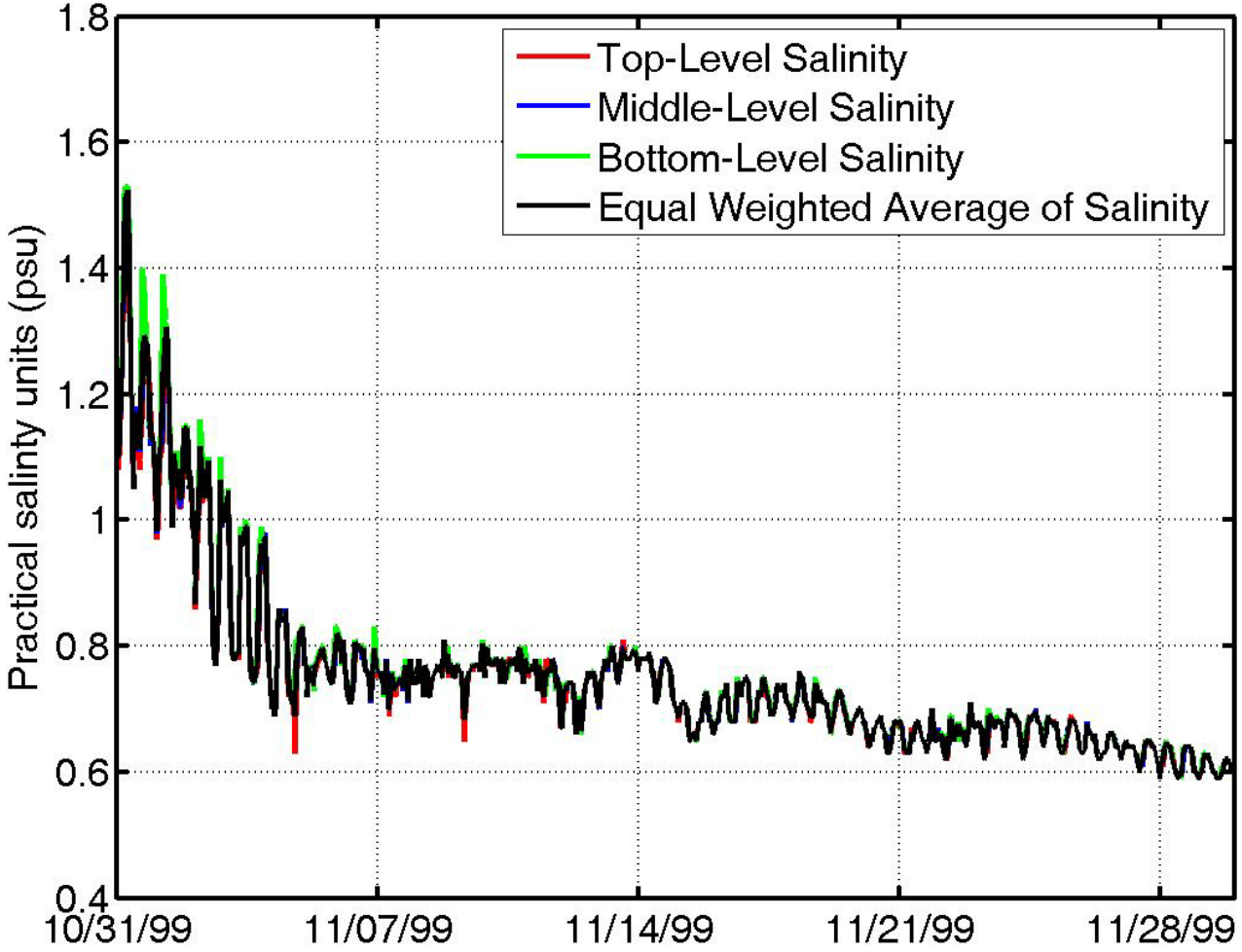

Figure A.9: Historical salinity data for Buckman Bridge during the *Low Extreme* event.

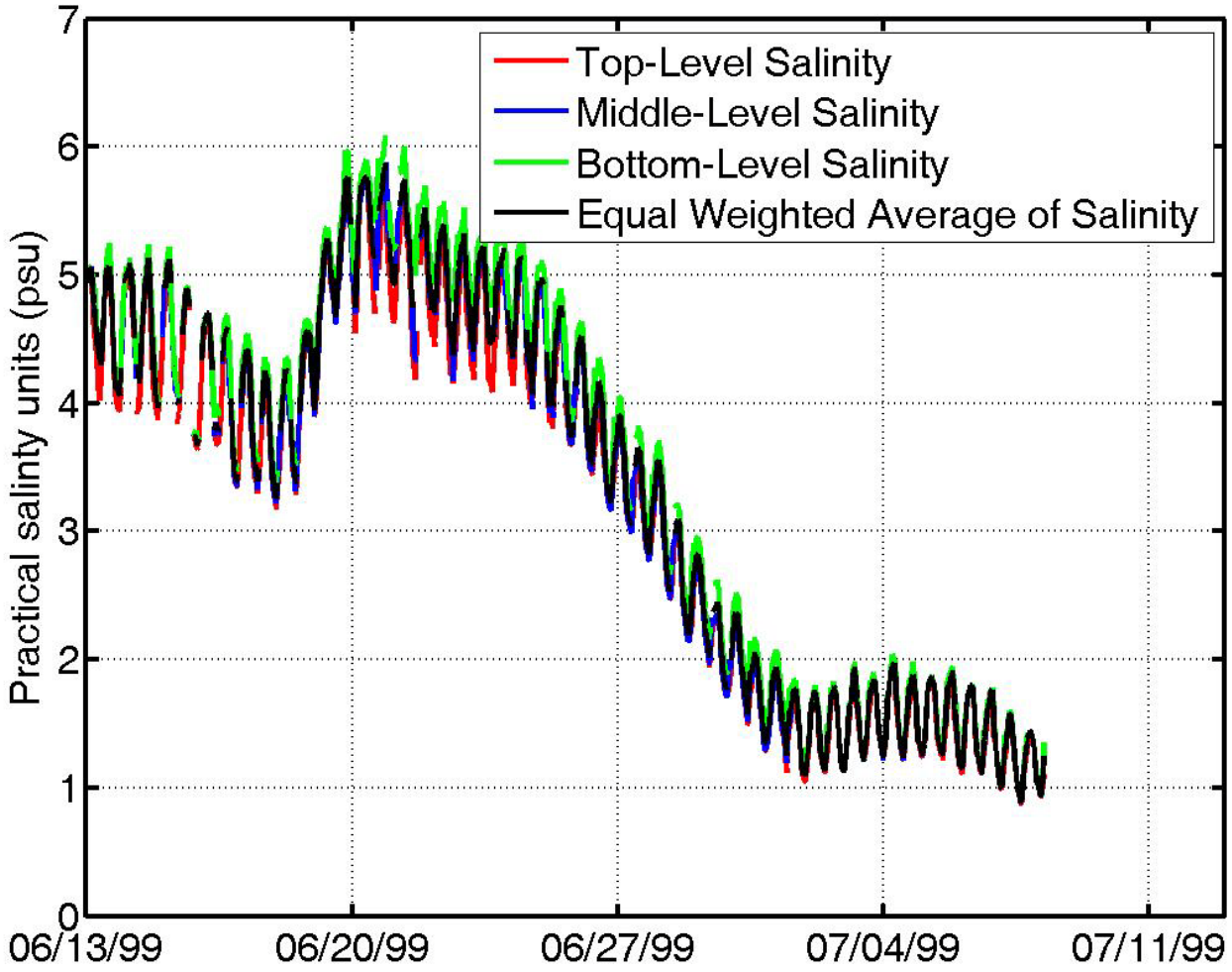

Figure A.10: Historical salinity data for Shands Bridge during the *High Extreme* event.

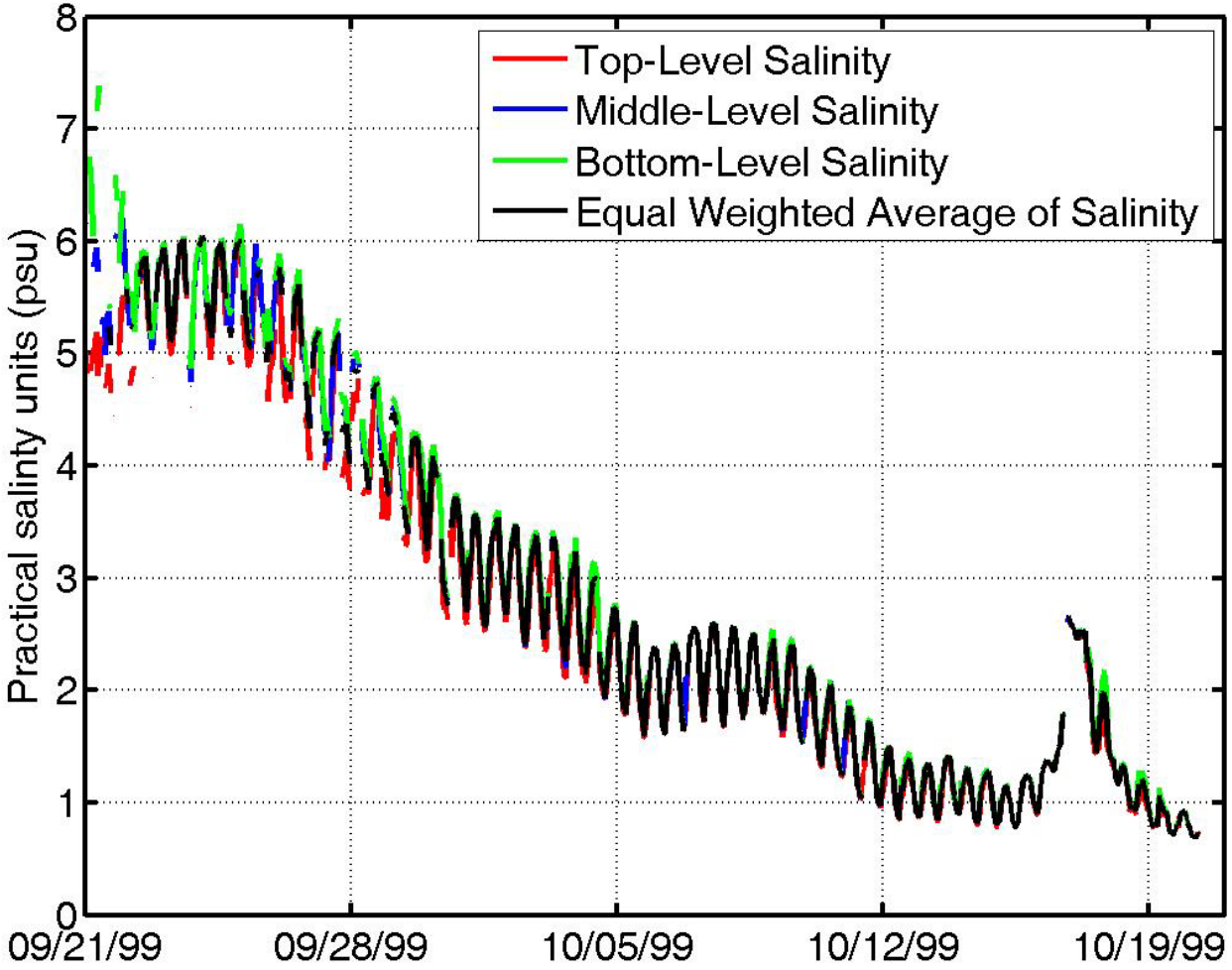

Figure A.11: Historical salinity data for Shands Bridge during the *Most Variable* event.

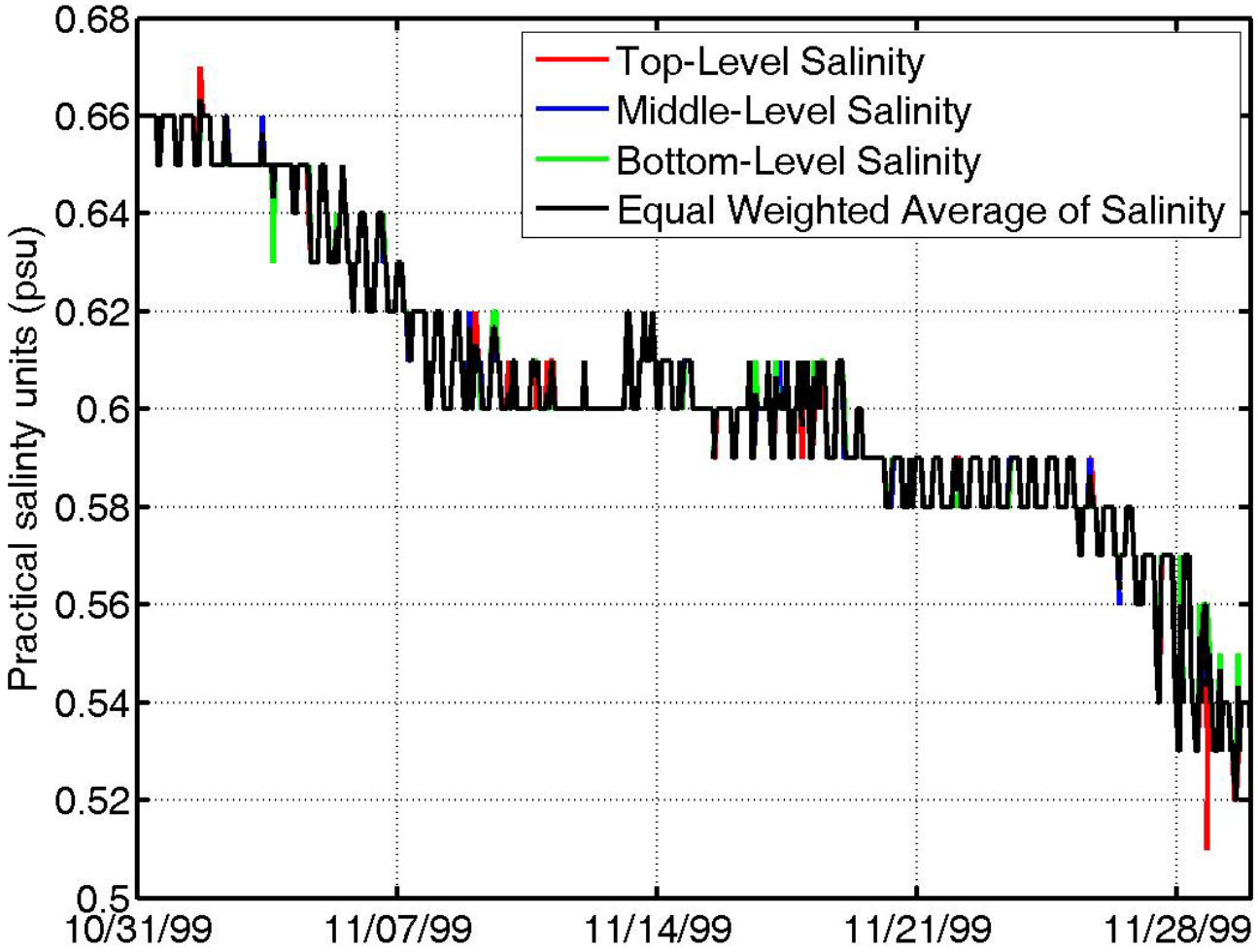

Figure A.12: Historical salinity data for Shands Bridge during the *Low Extreme* event.

APPENDIX B
TIDAL RESYNTHESIS PLOTS

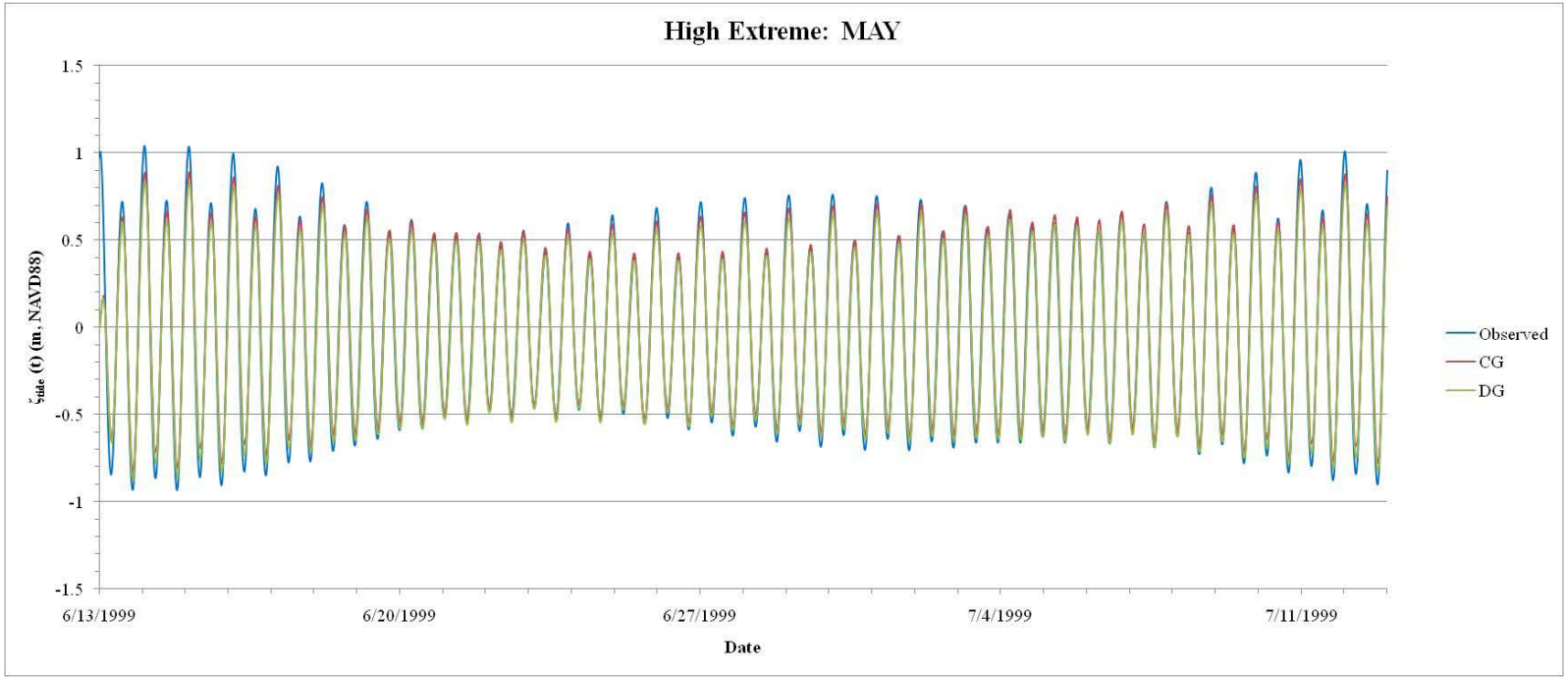

Figure B.1: Tidal resysnthesis for the MAY station during the *High Extreme* event. Water surface elevation levels were based on the NAVD88 datum.

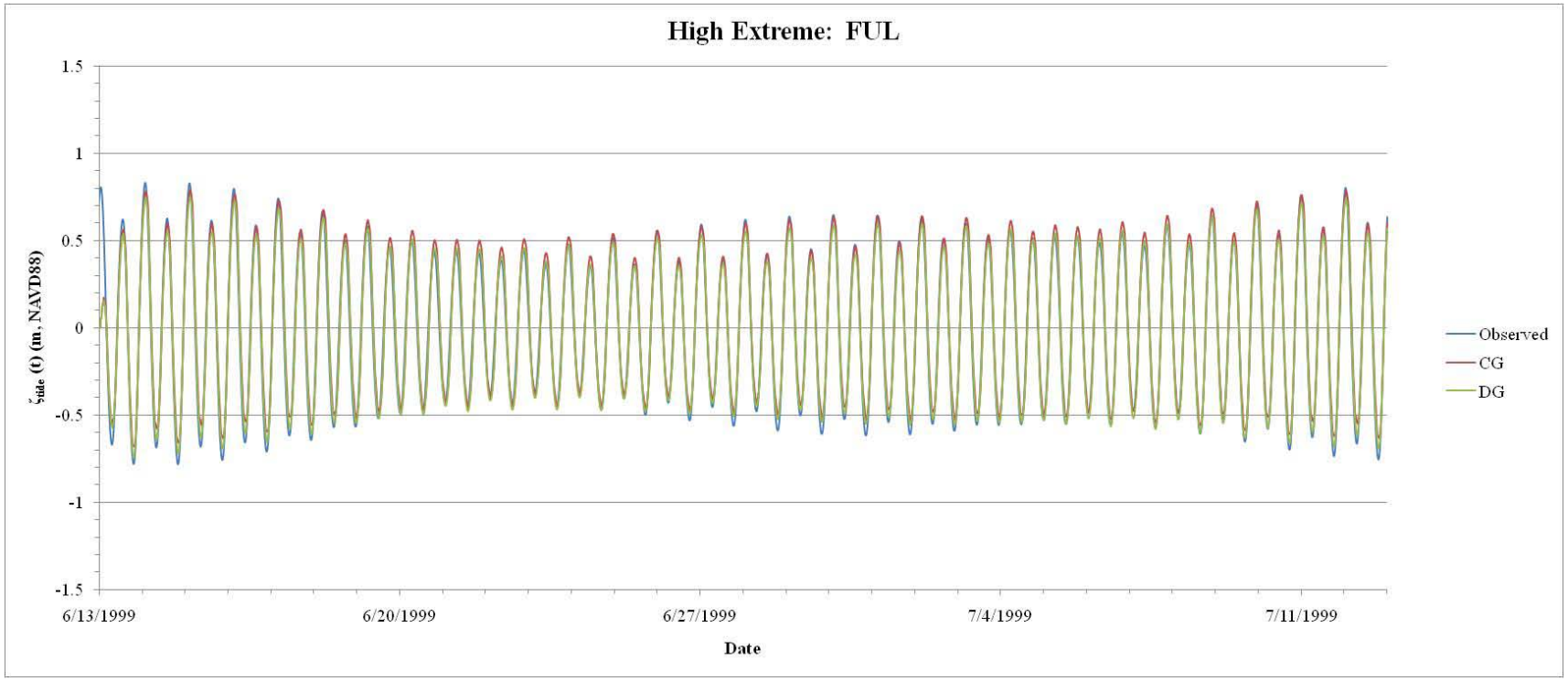

Figure B.2: Tidal resysnthesis for the FUL station during the *High Extreme* event. Water surface elevation levels were based on the NAVD88 datum.

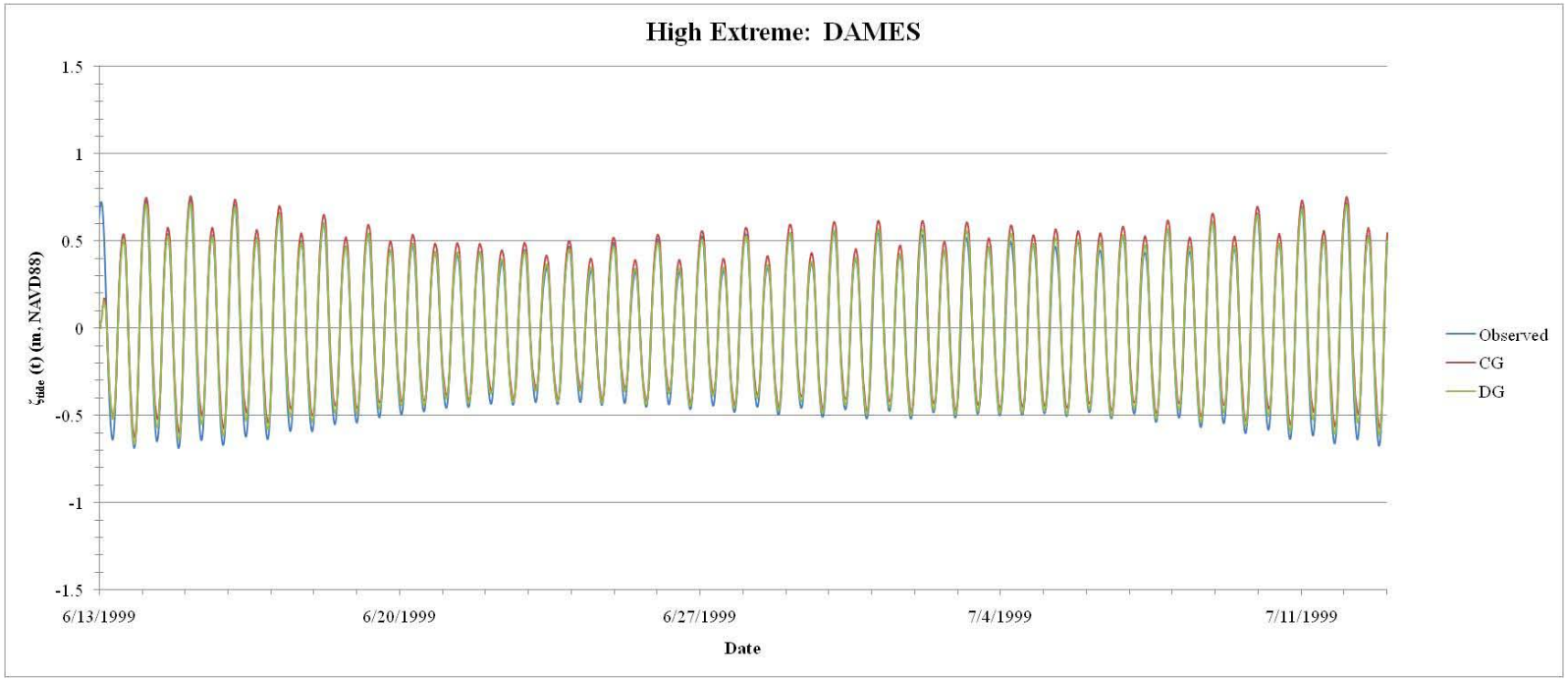

Figure B.3: Tidal resysnthesis for the DAMES station during the *High Extreme* event. Water surface elevation levels were based on the NAVD88 datum.

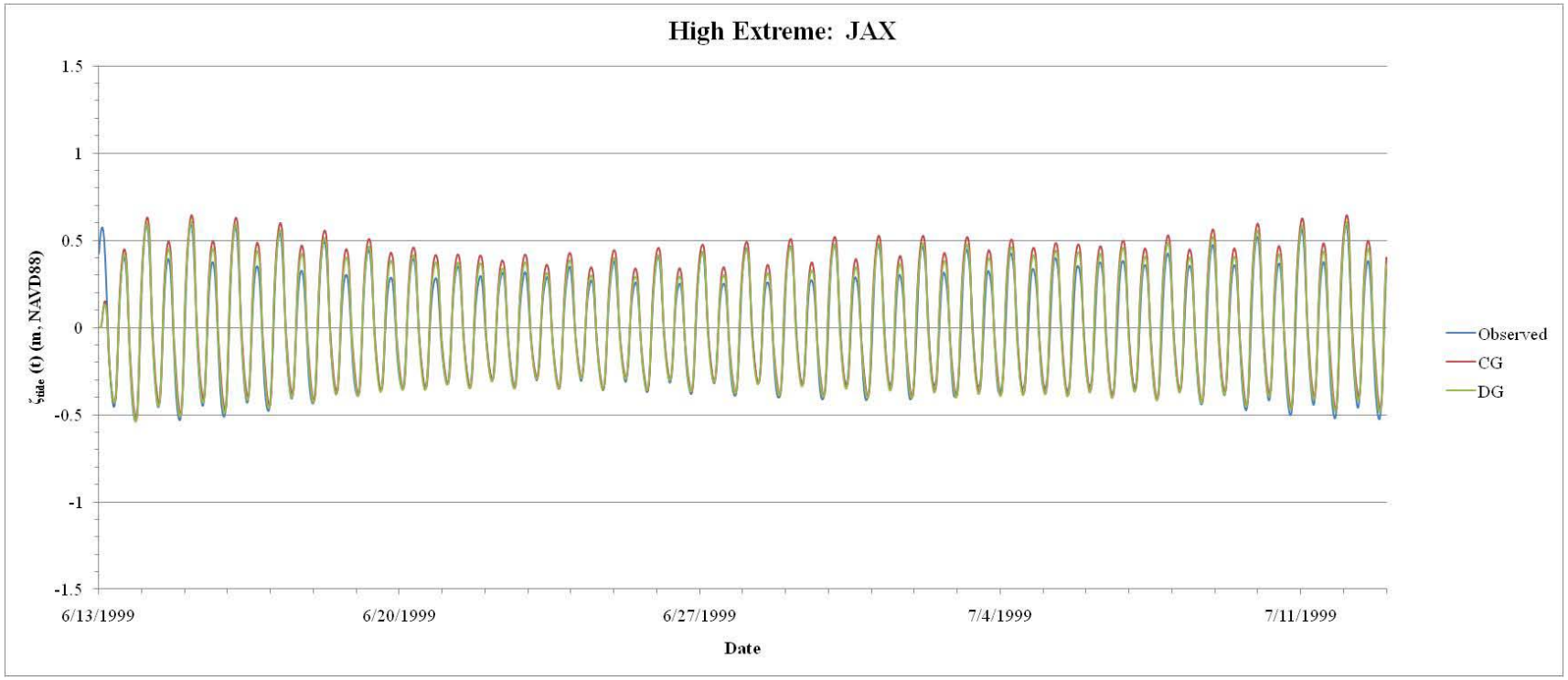

Figure B.4: Tidal resysnthesis for the JAX station during the *High Extreme* event. Water surface elevation levels were based on the NAVD88 datum.

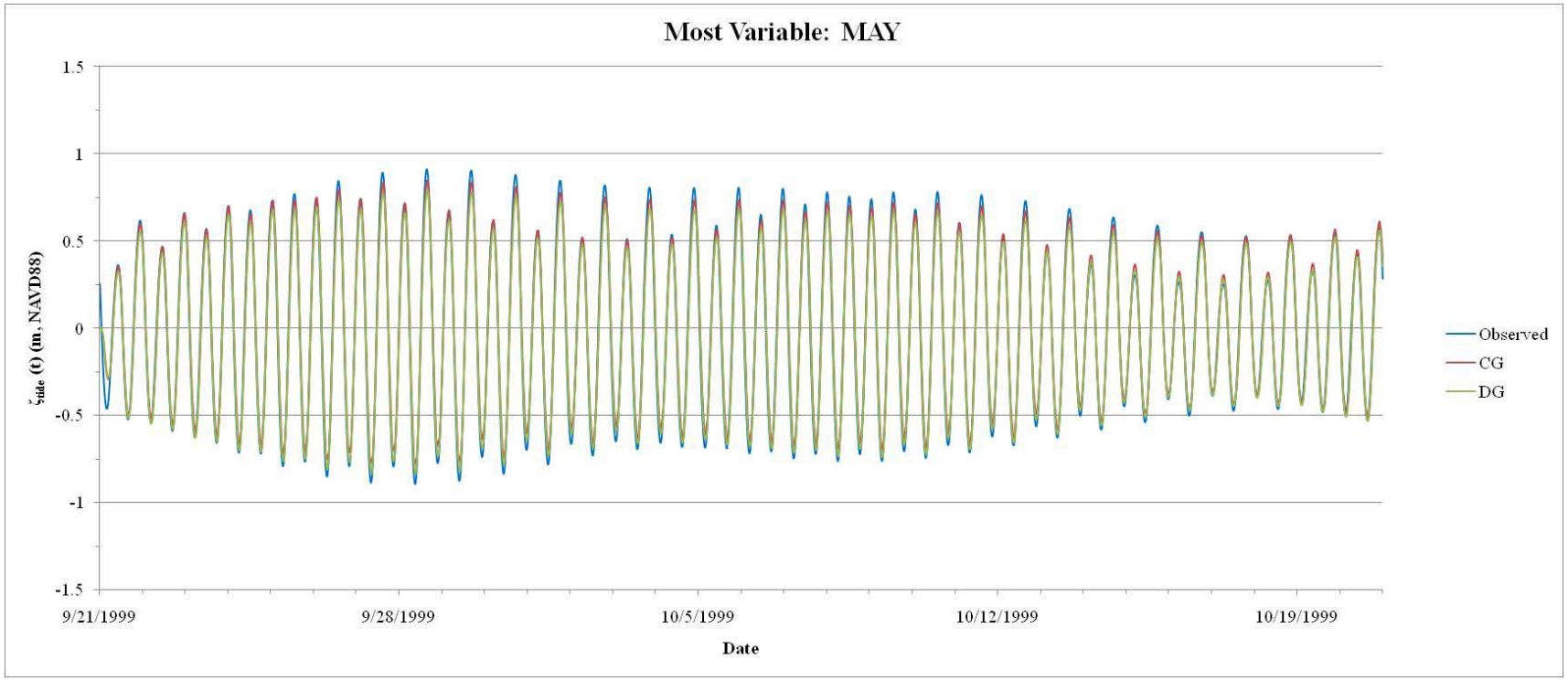

Figure B.5: Tidal resysnthesis for the MAY station during the *Most Variable* event. Water surface elevation levels were based on the NAVD88 datum.

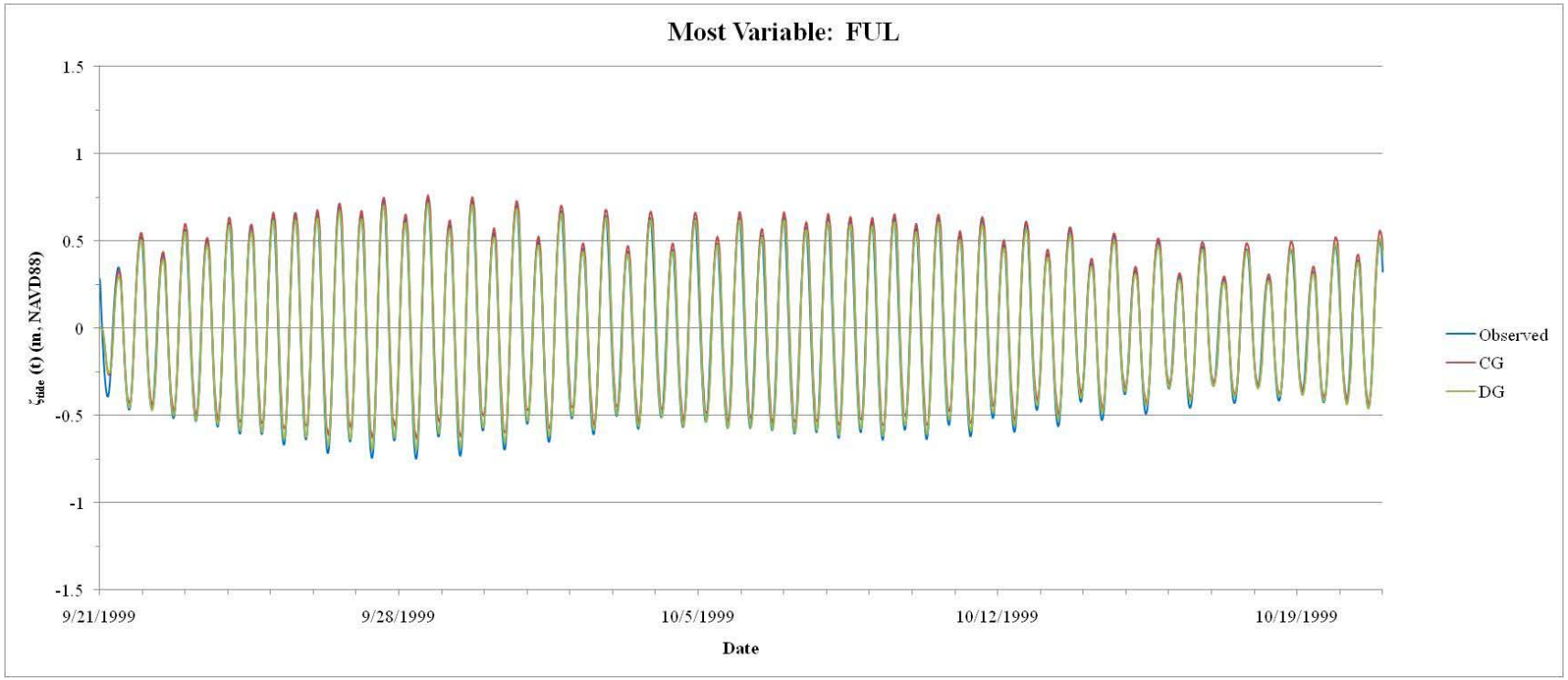

Figure B.6: Tidal resysnthesis for the FUL station during the *Most Variable* event. Water surface elevation levels were based on the NAVD88 datum.

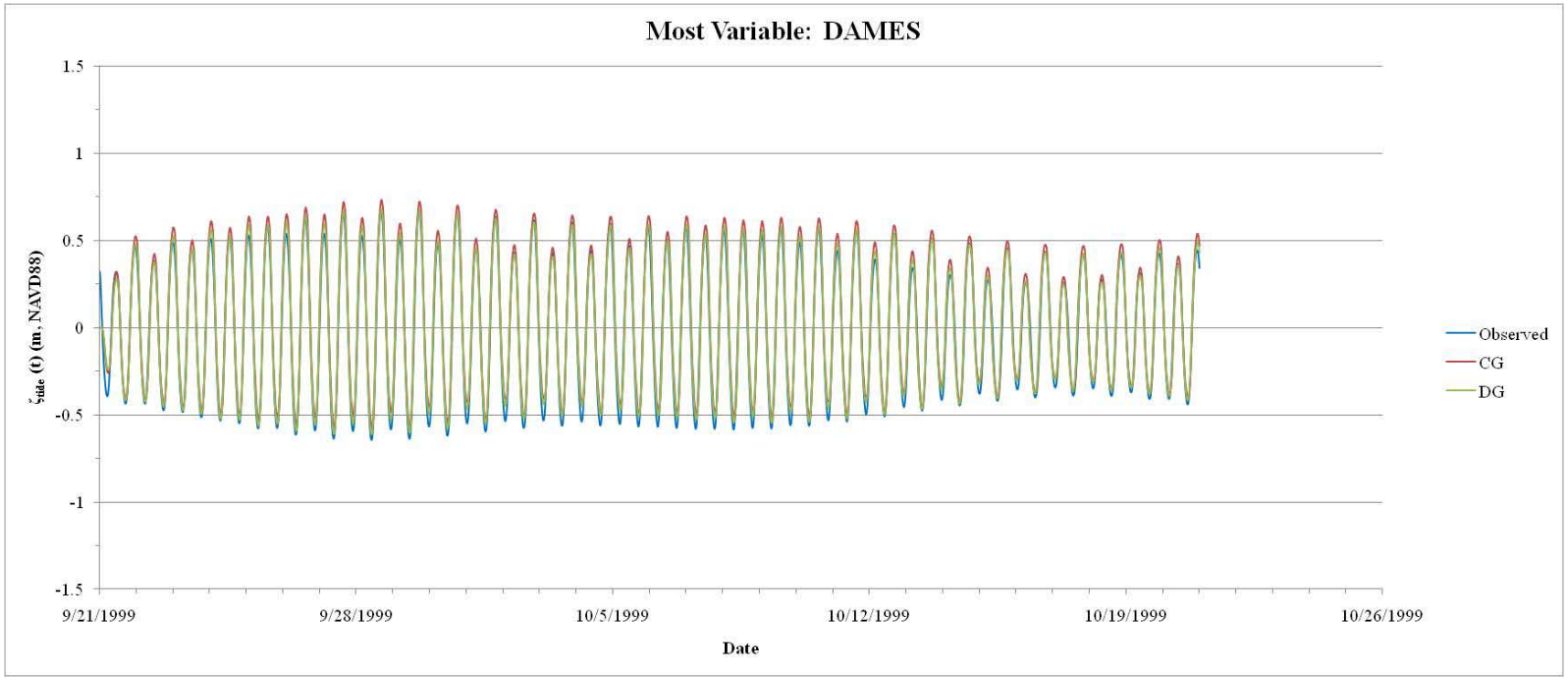

Figure B.7: Tidal resysnthesis for the DAMES station during the *Most Variable* event. Water surface elevation levels were based on the NAVD88 datum.

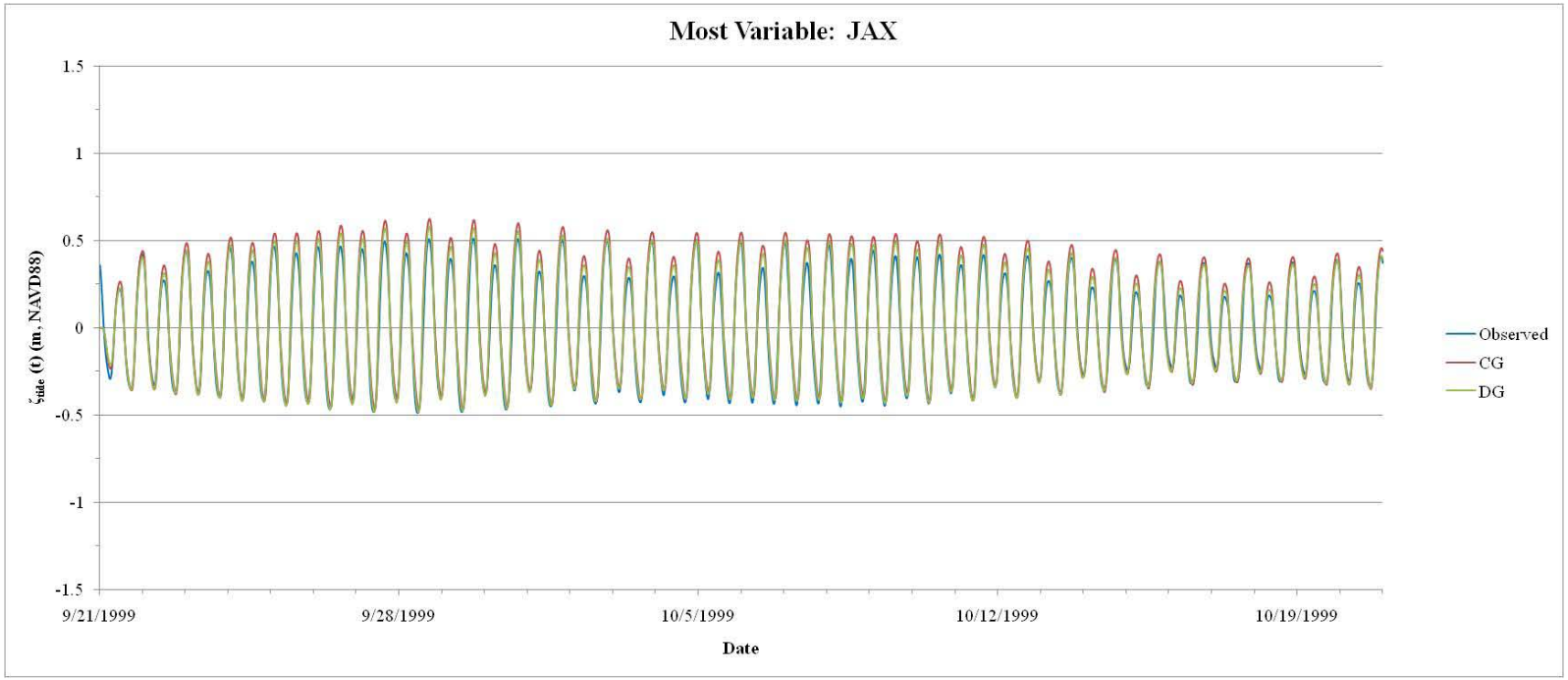

Figure B.8: Tidal resysnthesis for the JAX station during the *Most Variable* event. Water surface elevation levels were based on the NAVD88 datum.

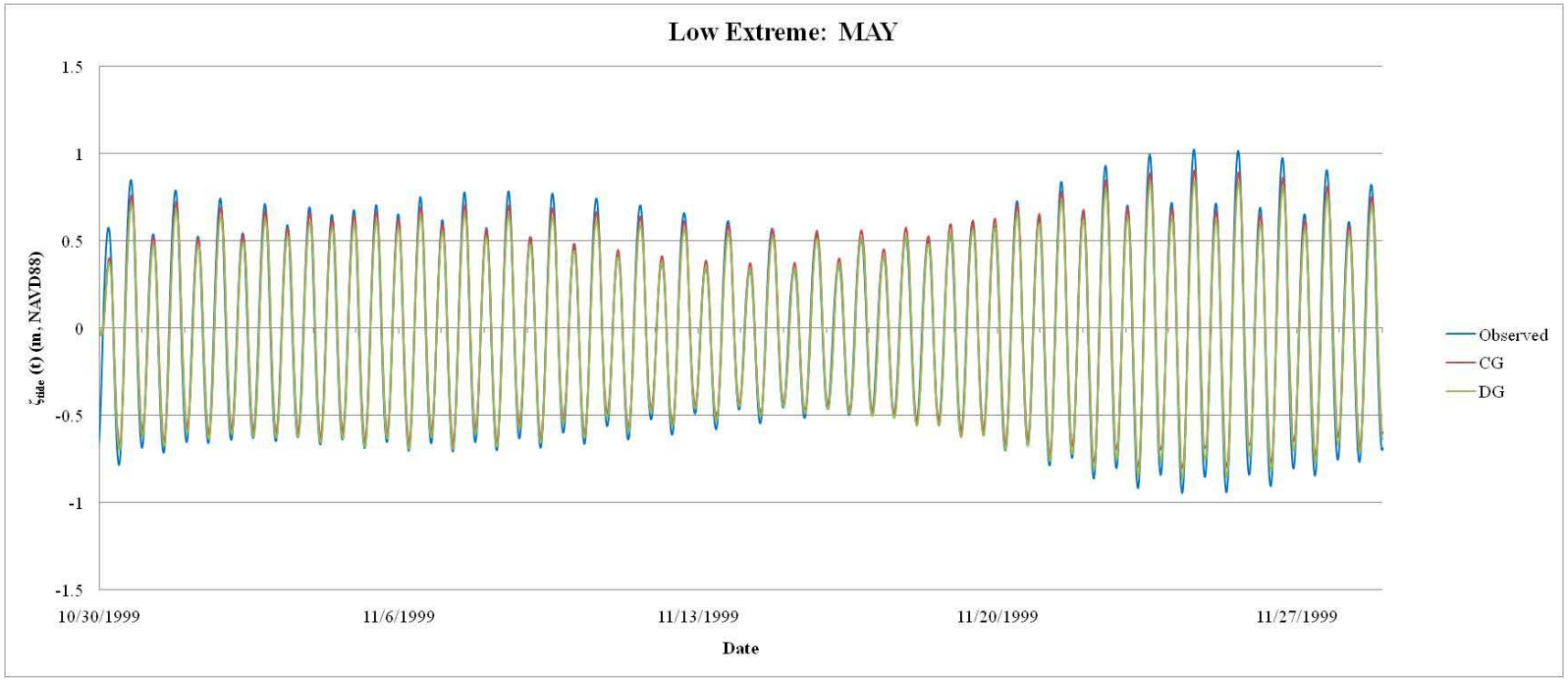

Figure B.9: Tidal resysnthesis for the MAY station during the *Low Extreme* event. Water surface elevation levels were based on the NAVD88 datum.

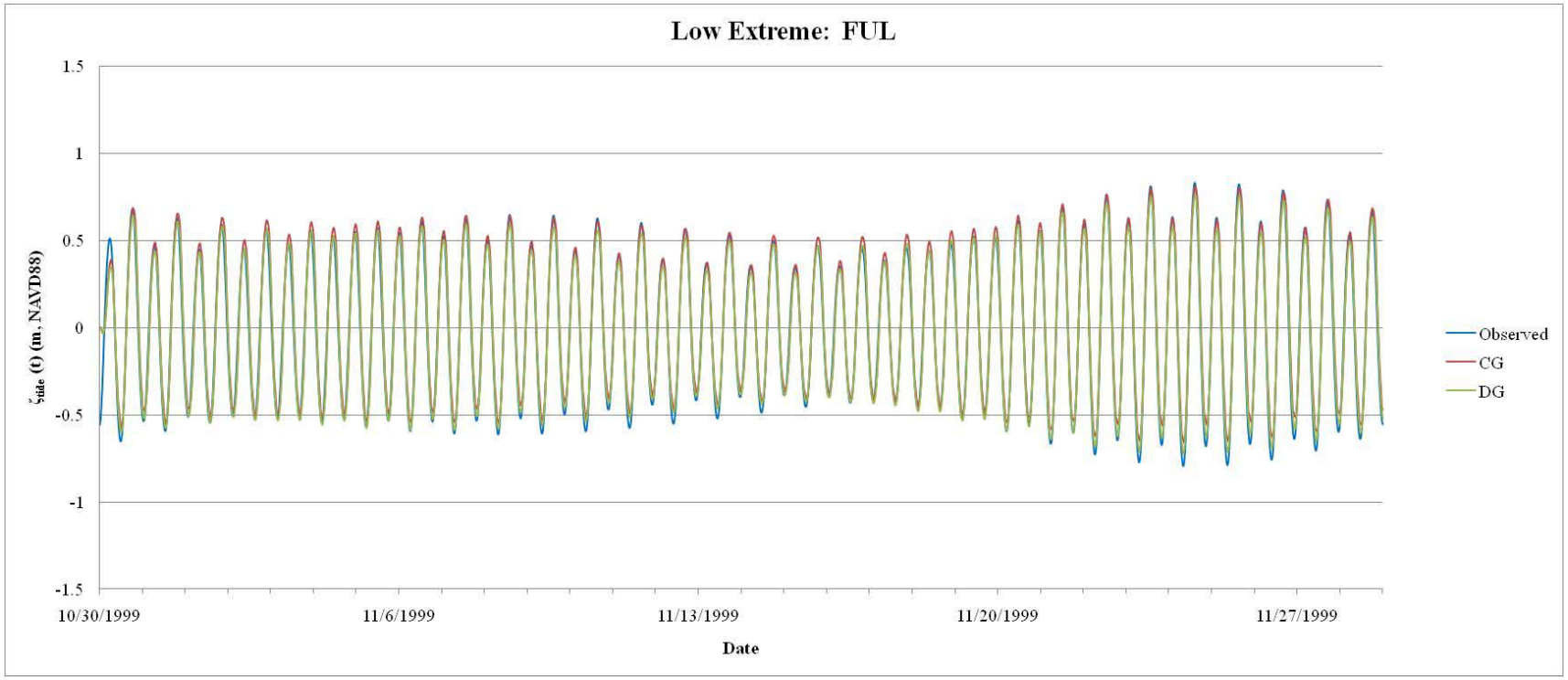

Figure B.10: Tidal resysnthesis for the FUL station during the *Low Extreme* event. Water surface elevation levels were based on the NAVD88 datum.

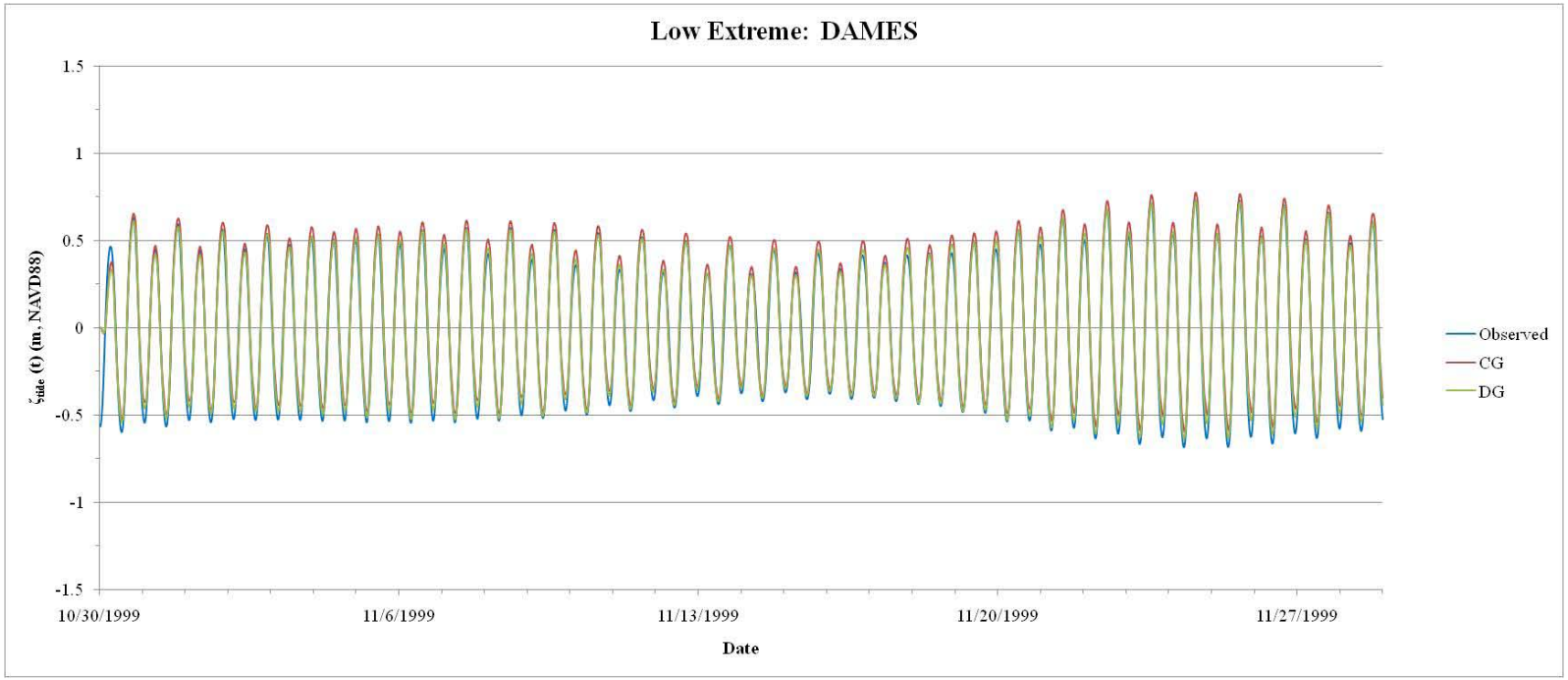

Figure B.11: Tidal resysnthesis for the DAMES station during the *Low Extreme* event. Water surface elevation levels were based on the NAVD88 datum.

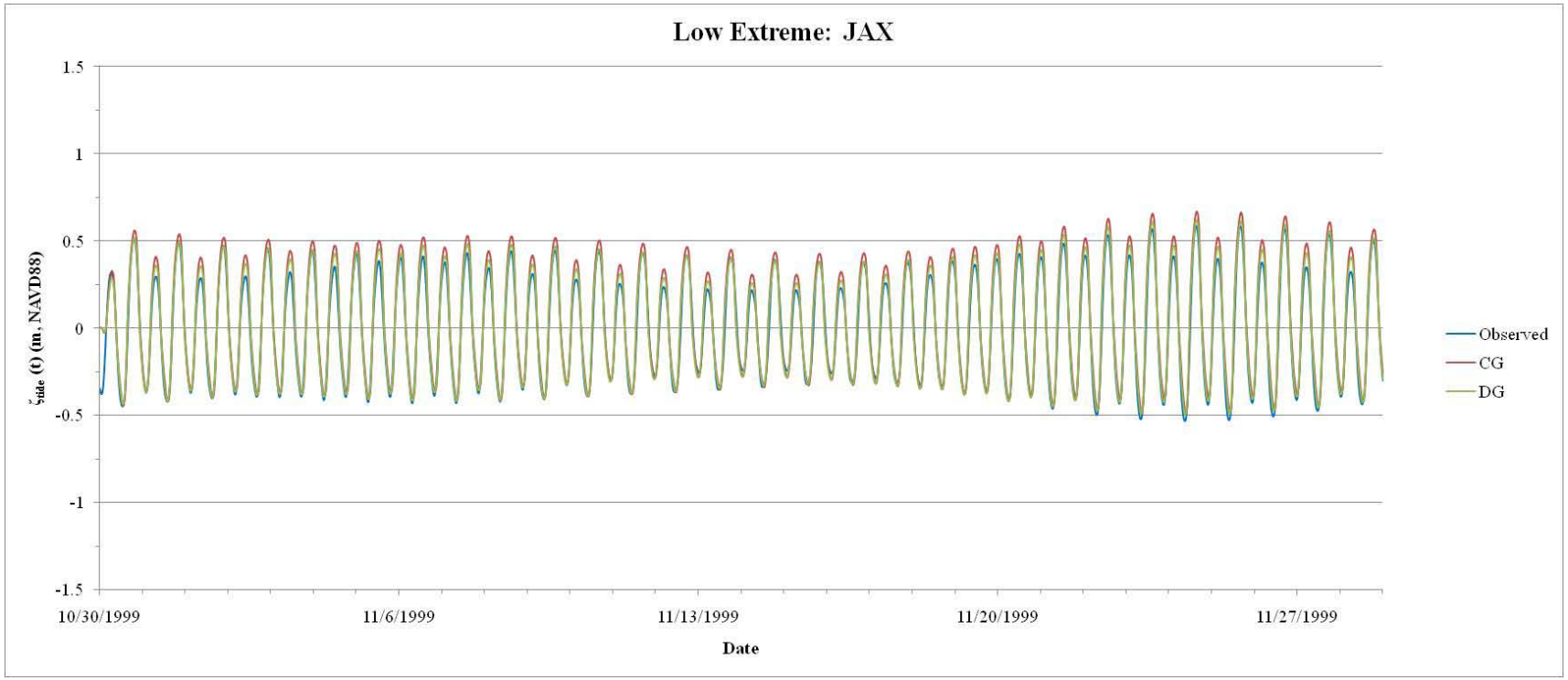

Figure B.12: Tidal resysnthesis for the JAX station during the *Low Extreme* event. Water surface elevation levels were based on the NAVD88 datum.

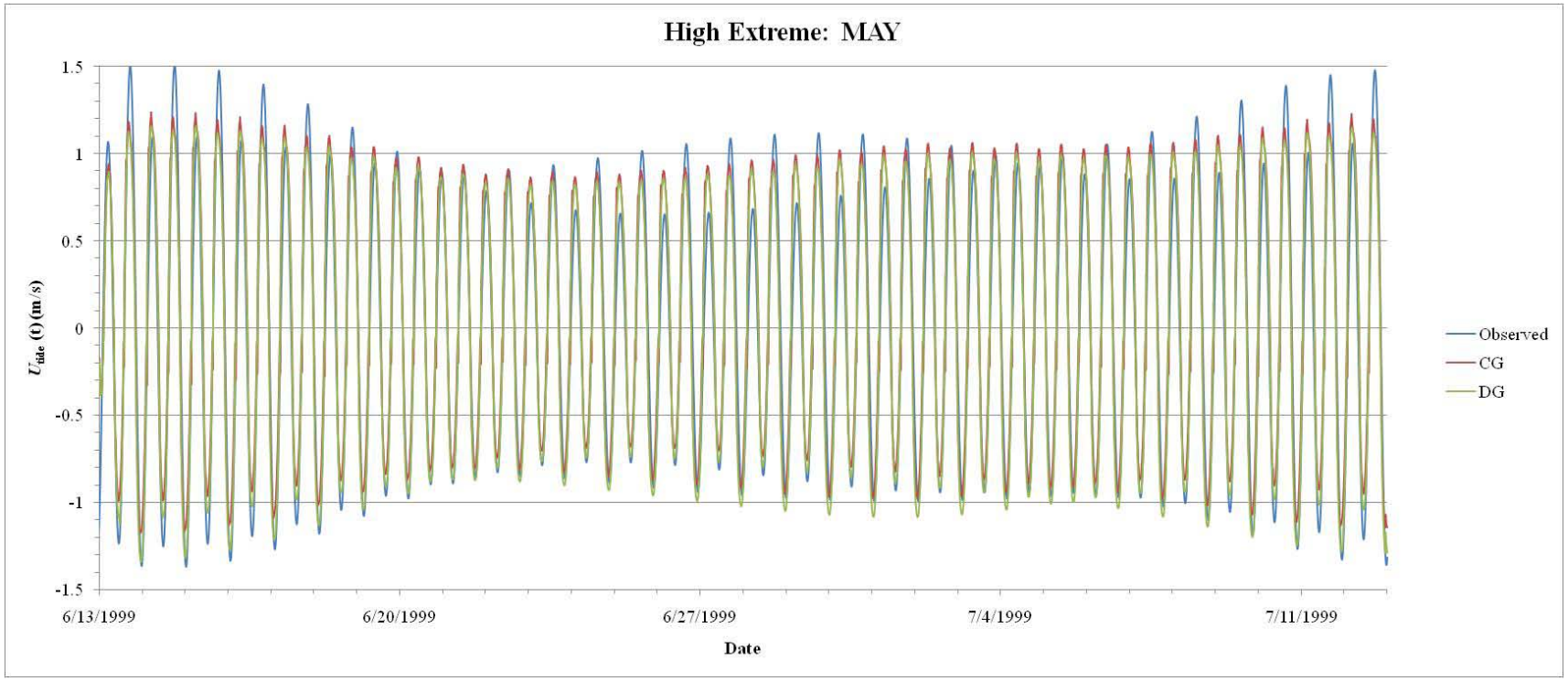

Figure B.13: Tidal resysnthesis of the along-channel (depth-integrated) velocity at the MAY station during the *High Extreme* event.

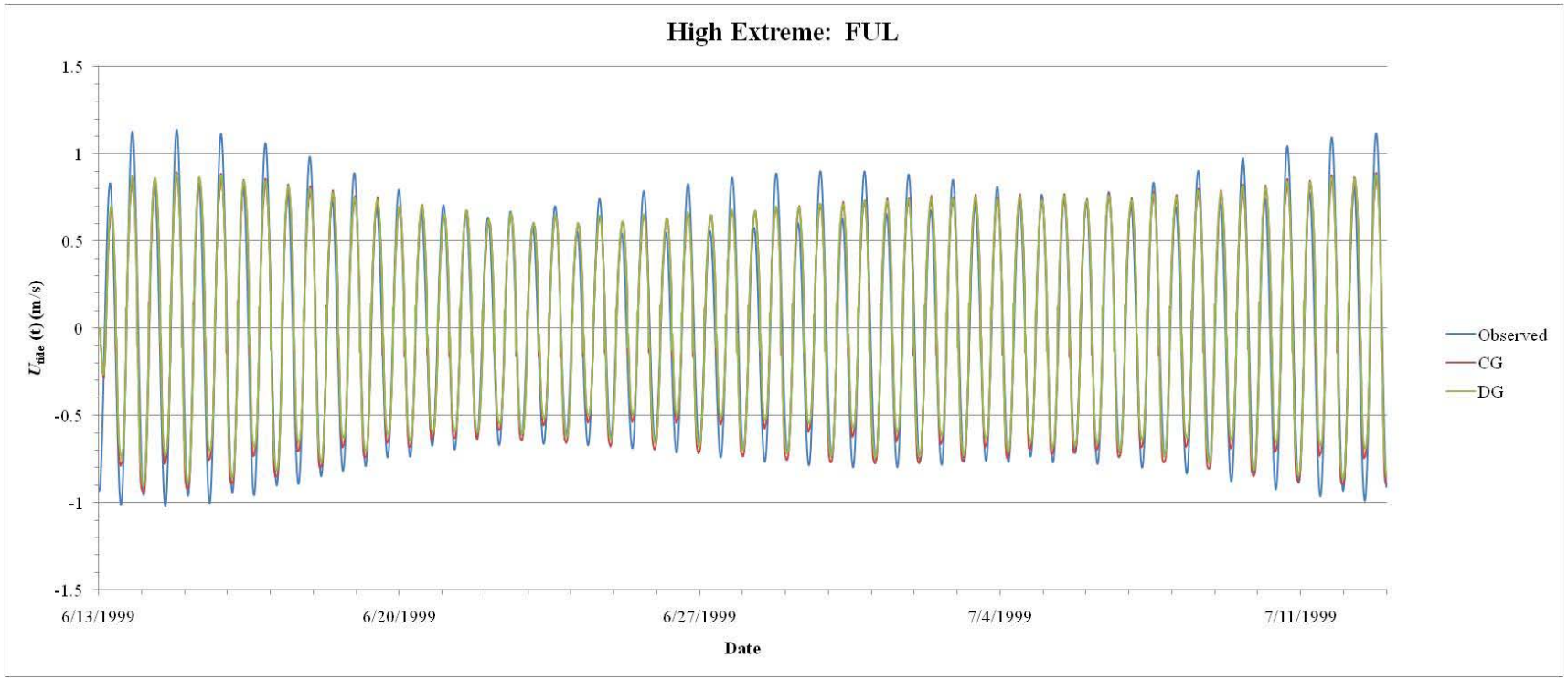

Figure B.14: Tidal resysnthesis of the along-channel (depth-integrated) velocity at the FUL station during the *High Extreme* event.

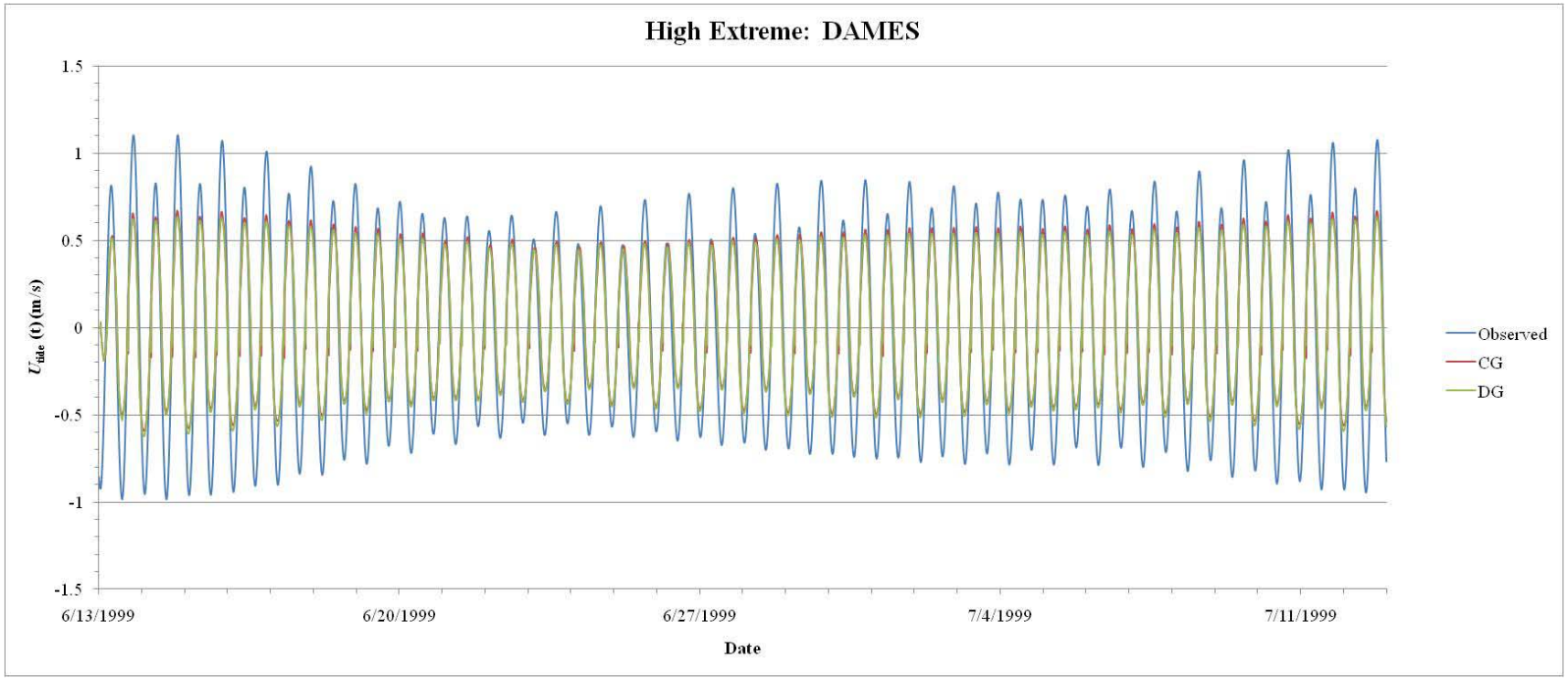

Figure B.15: Tidal resysnthesis of the along-channel (depth-integrated) velocity at the DAMES station during the *High Extreme* event.

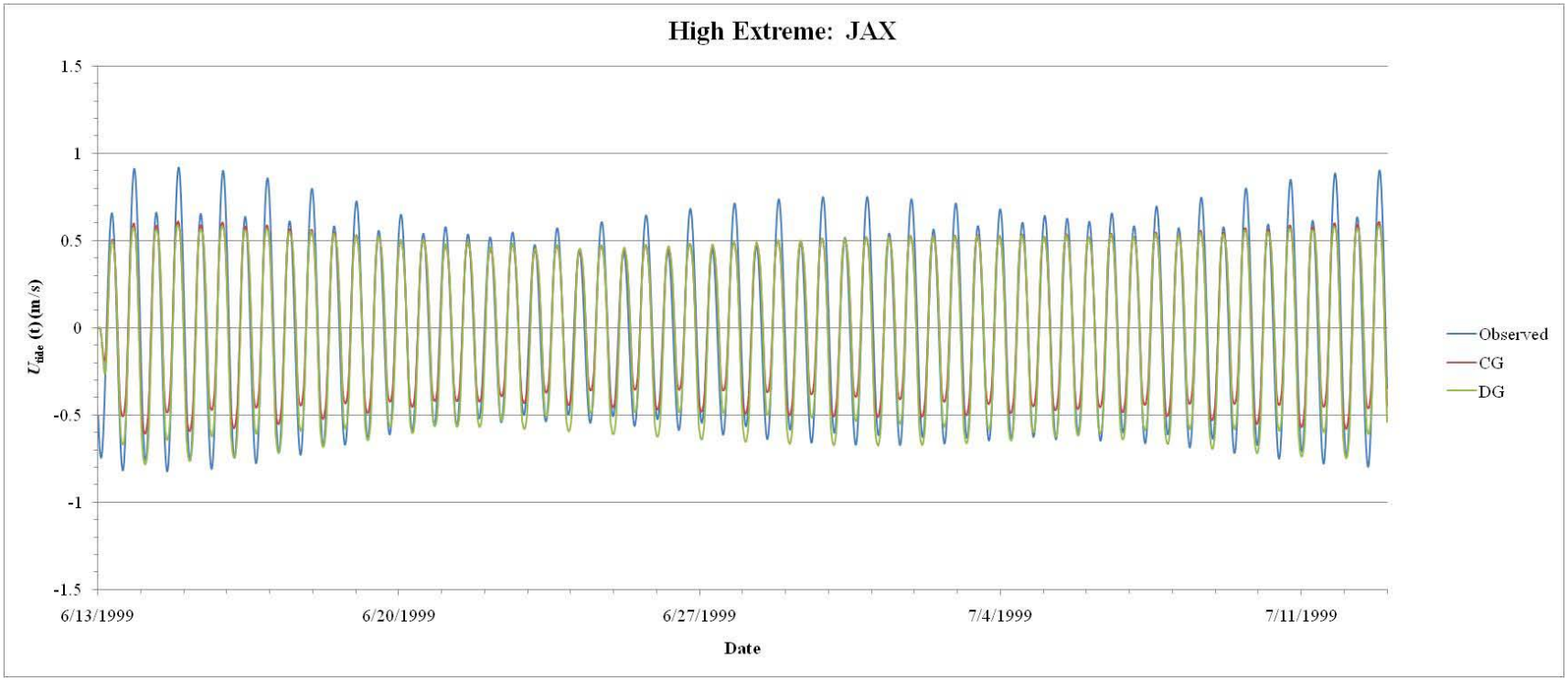

Figure B.16: Tidal resysnthesis of the along-channel (depth-integrated) velocity at the JAX station during the *High Extreme* event.

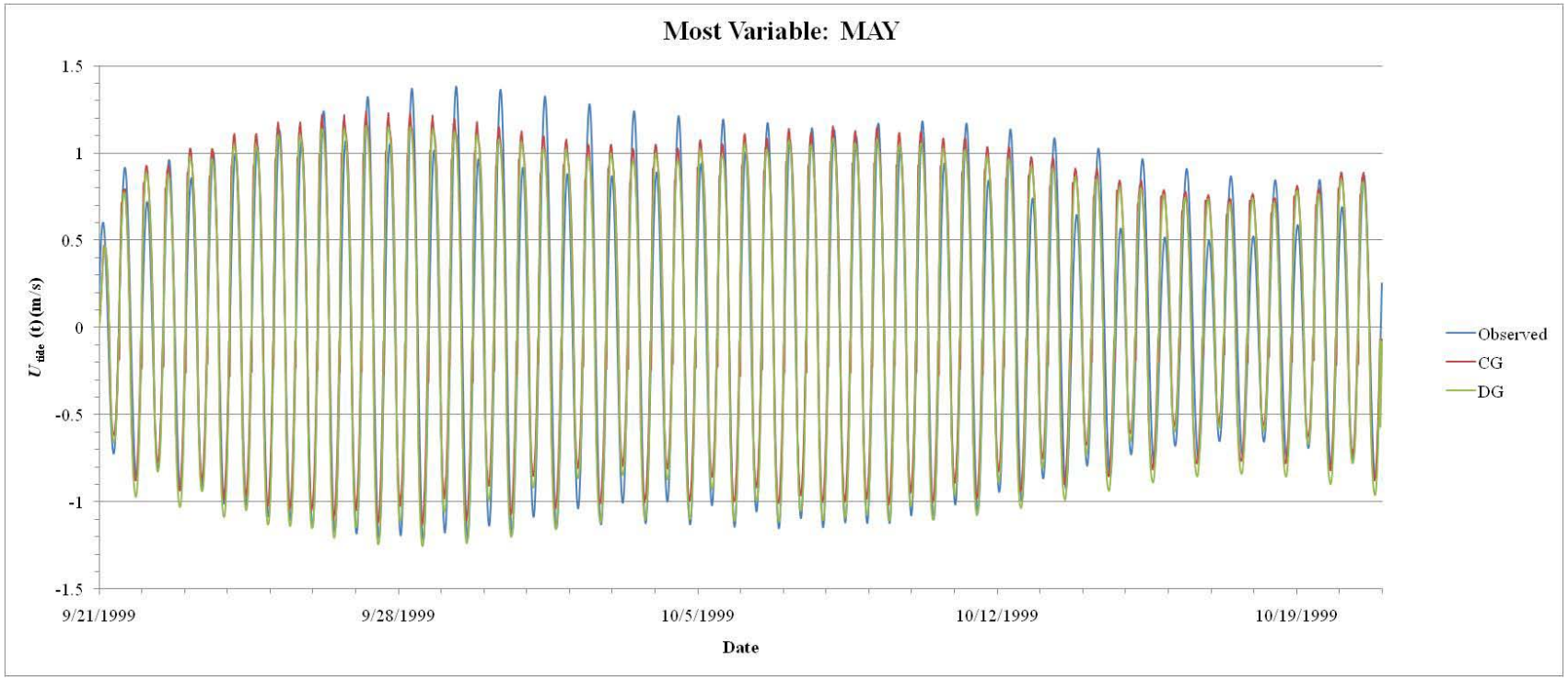

Figure B.17: Tidal resysnthesis of the along-channel (depth-integrated) velocity at the MAY station during the *Most Variable* event.

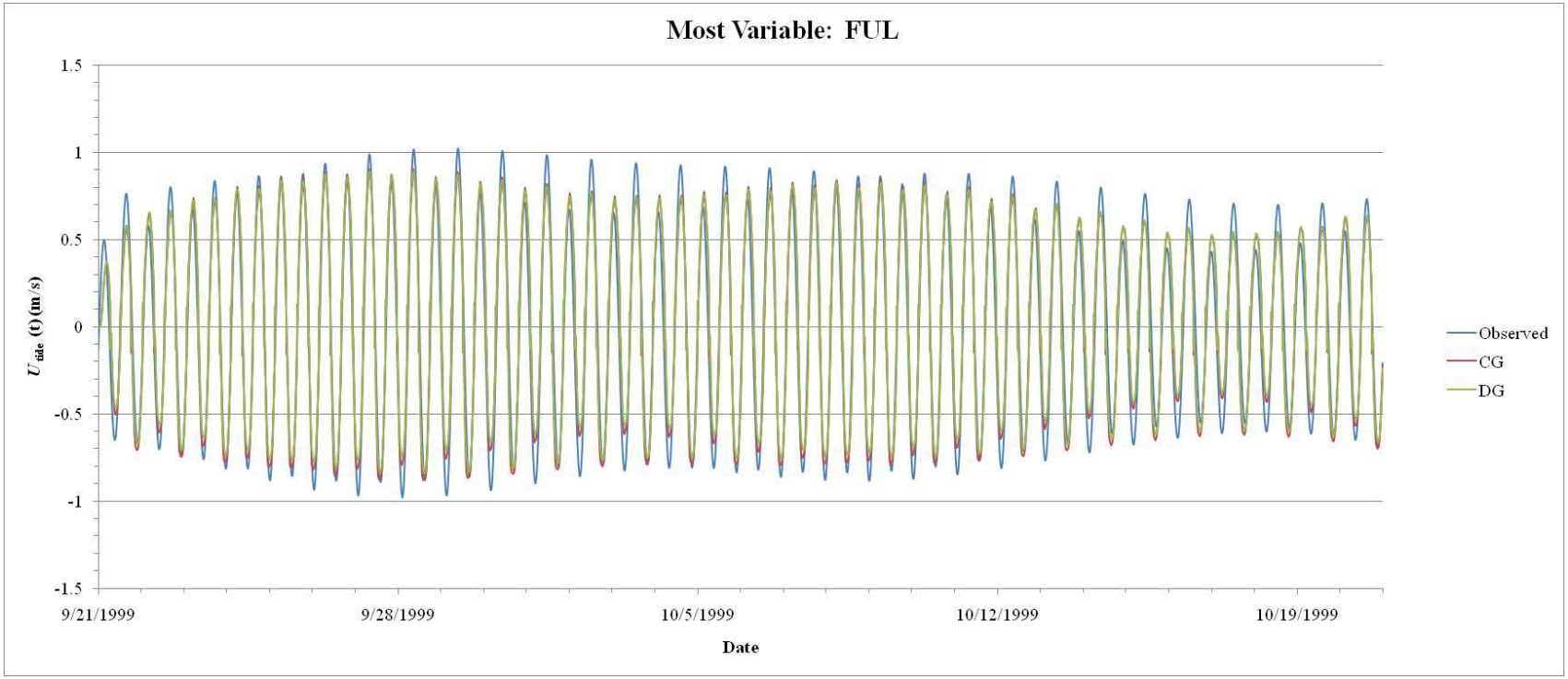

Figure B.18: Tidal resysnthesis of the along-channel (depth-integrated) velocity at the FUL station during the *Most Variable* event.

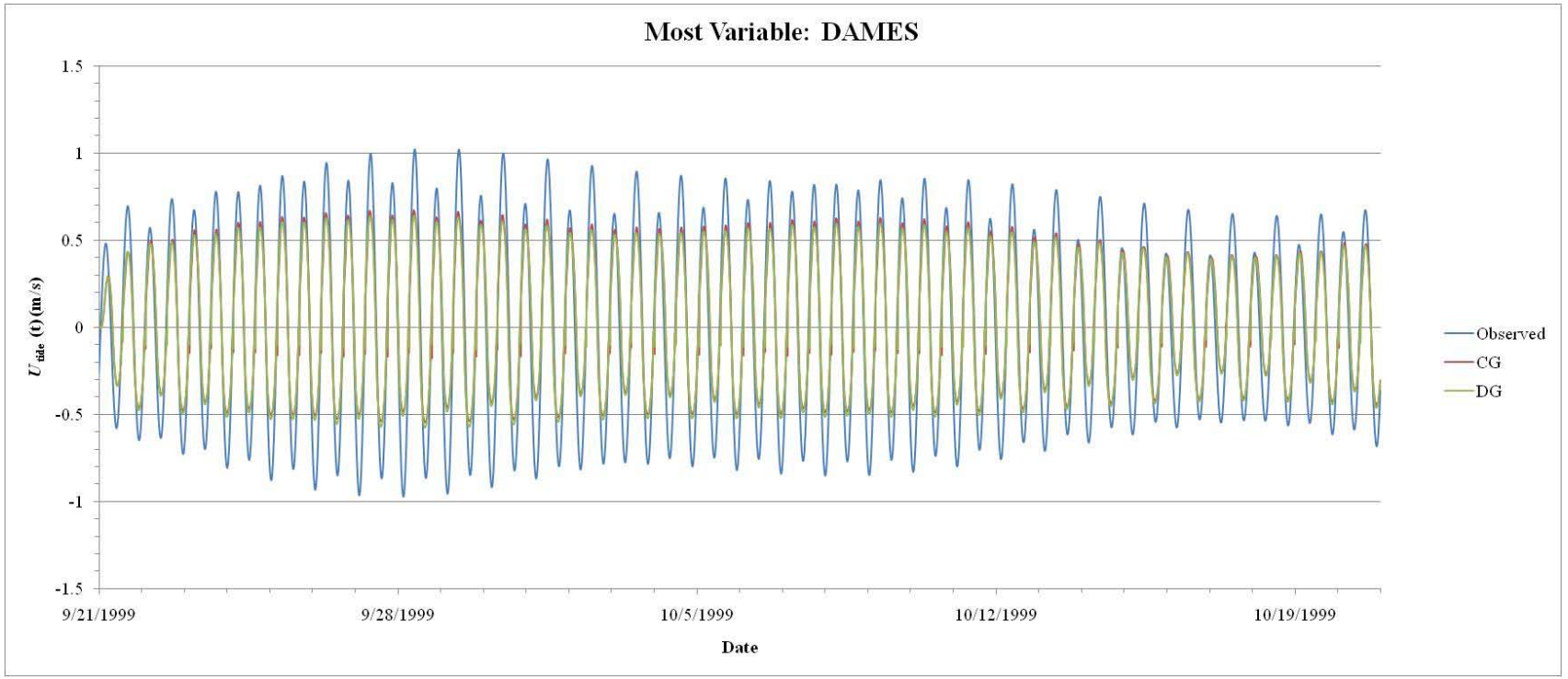

Figure B.19: Tidal resysnthesis of the along-channel (depth-integrated) velocity at the DAMES station during the *Most Variable* event.

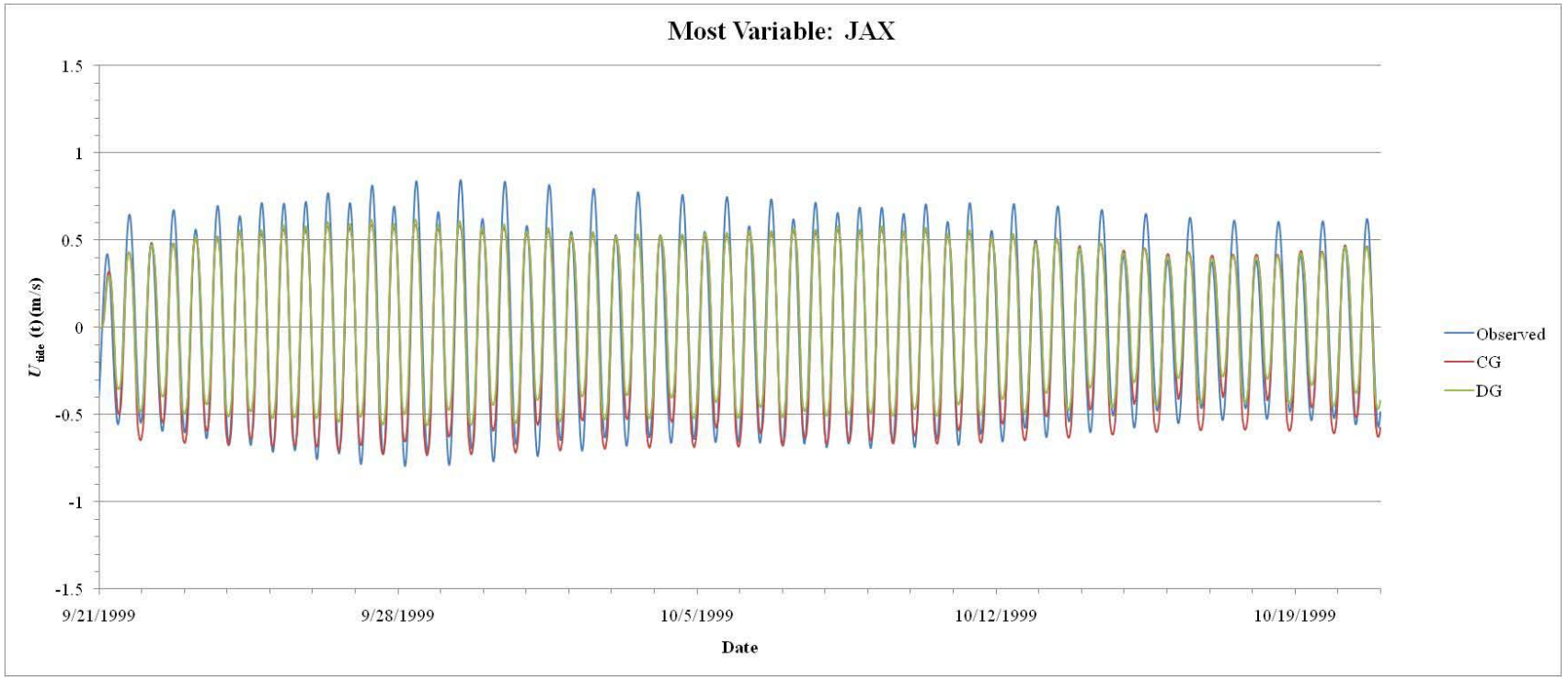

Figure B.20: Tidal resysnthesis of the along-channel (depth-integrated) velocity at the JAX station during the *Most Variable* event.

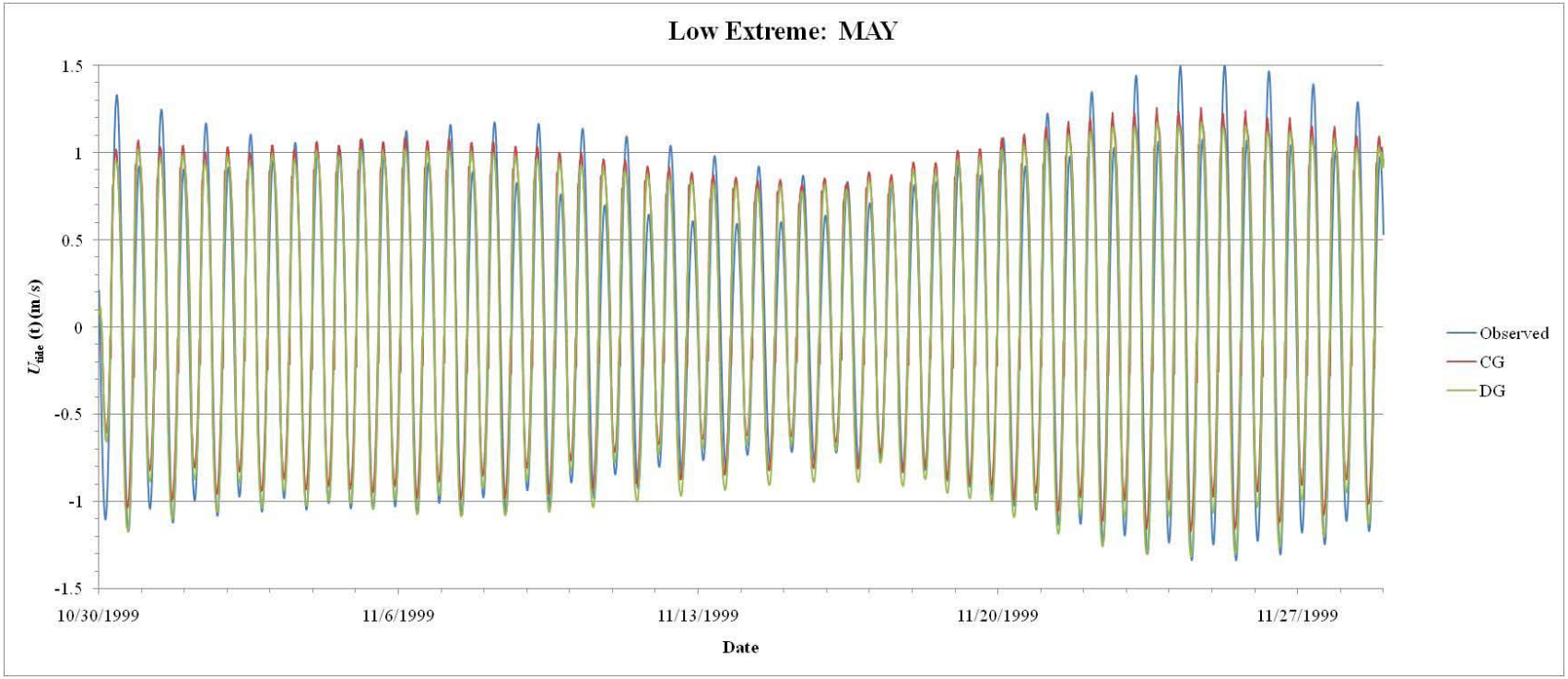

Figure B.21: Tidal resysnthesis of the along-channel (depth-integrated) velocity at the MAY station during the *Low Extreme* event.

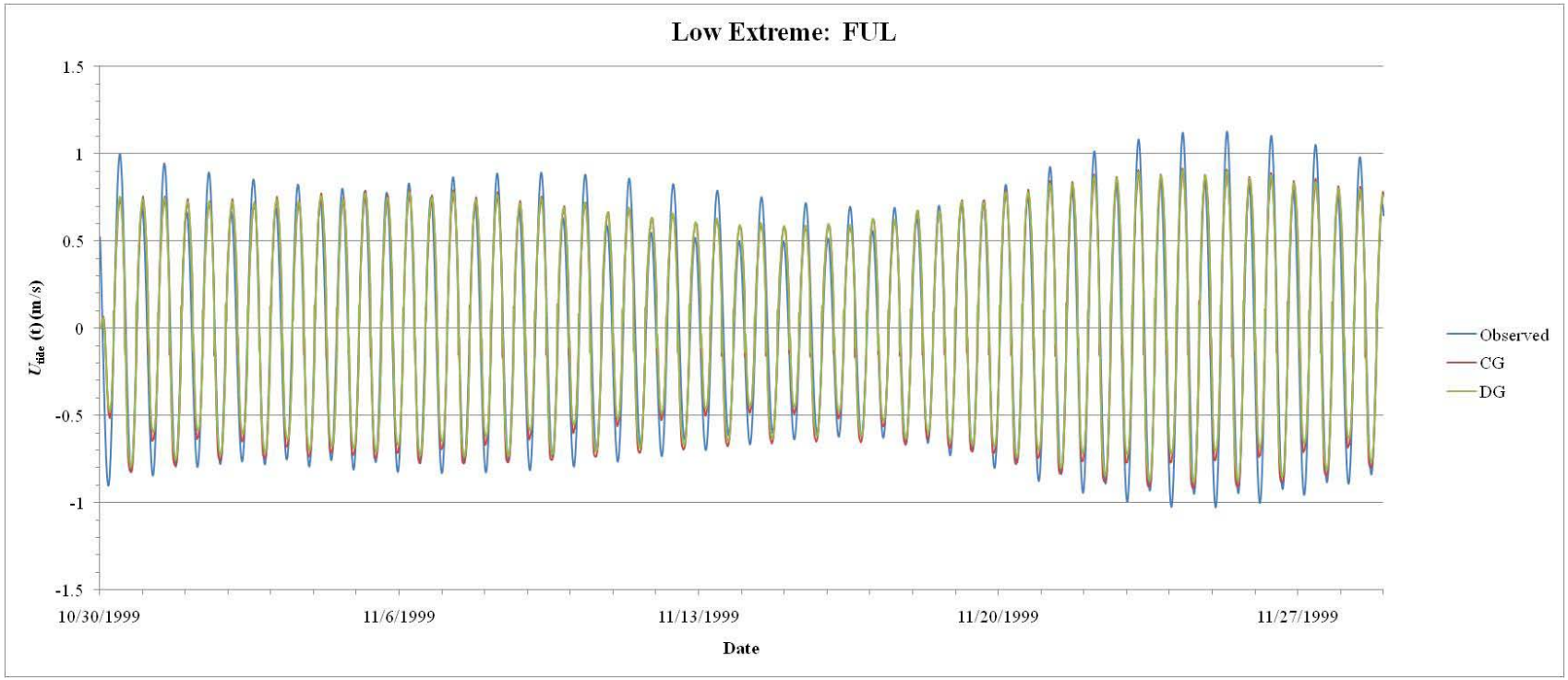

Figure B.22: Tidal resysnthesis of the along-channel (depth-integrated) velocity at the FUL station during the *Low Extreme* event.

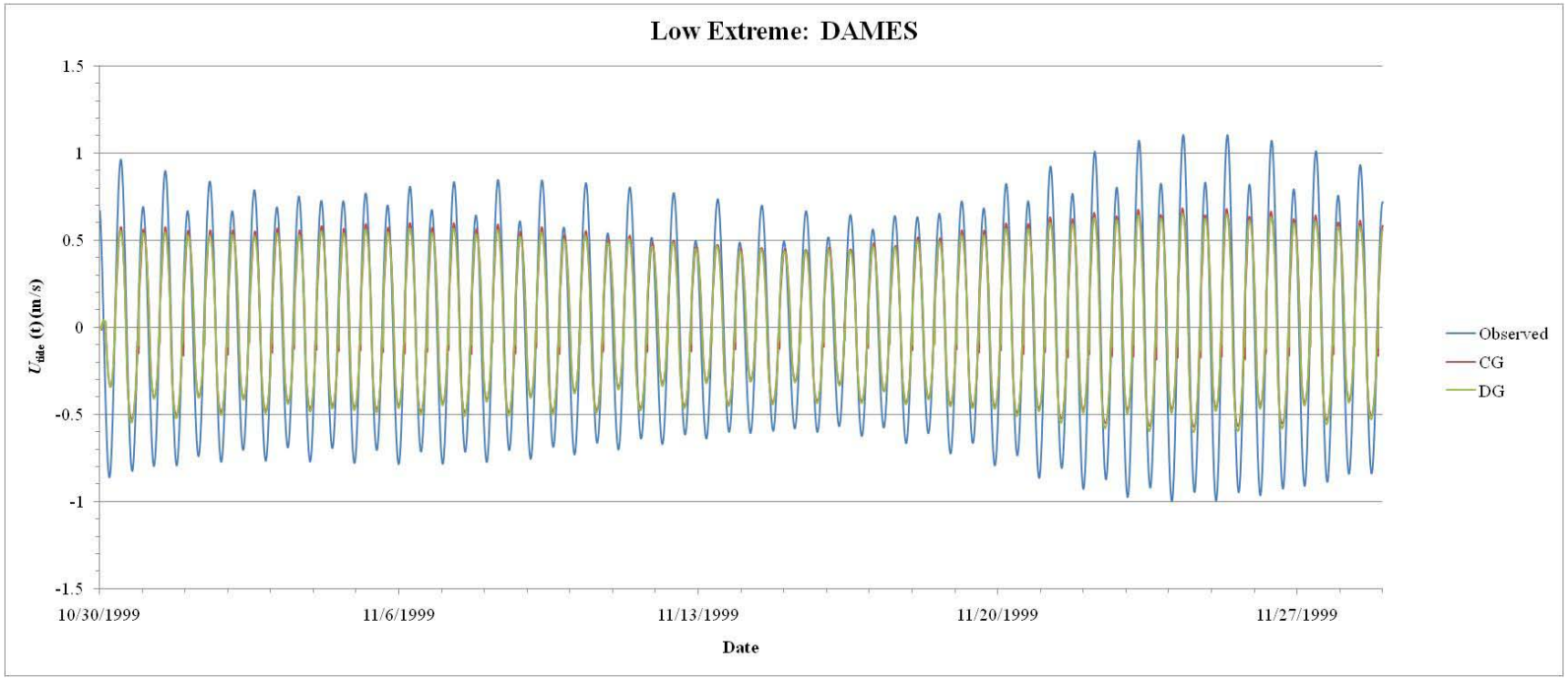

Figure B.23: Tidal resysnthesis of the along-channel (depth-integrated) velocity at the DAMES station during the *Low Extreme* event.

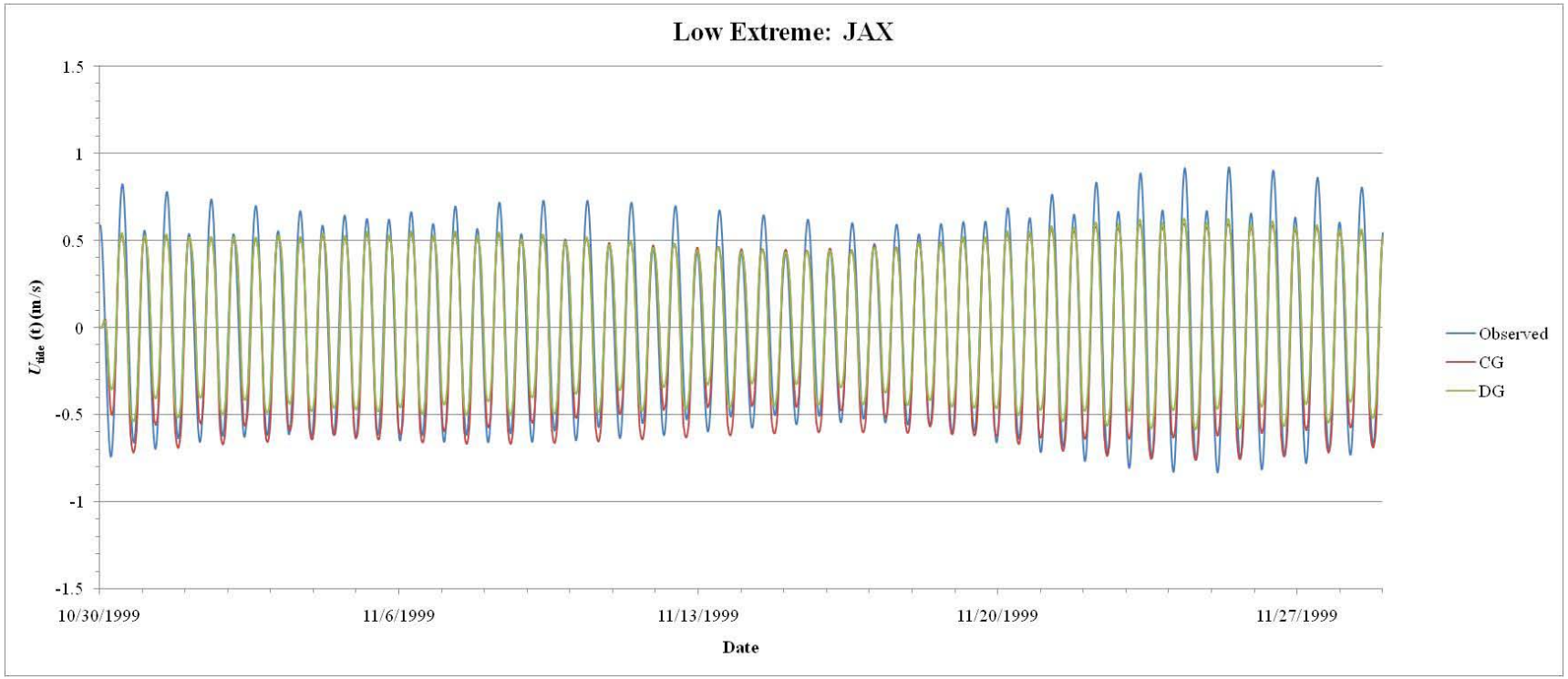

Figure B.24: Tidal resysnthesis of the along-channel (depth-integrated) velocity at the JAX station during the *Low Extreme* event.

APPENDIX C
WATER LEVEL VALIDATION PLOTS

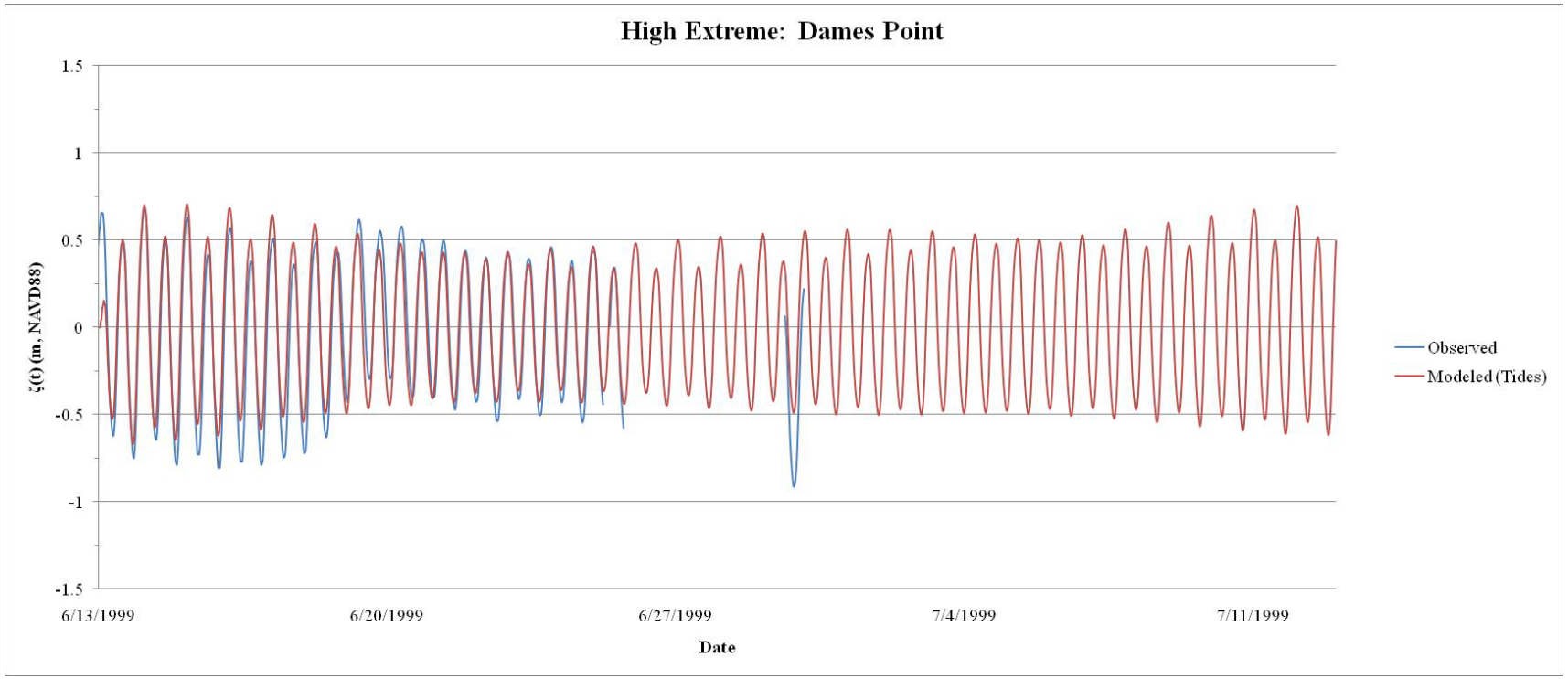

Figure C.1: Tidal resysnthesis using tides for the Dames Point station during the *High Extreme* event. Water surface elevation levels were based on the NAVD88 datum.

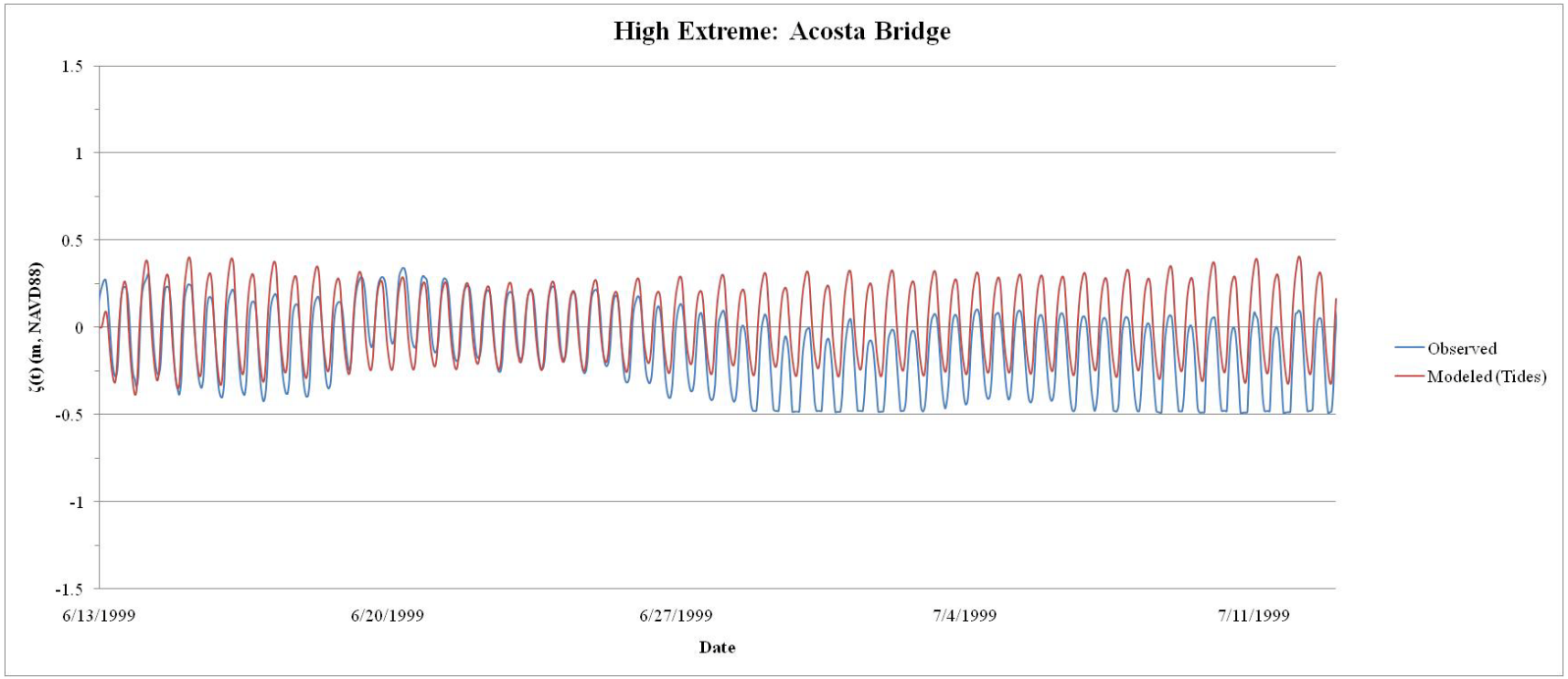

Figure C.2: Tidal resysnthesis using tides for the Acosta Bridge station during the *High Extreme* event. Water surface elevation levels were based on the NAVD88 datum.

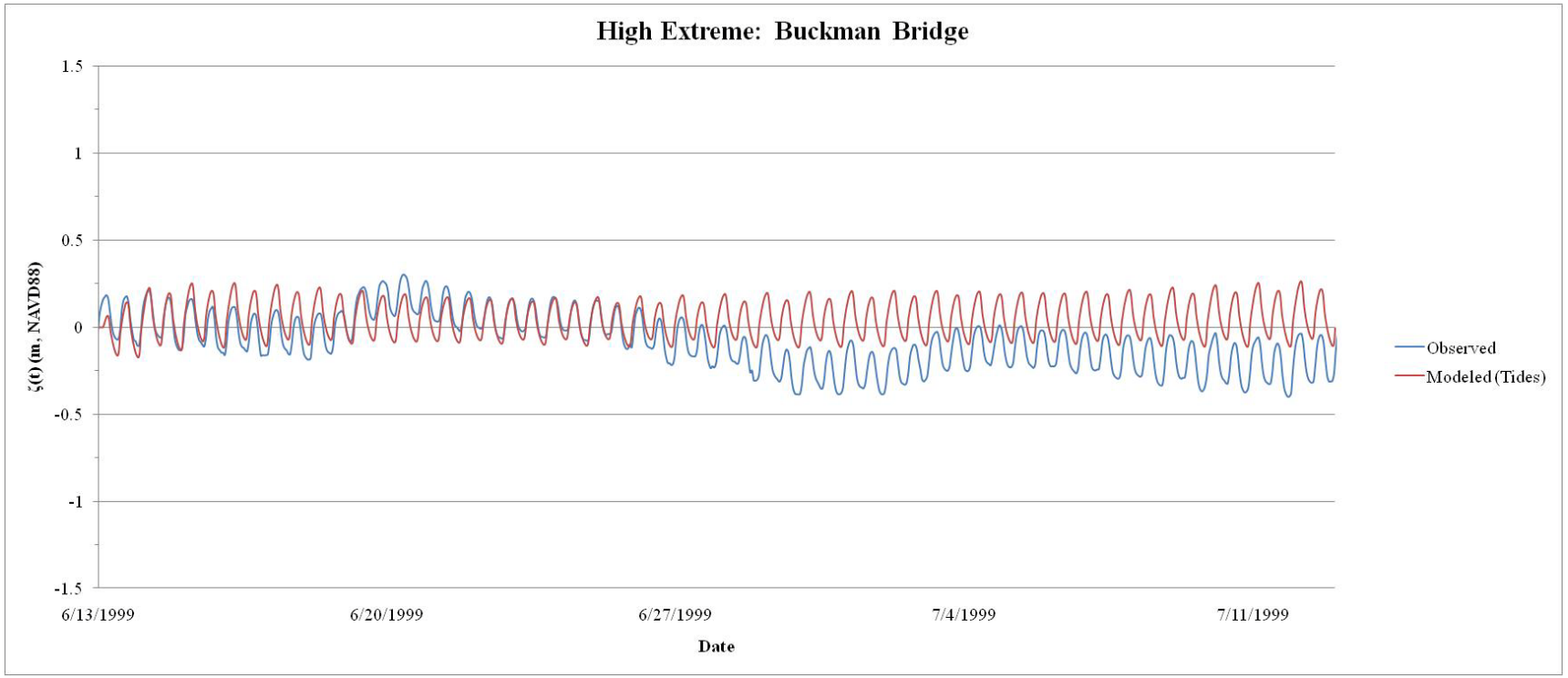

Figure C.3: Tidal resysnthesis using tides for the Buckman Bridge station during the *High Extreme* event. Water surface elevation levels were based on the NAVD88 datum.

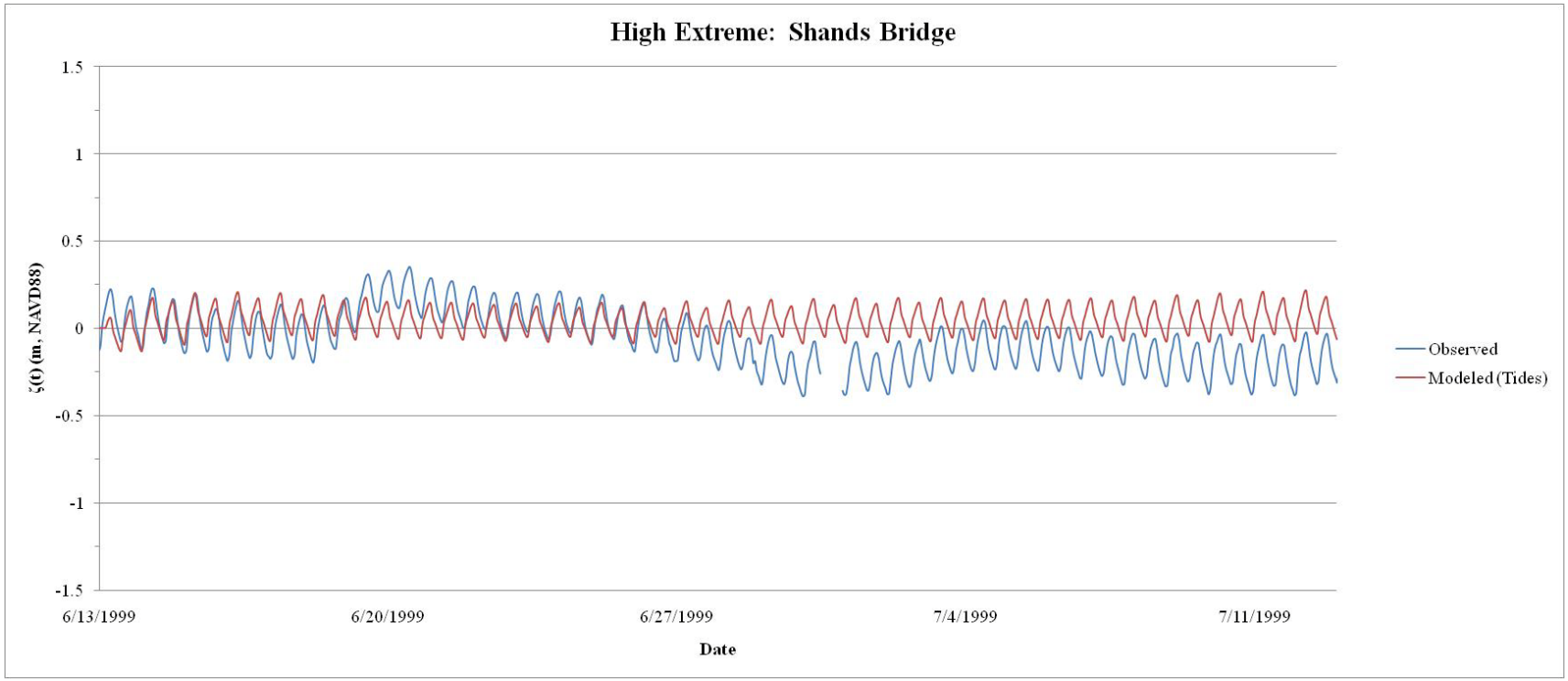

Figure C.4: Tidal resysnthesis using tides for the Shands Bridge station during the *High Extreme* event. Water surface elevation levels were based on the NAVD88 datum.

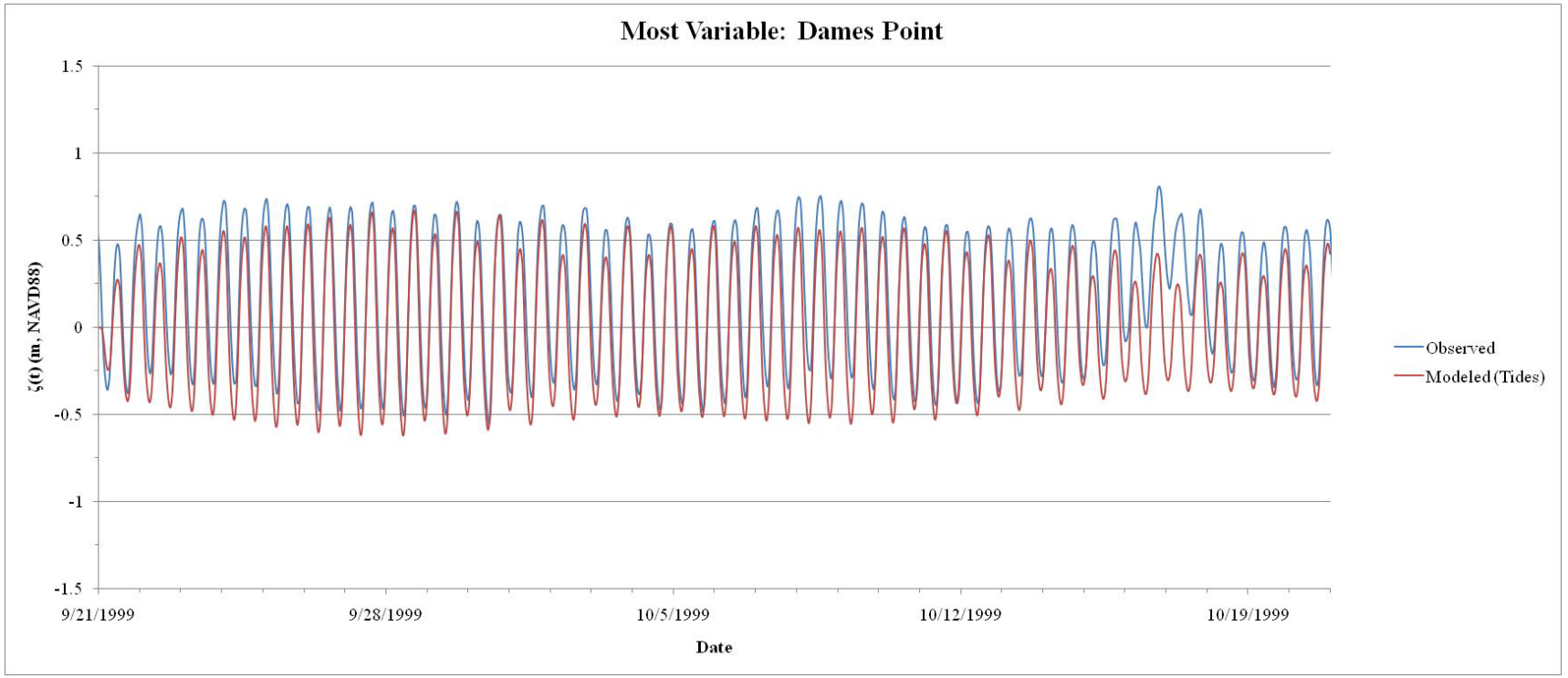

Figure C.5: Tidal resysnthesis using tides for the Dames Point station during the *Most Variable* event. Water surface elevation levels were based on the NAVD88 datum.

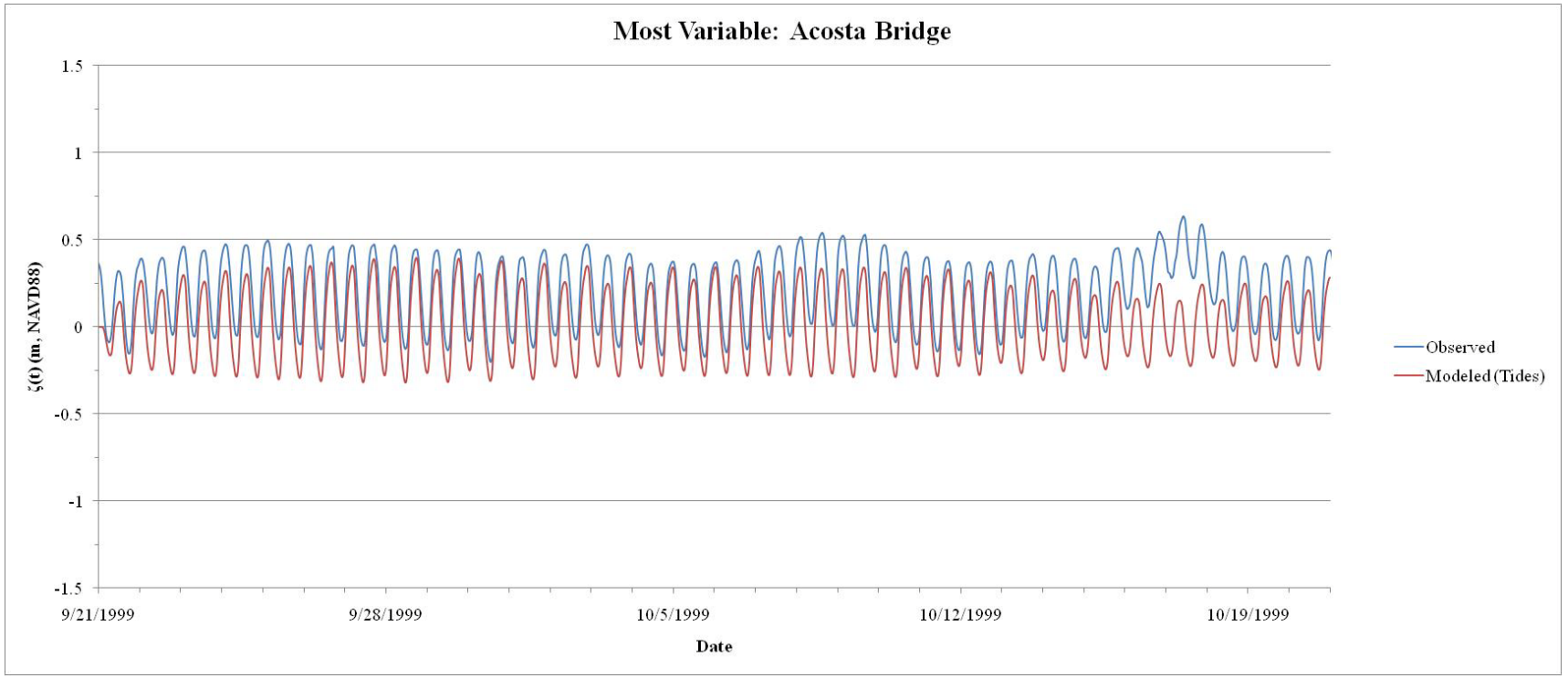

Figure C.6: Tidal resysnthesis using tides for the Acosta Bridge station during the *Most Variable* event. Water surface elevation levels were based on the NAVD88 datum.

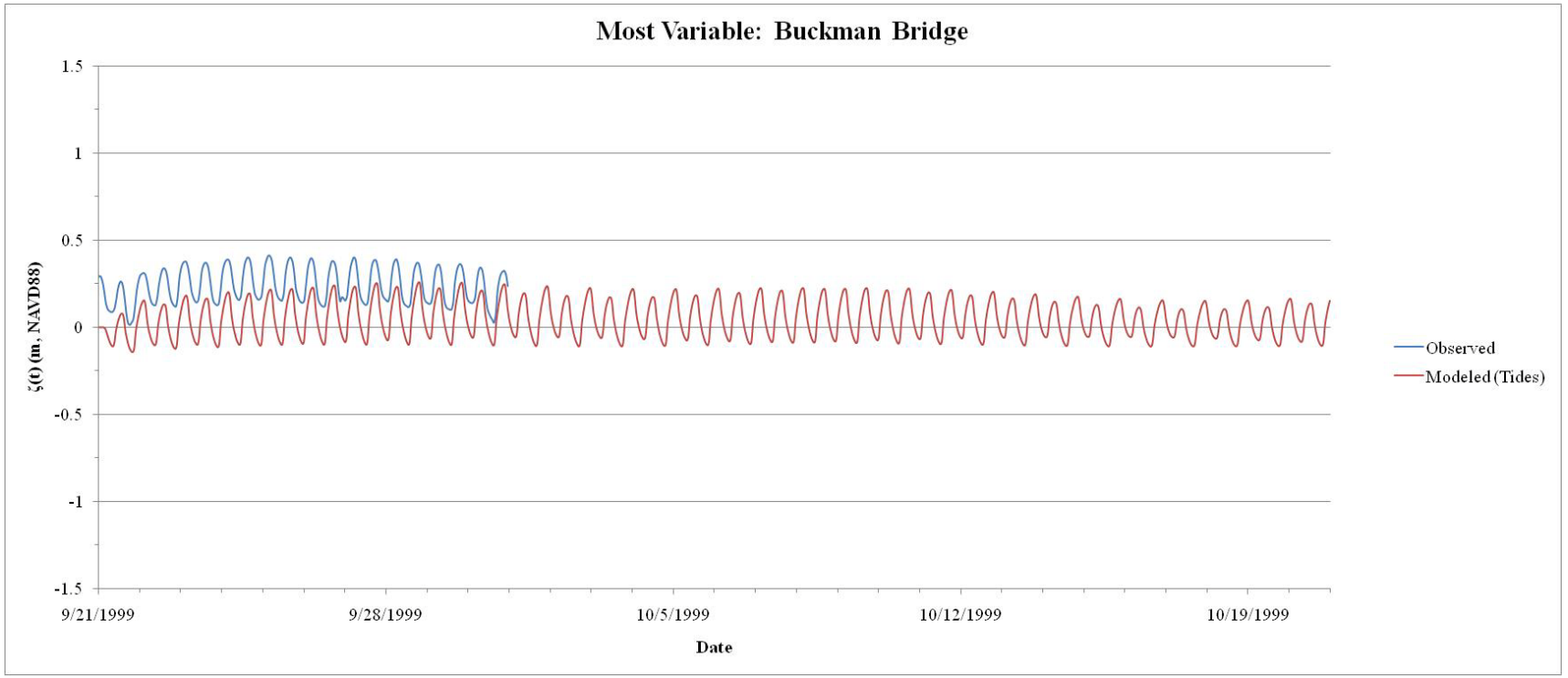

Figure C.7: Tidal resysnthesis using tides for the Buckman Bridge station during the *Most Variable* event. Water surface elevation levels were based on the NAVD88 datum.

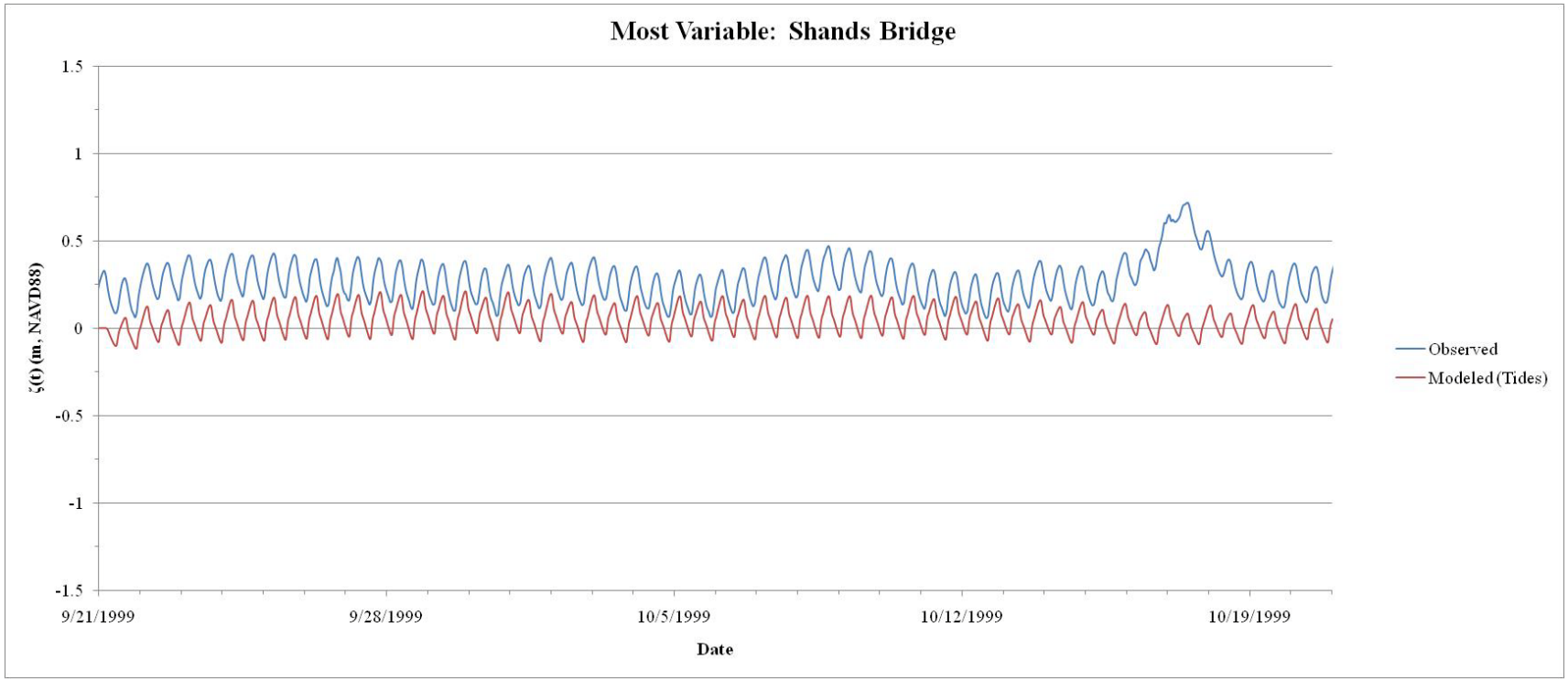

Figure C.8: Tidal resysnthesis using tides for the Shands Bridge station during the *Most Variable* event. Water surface elevation levels were based on the NAVD88 datum.

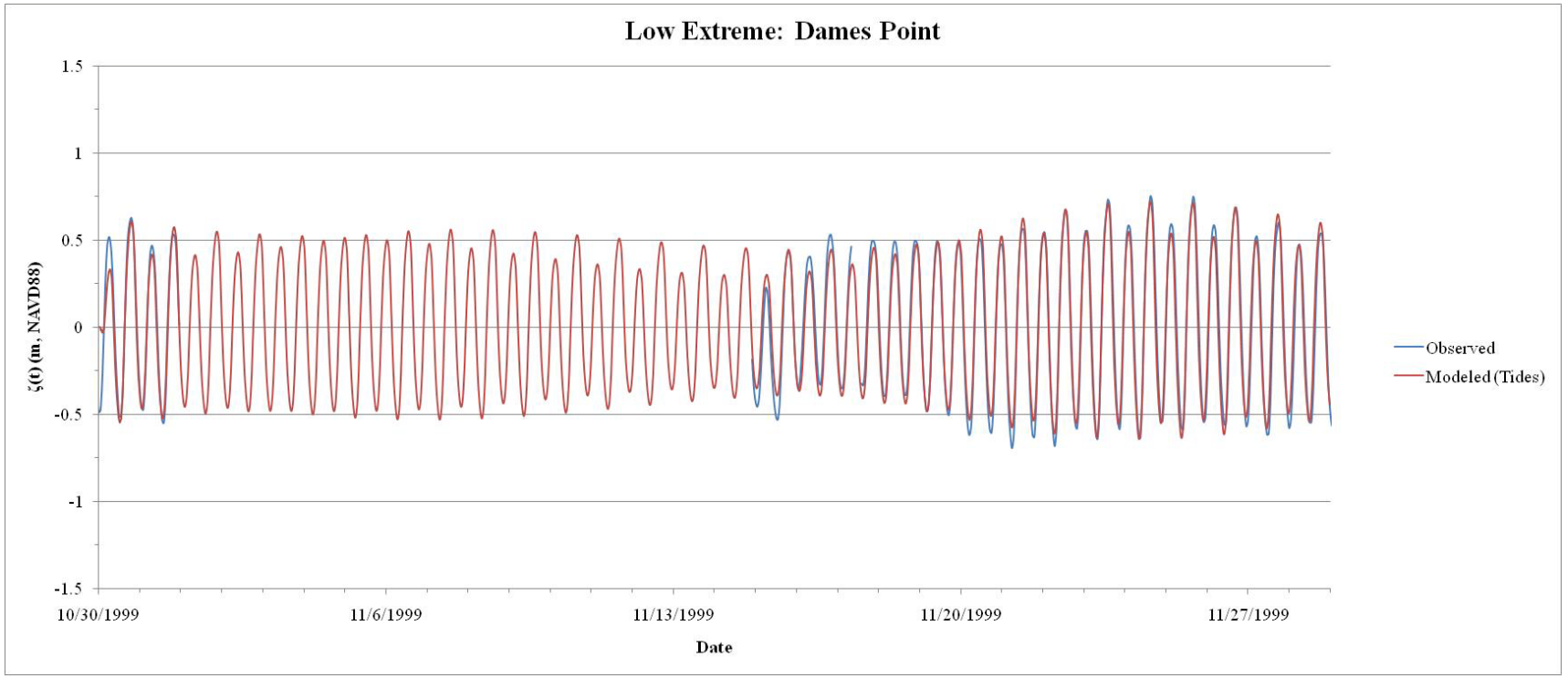

Figure C.9: Tidal resysnthesis using tides for the Dames Point station during the *Low Extreme* event. Water surface elevation levels were based on the NAVD88 datum.

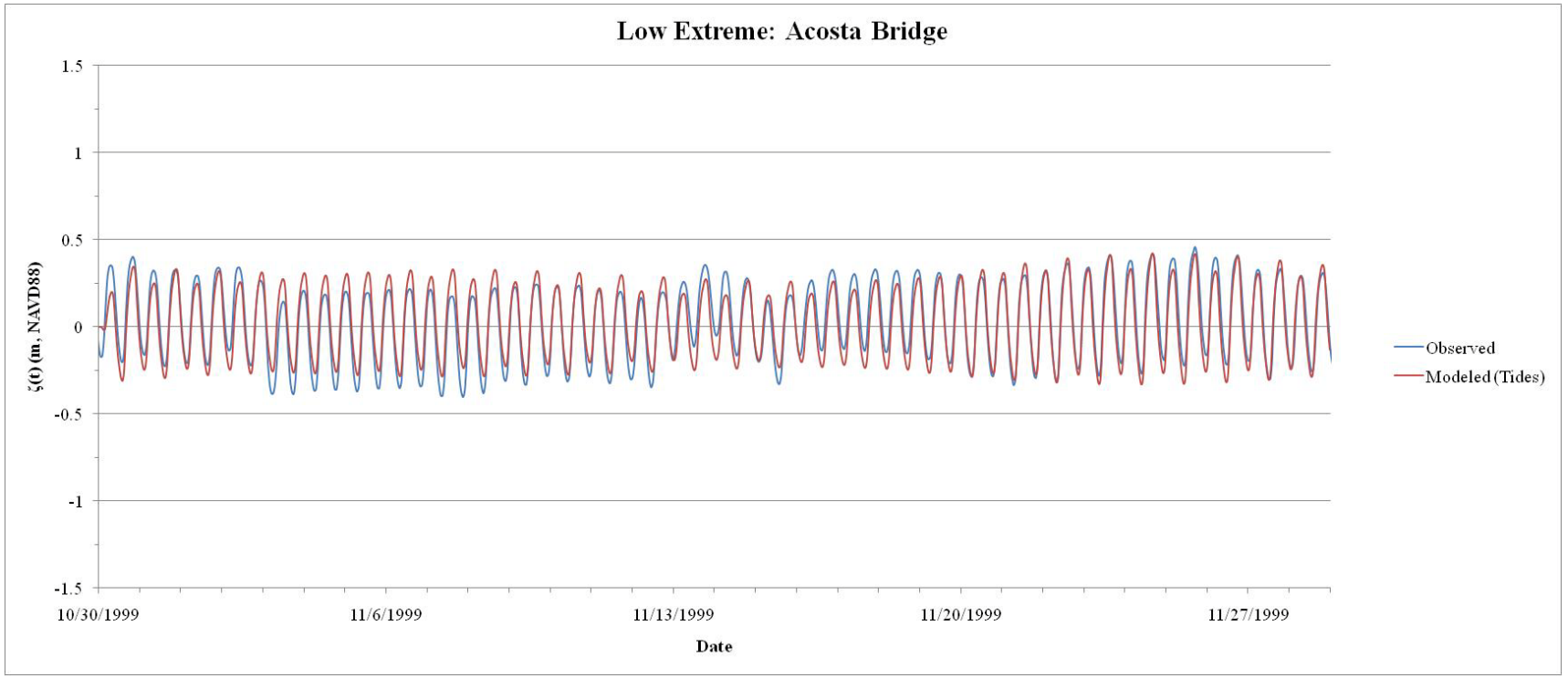

Figure C.10: Tidal resysnthesis using tides for the Acosta Bridge station during the *Low Extreme* event. Water surface elevation levels were based on the NAVD88 datum.

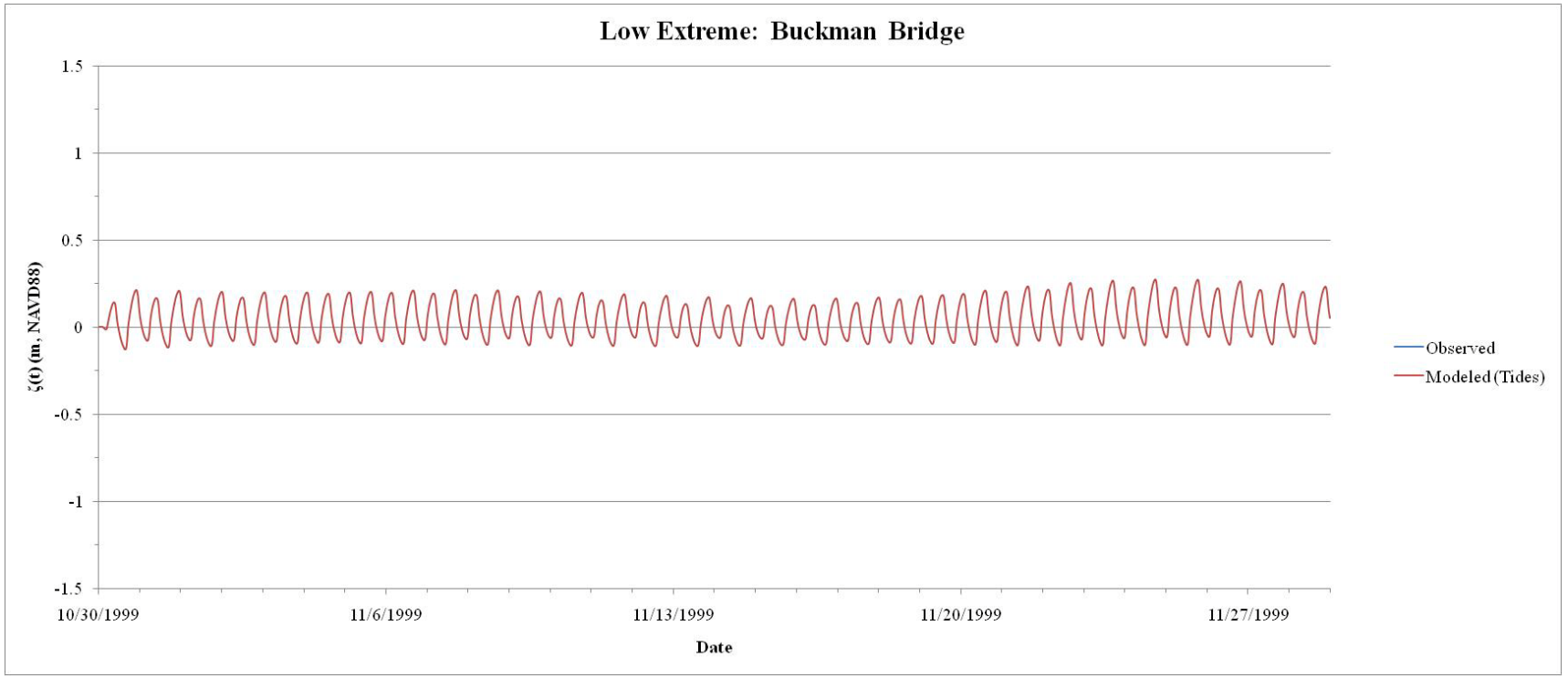

Figure C.11: Tidal resysnthesis using tides for the Buckman Bridge station during the *Low Extreme* event. Water surface elevation levels were based on the NAVD88 datum.

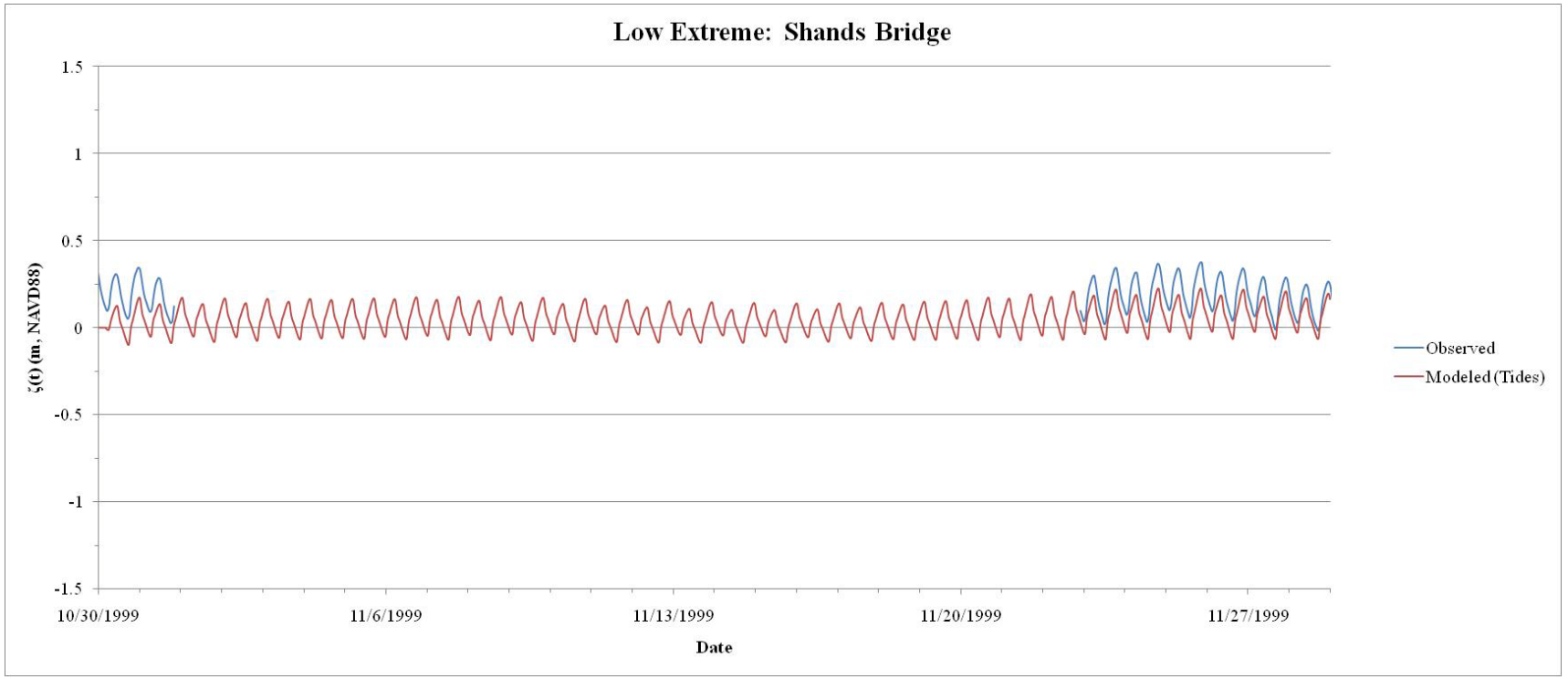

Figure C.12: Tidal resysnthesis using tides for the Shands Bridge station during the *Low Extreme* event. Water surface elevation levels were based on the NAVD88 datum.

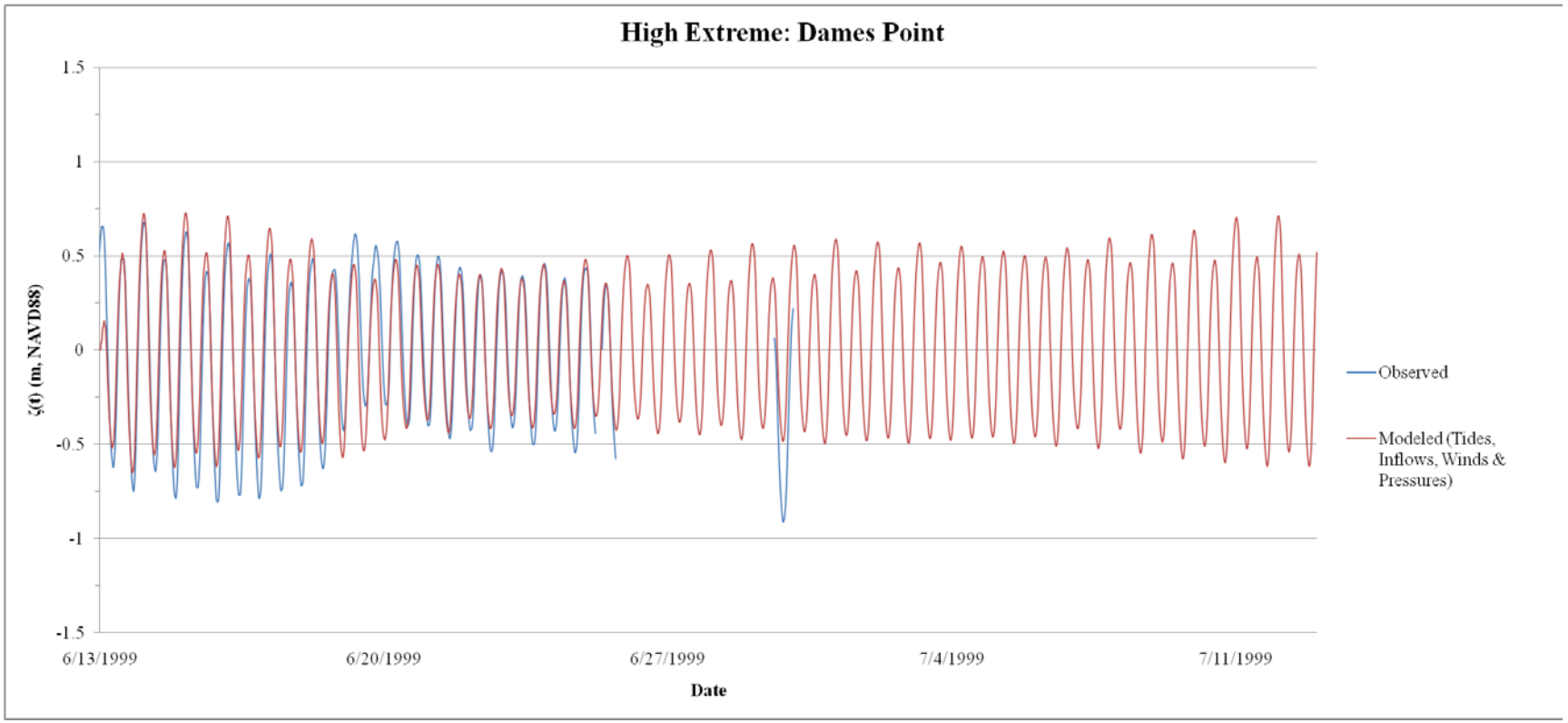

Figure C.13: Tidal resysnthesis using tides, river inflows, and winds and pressures for the Dames Point station during the *High Extreme* event. Water surface elevation levels were based on the NAVD88 datum.

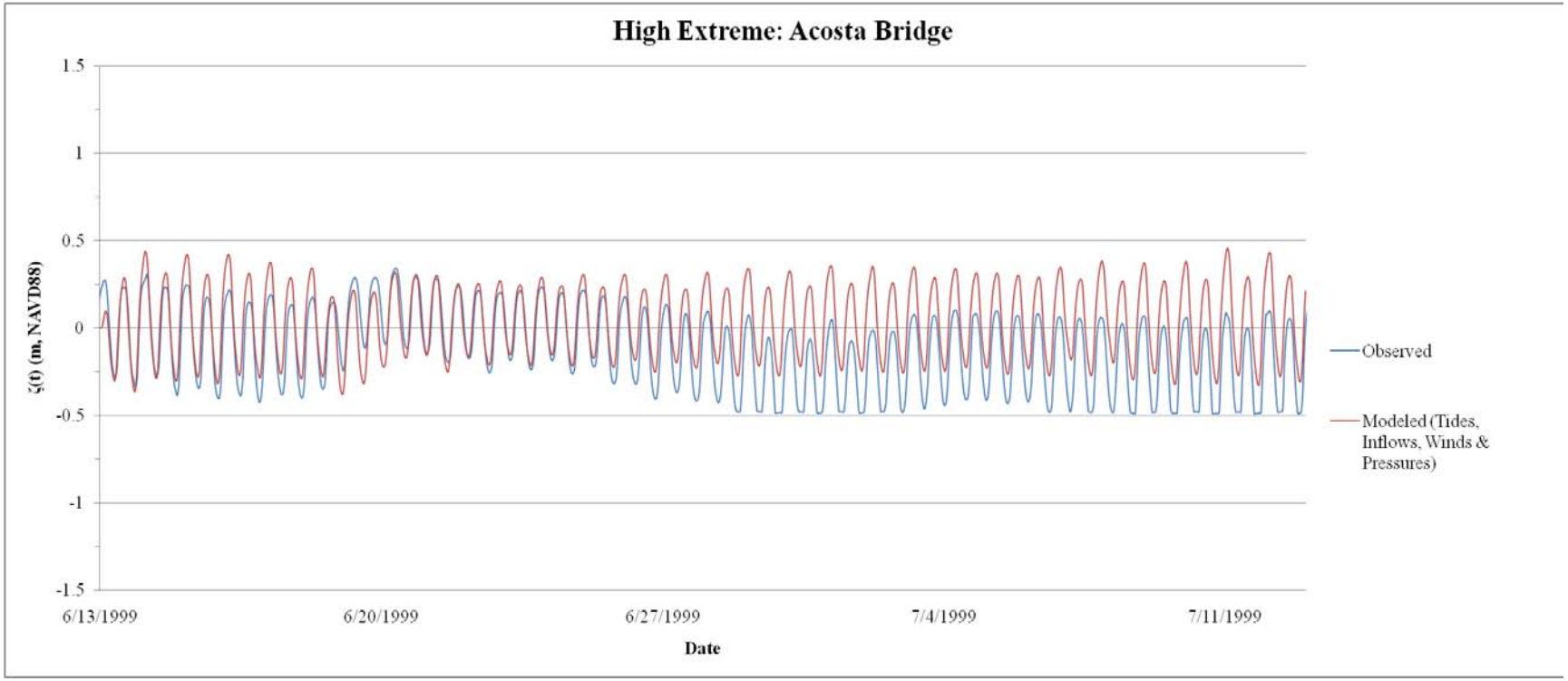

Figure C.14: Tidal resysnthesis using tides, river inflows, and winds and pressures for the Acosta Bridge station during the *High Extreme* event. Water surface elevation levels were based on the NAVD88 datum.

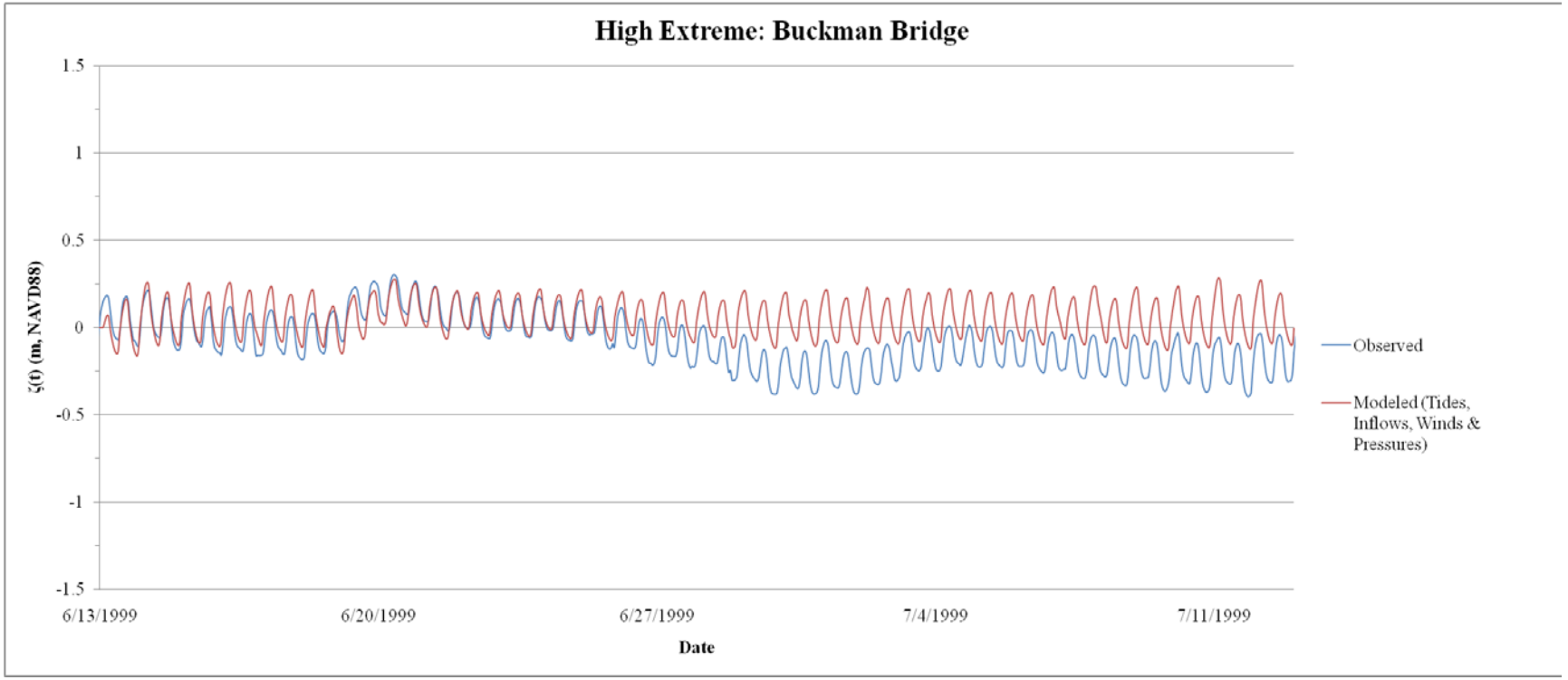

Figure C.15: Tidal resysnthesis using tides, river inflows, and winds and pressures for the Buckman Bridge station during the *High Extreme* event. Water surface elevation levels were based on the NAVD88 datum.

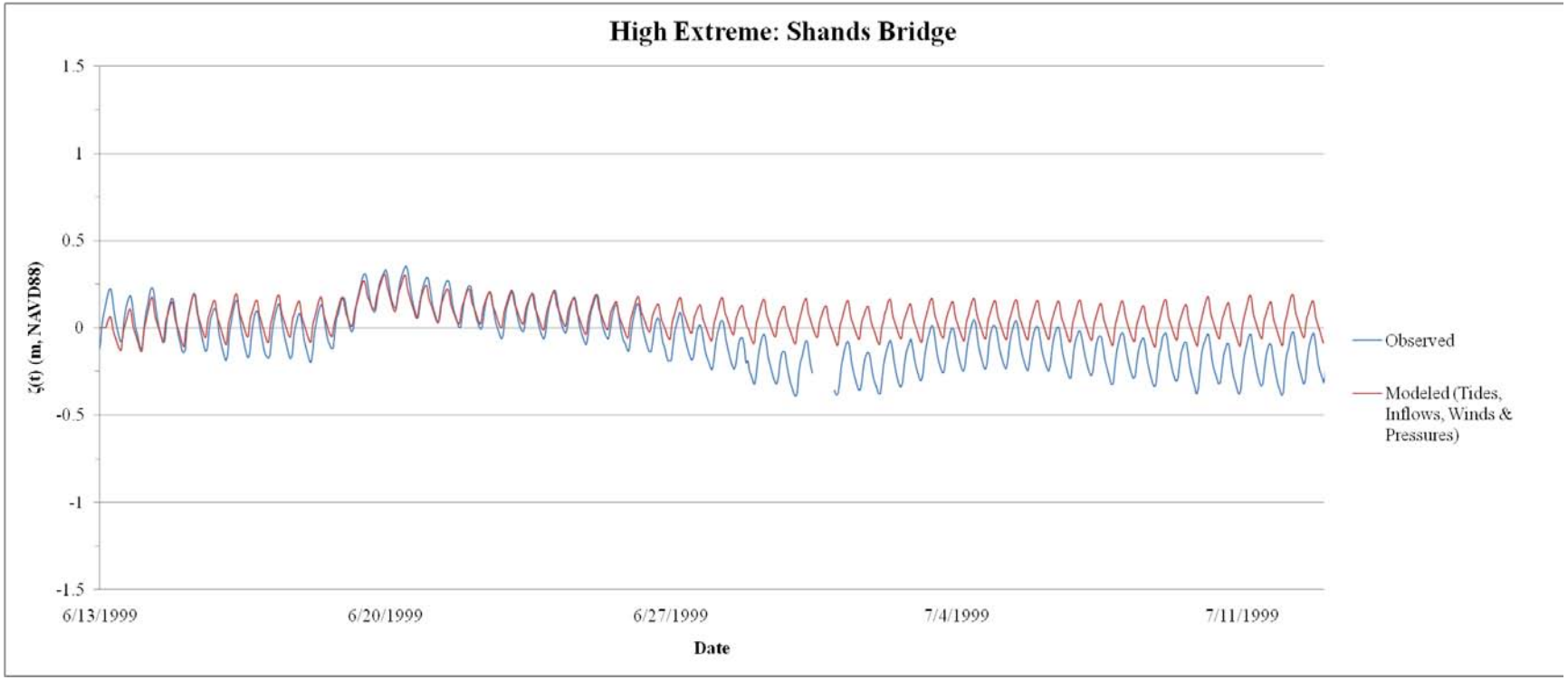

Figure C.16: Tidal resysnthesis using tides, river inflows, and winds and pressures for the Shands Bridge station during the *High Extreme* event. Water surface elevation levels were based on the NAVD88 datum.

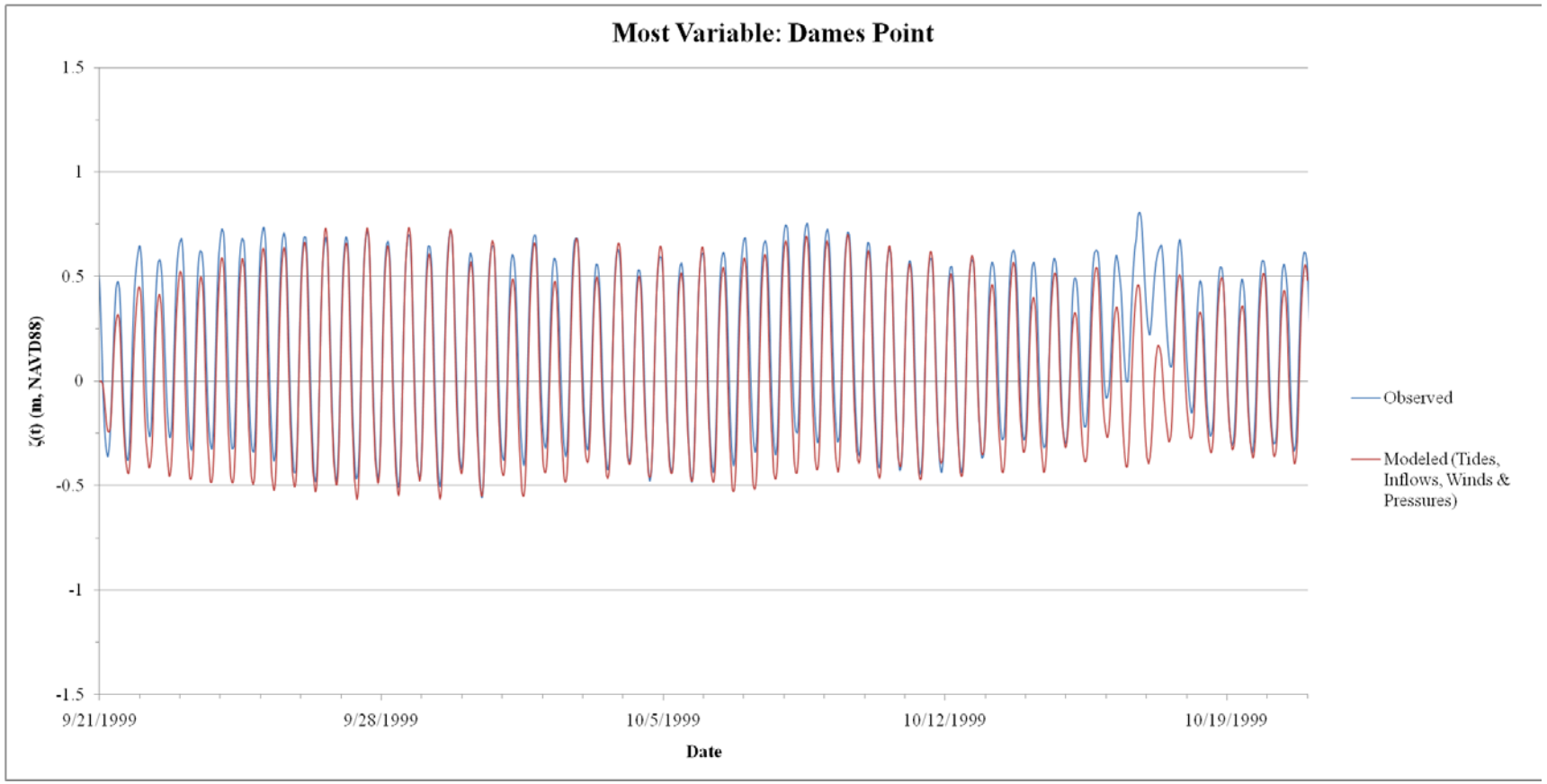

Figure C.17: Tidal resysnthesis using tides, river inflows, and winds and pressures for the Dames Point station during the *Most Variable* event. Water surface elevation levels were based on the NAVD88 datum.

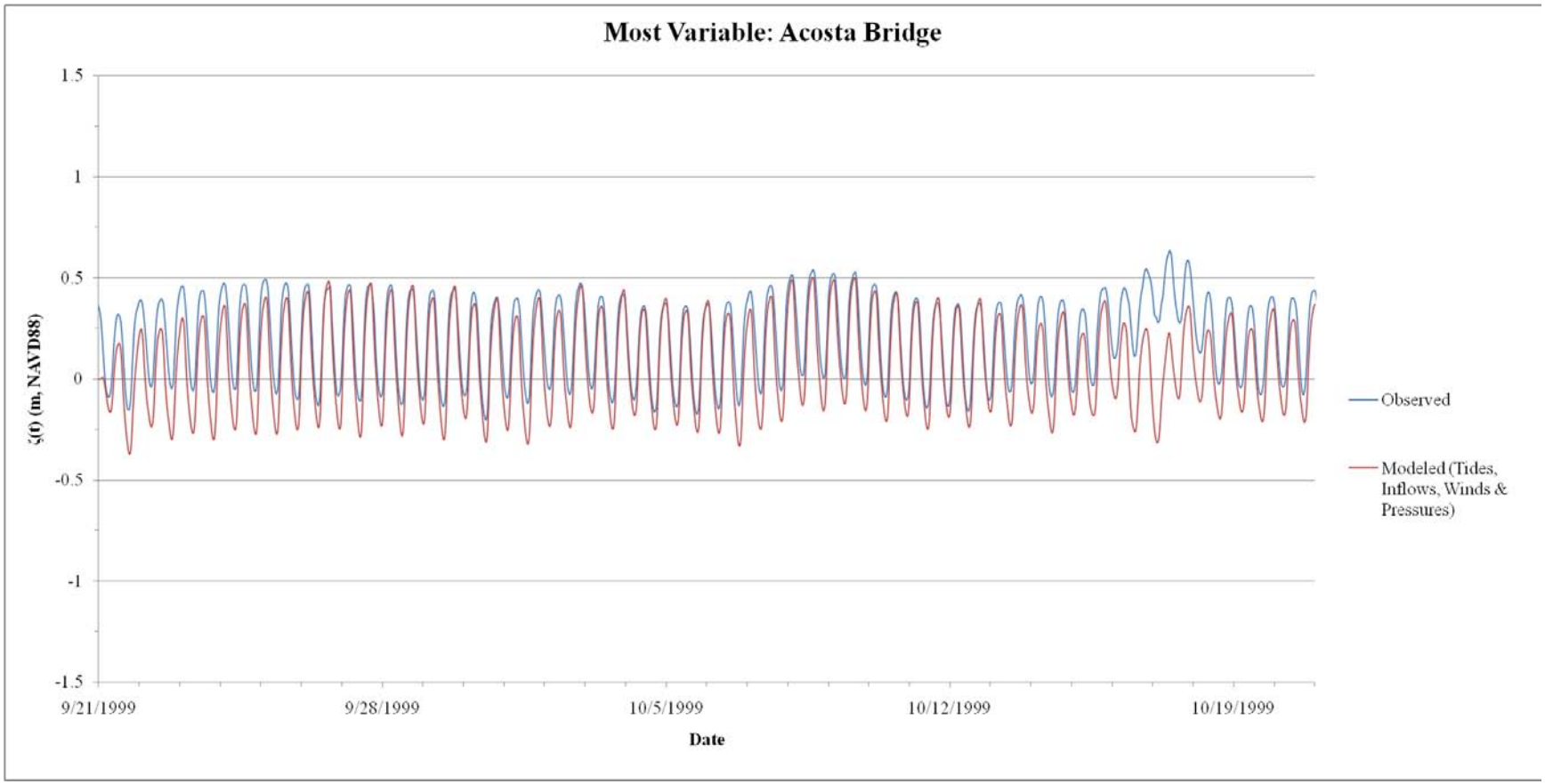

Figure C.18: Tidal resysnthesis using tides, river inflows, and winds and pressures for the Acosta Bridge station during the *Most Variable* event. Water surface elevation levels were based on the NAVD88 datum.

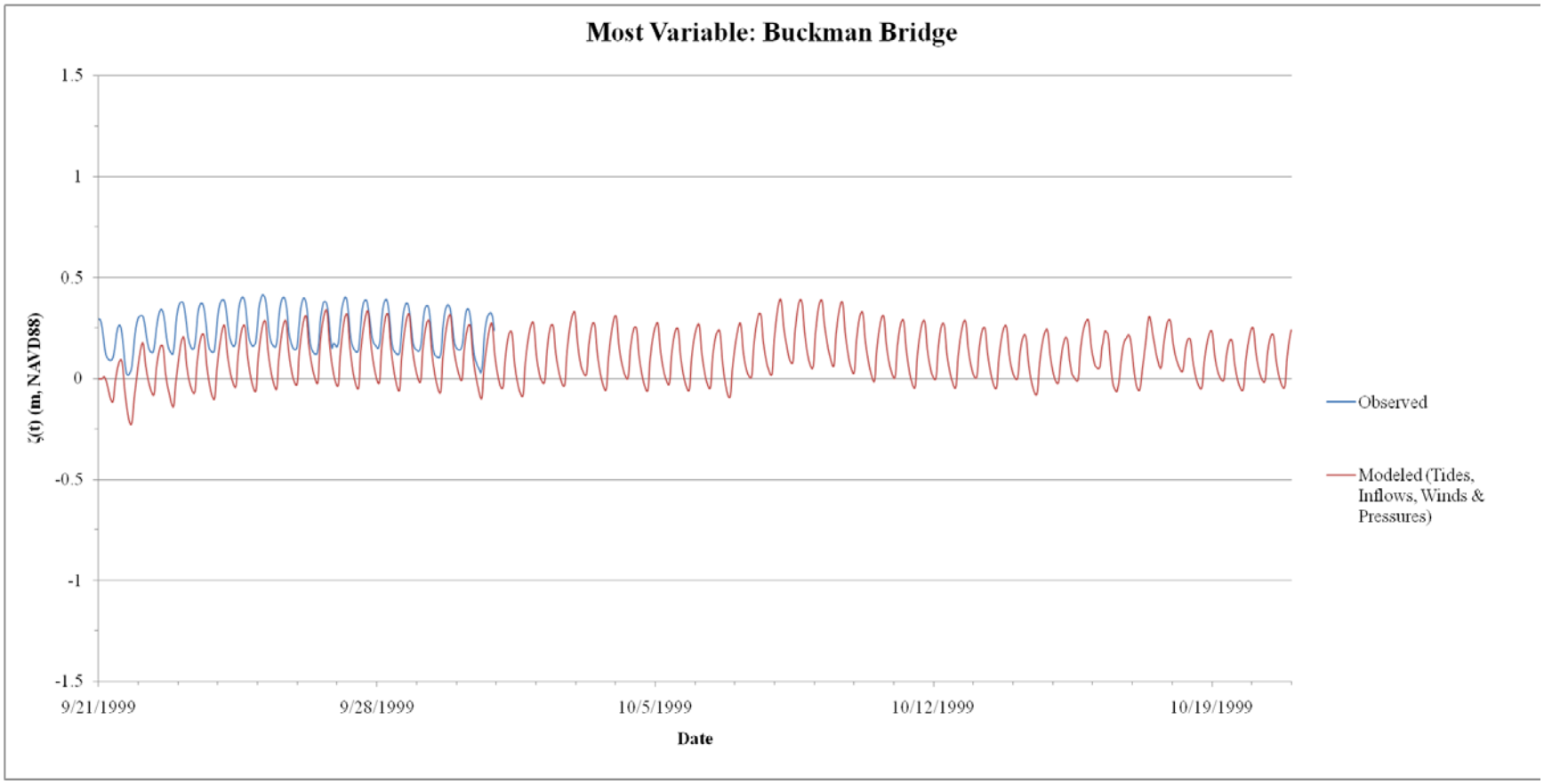

Figure C.19: Tidal resysnthesis using tides, river inflows, and winds and pressures for the Buckman Bridge station during the *Most Variable* event. Water surface elevation levels were based on the NAVD88 datum.

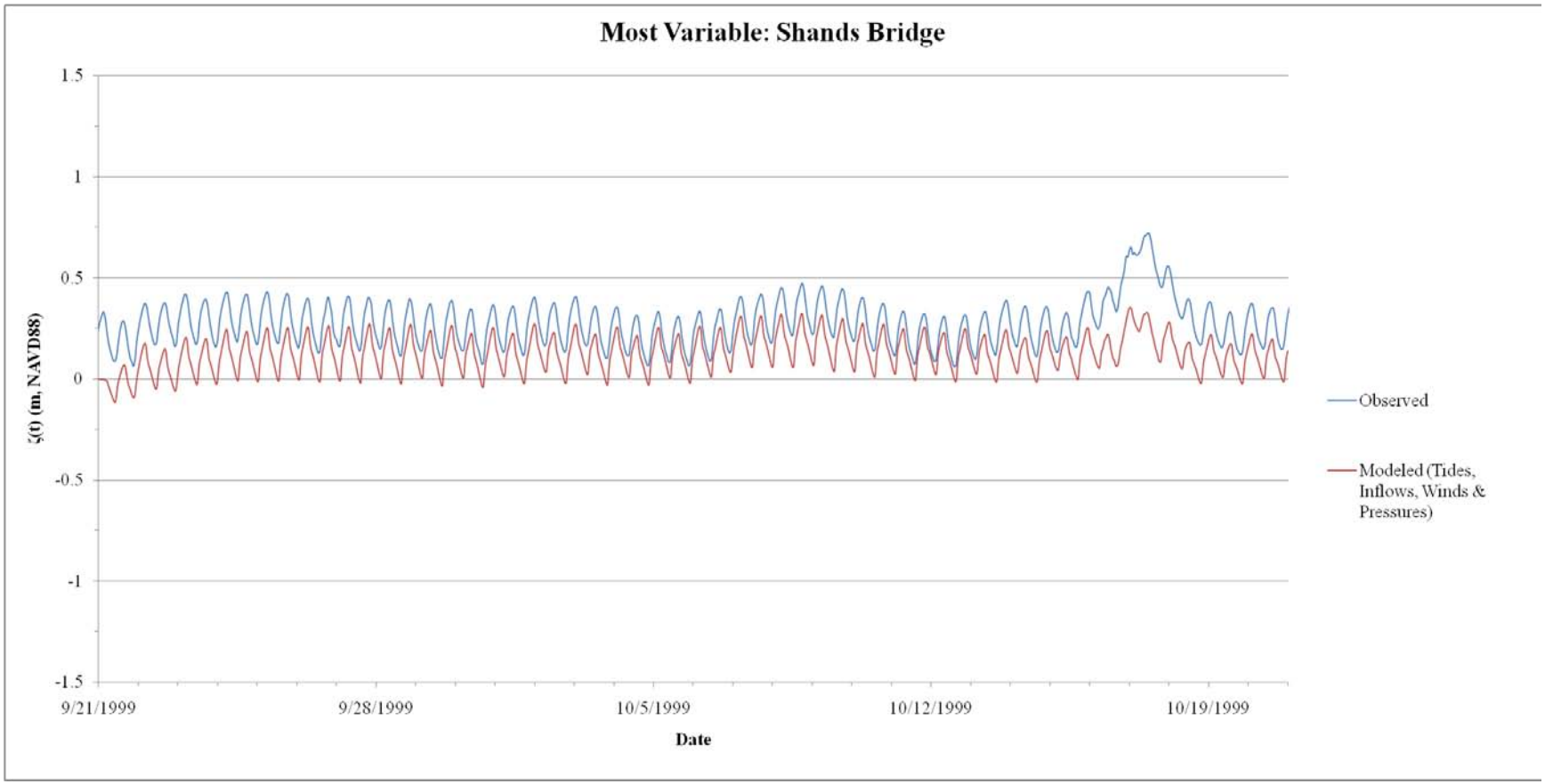

Figure C.20: Tidal resysnthesis using tides, river inflows, and winds and pressures for the Shands Bridge station during the *Most Variable* event. Water surface elevation levels were based on the NAVD88 datum.

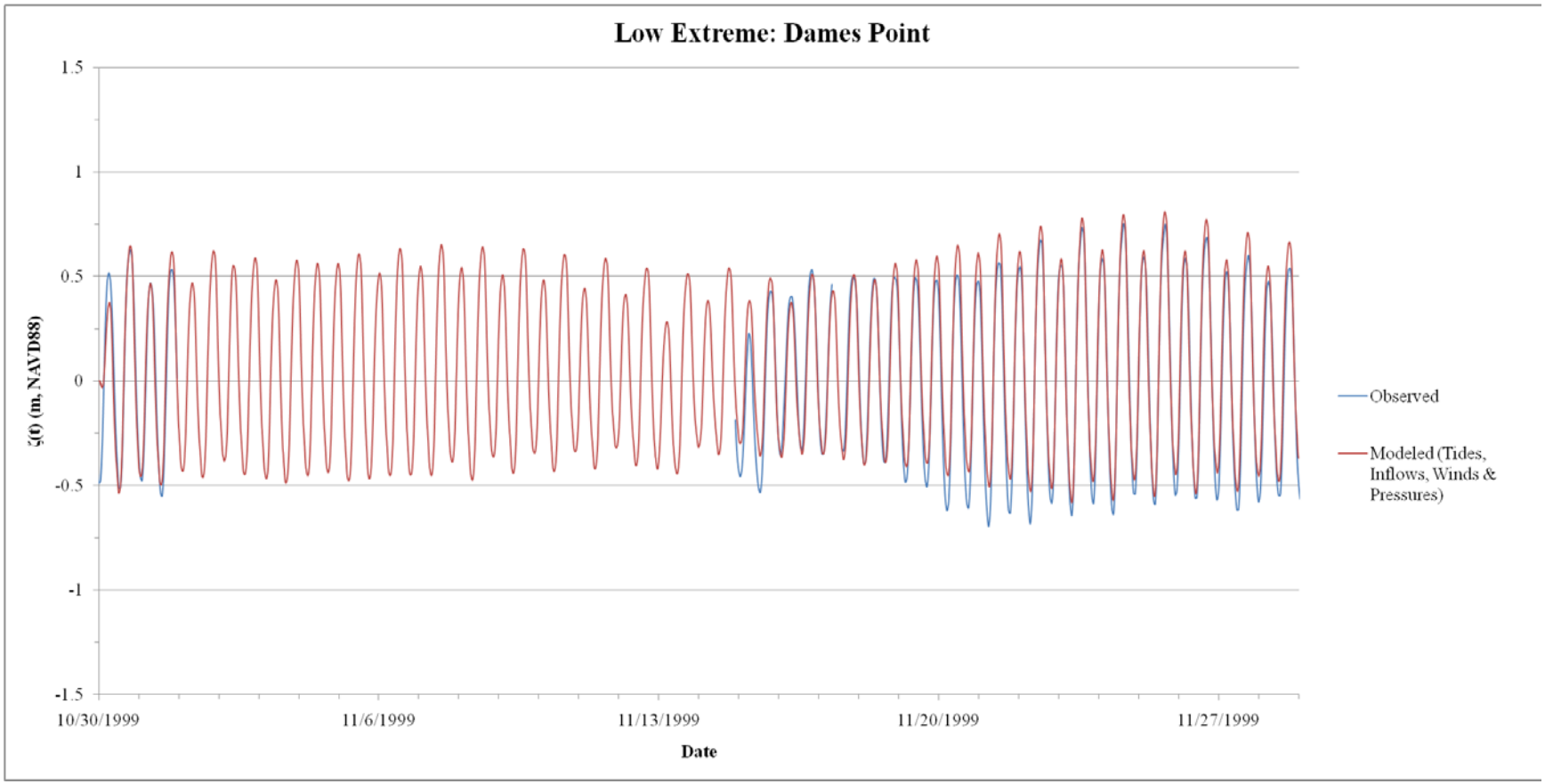

Figure C.21: Tidal resysnthesis using tides, river inflows, and winds and pressures for the Dames Point station during the *Low Extreme* event. Water surface elevation levels were based on the NAVD88 datum.

Figure C.22: Tidal resysnthesis using tides, river inflows, and winds and pressures for the Acosta Bridge station during the *Low Extreme* event. Water surface elevation levels were based on the NAVD88 datum.

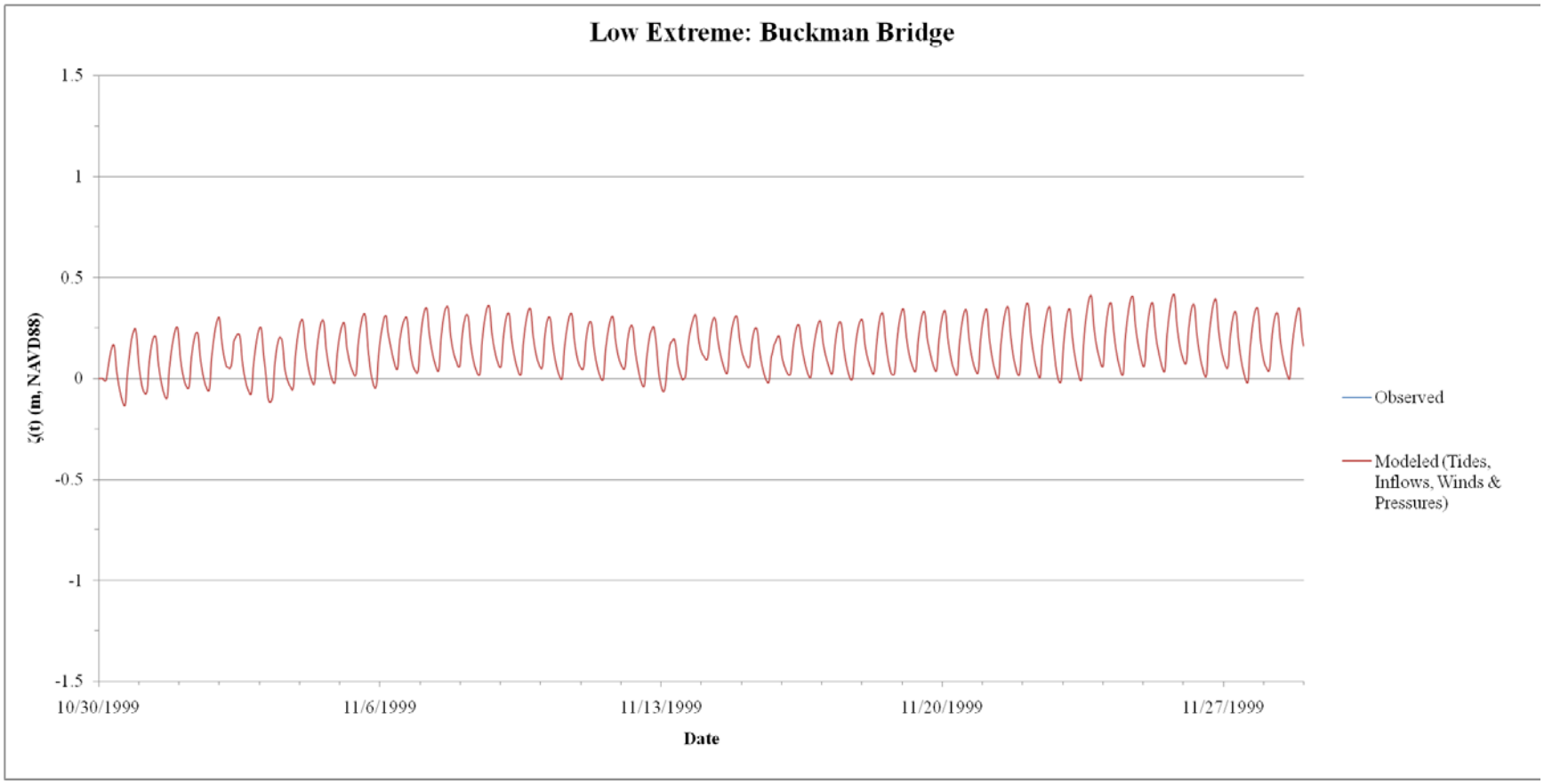

Figure C.23: Tidal resysnthesis using tides, river inflows, and winds and pressures for the Buckman Bridge station during the *Low Extreme* event. Water surface elevation levels were based on the NAVD88 datum.

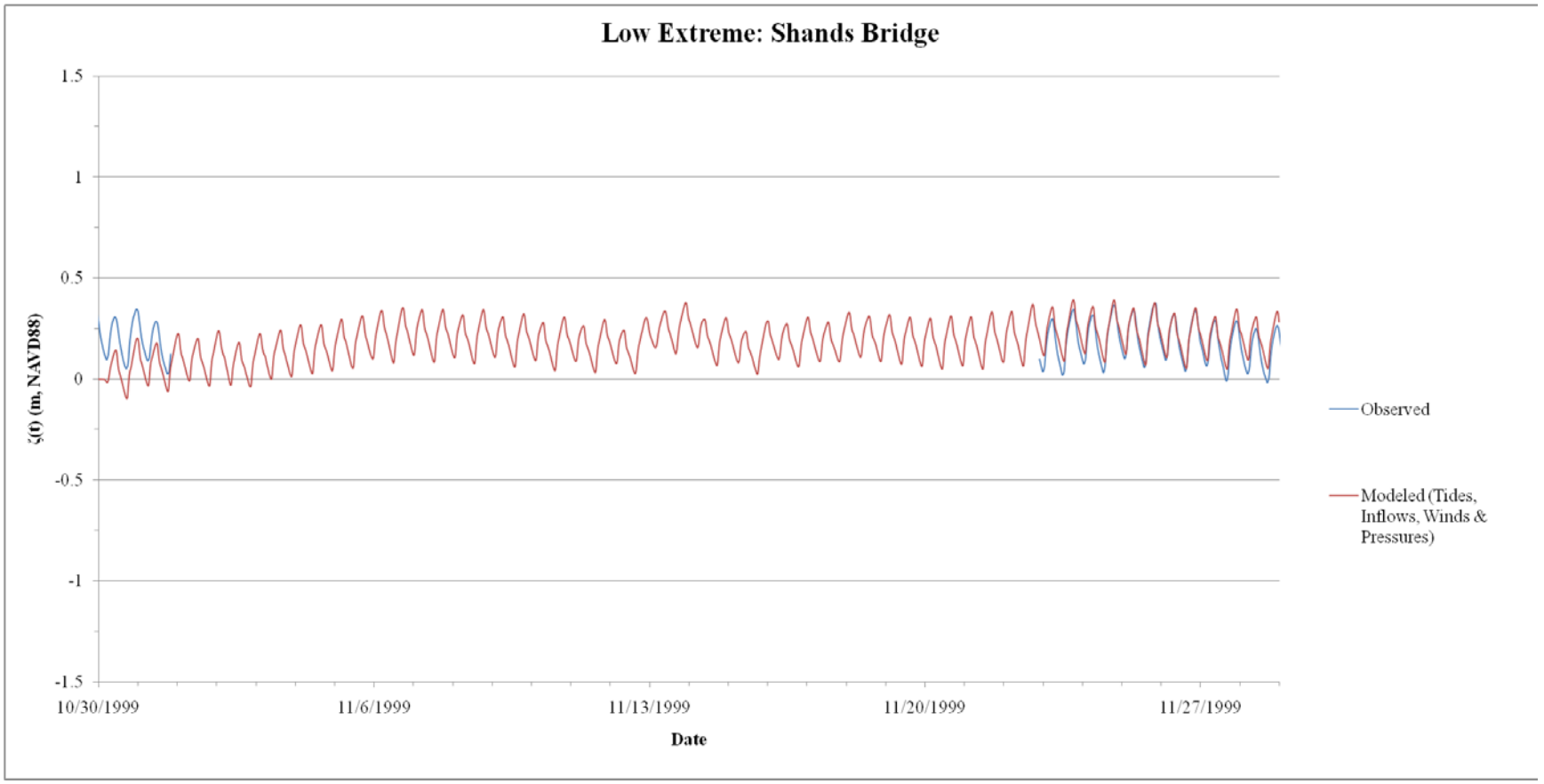

Figure C.24: Tidal resysnthesis using tides, river inflows, and winds and pressures for the Shands Bridge station during the *Low Extreme* event. Water surface elevation levels were based on the NAVD88 datum.

APPENDIX D
WIND SCATTER PLOTS

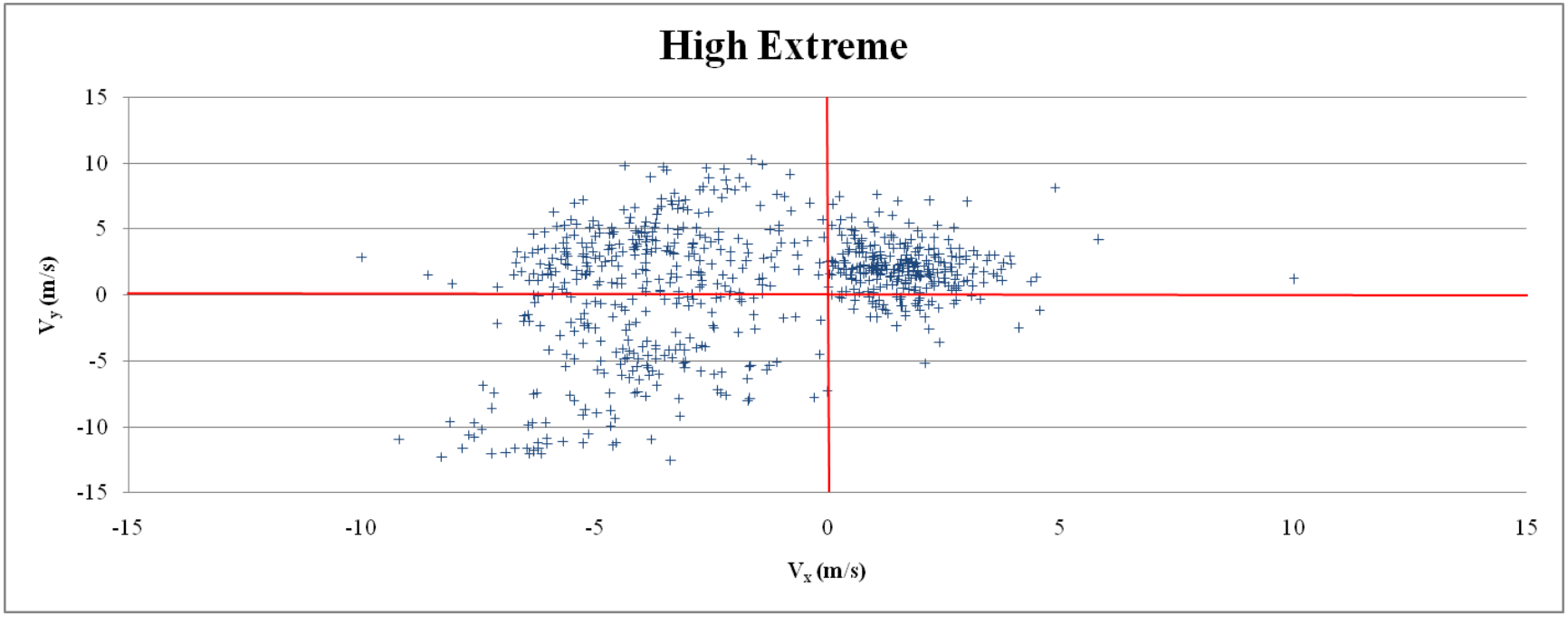

Figure D.1: Scatter plot of the Wind speed vector components for the *High Extreme* modeling scenario from the NOAA C-MAN Station SAUF1.

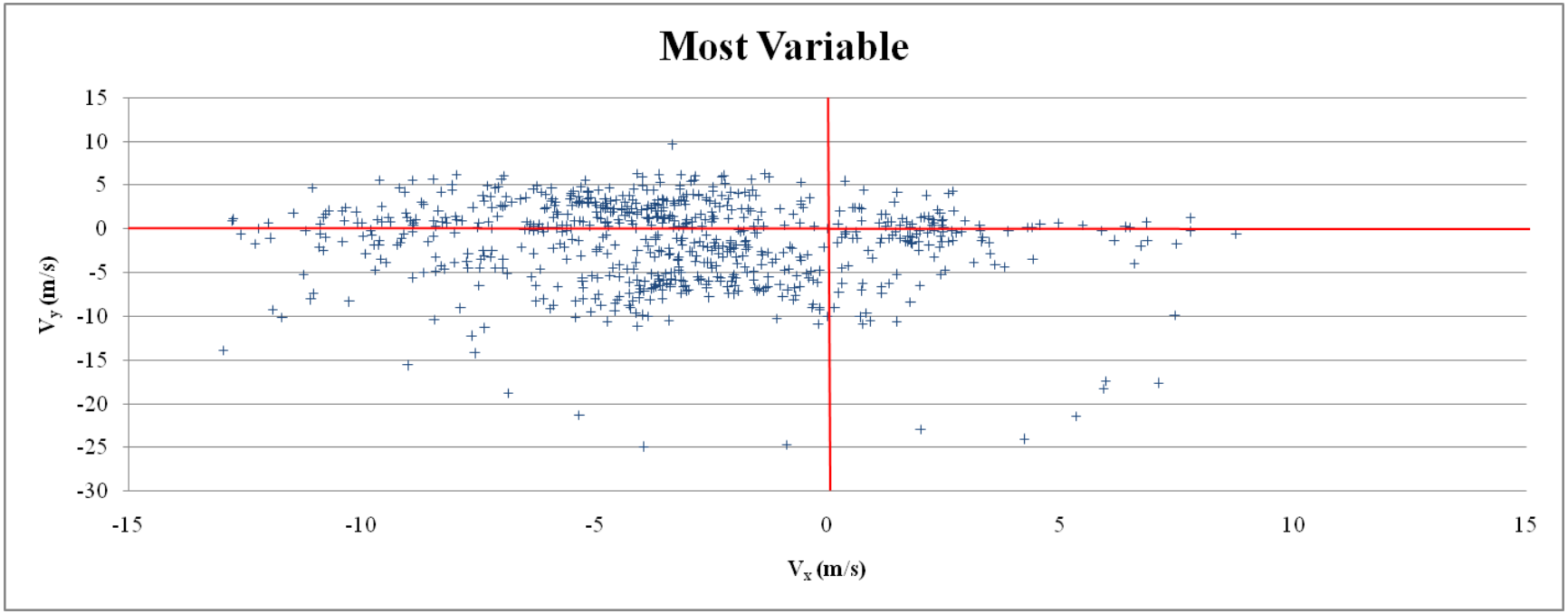

Figure D.2: Scatter plot of the Wind speed vector components for the *Most Variable* modeling scenario from the NOAA C-MAN Station SAUF1.

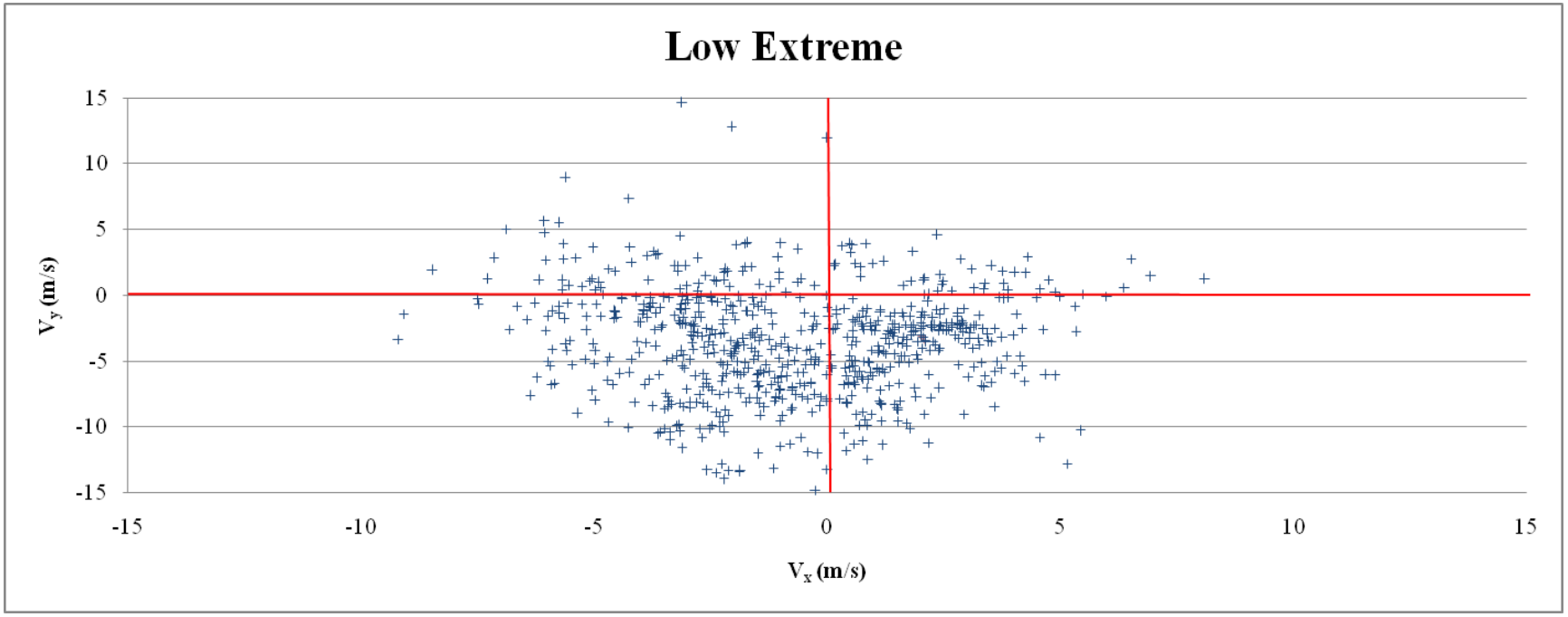

Figure D.3: Scatter plot of the Wind speed vector components for the *Low Extreme* modeling scenario from the NOAA C-MAN Station SAUF1.

APPENDIX E
RIVER INFLOW VALIDATION PLOTS

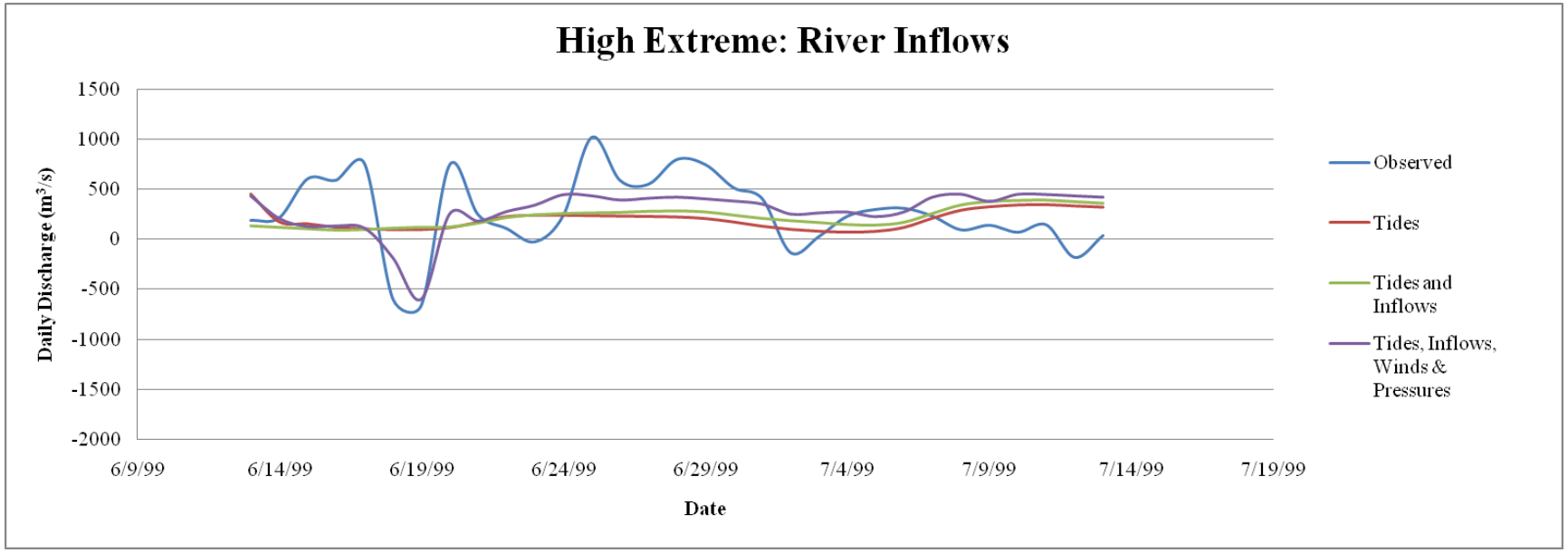

Figure E.1: River inflows from USGS Station 02246500 located in Jacksonville, FL during the *High Extreme* modeling scenario compared to the daily discharges modeled with three different combinations: (1) tides, (2) tides and inflows, and (3) tides, inflows, and winds and pressures.

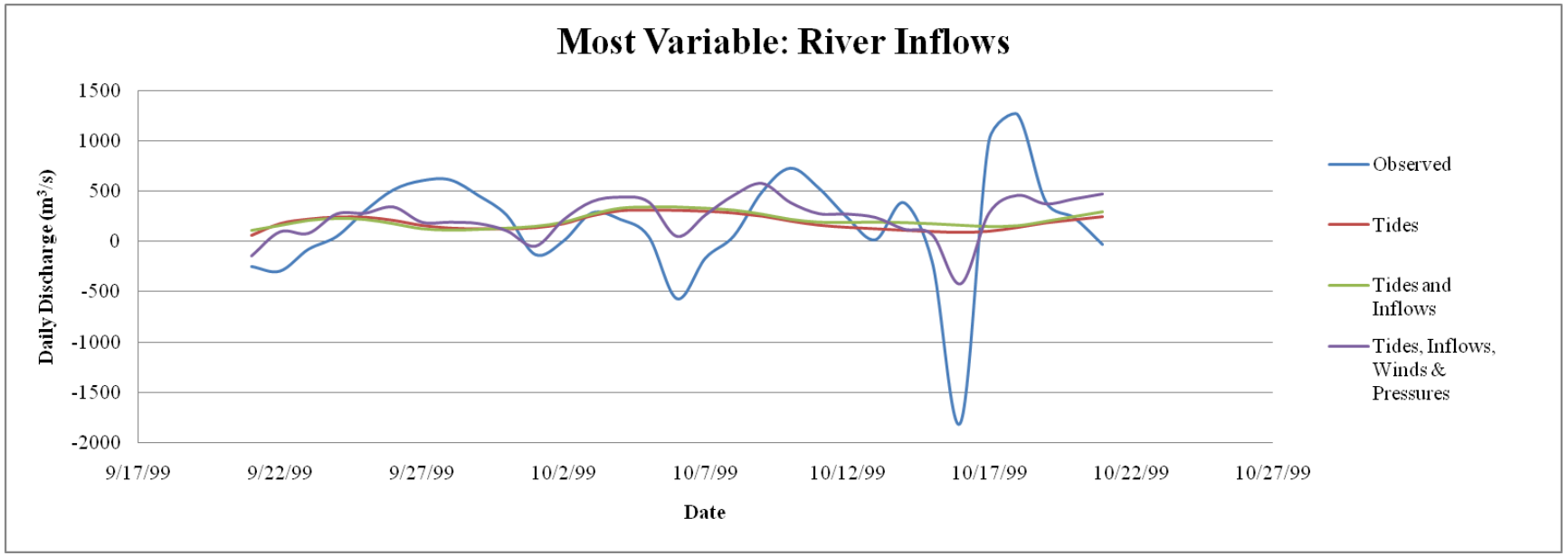

Figure E.2: River inflows from USGS Station 02246500 located in Jacksonville, FL during the *Most Variable* modeling scenario compared to the daily discharges modeled with three different combinations: (1) tides, (2) tides and inflows, and (3) tides, inflows, and winds and pressures.

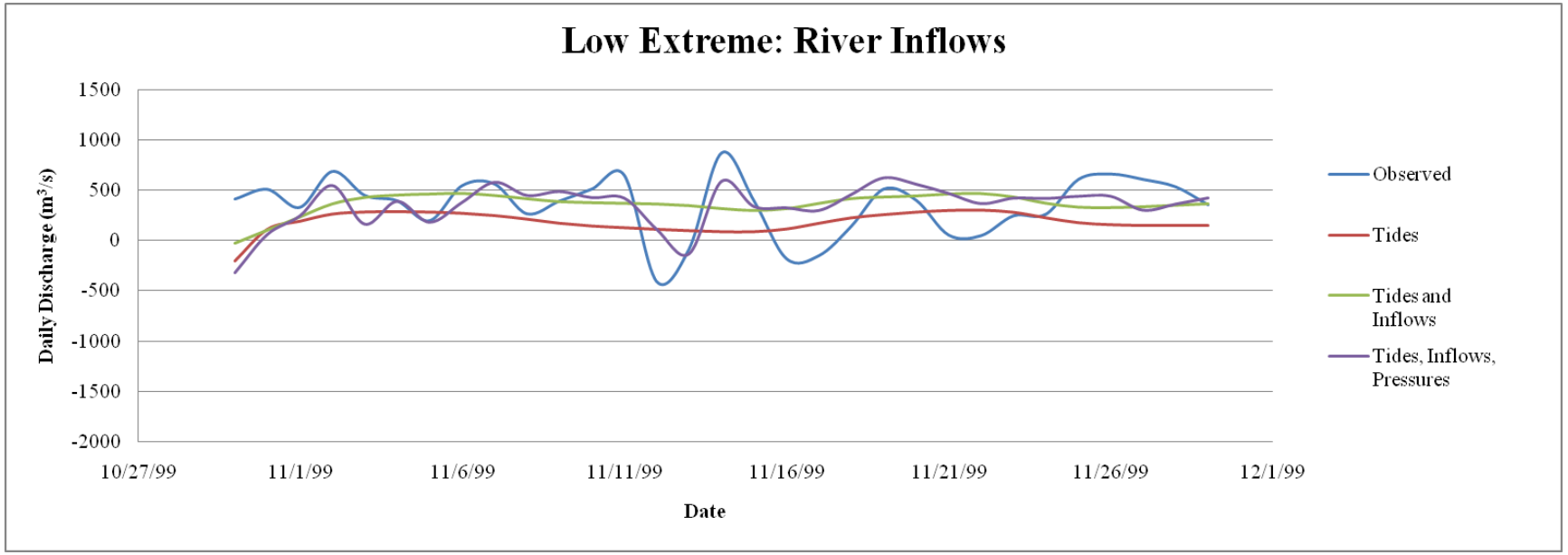

Figure E.3: River inflows from USGS Station 02246500 located in Jacksonville, FL during the *Low Extreme* modeling scenario compared to the daily discharges modeled with three different combinations: (1) tides, (2) tides and inflows, and (3) tides, inflows, and winds and pressures.

APPENDIX F
LAND COVER CLASS DESCRIPTION

Table F.1: NLCD 1992 Class Descriptions with reclassification based on NLCD 2001 classifications.

Enumerated Domain Value	2001 Class Value	Name	Definition
11	11	Open Water	All areas of open water, generally with less than 25% cover of vegetation or soil.
21	22	Low Intensity Residential	Includes areas with a mixture of some constructed materials and vegetation. Constructed materials account for 30 - 80 percent of the cover. Vegetation may account for 20 to 70 percent of the cover. These areas most commonly include single-family housing units. Population densities will be lower than in high intensity residential areas.
22	23	High Intensity Residential	Includes highly developed areas where people reside in high numbers. Examples include apartment complexes and row houses. Vegetation accounts for less than 20 percent of the cover. Constructed materials account for 80 to 100 percent of the cover.
23	24	Commercial/Industry/Transportation	Includes infrastructure (e.g. roads, railroads, etc.) and all highly developed areas not classified as High Intensity Residential.
31	31	Bare Rock/Sand/Clay	Perennially barren areas of bedrock, desert pavement, scarps, talus slides, volcanic material, glacial debris, beaches, and other accumulations of earthen material.
32	31	Quarries/Strip Mines/Gravel Pits	Areas of extractive mining activies with significant surface expression.
33	31	Transitional	Areas of sparse vegetative cover (less than 25 percent of cover) that are dynamically changing from one land cover to another, often because of land use activities. Examples include forest clearcuts, a transition phase between forest and agricultural land, the temporary clearing of vegetation, and changes due to natural causes (e.g. fire, flood, etc.).
41	41	Deciduous Forest	Areas dominated by trees where 75 percent or more of the tree species shed foliage simultaneously in response to seasonal change.
42	42	Evergreen Forest	Areas dominated by trees where 75 percent of more of the tree species maintain their leaves all year. Canopy is never without green foliage.
43	43	Mixed Forest	Areas dominated by trees where neither deciduous nor evergreen species represent more than 75 percent of the cover present.
51	52	Shrubland	Areas dominated by shrubs; shrub canopy accounts for 25 - 100 percent of the cover. Shrub cover is generally greater than 25 percent when tree cover is less than 25 percent. Shrub cover may be less than 25 percent in cases when the cover of other life forms (e.g. herbaceous or tree) is less than 25 percent and shrubs cover exceeds the cover of the other life forms.
61		Orchards/Vineyards/Other	Orchards, vineyards, and other areas planted or maintained for the production of fruits, nuts, berries, or ornamentals.
71	71	Grasslands/Herbaceous	Areas dominated by upland grasses and forbs. In rare cases, herbaceous cover is less than 25 percent, but exceeds the combined cover of the woody species present. These areas are not subject to intensive management, but they are often utilized for grazing.
81	81	Pasture/Hay	Areas of grasses, legumes, or grass-legumes, or grass-legume mixtures planted for livestock grazing or the production of seed or hay crops.
82	82	Row Crops	Areas used for the production of crops, such as corn, soybeans, vegetables, tobacco, and cotton.
85	21	Urban/Recreational Grasses	Vegetation (primary grasses) planted in developed settings for recreation, erosion control, or aesthetic purposes. Examples include parks, lawns, golf courses, airport grasses, and industrial site grasses.
91	90	Woody Wetlands	Areas where forest or shrubland vegetation accounts for 25-100 percent of the cover and the soil or substrate is periodically saturated with or covered with water.
92	95	Emergent Herbaceous Wetlands	Areas where perennial herbaceous vegetation accounts for 75-100 percent of the cover and the soil or substrate is periodically saturated with or covered with water.

Table F.2: NLCD 2001 and 2006 Class Descriptions

Enumerated Domain Value	Name	Definition
11	Open Water	All areas of open water, generally with less than 25% cover of vegetation or soil.
21	Developed, Open Space	Includes areas with a mixture of some constructed materials, but mostly vegetation in the form of lawn grasses. Impervious surfaces account for less than 20 percent of total cover. These areas most commonly include large-lot single-family housing units, parks, golf courses, and vegetation planted in developed settings for recreation, erosion control, or aesthetic purposes
22	Developed, Low Intensity	Includes areas with a mixture of constructed materials and vegetation. Impervious surfaces account for 20-49 percent of total cover. These areas most commonly include single-family housing units.
23	Developed, Medium Intensity	Includes areas with a mixture of constructed materials and vegetation. Impervious surfaces account for 50-79 percent of the total cover. These areas most commonly include single-family housing units.
24	Developed, High Intensity	Includes highly developed areas where people reside or work in high numbers. Examples include apartment complexes, row houses and commercial/industrial. Impervious surfaces account for 80 to100 percent of the total cover.
31	Barren Land	Barren areas of bedrock, desert pavement, scarps, talus, slides, volcanic material, glacial debris, sand dunes, strip mines, gravel pits and other accumulations of earthen material. Generally, vegetation accounts for less than 15% of total cover.
41	Deciduous Forest	Areas dominated by trees generally greater than 5 meters tall, and greater than 20% of total vegetation cover. More than 75 percent of the tree species shed foliage simultaneously in response to seasonal change.
42	Evergreen Forest	Areas dominated by trees generally greater than 5 meters tall, and greater than 20% of total vegetation cover. More than 75 percent of the tree species maintain their leaves all year. Canopy is never without green foliage.
43	Mixed Forest	Areas dominated by trees generally greater than 5 meters tall, and greater than 20% of total vegetation cover. Neither deciduous nor evergreen species are greater than 75 percent of total tree cover.
52	Shrub/Scrub	Areas dominated by shrubs; less than 5 meters tall with shrub canopy typically greater than 20% of total vegetation. This class includes true shrubs, young trees in an early successional stage or trees stunted from environmental conditions.
71	Herbaceous	Areas dominated by grammanoid or herbaceous vegetation, generally greater than 80% of total vegetation. These areas are not subject to intensive management such as tilling, but can be utilized for grazing.
81	Hay/Pasture	Areas of grasses, legumes, or grass-legume mixtures planted for livestock grazing or the production of seed or hay crops, typically on a perennial cycle. Pasture/hay vegetation accounts for greater than 20 percent of total vegetation.
82	Cultivated Crops	Areas used for the production of annual crops, such as corn, soybeans, vegetables, tobacco, and cotton, and also perennial woody crops such as orchards and vineyards. Crop vegetation accounts for greater than 20 percent of total vegetation. This class also includes all land being actively tilled.
90	Woody Wetlands	Areas where forest or shrubland vegetation accounts for greater than 20 percent of vegetative cover and the soil or substrate is periodically saturated with or covered with water.
95	Emergent Herbaceous Wetlands	Areas where perennial herbaceous vegetation accounts for greater than 80 percent of vegetative cover and the soil or substrate is periodically saturated with or covered with water.

LIST OF REFERENCES

Aizinger, V., & Dawson, C. (2002). A discontinuous Galerkin method for two-dimensional flow and transport in shallow water. *Advances in Water Resources* , 67-84.

Aizinger, V., & Dawson, C. (2007). The Local Discontinuous Galerkin Methods for Three-Dimensional Shallow Water Flow. *Comput. Methods Appl. Mech. Engrg* (196), 734-746.

Avila, L. (1999). *Hurricane Irene, 13 - 19 October 1999.* National Weather Service, National Oceanic and Atmospheric Administration. Miami, Florida: National Hurriane Center.

Bacopoulos, P. (2005). *Analysis, Modeling, and Simulation of the Tides in the Loxahatchee River Estuary (Southeastern Florida).* MS Thesis, University of Central Florida, Department of Civil and Environmental Engineering , Orlando.

Bacopoulos, P. (2009). *Estuarine Influence on Tidally Driven Circulation in the South Atlantic Bight.* PhD Thesis, University of Central Florida, Department of Civil, Environmental, and Construction Engineering, Orlando, FL.

Bacopoulos, P., Funakoshi, Y., Hagen, S. C., Cox, A. T., & Cardone, V. J. (2009). The role of meteorological forcing on the St. Johns River (Northeastern Florida). *Journal of Hydrology , 369*, 55 - 70.

Bacopoulos, P., Parrish, D., & Hagen, S. (2011). Unstructured mesh assessment for tidal model of the South Atlantic Bight and its estuaries. *Journal of Hydraulic Engineering* (Special Issue on Coastal and Maritime Hydraulics, accepted).

Berger, R., & Howington, S. (2002, January). Discrete Fluxes and Mass Balance in Finite Elements. *Journal of Hydraulic Engineering* , 87-92.

Blain, C. A., & Massey, T. C. (2005). Application of a coupled discontinuous-continuous Galerkin finite element shallow water model to coastal ocean dynamics. *Ocean Modelling , 10*, 283-315.

Blumberg, A. F. (1977, March). Numerical Model of Estuarine Circulations. *Estuarine Circulation* , 295-310.

Blumberg, A. F. (1978). The Influence of Density Variations on Estuarine Tides and Circulations. *Estuarine and Coastal Marine Science , 6*, 209-215.

Boon, J. D. (2004). *Tide and Tidal Current Analysis and Predictions, Storm Surges and Sea Level Trends.* England: Horwood Publishing Limited.

Borg, M. C., Calliari, D., Gorokhova, E., Thor, P., & Tiselius, P. (2008). Instantaneous salinity reductions affect the survival and feeding rates of the co-occuring copepods Acartia tonsa Dana and A. clausi Giesbrecht differently. *Journal of Experimental Marine Biology and Ecology* , 18-25.

Bourgerie, R. (1999). *Currents in the St. Johns River, Florida: Spring ad Summer of 1998.* Washington, D.C.: National Oceanic and Atmospheric Adminstration, National Ocean Service, U.S. Department of Commerce.

Bradley, P., & Morris, J. (1991). The influence of salinity on the kinetics of NH4+ uptake in Spartina alterniflora. *Oecologia , 85*, 375-380.

Brown, C., Pezeshi, S., & DeLaune, R. (2006). The effects of salinity and soil drying on nutrient uptake and growth of Spartina alterniflora in a simulated tidal system. *Environmental and Experimental Botany , 58*, 140-148.

Bulger, A. J., Hayden, B. P., Monaco, M. E., Nelson, D. M., & McCormick-Ray, M. G. (1993). Biologically-Based Estuarine Salinity Zones Derived from a Multivariate Analysis. *Estuaries , 16* (2), 311-322.

Calliari, D., Anderson Borg, M. C., Thor, P., Gorokhova, E., & Tiselius, P. (2008). Instantaneous salinity reductions affect the survival and feeding rates of the co-occurring copepods Acartia tonsa Dana and A. clausi Giesbrecht differently. *Journal of Experimental Marine Biology and Ecology , 362*, 18-15.

Carter, R. (1988). *Coastal Environments: An Introduction to the Physical, Ecological and Cultural Systems of Coastlines.* San Diego, CA, U.S.A.: Academic Press Inc.

Chau, K., & Jiang, Y. (2002). Three-dimensional pollutant transport model for the Pearl River Estuary. *Water Research , 36*, 2029-2039.

Cheeseman, J. M. (1988). Mechanisms of Salinity Tolerance in Plants. *Plant Physiology , 87*, 547-550.

Clivia Society - The Noble Family of Clive. (n.d.). Retrieved May 25, 2010, from http://www.cliviasociety.org/william_t_aiton_william_hooker_john_lindley.php

Cockburn, B. (2003). Discontinuous Galerkin methods: Plenary lecture presented at the 80th Annual GAMM Conference, Augsburg, 25-28 March 2002. *Math. Mech. , 83* (11), 731-754.

Cornell University Facilities Services Utilities and Energy Management. (n.d.). Retrieved May 6, 2010, from http://www.utilities.cornell.edu/utl_lsceis_glossary.html

Cronk, J., & Fennessy, M. S. (2001). *Wetland Plants: Biology and Ecology.* Boca Raton, FL: CRC Press LLC.

Dahl, E. (1956). Ecological Salinity Boundaries in Poikilohaline Waters. *Oikos , 7* (1), 1-21.

Dahl, T. E. (1998). *Florida's Wetlands: An Update on Status and Trends 1985 to 1996.* Washington, D.C.: U.S. Fish and Wildlife Service.

Dahl, T. E., & Stedman, S.-M. (2008). *Status and Trends of Wetlands in the Coastal Watersheds of the Eastern United States 1998 to 2004.* NOAA, National Marine Fisheries Service, and U.S. Dept. of the Interior, Fish, and Wildlife Services.

Dawson, C., & Mirabito, C. M. (2008, September 29). The Shallow Water Equations. Austin, Texas: University of Texas: Institute for Computational Engineering and Sciences.

Dawson, C., & Proft, J. (2004). Coupled Discontinuous and Continuous Galerkin Finite Element Methods for the Depth-Integrated Shallow Water Equations. *Comput. Methods Appl. Mech. Engrg* (193), 289-318.

Dawson, C., Sun, S., & Wheeler, M. F. (2004). Compatible algorithms for coupled flow and transport. *Computer Methods in Applied Mechanics and Engineering , 193*, 2565-2580.

Dawson, C., Westerink, J. J., Feyen, J. C., & Pothina, D. (2006). Continuous, Discontinuous, and Coupled Discontinuous - Continuous Galerkin Finite Element Methods for the Shallow Water Equations. *International Journal for Numerical Methods in Fluids , 52*, 63-88.

Dietrich, J., Kolar, R., & Dresback, K. (2008). Mass Residuals as a Criterion for Mesh Refinment in Continuous Galerkin Shallow Water Models. *Journal of Hydraulic Engineering* , 520-532.

Dyer, K. (1973). *Estuaries: A Physical Introduction.* Wiley-Interscience.

Elliott, A. (1976). *A numerical model of the internal circulation in a branching estuary.* Chesapeake Bay Institute. The Johns Hopkins University.

Ewing, K., Hester, M., McKee, K., & Mendelssohn, I. (1995). A comparison of indicators of sublethal salinity stress in the salt marsh grass, Spartina patens (Ait.) Muhl. *Aquatic Biology* , 59-74.

Fischer, H. B. (1976). Mixing and Dispersion in Estuaries. *Annual Review of Fluid Mechanics , 8*, 107-133.

Funakoshi, Y. (2006). *Coupling of Hydrodynamic and Wave Models for Storm Tide Simulations: A Case Study for Hurrican Floyd (1999).* PhD Thesis, University of Central Florida, Department of Civil and Environmental Engineering, Orlando.

Giardino, D. (2009). *Analysis of the Physical Forcing Mechanisms Influencing Salinity Transport for the Lower St. Johns River.* MS Thesis, University of Central Florida, Department of Civil, Environmental, and Construction Engineering, Orlando, FL.

Gourgue, O., Comblen, R., Lambrechts, J., Karna, T., Legat, V., & Dellersnijder, E. (2009). A flux-limiting wetting-drying method for finite-element shallow-water models, with application to the Scheldt Estuary. *Advances in Water Resources , 32*, 1726-1739.

Griffin, D. A., & LeBlond, P. H. (1990). Estuary/Ocean Exchange Controlled by Spring-Neap Tidal Mixing. *Estuarine, Coastal, and Shelf Science , 30* (3), 275-297.

Gunnison, D. (1978). *Mineral Cycling in Salt Marsh-Estuarine Ecosystems: Ecosystem Structure, Function, and General Compartment Model Describing Mineral Cycles.* U.S. Army Engineer Waterways Experiment Stations.

Hester, M. W., Mendelssohn, I. A., & McKee, K. L. (2001). Species and population variation to salinity stress in Panicum hemitomon, Spartina patens, and Spartina alterniflora:

morphological and physiological constraints. *Environmental and Experimental Botany , 46*, 277-297.

Hsu, M.-H., Liu, W.-C., & Kuo, A. Y. (2002). Modeling of Hydrodynamics and Cohesive Sediment Transport in Tanshui River Estuarine System, Taiwan. *Marine Pollution Bulletin* , 1076-1088.

Janzen, C. (2003). *Conductivity Sensors for Moored and Autonomous Operation.* Retrieved October 11, 2010, from Sea-Bird Electronics, Inc.: http://www.seabird.com/technical_references/condpaper.htm

Kolar, R., Westerink, J., Caniekin, M., & Blain, C. (1994). Aspects of Nonlinear Simulation using Shallow Water Models Based on the Wave Continuity Equation. *Computers Fluids , 23* (3), 523-538.

Kubatko, E. (2005). *Development, Implementation, and Verfication of hp Discontinuous Galerkin Models for Shallow Water Hydrodynamics and Transport.* University of Notre Dame, Civil Engineering and Geological Sciences. Notre Dame, IN: University of Notre Dame.

Kubatko, E. (2010, July 8). Discontinuous Galerkin (DG) Methods for Hydrodynamics and Transport. University of Central Florida: CHAMPS Laboratory, Guest Lecture. Orlando, FL, USA.

Kubatko, E. (2011, January 31). Finite Element Methods. University of Central Florida, CWR6535:Modeling Water Resources Systems Guest Lecture. Orlando, FL.

Kubatko, E. J., Bunya, S., Dawson, C., Westerink, J., & Mirabito, C. (2009). A Performance Comparison of Continuous and Discontinuous Finite Element Shallow Water Models. *Journal of Scientific Computing* , 315-339.

Kubatko, E. J., Westerink, J. J., & Dawson, C. (2006). hp Discontinuous Galerkin methods for advection dominated problems in shallow water flow. *Computational Methods in Applied Mechanics and Engineering* , 437-451.

Kuo, C. Y. (1973). *Effects of Salinity and Turbulent Diffusion of Pollutants.* Water Resources Research Institute. Washington, D.C.: U.S. Department of the Interior.

Lee, T., & Williams, E. (1988). Wind-forced transport fluctuations of the Florida Current. *Journal of Physical Oceanography , 18*, 937-946.

Lee, T., Scgott, F., & Zantopp, R. (1985). Florida Current: Low-Frequency Variability as Observed with Moored Current Meters during April 1982 to June 1983. *Science* (227), 298-302.

limgis 2001. (n.d.). Retrieved May 6, 2010, from http://ces.iisc.ernet.in/energy/monograph1/Glossary.html

Linthurst, R. A., & Seneca, E. D. (1981). Aeration, Nitrogen and Salinity as Determinants of Spartina alterniflora Loisel. Growth Response. *Estuares , 4* (1), 53-63.

Liu, W.-C., Hsu, M.-H., Kuo, A. Y., & Hung, H.-Y. (2007). Effect of channel connection on flow and salinity distribution of Danshuei River estuary. *Applied Mathematical Modelling , 31*, 1015-1028.

Liu, W.-C., Hsu, M.-H., Kuo, A. Y., & Kuo, J.-T. (2001). The Influence of River Discharge on Salinity Intrusion in the Tanshui Estuary, Taiwan. *Journal of Coastal Research , 17* (3), 544-552.

Macmillan, C. D. (1966). *Tides.* New York: American Elsevier Publishing Company.

Molles Jr., M. C. (2008). *Ecology: Concepts and Applications, Fourth Edition.* New York: The McGraw-Hill Companies.

Morris, F. (1995). *Volume 3 of the Lower St. Johns River basin Reconnaissance Hydrodynamics and salinity of surface water.* Palatka, FL: St. Johns River Water Management District.

Morris, J. T. (2000). Effects of Sea-Level Anomalies on Estuarine Processes. In J. E. Hobbie, *Estuarine Science: A Synthetic Approach to Research and Practice* (pp. 107-127). Washington, DC: Island Press.

Naifar, F., Wilders, P., Heemink, A. W., & Stelling, G. S. (2007). On the coupling of uncoupled flow and transport solvers. *Estuarine, Coastal, and Shelf Science , 74*, 732-741.

National Aeronautics Space Administration (NASA). (n.d.). Retrieved May 25, 2010, from http://science.nasa.gov/glossary/practical-salinity-unit

National Data Buoy Center. (2011). Retrieved 2011, from National Oceanic and Atmospheric Administration: http://www.ndbc.noaa.gov

Nestler, J. (1977). Interstitial Salinity as a Cause of Ecophenic Variation in Spartina alterniflora. *Estuarine and Coastal Marine Science , 5*, 707-714.

NOAA. (2008). *NOAA Ocean Service Education*. Retrieved April 1, 2010, from http://oceanscience.noaa.gov/education/kits/estuaries/estuaries04_geology.html

Oliveira, A., Fortunato, A. B., & Baptista, A. M. (2000, August). Mass Balance in Eulerian-Lagrangian Transport Simulations in Estuaries. *Journal of Hydraulic Engineering* , 605-614.

Pearcy, R. W., & Ustin, S. L. (1984). Effects of salinity on growth and photosynthesis of three California tidal marsh species. *Oecologia (Berlin)* , *62*, 68-73.

Philibert, J. (2005). One and a Half Century of Diffusion: Fick, Einstein, before and beyond. *Diffusion Fundamentals , 2*, 1.1 - 1.10.

Por, F. (1972). Hydrobiological notes on the high-salinity waters of the Sinai Peninsula. *Marine Biology , 14*, 111-119.

Ramey, V. (2004). *Evaporation and Evapotranspiration*. (B. Hassell, Editor) Retrieved August 27, 2010, from Plant Management in Florida Waters: http://plants.ifas.ufl.edu/guide/evaptran.html

Randall, D. A. (2006). *The Shallow Water Equations.* Colorado State University, Department of Atmospheric Science, Fort Collins, Colorado.

Sagan, J. J. (2007). *A Summary of Submerged Aquatic Vegetation (SAV) Status within the Lower St. Johns River: 1996-2007.* St. Johns River Water Management District.

Schroeder, W., Dinnel, S., & Wiseman, W. (1992). Salinity structure of a shallow, tributary estuary. In D. Prandle, *Dynamics and Exchanges in Estuaries and the Coastal Zone* (pp. 155-171). Washington DC: American Geophysical Union.

Schureman, P. (1941). *Manual of harmonic analysis and prediction of tides.* Washington, D.C.: Coast and Geodetic Survey, U.S. Department of Commerce, U.S. Government Printing Office.

Shaha, D., Cho, Y., Seo, G., Kim, C., & Jung, K. (2010). Using flushing rate to investigate spring-neap and spatial variations of gravitational circulation and tidal exchanges in an estuary. *Hydrology and Earth System Sciences , 14*, 1465-1476.

Stephenson, D., & Hodgson, D. (1996). Root Zone Moisure Gradients Adjacent to a Cedar Swamp in Southern Ontario. In G. Mulamoottil, B. G. Warner, & E. A. McBean, *Wetlands: Environmental Gradients, Boundaries, and Buffers* (pp. 79-90). Boca Raton, Florida , United States of America: CRC Press, Inc.

Stewart, J. B., Rouhani, S., & Sucsy, P. (2009, January). Chapter 1: Geostatistical Analysis of Observed Data in Support of the Analysis of the Impact of Alternative Water Supply Withdrawals from the St. Johns River, Florida. *Alternative Water Supply Assessment , 1* , 1 - 17. (E. Lowe, & L. E. Battoe, Eds.) Florida, United States of America: St. Johns River Water Management District.

Sucsy, P. V., & Morris, F. W. (2002). *Calibration of a Three-dimensional Circulation and Mixing Model of the Lower St. Johns River.* Palatka, FL: St. Johns River Water Management District.

Sucsy, P., & Christian, D. (2009, January). Chapter 3: Salinity Scenarios. *Alternative Water Supply Cumulative Impact Assessment , 1* , 1-16. (E. F. Lowe, & L. E. Battoe, Eds.) Florida, United States of America: St. Johns River Water Management District.

Sudirham, J., van der Vegt, J., & van Damme, R. (2006). Space-time discontinuous Galerkin method for advection-diffusion problems on time-dependent domains. *Applied Numerical Mathematics* (56), 1491-1518.

Sweet, W., Zervas, C., & Gill, S. (2009). *Elevated East Coast Sea Levels Anomaly: June - July 2009.* NOAA Technical Report NOS CO-OPS 051. Silver Spring, MD: NOAA National Ocean Service.

Tan, W.-Y. (1992). *Shallow Water Hydrodynamics.* New York: Elsevier Science Publishing Company, Inc.

Teh, S. Y., DeAngelis, D. L., da Silveira Lobo Sternberg, L., Miralles-Wilhelm, F. R., Smith, T. J., & Koh, H.-L. (2008). A simulation model for projecting changes in salinity concentrations and species dominance in the coastal margin habitats of the Everglades. *Ecological Modelling , 213,* 245-256.

Texas Grant Consortium. (n.d.). Retrieved May 21, 2010, from http://www.tsgc.utexas.edu/topex/activities/elnino/sld005.html

The International Plant Names Index. (n.d.). Retrieved May 25, 2010, from http://www.ipni.org/ipni/idPlantNameSearch.do?id=10360882&back_page=%2Fipni%2FeditSimplePlantNameSearch.do%3Ffind_wholeName%3Dspartina%2Bpatens%26output_format%3Dnormal

The Tortoise Reserve. (n.d.). Retrieved May 25, 2010, from http://www.tortoisereserve.org/research/Muhlenberg.html

Toth, D. J. (1993). *Volume 1 of the Lower St. Johns Rver Basin Reconnaissance: Hydrogeology.* Palatka, FL: St. Johns River Water Management District.

Tyrrell, H. (1964). The Origin and Present Status of Fick's Diffusion Law. *Journal of Chemical Education , 41* (7), 397 - 400.

U.S. Geological Survey (USGS). (n.d.). Retrieved May 21, 2010, from http://toxics.usgs.gov/definitions/pore_water.html

USGS. (2006, April 17). *Water-Use Estimates Based on Open-Water Evaporation and Evapotranspiration Losses.* Retrieved August 27, 2010, from USGS: http://pubs.usgs.gov/sir/2006/5036/section4.html

USGS WaterWatch -- Streamflow Conditions. (2011). Retrieved 2011, from USGS: http://waterwatch.usgs.gov

Vreugdenhil, C. B. (1994). *Numerical Methods for Shallow-Water Flow.* The Netherlands: Kluwer Academic Publishers.

Wang, C.-F., Wang, H. V., & Kuo, A. Y. (2008, August). Mass Conservative Transport Scheme for the Application of the ELCIRC Model to Water Quality Computation. *Journal of Hydraulic Engineering* , 1166-1171.

Wang, D.-P., & Kravitz, D. W. (1980). A Semi-Implicit Two-Dimensional Model of Estuarine Circulation. *Journal of Physical Oceanography , 10*, 441 - 454.

Weisstein, E. W. (1999-2011). *Divergence Theorem*. Retrieved March 21, 2011, from Wolfram MathWorld: http://mathworld.wolfram.com/DivergenceTheorem.html

Wolanski, E. (2007). *Estuarine Ecohydrology.* Netherlands: Elsevier B.V.

Woodhouse, W. J., Seneca, E., & Broome, S. (1974). *Propagation of Spartina alterniflora for substrate stabilization and salt marsh development.* Ft. Belvoir, VA: U.S. Army Corps of Engineers, Coastal Engineers Research Center.